Experimental and Computational Studies of Electric Thruster Plasma Radiation Emission

by

Murat Çelik
B.S., Aerospace Engineering and Physics, University of Michigan, 2000
M.S., Aeronautics, California Institute of Technology, 2001

Submitted to the Department of Aeronautics and Astronautics
in partial fulfillment of the requirements for the degree of

Doctor of Philosophy
at the
MASSACHUSETTS INSTITUTE OF TECHNOLOGY
May 2007

© Massachusetts Institute of Technology 2007. All rights reserved.

Author .....
Department of Aeronautics and Astronautics
May 14, 2007

Certified by .....
Manuel Martínez-Sánchez
Professor, Aeronautics and Astronautics
Thesis Supervisor

Certified by .....
Oleg Batishchev
Principal Research Scientist, Aeronautics and Astronautics
Thesis Supervisor

Read by .....
Daniel Hastings
Professor, Aeronautics and Astronautics

Read by .....
Vlad Hruby
President, Busek Co. Inc.

Read by .....
David Miller
Professor, Aeronautics and Astronautics

Accepted by .....
Jaime Peraire, Professor of Aeronautics and Astronautics
Chair, Committee on Graduate Students

Experimental and Computational Studies of Electric Thruster Plasma Radiation Emission

by

Murat Çelik

Submitted to the Department of Aeronautics and Astronautics
on May 14, 2007, in partial fulfillment of the
requirements for the degree of
Doctor of Philosophy

Abstract

Electric thrusters are being developed for in-space propulsion needs of spacecraft as their higher specific impulse enables a significant reduction in the required propellant mass and allows longer duration missions. Over the last few decades many different electric propulsion concepts have been proposed and studied. In studying the electric thrusters, in order to improve the thruster performance as well as to understand the underlying physics of thruster's operation, various diagnostics methods were employed.

As one unique method, emission spectroscopy provides a non-invasive, fast and economical diagnostic allowing also the ability to access hard to reach locations. In this study, emission spectroscopy is employed as a means to determine the trends in thruster operations as well as diagnosing the plasma parameters.

This study presents the spectral measurement results of three different electric thrusters and plasma sources. First, the BHT-200 Hall thruster emission spectra measurements are presented for varying discharge voltage and for various regions of observation. Second, spectral measurements of a TAL type laboratory mini-Hall thruster, MHT-9, were presented. Third, radiation emission measurements of an experimental Helicon plasma source being studied to assess the possibility of using Helicon discharge as a propulsive system are presented and the trends are discussed.

Two collisional-radiative (C-R) models are developed for Argon and Xenon plasmas to analyze the experimental spectra. In the C-R models, electron induced excitation, de-excitation and ionization collisions, and spontaneous radiative de-excitation transitions are simulated for neutral and singly charged ion species. The models are validated against measured spectra obtained using different experimental setups.

The BHT-200 Hall thruster has insulator ceramic annular walls made of Boron-Nitride (BN). Erosion of ceramic walls is one of the major life limiting factors for Hall thrusters. Emission spectroscopy is used as a means to determine the trends in the thruster wall erosion rate

by measuring the radiation emission of the Boron neutral 249.68nm and 249.77nm lines. Discussion about the spectral measurements and relevant analysis are presented.

Thesis Supervisor: Manuel Martínez-Sánchez
Title: Professor, Aeronautics and Astronautics

Thesis Supervisor: Oleg Batishchev
Title: Principal Research Scientist, Aeronautics and Astronautics

Acknowledgments

I have been calling myself a *student* for almost as long as I can remember. I have finally come to the end of the long educational journey that I embarked on more than two decades ago. I would like to express my gratitude and appreciation to all those countless individuals who had a part in my education in all those years.

First and foremost, I want to thank my parents, Mehmet and Necla, for always standing by me, supporting me in my decisions, and for believing in me. Without their support, I would not be where I am today.

I would also thank other members of my family for supporting me throughout my education. I would like to specifically thank my grandfather, Osman Nuri Berber, who definitely had an effect on me being the curious person that I am; my sister, Emel, who has always been supportive of me; and my uncle, Sezai Berber, who has been a role model to me while I was growing up.

I would like to thank my Ph.D. research advisor Prof. Martínez-Sánchez. His guidance was invaluable throughout my years at MIT. He was always available to answer my questions and he gave me the freedom to pursue my other interests along with my doctoral research. I am thankful for that.

I would like to thank my research advisor, Dr. Oleg Batischev. I am indebted to him for supporting me during the last year of my study at MIT. He brought a great deal of excitement into my research. He has always been supportive of me, and has always been the biggest encouragement to me in moments when I was most frustrated. He became a mentor and a good friend. I will always remember him being with me during the many late night experiments, and will definitely remember the oil spill in the lab. And here is a quote from one of his e-mails that will not be forgotten: "Hope floats, -O"

I would also like to thank the members of my thesis committee: Professor David Miller, Dr. Vlad Hruby, and Professor Daniel Hastings. I also thank Professor Marcus Zahn for giving me the opportunity and the challenge to teach a graduate level course. He was an incredible

mentor to me as I had my first real academic teaching experience. I learned a lot from him.

I would like to thank all those great people I met at MIT Space Propulsion Laboratory. Six years is a long time and unfortunately I won't be able to count the names of all the people I had the good fortune of meeting at this lab. I would particularly thank Tanya for being a great friend and for helping me with the editing of this thesis, my officemates Shannon, Blaise and Dan for creating a great office environment, my ex-roommate and good friend Felix for the many interesting discussions, and my Helicon plasma research partner and good friend Justin for sharing some of the pain with me during the last year and a half and for the exciting conversations we had.

Nareg, my friend, I also want to express a special thank to you for all your dedicated work in the lab helping me and others. Without your help I would not be able to do some of my experiments and I thank you for that.

I would also like to thank my high school friends who became my extended family and have always been supportive of me during my years away from my home country.

I also would like to thank Yu-Hui Chiu and Rainer Dressles of Air Force Research Laboratory at Hanscom for lending us the first set of spectral instruments that helped me start this doctoral research project. I also extend my thanks to Paul Pranzo of Acton Research Co. for allowing us to use the demonstration equipments. Also special thanks to people at Busek Co. for lending us the BHT-200 Hall thruster as well as the PMT detector.

Contents

1 Introduction **25**

1.1 Electric Propulsion 26

1.1.1 Hall Thruster 28

1.1.2 Helicon Thruster 29

1.2 Plasma Diagnostics 30

1.3 Emission Spectroscopy Physics 32

1.4 Emission Spectroscopy Setup 32

1.5 Collisional-Radiative Model (CRM) 38

1.6 Literature Review 40

1.6.1 Previous Emission Spectra Measurements of Electric Thrusters and Related C-R Modeling 40

1.6.2 Collisional-Radiative Modeling of Argon 41

1.7 Thesis Content, Objectives and Contributions 42

2 Plasma Radiation Emission **47**

2.1 Line Radiation 47

2.2 Continuum Radiation 51

2.2.1 Bremsstrahlung Radiation 51

2.2.2 Electron-Recombination Radiation 53

2.2.3 Electron Cyclotron Radiation 54

2.2.4 Blackbody Radiation 55

3 BHT-200 Hall Thruster Spectral Measurements 57

3.1 BHT-200 Hall Thruster 57

3.2 Experimental Setup 58

3.2.1 Radiation Collection and Transmission 59

3.2.2 Radiation Dispersion 60

3.2.3 Radiation Detection 61

3.3 BHT-200 Hall Thruster Measurement Results 61

3.3.1 Regions of Observation 61

3.3.2 Voltage Scan 68

3.4 Prediction of Plasma Temperature from Line Intensity Ratio 73

3.5 Chapter Summary 74

4 MHT-9 Hall Thruster Spectral Measurements 79

4.1 MHT-9 Hall Thruster 79

4.2 TAL vs. SPT type of Hall Thrusters 80

4.3 Experimental Setup 81

4.4 MHT-9 Hall Thruster Measurement Results 82

4.4.1 Discharge Voltage Scan 84

4.4.2 Flow Rate Scan 84

4.4.3 Comparison of MHT-9 and BHT-200 Spectra 87

4.5 Chapter Summary 89

5 Spectral Measurements of a Helicon Plasma Source 91

5.1 Mini Helicon Thruster Experiment (mHTX) 92

5.2 Experimental Setup 94

5.2.1 Radiation Collection and Transmission 95

5.2.2 Radiation Dispersion 96

5.2.3 Radiation Detection 97

5.2.4 Intensity Calibration 97

5.3 Helicon Plasma Source Spectral Measurements 98

5.3.1 Broad-spectrum Results 100

5.3.2 ICP vs. Helicon Regimes 102

5.3.3 Power Scan 103

5.3.4 Flow Rate Scan . . . 105
5.3.5 Magnetic Field Intensity Scan . . . 106
5.3.6 Short vs. Long Antenna . . . 108
5.3.7 Copper vs. Steel Antenna . . . 109
5.3.8 Antenna vs. Plume Region . . . 110
5.3.9 Side Window vs. Back Window . . . 111
5.3.10 Narrow band-pass filter Measurement . . . 112
5.4 Chapter Summary . . . 113

6 Argon Collisional-Radiative Model 115

6.1 Collisional Radiative Modeling . . . 116
6.1.1 Discussion about the Corona Model Assumption . . . 117
6.2 Important Processes . . . 117
6.2.1 Electron Induced Excitation Collisions . . . 118
6.2.2 Electron Induced Ionization Collisions . . . 121
6.2.3 Heavy Particle Induced Excitation and Ionization Collisions . . . 122
6.2.4 Spontaneous Radiative De-excitation . . . 123
6.2.5 Electron Induced De-excitation Collisions . . . 123
6.2.6 Radiative Recombination of Electrons . . . 125
6.2.7 Photo-absorption, Stimulated Emission and Photo-ionization . . . 125

6.3 Discussion of the Argon C-R Model 126

6.3.1 Modeling Assumptions 126

6.3.2 Time Dependent Equation for the Level Population Density 128

6.3.3 Calculation of the Excitation Collision Rate Function 129

6.3.4 Calculation of the De-excitation Collision Rate Function 130

6.3.5 Calculation of the Ionization Collision Rate Function 130

6.4 C-R Model Flow Chart and Description 131

6.4.1 Energy Levels and Corresponding Degeneracy 132

6.4.2 Emission Lines 132

6.4.3 Einstein's Spontaneous Emission Coefficients 132

6.4.4 Oscillator Strength 133

6.4.5 Collision Rate Functions and Relevant Collision Coefficients 134

6.4.6 Initialization of the Level Population Densities 135

6.4.7 Time Loop: Calculation of the Level Population Densities 136

6.4.8 Reaching Steady State Level Population Density 137

6.4.9 Obtaining Simulated Emission Spectra 138

6.5 Simulation Results and Discussion 140

6.6 Chapter Summary 146

7 Xenon Collisional Radiative Model **147**

7.1 Description of the Xenon Collisional-Radiative Model 147

7.1.1 Calculation of the Excitation Collision Rate Function 148

7.1.2 Einstein's Spontaneous Emission Coefficients 150

7.1.3 Calculation of Level Population Densities 150

7.2 Simulation Results and Discussion 152

7.3 Chapter Summary 152

8 Optical Diagnostics of the BHT-200 Hall Thruster Surface Erosion 155

8.1 Literature Review 157

8.2 Discussion of the Erosion Rate Calculation 159

8.3 Experimental Setup 161

8.3.1 Radiation Collection and Transmission 161

8.3.2 Radiation Dispersion 163

8.3.3 Radiation Detection 163

8.4 Measurement Results 164

8.4.1 Voltage Scan 166

8.4.2 Anode Propellant Flow Rate Scan 170

8.5 Chapter Summary 171

9 Conclusions and Recommendations 175

9.1 Summary and Contributions 175

9.1.1 Experimental Study 176

9.1.2 Theoretical and Computational Study 178

9.2 Recommended Future Work 178

9.2.1 Experimental Measurements 178

9.2.2 Theoretical and Computational Work 179

A BHT-200 Hall Thruster Measured Spectral Graphs 183

B MHT-9 Hall Thruster Measured Spectral Graphs 195

C mHTX Helicon Plasma Source Measured Spectral Graphs 205

D CRM Simulated Argon Emission Lines 215

E CRM Simulated Xenon Emission Lines 227

List of Figures

1-1 Picture of an electric thruster, BHT-200 Hall Thruster, in operation 27

1-2 Schematic of a Hall Thruster [40] 29

1-3 Schematic of a Helicon Thruster 30

1-4 Illustration of the electronic energy levels and radiative emission 32

1-5 Illustration of the experimental setup for spectroscopic measurements 34

2-1 a)Spontaneous emission and b)Photo-absorption processes 48

2-2 Photon induced de-excitation process 49

2-3 Electron impact excitation and spontaneous emission processes 50

2-4 Heavy particle inelastic excitation collision and spontaneous de-excitation emission processes 50

2-5 Bremsstrahlung radiation 51

2-6 Electron recombination radiation 53

2-7 Electron cyclotron radiation 54

3-1 Optical shelf attached to the window port of the MIT-SPL vacuum tank . . 59

3-2 a)Acton Research 1m long fiber bundle, b) fiber end with single column of 19 200μm diameter fibers 60

3-3 a)Acton Research SpectraPro-500i Spectrometer, b)Roper Scientific Photometrics Cascade:650 CCD Detector 61

3-4 BHT-200 Hall Thruster in operation inside the MIT-SPL vacuum chamber . 62

3-5 Illustration of the regions of observation for the BHT-200 Hall Thruster . . . 63

3-6 Comparison of the discharge region emission spectra from Region-I (top) and Region-VII (bottom) 64

3-7 Comparison of the plume vs. discharge spectra 65

3-8 Comparison of the cathode vs. discharge region spectra 66

3-9 Comparison of the plume spectra along the thruster axis 67

3-10 Line emission intensity versus the plume region 68

3-11 Comparison of the discharge spectra for varying discharge voltages:100V-300V 69

3-12 Line emission intensity versus the discharge voltage variation 72

3-13 Calculated electron temperature dependence of the XeI line intensity ratios [51] 73

3-14 Comparison of the emission spectra in the plume region 75

4-1 Experimental setup for MHT-9 spectral measurements 81

4-2 MHT-9 Hall Thruster in operation inside the MIT-SPL vacuum chamber . . 82

4-3 Comparison of the MHT-9 spectra for varying discharge voltages: 100V-300V 83

4-4 Line emission intensity versus the discharge voltage variation 85

4-5 Comparison of the MHT-9 spectra for varying anode flow rate: $5.5 - 7.5 sccm$ 86

4-6 Line emission intensity versus the anode flow rate variation 87

4-7 Comparison of the MHT-9 and BHT-200 Hall thruster emission spectra . . . 88

5-1 Helicon Plasma Source Setup placed inside the MIT-SPL vacuum facility . . 92

5-2 Helical antenna placed around the quartz tube between the Helmholtz pair of electromagnets 93

5-3 Pictures of the helical RF antennas used in the Helicon plasma source experiments 94

5-4 Illustration of the experimental setup for spectroscopic measurements 94

5-5 Collimating-focusing lens system on the optical shelf attached to the MIT-SPL vacuum tank window port 95

5-6 Jarrel Ash MonoSpec-18 Spectrometer and Andor iDus DU420A CCD Detector 96

5-7 Manually changeable gratings and slits for MonoSpec18 spectrometer 97

5-8 Measured emission spectrum of the tungsten intensity calibration lamp . . . 98

5-9 Broadband spectra comparison for the ICP and Helicon discharge plasmas . 101

5-10 Comparison of the ICP and the Helicon discharge plasma in the 405-485nm region. The ICP spectrum is amplified 50 times in comparison to the Helicon spectrum. 102

5-11 Comparison of the Argon Plasma Spectra for Helicon and ICP modes of operation 104

5-12 Comparison of the Argon Plasma Spectra for Helicon and ICP modes of operation in 800-850nm region 105

5-13 Argon discharge antenna region spectrum for varying delivered power 106

5-14 Argon ion 434.8nm line emission as RF power delivered is varied 106

5-15 Argon ion 434.8nm line emission intensity versus RF power delivered 107

5-16 Argon ion 434.8nm line emission intensity as Argon flow rate is varied 107

5-17 Argon ion 434.8nm line emission intensity versus Argon propellant flow rate 108

5-18 Argon ion 434.8nm line emission intensity as the magnetic field intensity is varied 108

5-19 Argon ion 434.8nm line emission intensity versus Magnet current 109

5-20 Comparison of the emission spectra for short and long copper antennae . . . 109

5-21 Comparison of the emission spectra for Steel and Copper antennas 110

5-22 Comparison of the emission spectra for antenna and plume regions 111

5-23 Comparison of the emission spectra for side and back window observations . 112

5-24 Comparison of the emission spectra for with (bottom) and without (top) a narrow band filter centered at 489.5nm with a 9nm FWHM 114

6-1 Schematic of the electronic energy levels of an atom or an ion 117

6-2 Argon neutral and single ion energy levels 128

6-3 Illustration of the processes simulated in the Argon C-R model 129

6-4 Simulated population density of Argon neutral atom energy levels 138

6-5 Simulated Argon neutral steady state energy level electron population density 139

6-6 Simulation of the line widening by using a Gaussian form-factor 140

6-7 Experimental Spectra of Helicon and ICP modes of Argon Plasma 141

6-8 Comparison of Experimental and Simulated Argon emission Spectra of 400-850nm Region 142

6-9 Comparison of Experimental and Simulated Argon emission Spectra of 750-800nm Region 143

6-10 Comparison of Experimental and Simulated Argon emission Spectra of 800-850nm Region 144

6-11 Comparison of Experimental and Simulated Argon emission Spectra of 450-500nm Region 145

7-1 Xenon neutral and single ion energy levels 148

7-2 Drawin's fit for the apparent electron impact excitation collision data for Xe-I 473.12nm line [27] 149

7-3 Illustration of the processes simulated in the Xenon C-R model 151

7-4 Comparison of the Experimental and Simulated Xenon emission Spectra for the 800-1000nm Wavelength Region 153

8-1 BHT-200 Hall thruster ceramic annular walls made of Boron-Nitride 156

8-2 Illustration of the neutral Boron energy levels and the 249.68 and 249.77nm resonant emission lines 159

8-3 Schematic of the Thruster Erosion Rate Spectral Measurement Setup 161

8-4 Picture of the BHT-200 Hall thruster and the collimating lens/fiber system inside the vacuum chamber 162

8-5 Pictures of the collimating lens and the vacuum fiber-feedthrough 162

8-6 Acton Research-750i spectrometer with CCD and PMT detectors attached at the exit ports 163

8-7 Region of the BHT-200 Hall thruster where the collimating lens was pointed 164

8-8 BHT-200 Hall thruster measured spectrum of 245-255nm wavelength region . 165

8-9 BHT-200 Hall thruster measured spectrum of 247-250nm wavelength region . 166

8-10 Boron 249.677nm and 249.773nm line emission as the discharge voltage is varied 167

8-11 Boron 249.677nm and 249.773nm emission lines total integrated intensity for varying discharge voltage 168

8-12 Boron 249.677nm and 249.773nm emission lines total integrated intensity for varying thruster power 168

8-13 Comparison of neutral Boron and singly charged ion emission lines total integrated intensities for varying discharge voltage 168

8-14 BHT-200 Hall thruster measured spectra comparison for the 175V and 300V discharge voltages in the 249.0-250.55nm wavelength region 169

8-15 Boron 249.677nm and 249.773nm emission lines total integrated intensity for varying anode propellant flow rate 171

8-16 Comparison of neutral Boron and singly charged Xenon ion emission lines total integrated intensities for varying anode propellant flowrate 172

A-1 BHT-200 Hall Thruster Discharge Region Emission Spectra 400-460nm . . . 184

A-2 BHT-200 Hall Thruster Discharge Region Emission Spectra 460-520nm . . . 185

A-3 BHT-200 Hall Thruster Discharge Region Emission Spectra 520-580nm . . . 186

A-4 BHT-200 Hall Thruster Discharge Region Emission Spectra 580-640nm . . . 187

A-5 BHT-200 Hall Thruster Discharge Region Emission Spectra 640-700nm . . . 188

A-6 BHT-200 Hall Thruster Discharge Region Emission Spectra 700-760nm . . . 189

A-7 BHT-200 Hall Thruster Discharge Region Emission Spectra 760-820nm . . . 190

A-8 BHT-200 Hall Thruster Discharge Region Emission Spectra 820-880nm . . . 191

A-9 BHT-200 Hall Thruster Discharge Region Emission Spectra 880-940nm . . . 192

A-10 BHT-200 Hall Thruster Discharge Region Emission Spectra 940-1000nm . . 193

A-11 BHT-200 Hall Thruster Discharge Region Emission Spectrum 400-1000nm . 194

B-1 MHT-9 Hall Thruster Discharge Region Emission Spectra 400-460nm 196

B-2 MHT-9 Hall Thruster Discharge Region Emission Spectra 460-520nm 197

B-3 MHT-9 Hall Thruster Discharge Region Emission Spectra 520-580nm 198

B-4 MHT-9 Hall Thruster Discharge Region Emission Spectra 580-640nm 199

B-5 MHT-9 Hall Thruster Discharge Region Emission Spectra 640-700nm 200

B-6 MHT-9 Hall Thruster Discharge Region Emission Spectra 700-760nm 201

B-7 MHT-9 Hall Thruster Discharge Region Emission Spectra 760-820nm 202

B-8 MHT-9 Hall Thruster Discharge Region Emission Spectra 820-880nm 203

B-9 MHT-9 Hall Thruster Emission Spectrum 400-900nm 204

C-1 mHTX Helicon Plasma Source Helicon Mode Emission Spectra of the Antenna Region 400-660nm 207

C-2 mHTX Helicon Plasma Source Helicon Mode Emission Spectra of the Antenna Region 635-845nm 208

C-3 mHTX Helicon Plasma Source ICP Mode Emission Spectra of the Antenna Region 400-745nm 209

C-4 mHTX Helicon Plasma Source ICP Mode Emission Spectra of the Antenna Region 735-845nm 210

C-5 mHTX Helicon Plasma Source Antenna Region ICP vs. Helicon Modes Emission Spectra Comparison for 400-750nm 211

C-6 mHTX Helicon Plasma Source Antenna Region ICP vs. Helicon Modes Emission Spectra Comparison for 735-845nm 212

C-7 mHTX Helicon Plasma Source Antenna Region Emission Spectrum for Helicon Mode 213

C-8 mHTX Helicon Plasma Source Antenna Region Emission Spectrum for ICP Mode 214

List of Tables

3.1 BHT-200 Hall Thruster [19] 58

3.2 List of Prominent XeI and XeII Lines in 400-1000nm Wavelength Region . . 77

4.1 MHT-9 Hall Thruster [76] 80

5.1 List of Prominent ArI and ArII Lines in 300-1000nm Wavelength Region [3] 100

Chapter 1

Introduction

Due to their higher specific impulse and more controllable thrust levels, electric propulsion systems provide an attractive alternative to traditional chemical thrusters for many in-space propulsive applications. As a result, electric thrusters are likely to be commonly used in future spacecraft applications as the main propulsion systems. Unlike chemical thrusters that rely on the stored energy within the chemical bonds of the propellant, electric thrusters use external power sources to supply energy to the propellant that is expelled from the thruster at high velocities to produce the desired thrust.

Over the last few decades many different thruster concepts that use external electrical energy to accelerate particles to produce thrust have been developed. Such electric propulsion concepts are being studied extensively in order to understand the complex physics behind their operation. In addition, issues regarding the integration of electric thrusters into the spacecraft and the effects of the thruster plumes on the components and the operations of the spacecraft represent an important area of research.

In studying the electric thrusters, in order to improve the thruster performance as well as to understand the underlying physics of thruster operation, there have been theoretical and experimental studies of electric thruster plasmas. On the theoretical front, many computational models have been developed to simulate physical processes in the thruster plasma. The experimental work has focused on characterizing the thruster, diagnosing the plasma

parameters, determining operational life limiting factors for the thrusters as well as studying the issues regarding the integration of electric thrusters into the spacecraft.

There have been numerous diagnostics techniques employed in the experimental studies. In this study, electric thruster plasmas have been diagnosed by the spectral measurement of the radiation emission of the plasma. In addition, to facilitate the analysis, collisional-radiative (C-R) models have been developed to simulate the radiation emission from electric thruster plasmas.

1.1 Electric Propulsion

When in deep space or in orbit, space objects require thrusters to accomplish various maneuvers such as orbit insertion, station-keeping, or orbit correction. These operations are performed by thrusters that expel the propellant at high velocities away from the spacecraft into the vacuum of space. Unlike boost phase rocket engines that take an object from the surface of Earth into the orbit, and require immense amount of thrust in order to counteract the gravitational forces acting on the object, in-space systems operate in a vacuum environment with negligible gravitational forces acting.

In-space propulsion for spacecraft is currently done mainly by chemical thrusters that expel pressurized or high temperature propellant gas that is heated by the exothermic chemical reaction of the propellants. In chemical thrusters, the energy released by a chemical reaction between the propellant species is converted into the kinetic energy of the expelled gas. Thus, chemical propulsion systems are limited by the energy that is stored in the chemicals being burned.

In electric propulsion systems, acceleration of propellant gases is achieved by electrical heating of the propellant and ensuing thermodynamic expansion, or by the electromagnetic forces acting on the charged propellant particles in order to provide thrust to the space vehicle. Since the energy limitation of electric thrusters is determined by the power supply onboard, electric thrusters have high specific impulse [40], but low thrust. A picture

of an electric thruster, BHT-200 Hall thruster, running inside the MIT Space Propulsion Laboratory vacuum chamber is shown in figure 1-1.

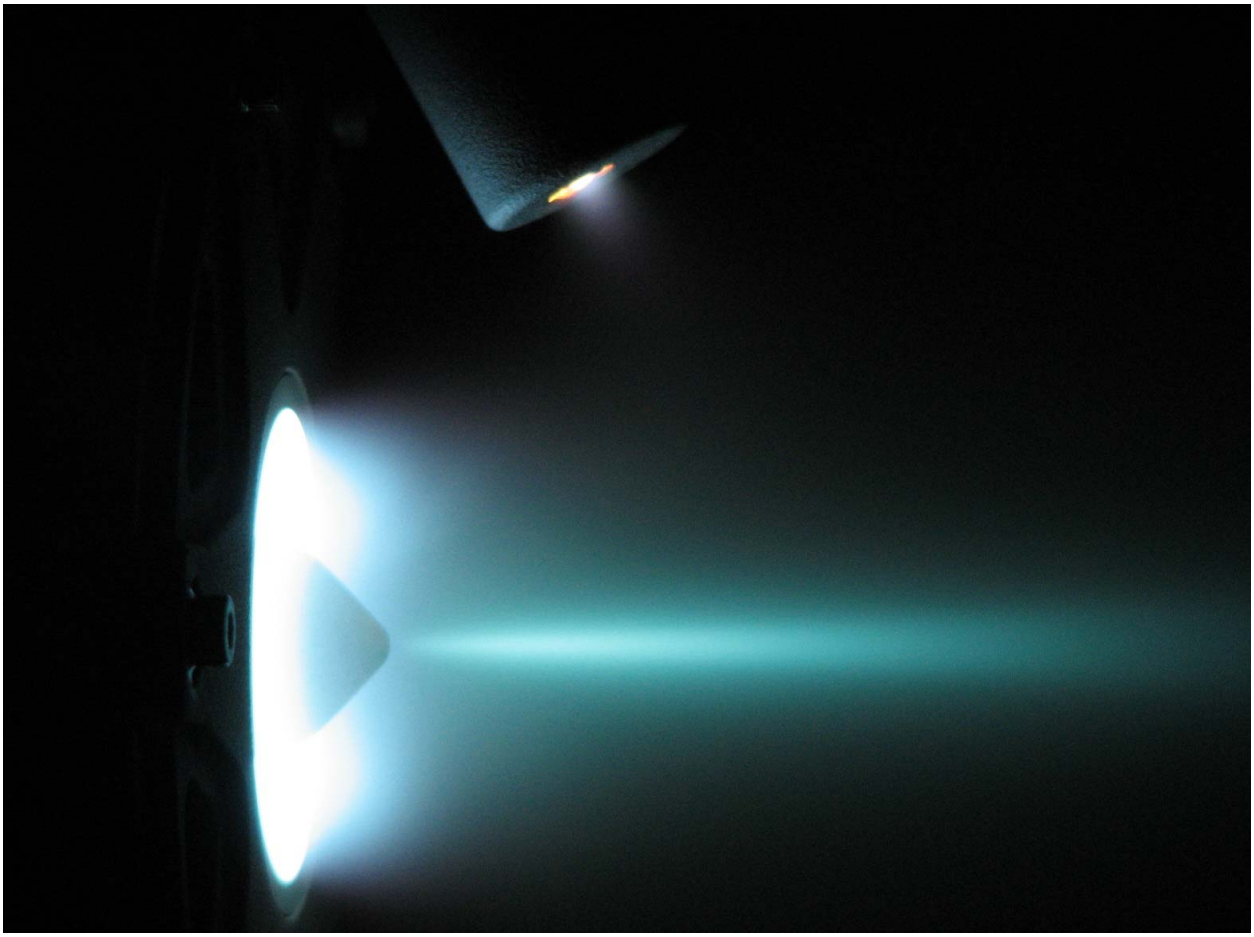

Figure 1-1: Picture of an electric thruster, BHT-200 Hall Thruster, in operation

There are numerous electric thruster concepts [61][29]. These concepts can be broadly grouped into three categories. The first category involves electrothermal propulsion. In this concept propellant is heated using electrical energy. The heated propellant gas is then thermodynamically expanded and accelerated through a conventional rocket nozzle. Resistojets and arcjets can be given as examples of electrothermal thrusters. In a resistojet the heating is achieved by using some sort of resistor filaments, in arcjet the heating is accomplished by creating an electric arc through the propellant that is being accelerated.

The second category involves electrostatic propulsion. In this concept the propellant is first ionized. The charged particles are then accelerated out of the thruster by electrostatic forces. The propellant can be in gas form as in ion engines and Hall thrusters, or in liquid form

as in electrospray thrusters. The ionization of the propellant can be done in many different ways. In standard ion engines, the ionization is achieved by electron bombardment of the neutral propellant gas in a chamber with cusped magnetic field structure that impedes the electron motion towards an anode, thus increasing the residence time of electrons in the chamber for effective ionization. Alternatively radio frequency waves, or microwaves can be used for ionization. In field emission or electro-spray thruster concepts, intense local electric fields extract ions or charged droplets from ionic liquids. Hall effect thrusters are described in more detail later in this section.

A third category for electric thrusters is called electromagnetic propulsion. In electromagnetic thruster concepts, the propellant is ionized and the charged particles are accelerated together, as a dense plasma, by electric and magnetic field forces. There are few varieties of electromagnetic thrusters; most well known concepts are pulsed plasma thrusters (PPT) and magneto-plasma-dynamic (MPD) thrusters. A new thruster concept called *Helicon thruster* is described in more detail later in this section. In pulsed-plasma thrusters a solid propellant, usually Teflon, is ablated and ionized by arc pulses created by a capacitor. The arc current induces a magnetic field, and the ablated material is then accelerated by the resulting Lorentz force, producing thrust. MPD thrusters have a coaxial geometry where the conducting center pole acts as a cathode and the annular wall acts as an anode. The propellant gas is introduced from the end of the annular channel and is ionized by the presence of a radial electric arc in the annular channel. If the current is high, the induced azimuthal magnetic field creates an axial Lorentz force, $(\mathbf{J} \times \mathbf{B})$, pushing the ions axially to produce thrust. The advantages and particular applications and operational status of such concepts are widely discussed in the literature [29].

1.1.1 Hall Thruster

In Hall thrusters, an axial electric field is created between a metallic anode located at the end of an annular channel and an external cathode that produces electrons. A radial magnetic field is created by external magnets. The propellant, injected from the anode region, collides with the electrons in the annular channel where the axial electron motion is impeded by

the presence of the strong radial magnetic field. The ionized propellant particles are then accelerated by the axial electric field, thus producing thrust. A schematic of a Hall thruster is shown in figure 1-2.

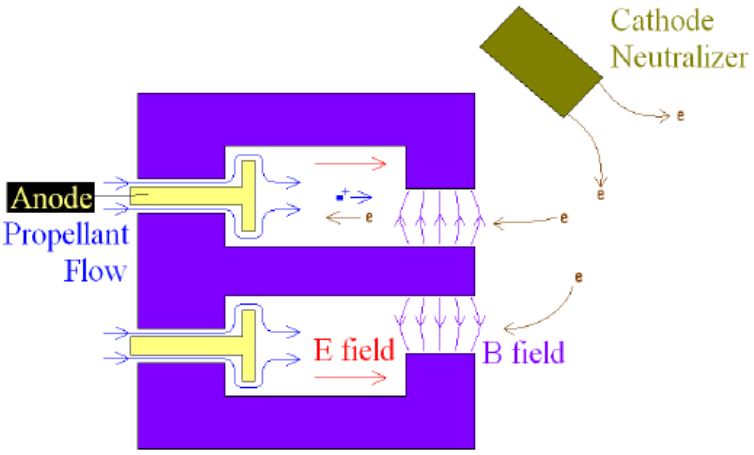

Figure 1-2: Schematic of a Hall Thruster [40]

1.1.2 Helicon Thruster

Using helical Radio Frequency (RF) antennas to create high density plasma is well known [13][24][4]. In electric thrusters, as discussed earlier in this section, external energy is used to ionize gas and then accelerate the plasma through electric and magnetic field forces. In thruster concepts such as the Variable Specific Impulse Magnetoplasma Rocket (VASIMR), a helicon source is used to produce high density plasma, while a secondary stage is used to heat the ions by ion cyclotron resonance heating using radio frequency waves and a magnetic nozzle is used to convert azimuthal momentum into axial momentum to accelerate the gas particles [32].

A new concept is being developed at MIT Space Propulsion Laboratory. The goal is to obtain high density plasma using a helicon discharge, and then accelerate it through thermal pressure and ambipolar potential gradients. In this thruster concept, the Argon propellant gas can be accelerated to velocities of up to 20 km/s [83]. In this concept, the power is delivered to the particles through wave-particle coupling using the helicon waves. The wave interaction with the electrons cause the electrons to heat up. The energetic electrons then

collide with the propellant gas and this results in electron impact ionizations. The process is very efficient to obtain plasmas of very high density ($\sim 10^{20}\ m^{-3}$).

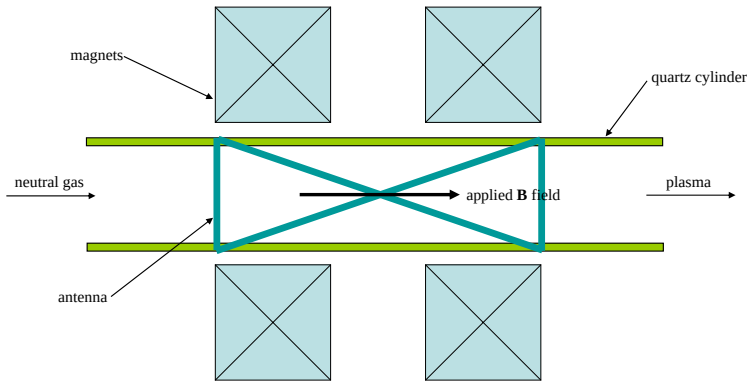

Figure 1-3: Schematic of a Helicon Thruster

Figure 1-3 shows a drawing of the helicon thruster concept. As seen from the figure, a pair of electromagnets in Helmholtz configuration produces an axial magnetic field in the region of the antenna. The helical shaped antenna is wrapped around a quartz tube. One end of the tube is attached to a propellant source. A controlled amount of propellant flows through the cylindrical quartz tube. The propellant is then ionized in the antenna region and plasma exits the tube at the open end into the vacuum chamber.

1.2 Plasma Diagnostics

The objective of plasma diagnostics is to obtain information about the state of the plasma through observation of the physical processes occurring in it as well as observing the interaction between the plasma and the diagnostics means. Deductions about the state of the plasma are only possible by understanding the physical processes causing the observations.

There are many techniques being used to characterize the plasma [50]. Depending on the property to be measured as well as the state of the plasma, the techniques to be used would vary. Most diagnostics methods require the use of probes in contact with the plasma: Rogowski coils are used to measure magnetic field; Langmuir probes are used to determine plasma density, electron temperature and plasma potential; Faraday probes are used to measure plasma ion currents; retarding potential analyzers are used to measure charged particle

energies. There are other less perturbing diagnostics techniques, which do not require the actual probes to be in contact with the plasma. Among such techniques there are intrusive and non-intrusive means. Intrusive plasma diagnostics might be done by mechanisms such as sending particles through the plasma; an example would be sending a neutral beam through the plasma as in the case of charge-exchange spectroscopy to determine spatial ion temperature [50]. Even less perturbing but still intrusive diagnostics is done by sending electromagnetic waves through the plasma; such as Thompson scattering, interferometry, reflectometry or laser-induced fluorescence (LIF) [62][41]. Emission spectroscopy is truly a non-intrusive diagnostics technique. In emission spectroscopy, electromagnetic radiation emission by the plasma is passively measured. The measured radiation emission might be continuum or line emission, or emission from molecular bands.

In our study, emission spectroscopy is used as a means to deduce information about the electric thruster plasma. Aside from being non-intrusive, emission spectroscopy is fast and economical, and also it allows access to hard to reach locations as long as there is an optical path. This is also the most likely approach for analyzing remote electric propulsion thrusters and plasma plumes in orbit. The opacity of the plasma must be well understood and be accurately accounted for. However, deducing quantitative information by analyzing the data obtained by only recording the radiation emission from a region of the plasma is quite challenging.

Through emission spectroscopy, it is possible to deduce information about the major physical processes occurring in the plasma. In addition, there have been certain recent space missions that have concerns about the radiation emission from the thruster plume plasma particles. In earlier studies [19, 20, 21], radiation emission from the electric thruster plasma and its effect on the observed astronomical signal was analyzed in the context of NASA's Terrestrial Planet Finder (TPF) mission . Work presented in this study will also be quite relevant in that area of research.

1.3 Emission Spectroscopy Physics

In a plasma, atoms and ions emit radiation when transition of electrons occur between the various energy levels of an atomic system. The emitted radiation is released in the form of narrow spectral lines. This radiation corresponds to the energy difference between the atomic energy levels. The frequency is given by $\nu_{ij} = \frac{E_j - E_i}{h}$ where E_i and E_j are the corresponding atomic energy levels and h is the Planck's constant. An illustration of the line emission is shown in figure 1-4. However, effects due to plasma properties, such as Doppler, Stark and Zeeman effects, would cause a broadening of the emitted lines. Such broadening effects can be used in deducing information about the state of the plasma. Additionally, the acceleration of the charged particles in the plasma will result in continuum radiation emission. Those processes are further discussed in chapter 2.

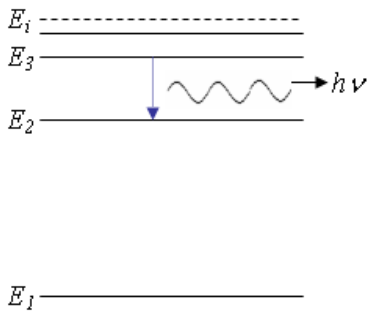

Figure 1-4: Illustration of the electronic energy levels and radiative emission

In atomic emission spectroscopy, the line emission from the plasma source is observed and the species causing the observed emission lines are identified. The analysis of the line intensities, locations and shapes could be used in deducing information about plasma density, electron and heavy species temperature, pressure, electric and magnetic field intensities, and particle velocities.

1.4 Emission Spectroscopy Setup

Measurement of emission spectrum from a radiation source requires a specific experimental setup depending on the application and the location of the source. There are several trade-

offs to be considered. The wavelength region of interest, such as ultra-violet (UV) or visible, or the spectral and spatial resolution required, or the correct wavelength span for a single measurement all depend on the instrumental factors. A longer focal-length spectrometer would allow a better resolution, at the expense of the span on wavelength range that can be measured without moving the grating. A finer grating similarly can provide better resolution, but for a much shorter wavelength range. Very fine gratings can only be used below a certain wavelength due to theoretical limits. The type of detector to be employed will depend on the application as well. If the desired wavelength is in the UV range, a Charged Coupled Device (CCD) detector for that wavelength range might not have sufficient quantum efficiency for higher wavelengths. The medium the signal has to pass through is very important for the wavelength region of the spectra that is observable. For IR detection, special kinds of detectors must be used, as well as the system must be cooled to prevent the black-body radiation from saturating the signal. For UV radiation, the setup has to allow the transmission of UV radiation. For higher energy UV radiation with wavelengths less than 200nm, the measurements have to be conducted under vacuum conditions because of the strong absorption of the electromagnetic radiation of these wavelengths by the oxygen in the air.

There are few major components needed for measuring the emission spectra of a laboratory electric propulsion plasma source operating inside a vacuum tank. The schematic of a typical setup for an external spectroscopic measurement is shown in figure 1-5.

Light Collection and Transmission

In order to collect radiation emission from the plasma source located inside a vacuum tank, various methods can be used. Collection of light from outside of one of the window ports is the easiest way of doing it. The spectrometer entrance slit could be placed next to the vacuum tank window in the line of sight of the radiation source. Such a setup will have poor spatial resolution.

An optical lens or mirror collection and focusing system located outside of the window port can be used to collect light from a region of interest. This method has to have a clear

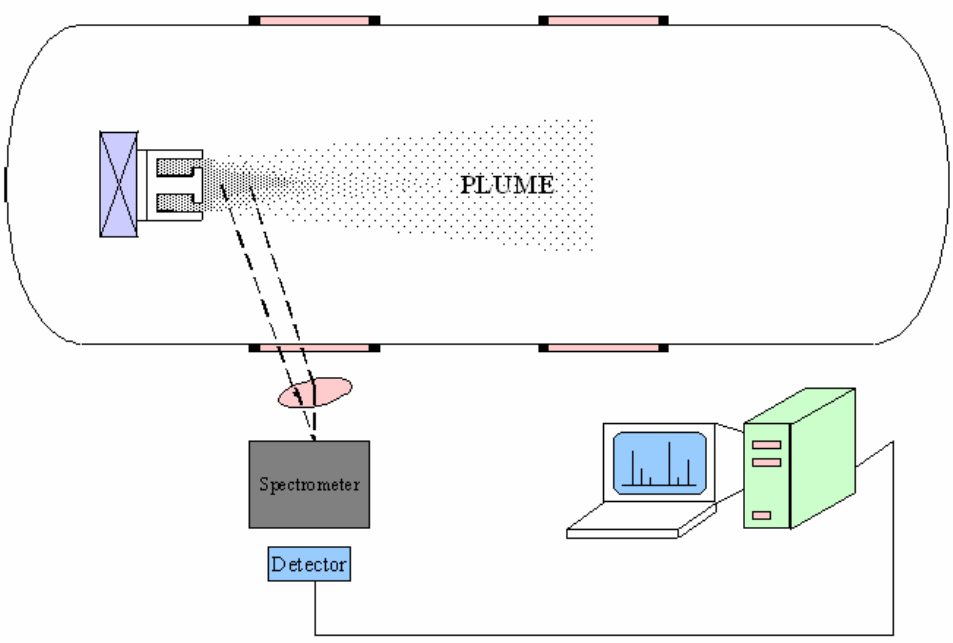

Figure 1-5: Illustration of the experimental setup for spectroscopic measurements

optical path to the region of observation. It is difficult to determine the exact collection volume, thus this method provides a limited spatial resolution, but can be improved by using apertures. Also this method is susceptible to stray light and the whole optical system must be covered in such a way to minimize stray light being collected. Alternatively, a fiber cable can be placed by the window and used to collect light in its field of view. In collecting light from outside the vacuum chamber, special attention must be paid to the optical transmissivity of the window port material.

It is also possible to collect the light from inside the vacuum tank. The entire spectrometer/detector setup can be placed inside the vacuum chamber. Such a configuration might be needed for measurements in the vacuum ultraviolet (VUV) range of the spectrum (wavelengths smaller than $\sim 200nm$). Or the spectrometer system could be located outside the vacuum chamber and a lens/fiber system could collect the signal inside the tank and then bring the signal outside the vacuum tank through some sort of vacuum fiber feed-through. The optical transmissivity of the fiber cable as well as all the collimating focusing lenses has to be good for the measured wavelength range. Additionally, optical fibers located inside the vacuum chamber might be exposed to the plasma. Thus, the fibers need to have protective cladding to withstand high temperatures. Also, the fiber ends or the collimating lenses will

be exposed to plasma and there are issues with material being deposited on them, resulting in a reduction in the optical transmissivity of the fibers or the lenses.

Light Dispersion

In order to obtain spectral information about the plasma radiation emission, the light is dispersed into its spectral components by a dispersive element such as a spectrometer/monochromator or a prism. A spectrometer is an instrument that disperses the light into its spectral components using a diffraction grating, thus allowing the measurement of the observed light wavelengths and intensities. In a spectrometer the light is admitted through a very narrow entrance slit. The light is then dispersed into its spectral components as it reflects from a grating. The dispersed light is then focused onto the exit port where, depending on the configuration, a narrow slit will allow the light to exit the system and be detected, or a window of light is focused onto a larger detector array.

Inlet Slit

The inlet slit determines the amount of light allowed into a spectrometer. In general, the inlet slit allows a thin column of light beam of several millimeters in height and tens of microns in width. The larger the slit size is, the larger the signal strength. However, a smaller slit size gives better spectral resolution.

Grating

Diffraction gratings are densely etched, parallel, equally spaced grooves on a reflecting surface. When light allowed from the inlet slit is incident on a diffraction grating, diffractive and interference effects cause the radiation of different wavelengths to be reflected in discrete directions.

The groove density of the grating determines the dispersion of the light allowed onto the grating. The grating density is given by the number of parallel grooves per millimeter. The dispersion angle of the incident light increases with higher grating density. Thus, for finer gratings the spectral resolution increases, however for a given detector area the portion of

the spectrum being observed for a given configuration decreases for array type detectors such as Charge Coupled Devices (CCD), reducing the observed wavelength range before rotating the grating angle.

There are two kinds of gratings: ruled and holographic. In ruled gratings, grooves are drawn on a reflective surface using high-quality ruling engines. A triangular profile is the most commonly used shape. The angle of the triangular groove is selected such that the diffraction is most efficient for a desired wavelength. This wavelength is called the *blazing wavelength*. In holographic gratings, photolithographic techniques are used to create sinusoidal reflective grooves.[67]

Exit Slit

Spectrometers can be used in *monochromator* or *spectrometer* modes of operation. In the monochromator mode, only a small portion of the dispersed light exits the device through a narrow exit slit. Thus, for monochromator mode of operation, the exit slit size determines the amount of dispersed light allowed on the detector surface. Smaller exit slit size gives better spectral resolution in the expense of reduced signal strength. For the spectrometer mode, no exit slit is used and an array type detector is attached to the exit port. The size of the active detector area determines the wavelength range that can be recorded, while the pixel size of the detector attached at the exit port affects the resolution of the obtained spectra.

Light Detection

The dispersed light is detected by a detector attached at the exit port of the spectrometer. The most commonly used detectors are Charge Coupled Device (CCD) and Photo Multiplier Tube (PMT) detectors.

A CCD is a detector that uses metal oxide semiconductor photocapacitors [1]. Exposure of discrete sites, called pixels, to photons results in the creation of an electron-hole charge pair. The number of electron-hole pairs in each pixel is linearly dependent on the the light

intensity and the exposure time [1]. The read-out of the pixels after a certain exposure time allows the detection of light falling on each pixel. In spectroscopy mode, the pixel intensities are read by adding up the electron-hole pairs of a vertical column of pixels.

A PMT is a sensitive detector that multiplies the signal from an incident light by producing a high number of electrons per photon. In photomultiplier tubes, incident photons cause the production of electrons on a photocathode material as a result of the photoelectric effect. The electrons are then accelerated and multiplied as a result of secondary electron emission as they collide with a series of electrodes which are held at a higher potential than a previous electrode. As this avalanche of electrons reaches the anode electrode, the rise in the current indicates the photons hitting the detector [2].

Calibration of the Measured Signal

In order to understand the measured spectra and to obtain accurate line intensity data, the raw spectral measurement results have to be calibrated. There are two calibration issues: wavelength calibration and line intensity calibration. In the wavelength calibration, a radiation source of known line emission spectrum is used to calibrate the wavelengths of the obtained spectrum.

The second calibration is the calibration of signal intensities as a function of wavelength. A continuum light source of known emission spectrum corresponding to a given black-body temperature can be used for intensity calibration. If the continuum radiation source is placed at the location of the observed plasma, keeping all the other parameters and the geometry the same, the effect of the optical path (windows, lenses, fibers), detector efficiencies, grating dispersive efficiencies, etc. can be all accounted for in the measured spectrum.

After the wavelength of the spectrometer setting is calibrated, the plasma emission measurements are conducted. Afterwards, the intensity of the obtained spectrum is scaled up according to the wavelength-dependent calibration coefficients obtained using the radiation source with known spectral intensity.

1.5 Collisional-Radiative Model (CRM)

In order to predict the radiation emission from the plasma, the expected population densities of atomic (ionic) energy states should be determined. In very high density, very high temperature plasmas, the population densities of electronic energy states can be determined using various equilibrium arguments. In complete *thermal equilibrium*, a Boltzmann distribution is achieved between the possible energy states and radiation energy density corresponds to the blackbody level for the average temperature of the system. However, such a state is almost never achieved in laboratory plasmas, definitely not in electric thruster plasmas. In *local thermal equilibrium* (LTE), Boltzmann distribution is achieved between the energy states, without the strict condition of radiation being in thermal equilibrium. Achieving LTE requires collisional transitions to dominate over the radiative transitions, thus it is only achieved in high density plasmas. McWhirter presents the condition for the LTE [49]:

$$n_e \gg 10^{19}(T_e)^{1/2}(\delta E)^3 \tag{1.1}$$

where T_e and δE are plasma temperature and the difference in the energy levels in eV, and n_e is the plasma density in m^{-3}. Electric thruster plasma does not satisfy the LTE condition. For example, a typical Hall thruster exit plane plasma density will be on the order of 10^{18} m^{-3} with a temperature of few eV, and the first excited state of Xenon is at 8.32eV. Thus, it is not possible to assume that the population densities will be determined by Boltzmann's distribution. However, in the high lying energy levels, where the energy difference, $\delta E = E_j - E_i$, is small, equilibrium assumption is applicable.

In most plasmas, more general models have to be employed to determine the level population densities instead of the statistical thermodynamics arguments [50]. Thus, it is necessary to take into account all of the processes that affect the population/depopulation of an energy level. A model that takes into account all those processes and calculates the dynamics of level population densities is called *collisional-radiative model* (CRM). First described by Bates et al. [6, 7], collisional-radiative (C-R) modeling of plasmas have been used to determine the population densities of the excited states in plasmas where *local thermal equilibrium*

conditions are not fulfilled.

The processes that determine the population of an energy state can be collisional or radiative. Collisional processes might involve electron induced excitation and de-excitation collisions, electron-impact ionizations collisions, or three body recombination processes, or heavy particle induced excitation, de-excitation and ionization processes. Radiative processes include spontaneous and induced radiative transitions between the bound energy levels, or transitions to and from the continuum such as photo-ionization and radiative electron recombination.

The success of the collisional-radiative model depends on the availability of accurate data on atomic transitions and interactions for the species being studied [55]. Thus, in general one has to obtain a great amount of collision cross section information from the available sources, both experimental and theoretical, for the plasma species being modeled, as well as radiative transition coefficient values. However, experimental data are not available for most processes. Thus, use of theoretical values is an unavoidable way for obtaining required cross-sections that are only order of magnitude accurate.

There are simplified models such as the *corona* model, that assume that certain processes dominate and allow a simpler way to calculate the radiation emission. In *Corona equilibrium*, it is assumed that collisional excitation from the ground state dominates and that all downward transitions are radiative [50]. It is also assumed that for low density plasmas, the emitted radiation escapes without being reabsorbed (thus causing no radiative excitations) elsewhere (optically thin plasma). Similarly, if the plasma density is low enough the collisional de-excitation is negligible compared to the rate of spontaneous radiative de-excitation. This is true because the collisional de-excitation time is much longer than the spontaneous radiative de-excitation time for low density plasmas.

As discussed by Hutchinson [50], the time scale for relaxation to excited state equilibrium is much shorter than the relaxation time to ionization state equilibrium. Thus, it is possible to decouple the modeling of the level population densities from that of the ionization equilibrium.

1.6 Literature Review

1.6.1 Previous Emission Spectra Measurements of Electric Thrusters and Related C-R Modeling

Electric thruster plasmas provide high luminosity emission, allowing the diagnostics of the plasma through optical emission spectroscopy. There are few earlier published work about electric propulsion plasma radiation emission measurements. Also, there are few simplified C-R models developed for electric thruster plasmas.

In 1993 Manzella [60] measured the radiation emission of an SPT-100 Hall thruster plume region in the 300-900nm wavelength range. The author also suggested in the paper that optical methods could be used in measuring the erosion products. However, no lines of erosion products were detected in the wavelength range of measurements.

In 1997 Leray et al. [58] measured the emission spectra along the discharge channel of a 50 mm outer channel diameter SPT type Hall thruster specially designed to allow access to the discharge region. Measurements of thruster radiation emission were performed for various discharge voltages, propellant flow rates and magnetic fields. Dramatic increase in the emission intensities of both Xenon neutral and ionic emission lines were observed near the exit plane in the region of high magnetic field. A discussion of a collisional-radiative model for Xenon was also presented where 10 Xenon neutral emission lines were studied.

Karabadzhak et al. have performed spectral measurements of radiation emission of several Hall effect thruster plasmas. In a 1997 paper [54], authors presented a discussion about the spectral measurements of a TAL type Hall thruster, D-55. In a separate paper by Karabadzhak et al. [52] emission spectra of the D-55 Hall thruster plume and discharge regions were presented. The thruster emission spectra results were compared to the spectra obtained from controlled experiments involving energetic electron, Xe^{+} and Xe^{++} beams on a Xenon neutral target gas.

Again, Karabadzhak et al. [51] developed a limited collisional-radiative model for Xenon

radiation emission. The model was used to predict the electron temperature for a TAL type Hall thruster using the emission line intensities of a few prominent near-infrared (NIR) Xenon neutral emission lines. The authors discussed the importance of the ion-impact emission processes in addition to the electron-induced inelastic collisions for the line radiation emission in Hall effect thrusters, as further discussed by Chiu et al. [27]

Collonna et al. [30] presented a discussion of collisional-radiative modeling of neutral Xenon. In that model, electron-atom excitation collision cross sections were calculated using the Gryzinski formulation [64]. The rate coefficients were determined by assuming a Maxwellian energy distribution for electrons. The results of steady-state level population densities were calculated and studied.

Most recently, Winter et al. [79] have measured the emission spectra of a radio frequency (RF) ion thruster running on Xenon propellant. The authors describe a corona model for the Xenon plasma. Comparisons of simulation results with the experimentally measured spectra were presented. Further discussion about this corona model and the spontaneous emission transition coefficients used in the model have been presented in a doctoral thesis by Pfrommer [68].

1.6.2 Collisional-Radiative Modeling of Argon

There have been several previous attempts to develop a collisional-radiative model for Argon plasma. In earlier extensive C-R models by Drawin and Katsonis [35], Gomes [43], a Maxwellian electron energy distribution function was assumed. Vlcek [75] investigated the electron energy distribution function in a non-equilibrium Argon plasma.

Vlcek [74] had developed a more extensive C-R model for neutral Argon where the numerical methods allowed the investigation of the excited state population mechanisms even for non-Maxwellian electron distribution functions. The Vlcek model, where the excited states are lumped into 65 effective energy levels, has been extended in later works by Bogaerts et al. [12], and Bultel et al. [16]. As these models are for discharges with low ionization fractions, they represent C-R modeling of Argon neutral atoms only.

The Argon C-R model by Gomes [43] was used to obtain the population number densities of the excited levels of both neutral Argon atoms and singly charged Argon ions. Gomes's C-R model used the analytical cross-sections proposed by Drawin [64] and Maxwellian electron energy distribution function was used to calculate the collision rate functions. The Argon neutral excited states are lumped into 20 and the Argon single ion excited states are lumped into 17 effective energy levels.

Another C-R model by Yanguas-Gil et al. [80] takes into account not only the electron impact collisions, but also the inelastic collisions induced by Argon atom. The C-R model is coupled into to a fluid model that studies stationary surface wave discharges. However, this model is very simplified as it lumps Argon neutral excited states into only 4 effective energy levels.

1.7 Thesis Content, Objectives and Contributions

The purpose of this thesis is to conduct non-intrusive diagnostics of electric thruster plasmas through emission spectroscopy and to provide computational means to analyze data obtained by the spectral measurements. The thesis is organized into nine chapters. Chapter 1 provides an introduction to the electric propulsion systems as well as to the experimental and computational studies presented in later chapters. A brief discussion of atomic radiation emission and various other emission processes in ionized gases is presented in Chapter 2.

Spectral measurements of three electric thruster plasma sources are presented in this thesis. Chapters 3, 4, and 5 describe the experimental setup and present the results of the plasma radiation emission measurements. Chapter 8 provides a discussion about the radiation emission due to erosion products and trends in the BHT-200 Hall thruster wall erosion rate.

Chapter 3 presents the discussions about the spectral measurements of the BHT-200 Hall thruster radiation emission in the 500 to 1000nm wavelength region. The BHT-200 Hall thruster is a well studied electric thruster. In the literature, there is an abundance of experimental and computational studies of the plasma properties for this thrusters. However, most

of the experimental measurements are done through intrusive diagnostics methods. There are no previous detailed study of the emission spectrum measurements for this thruster. In this study, radiation emission from ten different regions in the plume and the discharge zone of the truster is measured for the nominal thruster operational conditions. In addition, spectral measurements of the radiation emission from the thruster discharge region are conducted for varying discharge voltages from 75V to 300V with 25V increments. Measured emission spectra and the relevant spectral comparisons are presented. A set of relevant high resolution spectral graphs are further presented in Appendix A in more detail.

In Chapter 4, spectral measurements of a TAL type experimental Hall thruster, MHT-9, are presented. The MHT-9 Hall thruster is a scaled down version of the Russian D-55 Hall thruster. The measured spectra and comparison to the BHT-200 Hall thruster spectrum are presented. A set of relevant high resolution spectral graphs are further presented in Appendix B.

In Chapter 5, spectral measurements on an experimental Radio Frequency (RF) Helicon plasma source are presented together with a discussion of the major trends of the plasma source characterization and the level of ionization. The experimental Helicon plasma source is developed with a goal to characterize the helicon plasma source in order to gain a deeper understanding of the plasma generation by helical shaped RF antennae, and identify methods by which plasma parameters can be tuned to accelerate the obtained high density plasma in order to achieve an efficient propulsive system [69]. The spectral measurements allowed the study of the state of the plasma for varying operational conditions such as the propellant flow rate, magnetic field intensity and the RF power delivered to the plasma by the helical antenna. The use of intrusive probes in the antenna region would be perturbing the high density plasma, thus non-intrusive nature of optical emission spectroscopy diagnostics allowed the preliminary determination of the plasma conditions in this region. More detailed spectral graphs for the Helicon and inductively coupled plasma (ICP) are presented in Appendix C.

In Chapter 6, a collisional-radiative model for Argon plasma is described. The chapter presents the discussion about the major collisional and radiative processes that affect the

population densities of atomic and ionic energy levels. Detailed discussion of the model and the major modeling assumptions are provided. The simulated spectra and the comparison to the measured Helicon plasma source Argon spectra are presented. Even though the described Argon C-R model is not the first of its kind, in the presented model the energy states are simulated without lumping the energy levels into fictitious levels corresponding to groups of close energies [43][75][74][12][16]. Thus, the Argon C-R model simulates all the energy levels that are involved in the reported radiative transitions for the wavelengths less than 1000nm. The developed model allows easy modification of the major assumptions and the collisional and radiative transition parameters. The simulated spectrum's coverage of all the major Argon neutral (Ar-I) and single ion (Ar-II) emission lines in the 0 to 1000nm wavelength region makes this C-R model unique and shows its utility in predicting the plasma emission spectrum for the ultraviolet, visible and near-infrared regions of the electromagnetic spectrum. All the Ar-I and Ar-II emission lines simulated by the C-R model are tabulated in Appendix D along with the other relevant energy level and transition data.

In Chapter 7, a collisional-radiative model for Xenon plasma is described. Albeit, less detailed than that of the Argon C-R model, this model allows the simulation of the most prominent Xenon neutral and single ion emission lines in the visible and the near-infrared regions of the electromagnetic spectrum. The modeled spectrum and the comparison to the measured Hall thruster spectrum are presented. The obtained simulated spectra show good match with that of the measured spectra in the near-infrared region. All the Xe-I and Xe-II emission lines simulated by the Xenon C-R model are presented in Appendix E along with the other relevant energy level and transition data.

For SPT type Hall thrusters, a major life limiting factor is the erosion of the ceramic walls of the thruster annular channel. The determination of the ceramic erosion rate is traditionally carried out by long duration operation of the thruster inside vacuum chambers and measuring the change in the wall thickness before and after the testing. However, such experiments are long and expensive. In addition, the analysis of the findings is difficult due to the uncertainty in the deposition rates and other vacuum tank effects, as well as the difficulties in establishing a non-varying reference for surface geometry measurements. Optical emission spectroscopy can be an ideal method in evaluating the erosion rate, as

such measurements do not intrude the plasma as well as provide real time data acquisition capability. In Chapter 8, emission spectroscopy measurements of the BHT-200 Hall thruster ceramic wall erosion particles are presented, accompanied by a discussion aimed at predicting the wall erosion rate.

In Chapter 9, the overall conclusions and contributions of the thesis are presented. Also presented are the recommendations for future work to be completed in diagnosing electric thrusters using optical emission spectroscopy and a discussion about the further improvements to the collisional-radiative models.

Chapter 2

Plasma Radiation Emission

The radiation emission from the thruster plasma can be in the form of narrow emission lines due to electronic transitions, or broad continuum spectrum due to charged particle acceleration processes. The discussions of various radiation processes are presented in this chapter. Since Xenon is the most common propellant for electric thrusters, the example discussions assume a Xenon plasma.

2.1 Line Radiation

Electronic transitions between the various energy levels of atomic and ionic states result in the emission of radiation at distinct frequencies in a narrow line form. Multi-electron atoms have very complicated atomic structure, resulting in energy levels determined by the various spin and angular momentum couplings between the electronic states and with the heavy nucleus.

In a many-electron atom (or ion), electrons would occupy the energy levels according to the *Pauli's exclusion principle*, thus no two electrons in a single atom would have the same set of quantum numbers [57]. As the energy levels are filled with the electrons, the lowest energy configuration would be called the ground state. This state would have an associated

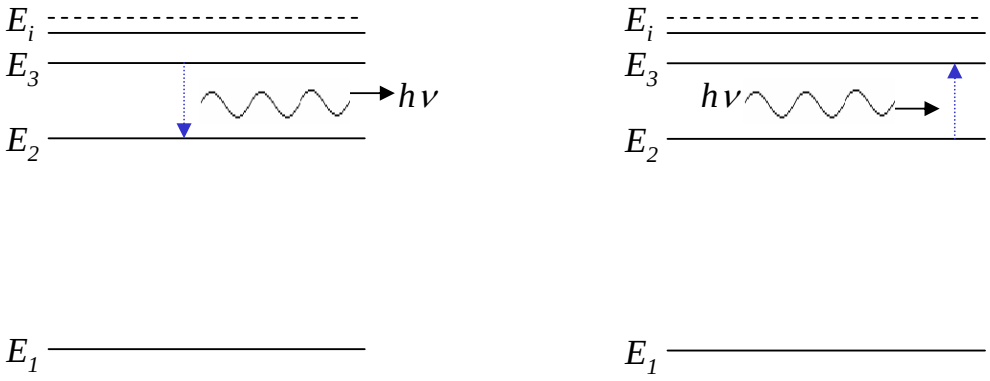

Figure 2-1: a)Spontaneous emission and b)Photo-absorption processes

energy defined as zero with respect to all other possible higher energy configurations.

When one of the *outer* electrons is excited to a higher energy state, the excited electron would de-excite to a lower energy state either due to de-excitation collisions, or by an induced or spontaneous radiative process. In the radiative de-excitation of the electron, a photon with an energy corresponding to the energy difference of the initial and final energy levels is released. The spectral line arising from the radiative transition between energy levels i and j would have a wavelength $\lambda_{ij} = \frac{hc}{E_j - E_i}$ where h is the Planck's constant, c is the speed of light, E_i and E_j are the energies of the respective levels, and $j > i$.

Between the energy levels i and j, electrons can make three different kind of radiative transitions [50]. The first of these transitions is called spontaneous de-excitation, in which an electron at an upper energy level decays spontaneously to a lower energy state. The probability per unit time for an electron in any one of g_j degenerate energy states of level j to make a spontaneous transition to any of the g_i degenerate energy states of level i is given by Einstein's spontaneous emission transition coefficient, A_{ij}. Thus, for a given energy level j, the lifetime, τ_j, of that electron configuration for the atom would be given by $\tau_j = \left(\sum_{i=1}^{j} A_{ij}\right)^{-1}$ [33].

The second radiative transition process is photo-absorption. In this process, a photon of the corresponding frequency is absorbed by the atom, causing an electron to transition to a higher energy state. The probability of the absorption process per unit time is given by $I(\nu_{ij})B_{ij}$ where $I(\nu)$ is the energy density per unit frequency of the electromagnetic radiation and B_{ij} is the Einstein absorption coefficient. Illustration of spontaneous emission

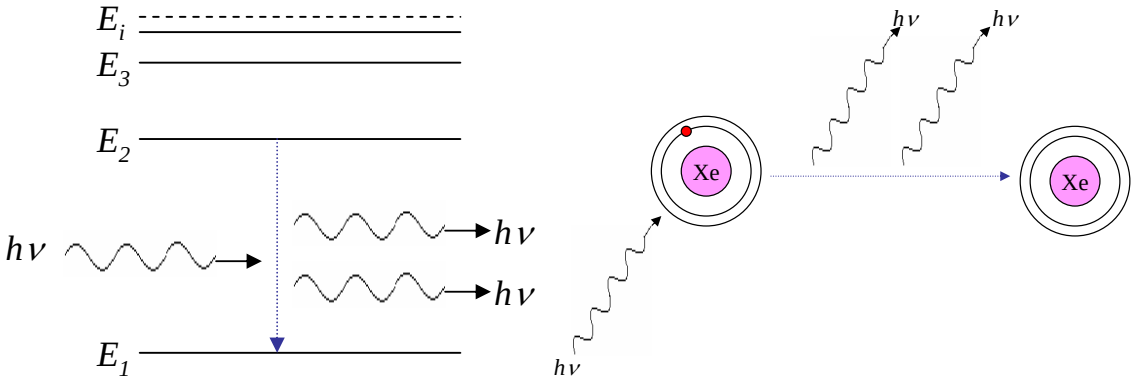

Figure 2-2: Photon induced de-excitation process

and photo-absorption processes are shown in figure 2-1.

The third radiative transition process is stimulated emission. In this process, an electron at a higher energy level is induced to decay to a lower energy state by the presence of electromagnetic radiation at the frequency of the transition. The probability of the stimulated emission process per unit time is given by $I(\nu_{ij})B_{ji}$ where $I(\nu)$ is again the energy density per unit frequency of the electromagnetic radiation and B_{ji} is the Einstein coefficient for stimulated emission. For low density plasmas stimulated emission processes are negligible. Figure 2-2 shows an illustration of the photon induced radiative de-excitation process.

The Einstein coefficients A_{ij}, B_{ij} and B_{ji} are atomic properties and do not depend on the state of the plasma. These coefficients are related and the *principle of detailed balance* can be used to determine the relationships given in equations 2.1 and 2.2 [50].

$$A_{ij} = \frac{8\pi h\nu_{ij}^3}{c^3} B_{ij} \tag{2.1}$$

$$g_j B_{ji} = g_i B_{ij} \tag{2.2}$$

The most common excitation mechanism is the electron impact excitation. In electron impact excitation a free electron colliding with an atom causes one of the outer electrons to excite to a higher bound energy level. The colliding free electron loses certain fraction of its initial energy in the collision process. A depiction of such a collisional event and the ensuing radiative de-excitation of the electron is shown in figure 2-3.

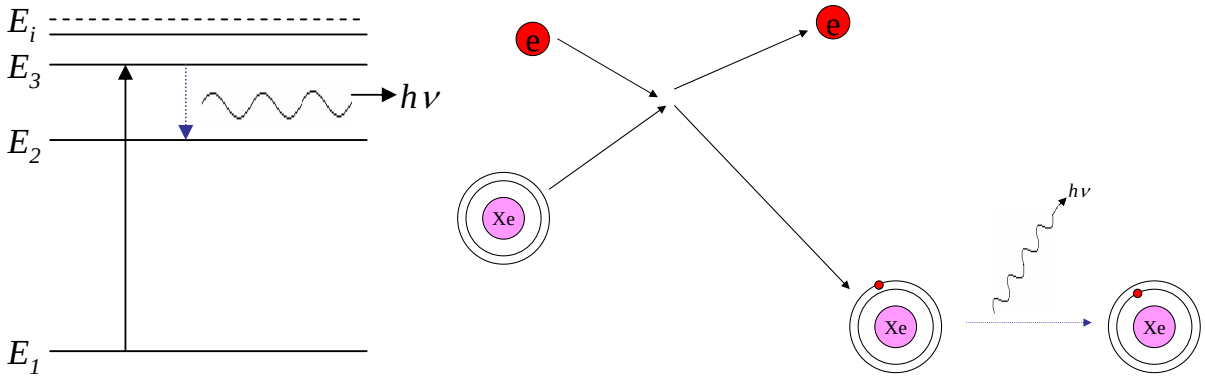

Figure 2-3: Electron impact excitation and spontaneous emission processes

$$Xe + e \rightarrow Xe^* + e$$
$$Xe^* \rightarrow Xe + h\nu$$

Alternatively, inelastic collisions between heavy species result in the excitation of an outer electron to a higher energy level. For electric thrusters, where high energy ions collide with slow neutrals, heavy particle excitation processes are reported to be significant [27]. Figure 2-4 shows a portrayal of a Xenon ion inelastic collision with a Xenon neutral atom and the ensuing spontaneous radiation emission process.

$$Xe^+ + Xe \rightarrow Xe^+ + Xe^*$$
$$Xe^* \rightarrow Xe + h\nu$$

Inelastic collisions with electrons or other heavy particles also result in the ionization of the atom. A brief discussion of these and other processes is presented in section 6.2.

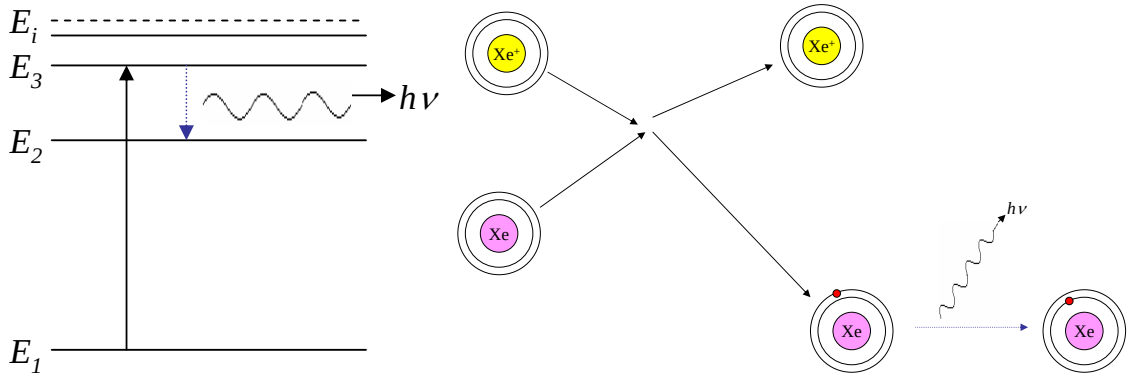

Figure 2-4: Heavy particle inelastic excitation collision and spontaneous de-excitation emission processes

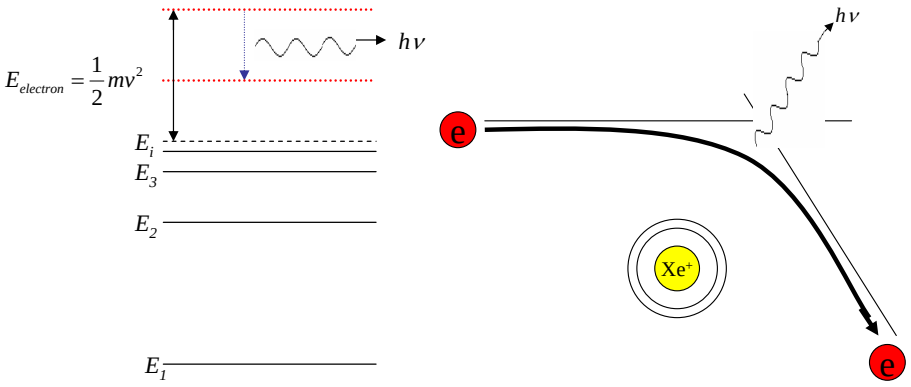

Figure 2-5: Bremsstrahlung radiation

2.2 Continuum Radiation

When a charged particle, such as an electron, is accelerated (or decelerated) it radiates electromagnetic energy. There are three main mechanisms of such radiation emission. These processes are Bremsstrahlung radiation, electron recombination radiation, and electron cyclotron radiation.

2.2.1 Bremsstrahlung Radiation

In the Bremsstrahlung radiation process, an electron is subjected to an acceleration/deceleration due to the electric field of a nearby charged particle such as an ion. As a result of this process, electromagnetic radiation is emitted. An illustration of this process is presented in figure 2-5.

$$Xe^+ + e \rightarrow Xe^+ + e + h\nu$$

For thermal (Maxwellian) electrons, the power emitted due to a Bremsstrahlung process per unit volume per unit frequency is given by the equation [50]:

$$J(\nu) = (\frac{q^2}{4\pi\epsilon_o})^3 \frac{32\pi^2}{3\sqrt{3}m_e^2c^3}(\frac{2m_e}{\pi kT})^{1/2} e^{-\frac{h\nu}{kT}} n_e n_i Z^2 \overline{g} \qquad [Wm^{-3}Hz^{-1}] \qquad (2.3)$$

where q is the elementary charge, ϵ_o is the permittivity of free space, m_e is the electron mass, c is the speed of light, k is the Boltzmann's constant, Z is the ion charge number, and $\overline{g}$ is the Bremsstrahlung Gaunt factor. Evaluating the fundamental constants in equation 2.3 gives

$$J(\nu) = 6.321 \times 10^{-53} T^{-1/2} e^{-\frac{h\nu}{T}} n_e n_i Z^2 \overline{g} \qquad [Wm^{-3}Hz^{-1}] \tag{2.4}$$

where T has units of eV and h has units of $eV \cdot s$. The number of photons released for a given frequency range per unit volume per unit time per unit frequency can be found by the expression $J_{photon_\nu}(\nu) = J(\nu)/(h\nu)$. Similarly, the expression for the number of photons emitted at a given wavelength per unit volume per unit time per unit wavelength can be obtained:

$$J_{photon_\lambda}(\lambda) = 9.54 \times 10^{-20} T^{-1/2} e^{-\frac{hc}{\lambda T}} n_e n_i Z^2 \overline{g} \qquad [m^{-3}s^{-1}m^{-1}] \tag{2.5}$$

For a quasi-neutral plasma of density n_e and temperature T, the number of photons released per meter cubed per second in the wavelength range of λ_1 to λ_2 will be given by:

$$\int_{\lambda_1}^{\lambda_2} J_{photon_\lambda}(\lambda) d\lambda = 9.54 \times 10^{-20} T^{-1/2} n_e^2 Z^2 \overline{g} \left[\Gamma(0, \frac{hc}{\lambda_2 T}) - \Gamma(0, \frac{hc}{\lambda_1 T}) \right] \tag{2.6}$$

where $\Gamma[a, x]$ is the incomplete gamma function where a is a constant, and x is a variable. Using the continued fraction representation for the incomplete gamma function [37], the above expression can be written in a form that can be easily incorporated into a computational model:

$$\int_{\lambda_1}^{\lambda_2} J_{photon_\lambda}(\lambda) d\lambda = 9.54 \times 10^{-20} T^{-1/2} n_e^2 Z^2 \overline{g} \left[\frac{e^{-\frac{1.24}{T\lambda}}}{1 + \frac{1.24}{T\lambda} - \frac{1}{3 + \frac{1.24}{T\lambda} - \frac{4T\lambda}{1.24 + 5T\lambda}}} \right|_{\lambda_1}^{\lambda_2} \tag{2.7}$$

where T is in eV and λ is in μm. The above expression for the Bremsstrahlung photon emission can be implemented in a kinetic model for the plasma [20]. Using equation 2.4, for an optically thin plasma, expected radiative power losses due to Bremsstrahlung processes can be calculated [20]. For electric propulsion plasmas Bremsstrahlung radiation emission intensity in the UV, visible and near-infrared (NIR) regions of the spectrum is found to be small [20].

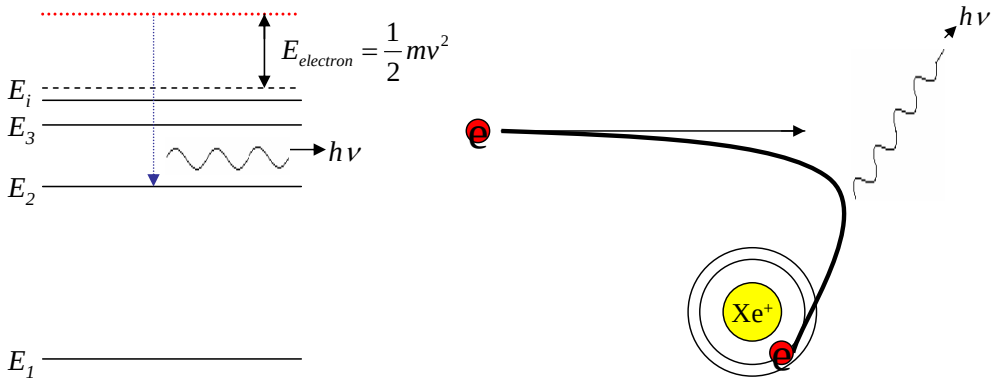

Figure 2-6: Electron recombination radiation

2.2.2 Electron-Recombination Radiation

Electron recombination radiation is the radiation emitted by an accelerating (decelerating) electron in the field of a nearby charged particle during its capture by that particle. A visual representation of this process is shown in figure 2-6.

$$Xe^+ + e \rightarrow Xe^* + h\nu$$

For thermal (Maxwellian) electrons, the power emitted due to an electron-recombination process per unit volume per unit frequency is given by the following equation [50]:

$$J(\nu) = (\frac{e^2}{4\pi\epsilon_o})^3 \frac{32\pi^2}{3\sqrt{3}m_e^2c^3}(\frac{2m_e}{\pi kT})e^{-\frac{h\nu}{kT}} n_e n_i Z^2 \left[\frac{Z^2R_y}{T}\frac{2}{n^3}e^{Z^2R_y/n^2T}G_n\right] \qquad [Wm^{-3}Hz^{-1}] \tag{2.8}$$

where G_n is the electron-recombination Gaunt factor, and R_y is the Rydberg energy and n is the principal quantum number of the recombined level. Except for the expression in the bracket, the above formula is identical to the Bremsstrahlung formula without the Gaunt factor, $\overline{g}$. Thus, the relative importance of the recombination radiation to that of Bremsstrahlung is given by the ratio:

$$\frac{Z^2R_y}{T}\frac{2}{n^3}\frac{G_n}{\overline{g}}e^{\frac{Z^2R_y}{n^2T}} \tag{2.9}$$

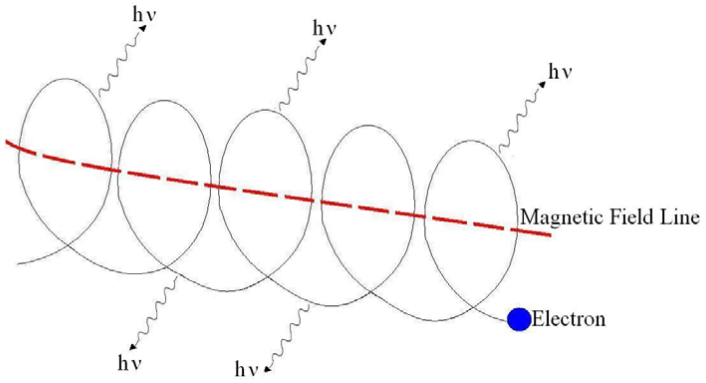

Figure 2-7: Electron cyclotron radiation

Due to the n^{-3} dependence, recombination radiation is negligible for outermost (high lying) energy levels that contribute to low frequency radiation emission [50]. Thus, recombination radiation becomes small for higher wavelengths such as the IR range of the spectrum.

2.2.3 Electron Cyclotron Radiation

Cyclotron radiation is the electromagnetic radiation emitted by charged particles moving in a magnetic field. The Lorentz force acts on the particles perpendicular to both the magnetic field lines and the particle's velocity vector, causing the particle to spiral around the magnetic field lines, thus accelerating charged particles and causing them to emit radiation as illustrated in figure 2-7. This radiation consists of a series of discrete harmonics. For non-relativistic plasma, the emission occurs at the fundamental frequency ν_c and higher. The fundamental frequency is given by:

$$\nu_c = \frac{eB}{m_e} \approx 28 \cdot B \quad [GHz] \tag{2.10}$$

where B is the magnetic field strength in units of *Tesla*. From the equation above, it is clear that electron cyclotron emission in the infrared or visible frequency range requires extremely high magnetic field strength. Thus, for electric thrusters of interest, cyclotron radiation emission is neglected.

2.2.4 Blackbody Radiation

All objects above *absolute zero* temperature will emit radiation corresponding to their temperature and emissivity. The power per unit area per unit wavelength of this emission, called blackbody radiation, is given by Planck's formula:

$$R(\lambda) = \frac{2\pi hc^2}{\lambda^5} \frac{1}{e^{hc/\lambda kT} - 1} \tag{2.11}$$

Such radiation emission can be significant when conducting spectral measurements at infrared (IR) wavelengths. Emission from the surfaces of the thruster or the components of the vacuum system might have higher intensity than the signal being detected.

Chapter 3

BHT-200 Hall Thruster Spectral Measurements

Radiation emission spectral measurements of a BHT-200 Hall thruster were conducted. The measurement results and the accompanying discussion and analysis are presented in this chapter. More detailed spectral graphs of the discharge region are presented in Appendix A.

3.1 BHT-200 Hall Thruster

BHT-200 is an SPT type Hall thrusters with a nominal operational power of 200W. The thruster has been developed by Busek Corporation based in Natick, MA. It nominally runs on Xe propellant. A picture and various nominal operational parameters of this thruster are presented in table 3.1. For the testing, the thruster was equipped with a hollow cathode built by Busek Co.

The BHT-200 Hall thruster is one of the most studied electric thrusters. In the literature, there is an abundance of experimental measurements of the plasma properties in the discharge and plume regions of this thruster [9][48][10]. Most of those measurements were

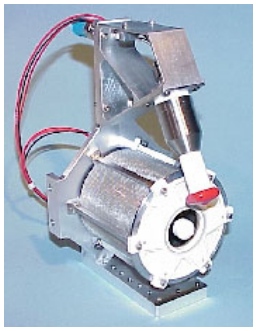

Nominal Thruster Parameters	
Power	200 W
Discharge Voltage	250 V
Propellant Flow Rate	0.94 mg/s (Xe)
Thrust	12.4 mN
Efficiency	42 %
Specific Impulse	1300 s
Mass	0.9 kg

Table 3.1: BHT-200 Hall Thruster [19]

performed using intrusive diagnostics probes. The BHT-200 discharge and plume region have also been modeled using complicated computer simulation models [22][71][14][17].

3.2 Experimental Setup

The spectral measurements were performed at the MIT Space Propulsion Laboratory. The thruster was operated inside the MIT-SPL AstroVac vacuum chamber which is 1.5m in diameter and 1.6m in length. The chamber is equipped with a mechanical roughing pump and two cryogenic pumps. The total pumping capacity is 7000 L/s for Xenon [65]. The base pressure was 1.2×10^{-7} Torr before the thruster operation began. The chamber pressure during the testing was 3.56×10^{-5} Torr for the nominal operational flow rates. The pressure inside the vacuum chamber was monitored by a thermocouple gauge for down to 10^{-3} Torr. A cold cathode pressure gauge was used for measuring lower pressures (accuracy down to 10^{-9} Torr).

The thruster was mounted on top of a metal stand inside the chamber. The metal stand was placed such that the thruster was approximately on the centerline and the exit plane of the thruster was aligned with one of the side window ports of the vacuum chamber. In order to allow better viewing of the the thruster acceleration channel from the side window, the thruster pointing direction was rotated ~ 6 degrees from the chamber's center axis towards the window port. The thruster was run with Xenon propellant with flow rates of 8 *sccm* to the anode and 1 *sccm* to the cathode for all tests.

For the spectral measurements, the radiation emitted by the thruster plasma was collected by an optical system located outside the vacuum window port and was transmitted to the entrance slit of a spectrometer. A schematic of the experimental setup is shown in figure 1-5 in chapter 1.

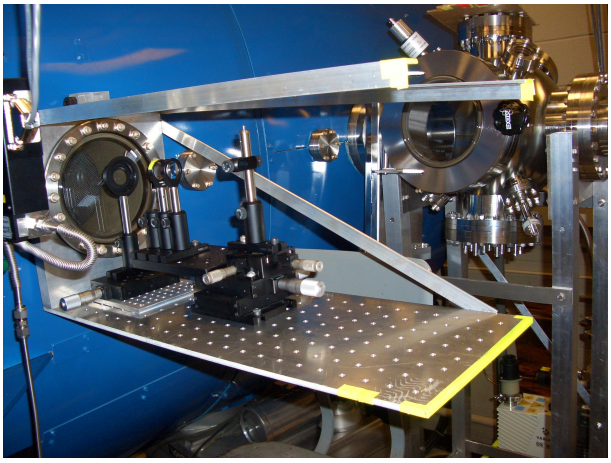

Figure 3-1: Optical shelf attached to the window port of the MIT-SPL vacuum tank

3.2.1 Radiation Collection and Transmission

A collimating-focusing lens system was used to collect the light from the plasma region of interest. The whole optical setup was placed on a metal optical shelf attached to the vacuum tank window as shown in figure 3-1. The radiation collection was accomplished by a pair of 1 inch diameter lenses. The collimating lens has a focal length of $1000mm$ and was placed outside the vacuum tank window at a distance of $1000mm$ from the center of the thruster axis. The $100mm$ focal length second lens was placed in line with the first one, forming a telescopic configuration. The end of a $1m$ long fiber bundle was placed at the focal point of this second focusing lens. A mechanical diaphragm was placed before the collimating lens in order to adjust the intensity of the collected light and gain spatial resolution. In order to reduce stray light, the window was covered with black optical card board with a 1 inch diameter hole cut in the middle in line with the lens axis. Additionally, the shelf is covered with optically opaque black cloth during the data taking. Mechanical translation stages were used to adjust the exact location and the proper alignment of the optical components.

A $1m$ long Acton Research LG-456-020 fiber bundle carried the collected signal to the

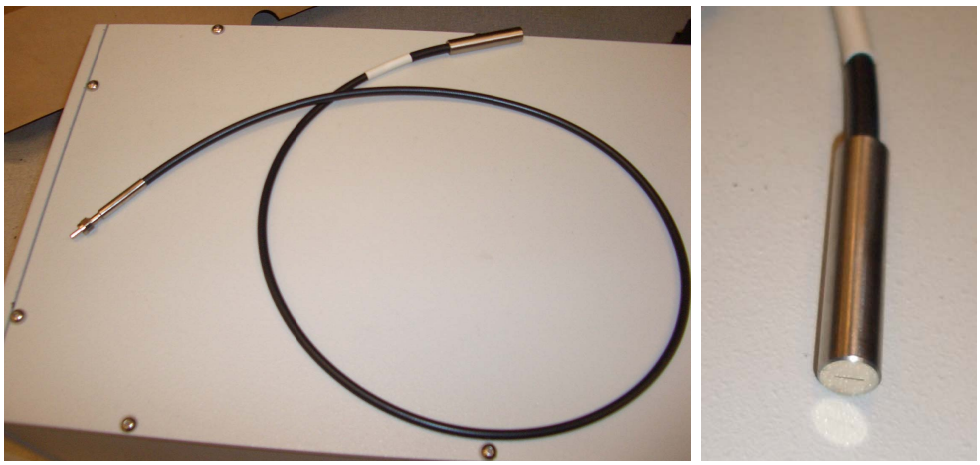

Figure 3-2: a)Acton Research 1m long fiber bundle, b) fiber end with single column of 19 200μm diameter fibers

entrance slit of the spectrometer. The 10mm diameter fiber bundle contains a single column of 19 fibers, each 200 μm in diameter (245-μm diameter with cladding) at the spectrometer end. The fiber has good transmissivity from 400 to 2200 nm. Pictures of the fiber bundle and the fiber ferrule end are shown in figure 3-2. An adjustable fiber adapter, Acton model FC-466-020, was used to hold the fiber bundle directly at the entrance slit of the spectrometer.

3.2.2 Radiation Dispersion

An Acton Research SpectraPro-500i spectrometer was used as the dispersive instrument. This fully automated, 500mm focal length, f/6.5 aperture Czerny-Turner type spectrometer provided a resolution of 0.08nm at 435nm using a 1200 g/mm grating for the CCD detector attached to it. The inlet port was equipped with an adjustable slit assembly. This spectrometer was obtained as a demo unit from Acton Research Corp. The spectrometer has a triple-grating turret, and was equipped with 3 different diffraction gratings. A grating with 300 grooves/mm blazed at 500nm was used to obtain broader range spectra. The second grating at 1200 grooves/mm blazed at 500nm was widely used due to its better wavelength range at relatively good resolution. The high resolution grating at 1800 grooves/mm blazed again at 500nm provided high resolution spectra with small wavelength range. A picture of the spectrometer is shown in figure 3-3a.

Figure 3-3: a)Acton Research SpectraPro-500i Spectrometer, b)Roper Scientific Photometrics Cascade:650 CCD Detector

3.2.3 Radiation Detection

A CCD detector, Roper Scientific Photometrics Cascade:650, is attached to the exit port of the spectrometer. The CCD detector has 572×1024 pixels with a pixel size of 7.4 × 7.4-μm. This thermoelectric cooled detector has good quantum efficiency in the visible wavelength range. A picture of the CCD detector is shown in figure 3-3b.

3.3 BHT-200 Hall Thruster Measurement Results

The spectral measurement graphs for the BHT-200 Hall thruster emission in the 500-1000nm range are presented in this section. A list of prominent visible and near-infrared Xenon neutral (Xe-I) and Xenon single ion (Xe-II) emission lines are tabulated in table 3.2 at the end of the chapter. For the presented measurements, the grating with 1200 g/mm blazed at 500nm was used. The spectral resolution was ∼0.08nm at 435nm wavelength.

3.3.1 Regions of Observation

Figure 3-4 presents a picture of the BHT-200 Hall thruster operating inside the vacuum chamber. The picture was taken from the side window where the optical shelf was located.

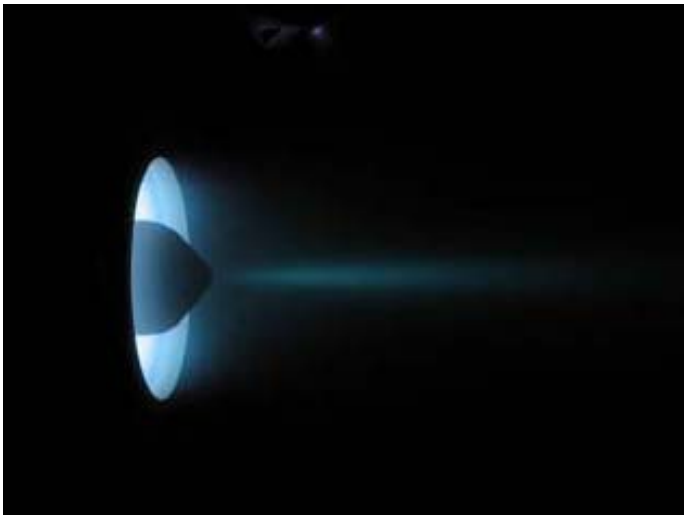

Figure 3-4: BHT-200 Hall Thruster in operation inside the MIT-SPL vacuum chamber

In order to compare the radiation emission originating from different regions of the thruster, the collecting optics system was pointed at 10 different locations. Figure 3-5 shows the regions of observation for the Hall Truster measurements in an inverse-color image of the picture presented in figure 3-4. All the measurements were taken for the nominal thruster operation conditions with a discharge voltage of 250V and a discharge current of 0.81A.

As seen in figure 3-5, three of the observation regions were in the discharge channel region, five were in the plume region, one was in the cathode region and one was at the region of the thruster metal zone away from the plasma.

As seen in table 3.2, the near-infrared (NIR) region of the spectrum is dominated by strong Xenon neutral emission lines. Thus, the wavelength region from 800 to 1000nm presents the trends for the Xenon neutral (Xe-I) emission intensity. On the other hand, the wavelength region around 500-600nm has predominantly Xenon single ion (Xe-II) emission lines. Thus, the intensity of lines in this wavelength region is indicative of ionic emission of the Xenon propellant.

Discharge Spectra

Figure 3-6 shows the measured spectra in the discharge region of the thruster. The top plot shows the spectrum observed in region-I whereas the bottom is from region-VII. As seen in

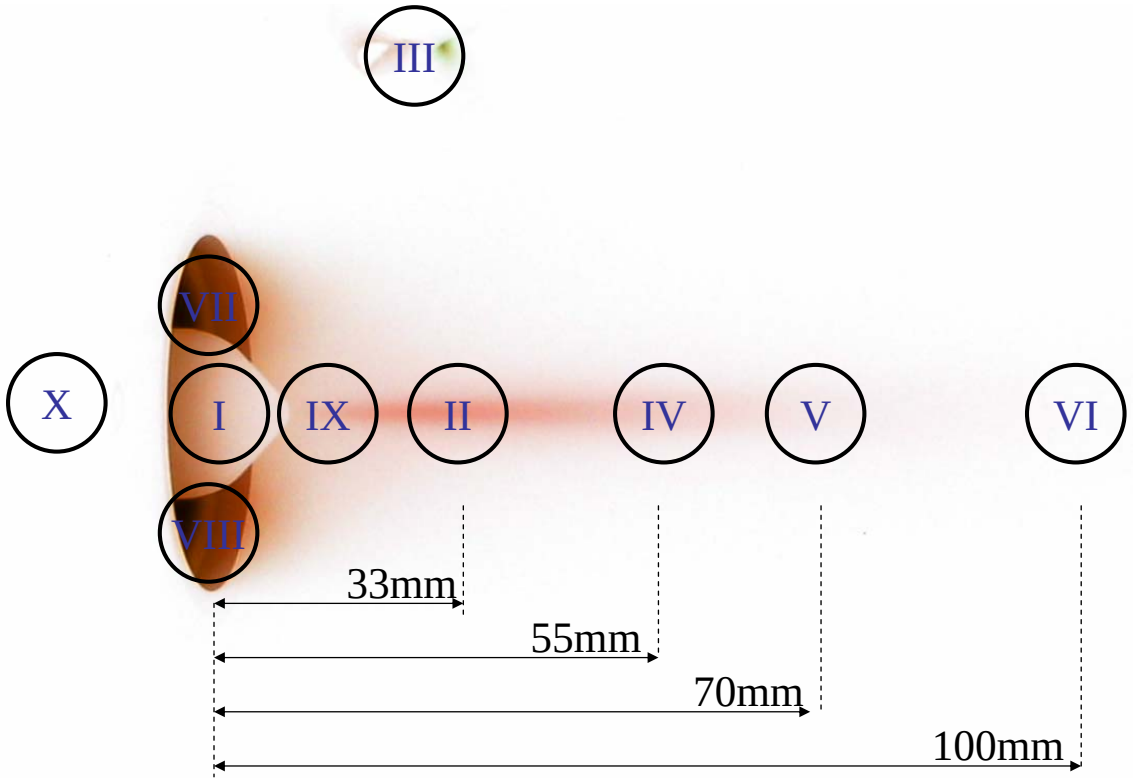

Figure 3-5: Illustration of the regions of observation for the BHT-200 Hall Thruster

figure 3-5, for the measurements of region-I, the optics were pointed at the ceramic center pole of the BHT-200 Hall thruster, and for the measurements of region-VII, the optics were pointed at the annular discharge channel exit region.

The observed spectra look slightly different between these two discharge regions. The emission from region-VII has higher intensity. Additionally, more emission lines are visible in the spectrum from region-VII. However, the relative intensities of the prominent lines seem unchanged. For the spectrum at the bottom, the 881.94nm 6s[3/2]-6p[5/2] Xenon neutral line is saturated, thus for later comparisons with other regions, region-I spectrum is chosen as the discharge spectrum.

Plume vs. Discharge Spectra Comparison

Figure 3-7 shows the comparison of the spectra for the discharge and plume regions. The discharge region is region-I in figure 3-5 and the plume spectrum is region-II corresponding to the plume region at 33mm away from thruster exit plane.

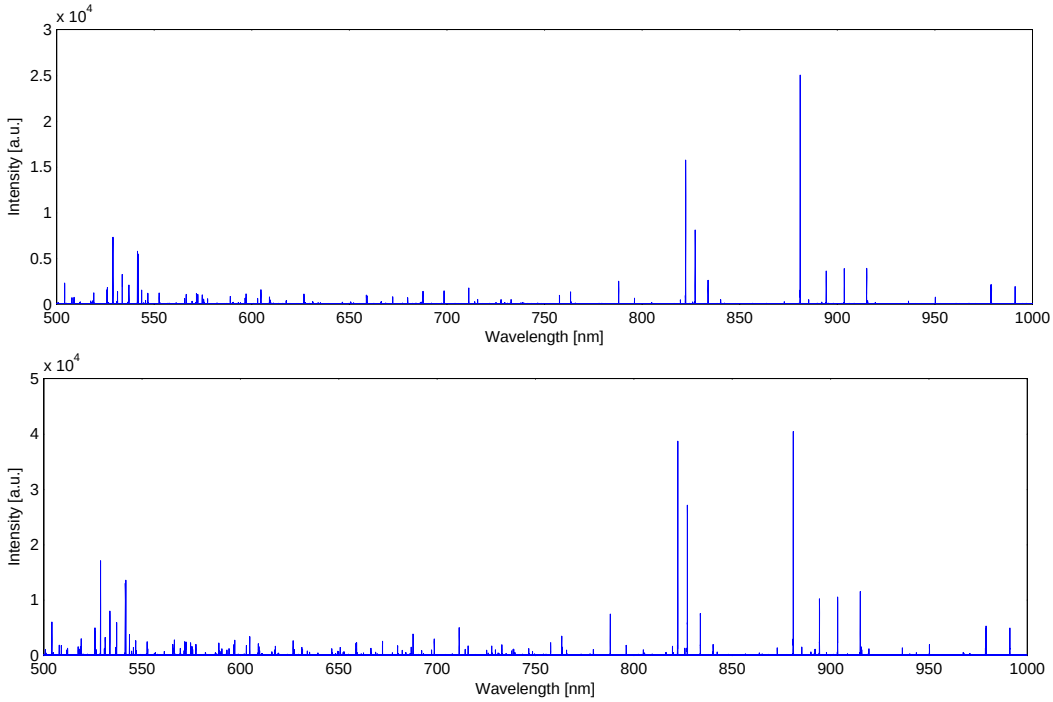

Figure 3-6: Comparison of the discharge region emission spectra from Region-I (top) and Region-VII (bottom)

It is observed that the intensity of the emission is lower for the plume region. In addition to the drop in the emission intensity, the relative intensity of Xe-II (Xenon single ion) lines to Xe-I (Xenon neutral) emission lines seems to be dropping in the plume region in comparison to the discharge region. This might be attributed to the faster drop in the ion density as the ions have much shorter residence times in the near plume region due to their high velocities. One other possible explanation could be the sharp drop in the plasma electron temperature. As Xenon ions have higher excitation energies, lower energy electrons will result in lower ionic emission intensity.

Hollow Cathode Region

Figure 3-8 shows the comparison of the measured spectra for the discharge and cathode regions. The discharge region is region-I in figure 3-5 and the cathode region is region-III. As observed from the presented graph, the cathode region radiation emission is dominated by the emission due to Xenon neutrals. This is expected as the cathode is a source of electrons and due to the higher potential for the keeper, only the neutrals leave the cathode. As the

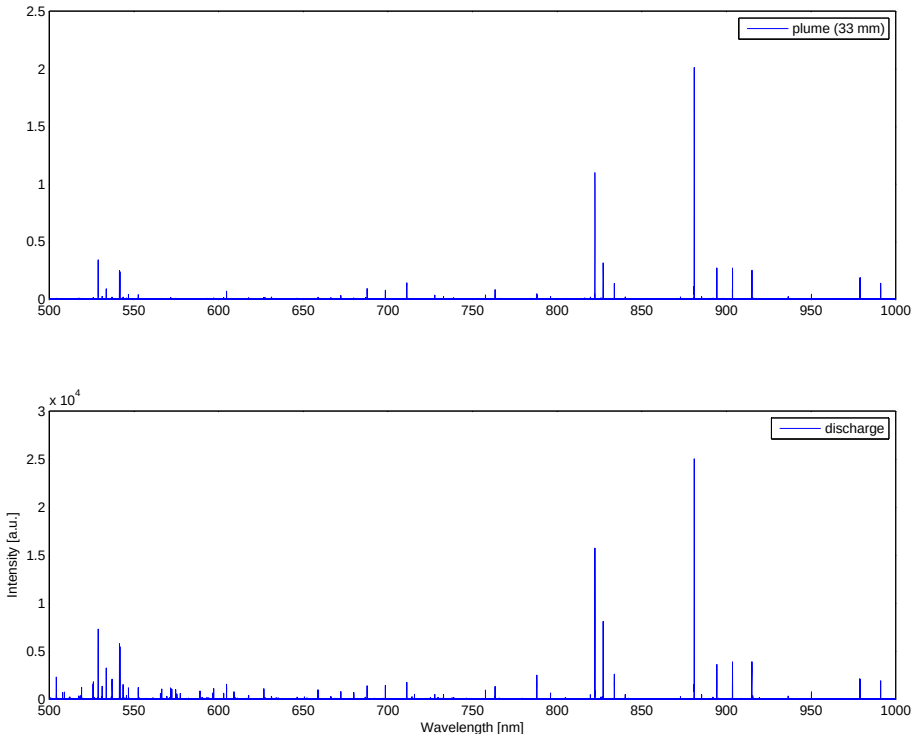

Figure 3-7: Comparison of the plume vs. discharge spectra

electron temperature in the cathode orifice region is 1-2eV [42][63], the ionization in this region will be negligible. Thus, the emission from this region will be due to the neutrals leaving the cathode.

Plume Spectra Comparison

Figure 3-9 shows the comparison of the spectra from five different plume regions all along the thruster axis, as shown in figure 3-5. As expected, the spectrum in the plume spike region (region-IX) is the brightest. The spike region also has the highest relative intensity of the Xenon ion emission. As observed from the emission spectra, the composition of the emitting particles are more and more neutrals as the plume expands. This can be attributed to the ions leaving the near plume region much faster than the slow neutrals. Also, some ions might be recombining with the cathode electrons. However, due to long mean free paths for the ion electron recombination processes, the neutralization is probably not the main factor. A better explanation lies with the effects of the non-ideal vacuum condition inside a vacuum chamber. According to computational modeling of the near plume plasma

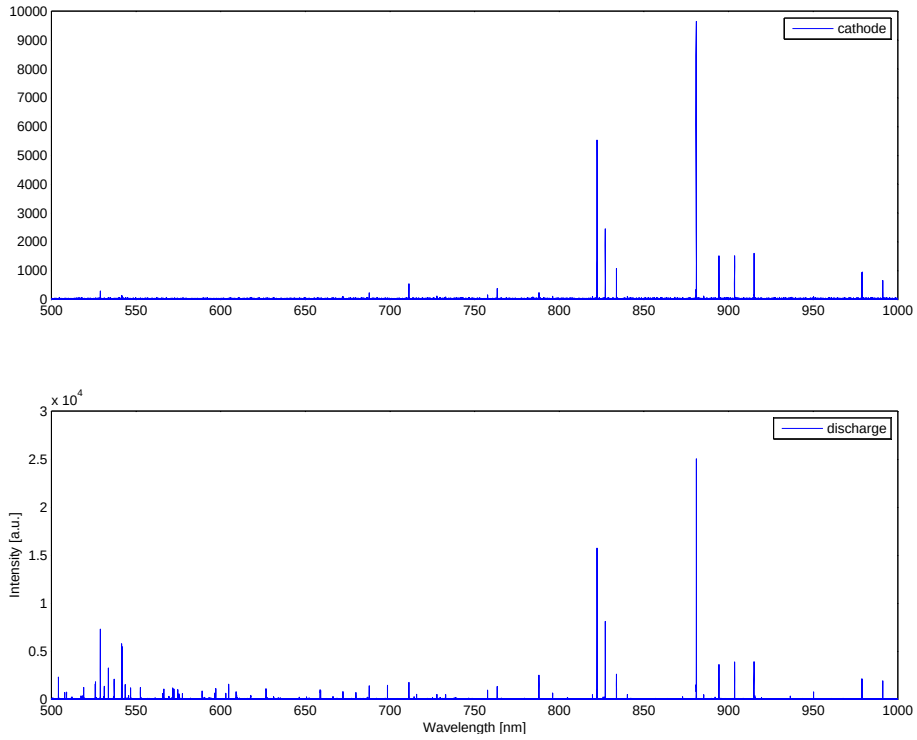

Figure 3-8: Comparison of the cathode vs. discharge region spectra

of the BHT-200 Hall thruster running inside the MIT-SPL vacuum chamber, in most of the plume region neutrals are mainly from the background and hence roughly constant, whereas the ion density falls off rapidly [22].

Figure 3-10 shows the linear plot of the intensity of 834.68nm Xenon neutral and 529.22nm Xenon single ion emission lines in the plume regions of observation. The x-axis for the plots represents the distance in *mm* from the thruster exit plane. As seen from the linear plots, the emission intensity drops as the distance from the thruster exit plane increases. However, the decrease in the ion emission intensity is faster. The ratio of neutral emission intensity between the plume spike region and the 33mm plume region is only $\sim$ 2.2 whereas, the intensity ratio of ion emission lines for the same two regions is $\sim$ 5.3.

Another observation from the two plots is that, the emission intensity is lower at 33mm distance than at 55mm distance in the plume region. One possible explanation for this observation is that the annular geometry of the thruster causes the spike region to have high collisionality and the region right after the spike region has a lower collisionality. Since the particle flux from the annular channel has a radial direction [26], this can cause the

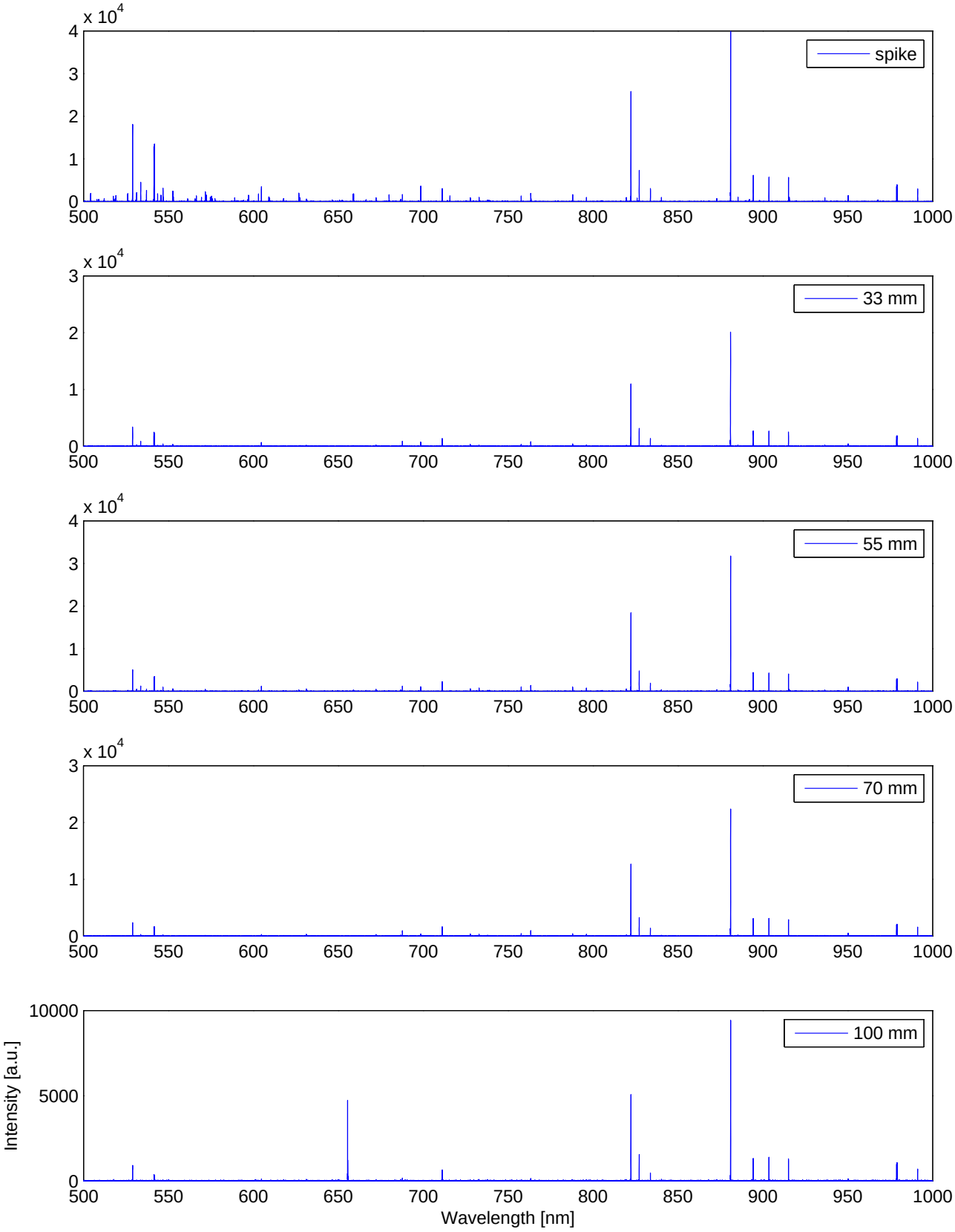

Figure 3-9: Comparison of the plume spectra along the thruster axis

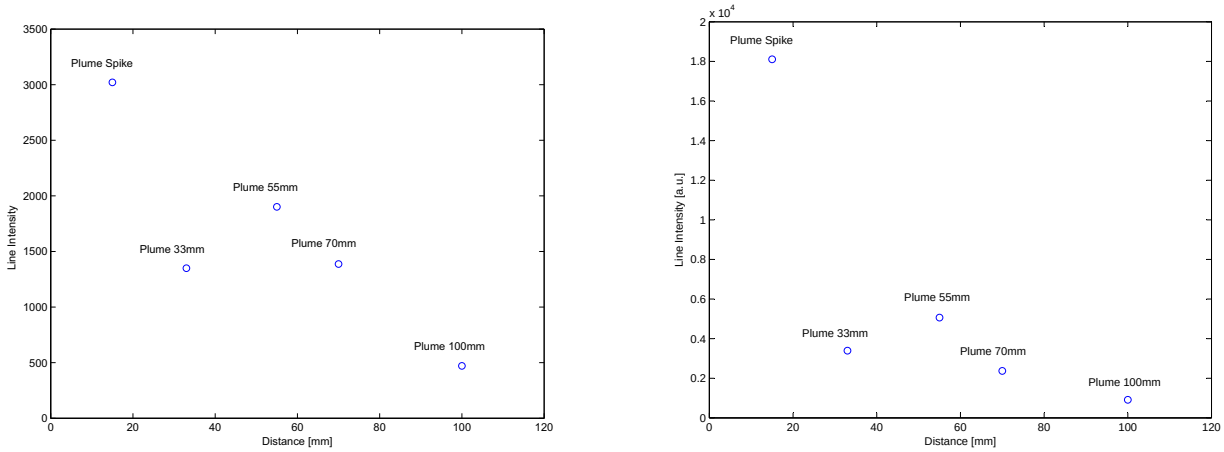

(a) Xe-I 834.68nm (b) Xe-II 529.22nm

Figure 3-10: Line emission intensity versus the plume region

region around 33mm away from the thruster exit plane to have a lower particle density.

Back Plate Region

In order to understand the backscattered particle identities, the focusing optical system was directed at the back of the BHT-200 thruster (region-X). No identifiable emission lines were detected in this measurement. The obtained spectrum is used as the background emission intensity to calibrate other measurement results.

3.3.2 Voltage Scan

In order to observe the variation in the emission spectrum of the BHT-200 Hall thruster, the thruster discharge voltage was varied from 75V to 300V with 25V increments and the emission spectra from the discharge region were measured. Figure 3-11 show the comparison of the spectra for the discharge region for varying discharge voltage values. For the measurements the optical system was pointed at region-VII shown in figure 3-5. Region-VII is selected because it is expected to be the region where the ionized particles accelerate. Also, as observed from the regional emission spectra comparison graphs, region-VII along with region-VIII has the highest emission intensity.

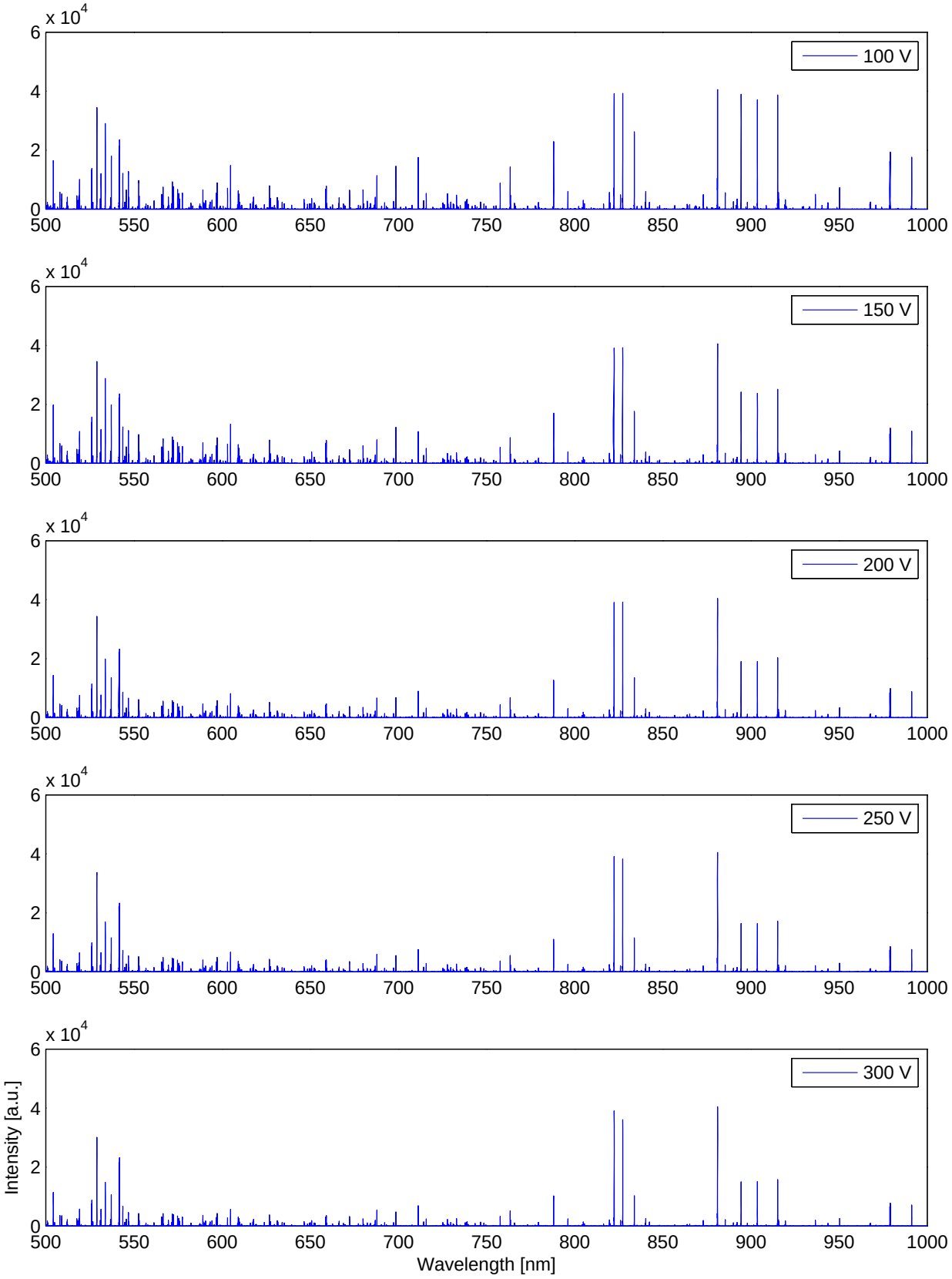

Figure 3-11: Comparison of the discharge spectra for varying discharge voltages:100V-300V

Since the ionized propellant particles would fall through a potential drop on the order of the discharge voltage, the discharge voltage determines the specific impulse obtainable. By conservation of energy, this relationship is:

$$\frac{1}{2}M_i v^2 \cong q_i V_d \tag{3.1}$$

where M_i is the mass of the ion, v is the velocity of the ion, q_i is the electrical charge of the ion, and V_d is the discharge potential. Thus the I_{sp} of the thruster is given by:

$$I_{sp} \cong \sqrt{\frac{2q_i V_d}{M_i g^2}} \tag{3.2}$$

where g is the gravitational acceleration constant on Earth.

In addition, it is observed that the plasma electron temperature increases as the discharge voltage is increased [78]. Thus, one would expect that as the discharge voltage is increased the plasma temperature would go up, resulting in an increase in the ionization fraction of the propellant. An increase in the discharge voltage is also likely to increase the doubly ionized propellant fraction. Thus, one would expect the spectra to be quite different as the voltage is varied. One would expect to see higher ratios of ionic to neutral line emission intensities.

However, according to recent publications where excitation cross section results were presented [27][51], the heavy particle induced excitation collisions are important in electric thruster plasmas. Thus, as the voltage is increased, the excitation processes as a result of heavy particle inelastic collisions would be expected to increase. This makes the interpretation of the observed spectra more difficult.

Figure 3-12 shows the linear plots of the intensities of a few prominent Xenon neutral and Xenon single ion emission lines as the discharge voltage is varied from 75V to 300V in increments of 25V. The top plots show the emission intensity of Xenon ion 529.22nm and 541.915nm lines as a function of discharge voltage. Similarly, the bottom plots show the measured emission intensity of Xenon neutral 788.74nm and 834.68nm lines as the discharge voltage is varied. As seen from these linear plots, the change in emission intensity is quite

different between the neutral and ion species.

As the discharge voltage increases, the intensities of both Xenon neutral 788.74nm and 834.68nm emission lines drop. The intensity drop is much steeper at lower voltages. From 75V to 100V, the 834.68nm line intensity drops by $\sim 40\%$, and the intensity drop is much less between 200V and 300V. Such a drop in the neutral emission intensity can be attributed to an increase in the ionization fraction of the propellant gas as the increase in the discharge voltage results in higher electron temperature and thus higher ionization.

For Xenon ionic emission, both 529.22nm and 541.92nm line intensities remain approximately constant as the voltage is varied. For the 529.22nm line, the intensity drops by about $10 - 15\%$ between 250V and 300V. In light of the trend in the neutral emission line intensity as the voltage is varied, the reasons for why the ion emission remains constant can be explained by calculating the expected ionization and ensuing axial acceleration of the ionized propellant gas particles. As the discharge voltage is increased, the electron temperature is increased and the propellant is more efficiently ionized. At the same time, as the discharge voltage is increased, the potential drop experienced by the ionized gas is increased as well, and the ionized particles leave the region of observation at a faster rate. From this observation, it seems that the rates balance and the total emission intensity of the ions remains relatively constant. This behavior is known from particle-in-cell (PIC) plasma simulations of the Hall thruster discharge channel. In plasma simulations it is observed that as the discharge voltage is increased, for the same propellant flow rate, the neutral density in the discharge channel drops, however the ion density does show little variation [11]. Due to lack of information about the actual electron temperature and a complete collisional radiative model, the explanation to this observation requires further analysis.

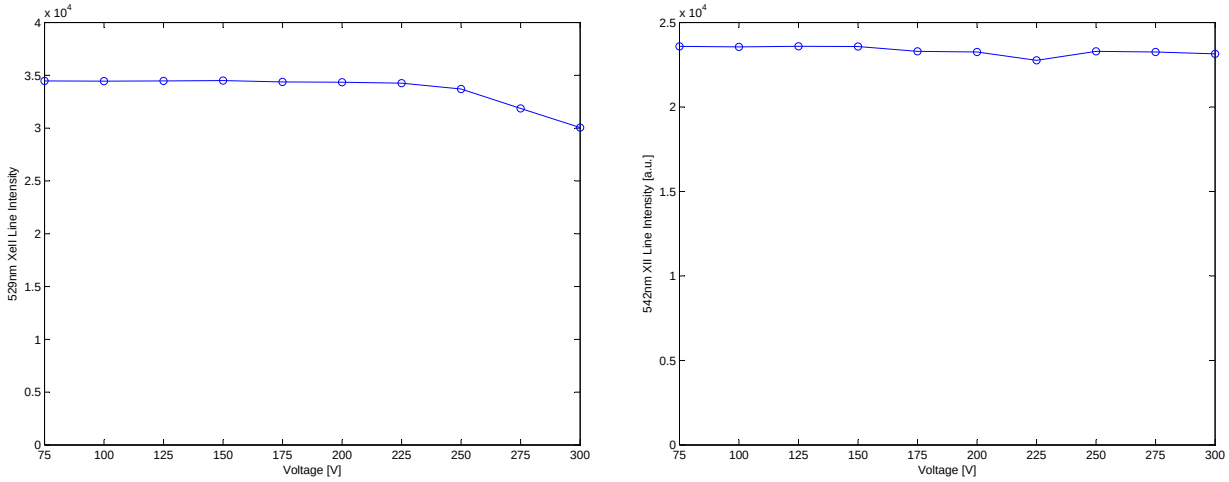

(a) XeII 529.22nm

(b) XeII 541.92nm

(c) XeI 834.68nm

(d) XeI 788.74nm

Figure 3-12: Line emission intensity versus the discharge voltage variation

3.4 Prediction of Plasma Temperature from Line Intensity Ratio

In a recent paper by Karabadzhak et al. [51], the authors claim that for Xenon plasma, the electron temperature can be predicted by simple fits to the line intensity ratios of three prominent Xenon neutral NIR emission lines at 823.16nm, 828.01nm and 834.68nm. The authors present an analytical fit for the line intensity ratio versus plasma electron temperature. Figure 3-14 shows the spectra for the plume regions in the 820-835nm wavelength range. The line intensities for these three lines are used to determine the plasma temperature using the analytical fit proposed by Karabadzhak et al. A graph of the fit is presented in figure 3-13, where α is the ratio of single ion density to electron density. For most Hall thrusters, the double ionization fraction is low, and α has values ranging from 0.70 to 0.95, depending on the specific thruster and operational parameters [60][56][47].

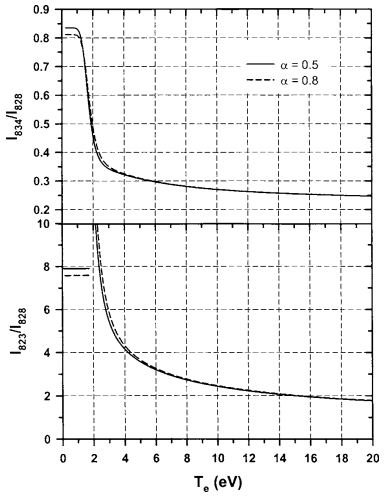

Figure 3-13: Calculated electron temperature dependence of the XeI line intensity ratios [51]

The intensity ratio of measured 823.16nm and 828.01nm lines was used to obtain the electron temperature in the thruster plume region using the fit in figure 3-13. According to the ratios of the 823.16 and 828.01 nm lines, the electron temperature is predicted to be 17eV for the discharge region (region-I), 5.5eV in the plume spike region (region-IX), 5.4eV in the 33mm plume region (region-II), 4.5eV in the 55mm plume region (region-IV), 4.5eV in the 70mm plume region (region-V) and 6.0 eV in the 100mm plume region (region-VI). The

obtained results and the comparison with the measurements reported by Beal et. al. [9] show discrepancies. According to Beal et. al., for the BHT-200 Hall thruster, the electron temperature at a distance of 5mm from the exit plane in the plume axis is measured to be 2.56eV and the measured temperature values agree with the value predicted by the equation: $T_e = T_{e,o}(n_e/n_{e,o})^{\gamma-1}$ for $T_{e,o} = 2.56eV$ and $n_{e,o} = 9.89 \times 10^{17}\ m^{-3}$ and $\gamma = 1.3$. Thus, according to this equation, the electron temperature drops in the plume region as the plasma density drops with distance from the thruster exit plane. However, one has to take into consideration that the regions of observation are not small volume elements in the axial region of the plume but rather long cylindrical (conical) regions that collect light from a chord of a cylindrical plasma region. Thus the region of observation for the measured spectra represents plasma regions with different plasma density and temperature. Nevertheless, the deduced plasma temperature values show similar trend to what would be expected.

3.5 Chapter Summary

In this chapter, spectral measurement results of the BHT-200 Hall thruster were presented and the observations were discussed. First, radiation emission measurement results from ten different regions of the thruster were presented for thruster's nominal operational conditions. Later, spectral measurements of the radiation emission from the thruster discharge region were presented for varying discharge voltages from 75V to 300V with 25V increments.

The emission spectrum in the cathode region is mainly composed of lines of neutral Xenon, indicating the small ionization fraction of the gases at the exit plane of the cathode. This is expected due to the very low temperatures for the electrons leaving the hollow cathode.

In the plume region, the measured emission intensity of both the ion and the neutral lines decrease along the thruster axis away from the exit plane. This can be explained by the decrease of plasma density away from the thruster exit plane, as the plasma expands into the vacuum of the chamber interior. The sharper decrease in the ion emission intensity in comparison to the neutral emission intensity might be attributed to fact that ion density

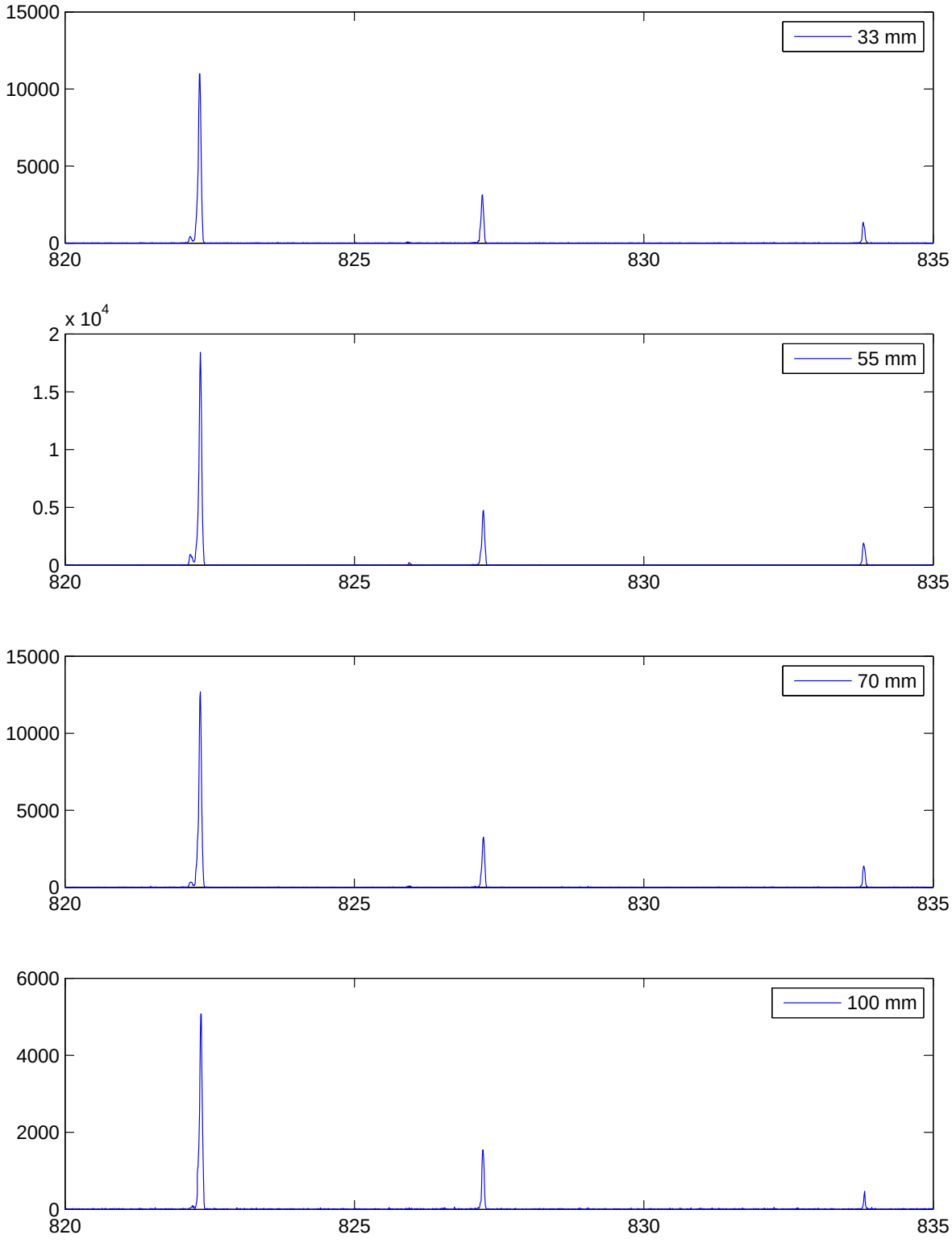

Figure 3-14: Comparison of the emission spectra in the plume region

falls of rapidly by expansion, however the neutral density falls of much slower due to the dominating effects of the constant neutral background density inside the vacuum chamber. Effects of the metastable levels in Xenon neutrals might also be causing some of the emission after the hot plasma region is passed.

The possibility of using the intensity ratio of Xe-I 823.16nm versus 828.01nm lines for electron temperature diagnostics was investigated for the plume region. It was found that the plasma temperature deduced from the line intensity ratio did not match with the intrusive probe measurements. However, the deduced temperature value showed similar trends to what was expected.

It was observed that for increased discharge voltage, in the discharge region of the thruster, the ion emission intensity remains fairly constant whereas the neutral emission intensity drops. One explanation provided for this observation was that as the discharge voltage is increased the ionization rate increases due to the increase in electron temperature causing a reduction in the neutral density, at the same time ionized particles leave the region faster due to the increased potential drop. For ions, this two effects seem to balance each other and the net ionic emission intensity remains unaffected by the variation of the discharge voltage.

In the BHT-200 Hall thruster measurements, no emission lines due to Xe double or triple ions (Xe-III and Xe-IV) were detected. Additionally, no radiation emission lines due to the thruster wall erosion products were measured.

Prominent Xenon Neutral and Single Ion Emission Lines in 400-1000nm Region									
Xe II	403.729	Xe II	461.506	Xe II	536.807	Xe II	627.082	Xe I	758.468
Xe II	403.759	Xe II	461.55	Xe II	537.239	Xe II	627.754	Xe II	761.857
Xe II	405.746	Xe II	461.55	Xe I	539.2795	Xe I	628.6011	Xe I	764.391
Xe I	407.88202	Xe II	465.194	Xe II	541.915	Xe II	630.086	Xe II	767.066
Xe II	409.889	Xe II	466.849	Xe II	543.896	Xe I	631.8062	Xe II	778.704
Xe II	415.804	Xe II	467.646	Xe II	544.545	Xe II	634.396	Xe I	780.2651
Xe II	418.01	Xe I	469.097	Xe II	545.045	Xe II	635.635	Xe I	788.7393
Xe II	419.315	Xe II	469.801	Xe II	546.039	Xe II	637.528	Xe II	800.845
Xe I	419.3528	Xe II	471.518	Xe II	547.261	Xe I	646.9705	Xe I	802.967
Xe II	420.848	Xe II	473.119	Xe II	553.107	Xe I	647.2841	Xe I	802.967
Xe II	420.947	Xe II	476.905	Xe I	556.6615	Xe I	648.7765	Xe II	803.164
Xe II	421.372	Xe II	478.777	Xe II	561.667	Xe I	649.8717	Xe II	803.826
Xe II	421.56	Xe II	481.802	Xe II	565.938	Xe I	650.418	Xe I	805.7258
Xe II	422.3	Xe II	482.335	Xe II	566.756	Xe II	651.283	Xe I	810.198
Xe II	423.825	Xe I	482.9708	Xe I	569.575	Xe II	652.865	Xe II	815.18
Xe II	424.538	Xe I	484.32934	Xe II	569.961	Xe I	653.3159	Xe I	817.102
Xe II	425.157	Xe II	484.433	Xe II	571.61	Xe II	659.501	Xe I	820.6336
Xe II	429.64	Xe II	486.245	Xe II	571.961	Xe I	659.5561	Xe I	823.16336
Xe II	431.051	Xe II	487.65	Xe II	572.691	Xe II	659.725	Xe I	826.652
Xe II	433.052	Xe II	488.353	Xe II	575.103	Xe II	662.002	Xe I	828.01162
Xe II	436.92	Xe II	488.415	Xe II	575.865	Xe I	666.892	Xe II	829.755
Xe II	437.378	Xe II	488.73	Xe II	577.639	Xe II	669.432	Xe I	834.68217
Xe I	438.3908	Xe II	489.009	Xe I	582.389	Xe I	672.8008	Xe II	834.724
Xe II	439.32	Xe II	489.009	Xe I	582.48	Xe II	678.871	Xe I	857.601
Xe II	439.577	Xe II	491.966	Xe I	587.5018	Xe II	680.574	Xe I	864.854
Xe II	440.688	Xe II	492.148	Xe II	589.329	Xe I	682.7315	Xe I	869.22
Xe II	441.484	Xe I	492.3152	Xe I	589.4988	Xe I	687.2107	Xe I	869.686
Xe II	441.484	Xe II	497.171	Xe II	590.513	Xe I	688.2155	Xe I	873.9372
Xe II	441.607	Xe II	497.271	Xe I	593.4172	Xe II	691.022	Xe I	875.82
Xe II	444.813	Xe II	498.877	Xe II	594.553	Xe I	692.553	Xe I	886.232
Xe II	446.219	Xe I	502.82794	Xe II	597.113	Xe I	697.6182	Xe I	890.873
Xe II	448.086	Xe II	504.492	Xe II	597.646	Xe II	699.088	Xe I	893.083
Xe II	452.186	Xe II	508.062	Xe II	600.892	Xe II	708.215	Xe I	898.105
Xe II	452.421	Xe II	512.242	Xe II	603.62	Xe I	711.9598	Xe I	898.757
Xe II	453.249	Xe II	518.804	Xe II	605.115	Xe II	714.75	Xe I	904.54466
Xe II	454.089	Xe II	519.137	Xe II	609.35	Xe II	714.903	Xe I	916.2652
Xe II	454.523	Xe II	526.044	Xe II	609.759	Xe II	716.483	Xe I	916.752
Xe II	455.594	Xe II	526.195	Xe II	610.143	Xe II	728.434	Xe I	937.476
Xe II	457.706	Xe II	529.222	Xe I	617.8303	Xe II	730.18	Xe I	951.3377
Xe II	458.548	Xe II	530.927	Xe I	617.9665	Xe II	733.93	Xe I	968.532
Xe II	459.205	Xe II	531.387	Xe I	618.242	Xe I	738.6003	Xe I	971.816
Xe II	460.303	Xe II	533.933	Xe II	619.407	Xe I	739.3793	Xe I	979.9697
Xe I	461.18882	Xe II	536.32	Xe I	619.826	Xe II	754.845	Xe I	992.3198

Table 3.2: List of Prominent XeI and XeII Lines in 400-1000nm Wavelength Region

Chapter 4

MHT-9 Hall Thruster Spectral Measurements

Emission spectroscopy measurements of an experimental laboratory model Hall Thruster, MHT-9, running on Xenon propellant were conducted. The measured spectra are presented in this chapter along with the discussion of the observations. The measured emission spectrum for MHT-9 is also compared with the BHT-200 Hall thruster emission spectrum. More detailed spectral graphs are presented in Appendix B. MHT-9 Hall Thruster spectral measurements were conducted in June of 2006, during initial characterization tests of the thruster.

4.1 MHT-9 Hall Thruster

The Miniature Hall Thruster (MHT-9) is a TAL type Hall thruster built by Warner [76] [77] at the MIT Space Propulsion Laboratory in order to study the scaling methods for Hall thrusters. It has a $9mm$ mid-channel diameter. The thruster was designed to operate at a nominal power of $200W$. However, a power level of $\sim 350W$ seems more of a nominal operational power level for this thruster. The thruster was equipped with a hallow cathode built by Busek Co. The hollow cathode is the same type that was used with the BHT-200

Hall thruster described in chapter 3.

The MHT-9 Hall thruster is a scaled version of a Russian made TAL type Hall thruster, D-55. Thus, the major dimensions and operating conditions of the MHT-9 thruster are based on the D-55 Hall thruster. The D-55 Hall thruster has a $45mm$ diameter acceleration channel and has a nominal operation power of $1230W$. It was intended that MHT-9 would have similar performance characteristics as the D-55 but at lower power levels [76].

Observed Thruster Operation Parameters	
Power	347 W
Discharge Voltage	300 V
Propellant Flow Rate	0.84 mg/s (Xe)
Thrust	12.3 mN
Efficiency	30 %
Specific Impulse	1706 s

Table 4.1: MHT-9 Hall Thruster [76]

4.2 TAL vs. SPT type of Hall Thrusters

Historically, Soviet researchers developed two Hall thruster variants that are denoted by SPT and TAL acronyms. SPT stands for *Stationary Plasma Thruster* and TAL stands for *Thruster with Anode Layer*. The name *stationary plasma thruster* came from the Russian translation of the name given to these thrusters, the name possibly stems from the need to differentiate it from *pulsed* plasma thrusters [28]. These thrusters have annular acceleration channels that have walls made of insulator material, typically boron nitride ceramic. The name *thruster with anode layer* is also a translation of the name given to this type of thruster in Russian. TAL type Hall thrusters have metallic walls. In addition, the TAL type thrusters have shorter acceleration region which is confined to a sharp potential drop in a thin layer at the anode [28]. The TAL type Hall thrusters also have considerably higher electron temperatures compared to the SPT type Hall thrusters, due to the absence of strong secondary electron emission from the floating metal walls.

The Russian made Hall thrusters are generally named after the size of the outer diameter

(in millimeters) of the annular acceleration channel. So for example, the SPT-100 thruster has an outer diameter of 100mm. In Russian notation, the SPT and T prefixes are used for SPT type and D is used for TAL type Hall thrusters (SPT-70, SPT-100, SPT-140, T-100 are stationary plasma thrusters, and D-55, D-100 are TAL type thrusters, etc.). In the US the thrusters are mostly named with their manufacturer's name and the nominal power requirement for the thruster. For example, BHT-200 is a Busek Hall Thruster that has a nominal power requirement of 200 Watts, and BHT-4000 is a thruster by the same company with a nominal power requirement of 4000W. However, the assignment of thruster names still varies between manufacturers and no standard exists yet as in the case of MIT's MHT-9 thruster having its name not based on its nominal operational power level but based on the diameter of its annular acceleration channel of $9mm$ as it is a scaled model of a Russian thruster.

4.3 Experimental Setup

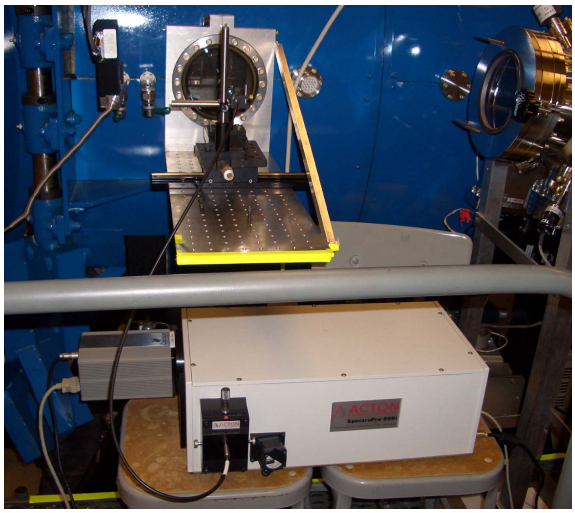

Figure 4-1: Experimental setup for MHT-9 spectral measurements

Spectral measurements on the MHT-9 Hall thruster were conducted in the MIT Space Propulsion Laboratory vacuum chamber during the thruster's preliminary testing in June of 2006, when it was fired for two hours. The thruster was placed on top of a metal platform in the central axis of the cylindrical chamber aligned with the window port. The thruster firing direction was aligned with the vacuum tank cylindrical axis. The pressure of the

vacuum chamber was measured to be 2.34×10^{-7} Torr before the firing of the thruster, and the pressure during testing did not exceed 3.5×10^{-5} Torr [76].

The experimental setup for the spectral measurements was the same as the one described in section 3.2 for the BHT-200 Hall Thruster measurements. A picture of the spectroscopy setup is shown in figure 4-1.

4.4 MHT-9 Hall Thruster Measurement Results

In this section, the spectral graphs for the MHT-9 Hall thruster emission in the 400-900nm wavelength range are presented. A picture of the MHT-9 Hall thruster running inside the vacuum chamber is shown in figure 4-2. The collecting optics system was pointed at the thruster exit plane visible from the picture. Prominent emission lines for Xenon neutral and single ion in the wavelength region of measurements are tabulated in table 3.2. As discussed earlier in chapter 3, the near-infrared (NIR) region of the spectrum is dominated by strong Xenon neutral emission lines and the 400-600nm wavelength region has predominantly Xenon single ion emission lines. Thus, the emission intensity in the wavelength region from 800 to 900nm presents the trends for the Xenon neutral atoms, whereas the intensity of the emission lines in the 400-600nm wavelength region represents the trends for the Xenon single ions.

Figure 4-2: MHT-9 Hall Thruster in operation inside the MIT-SPL vacuum chamber

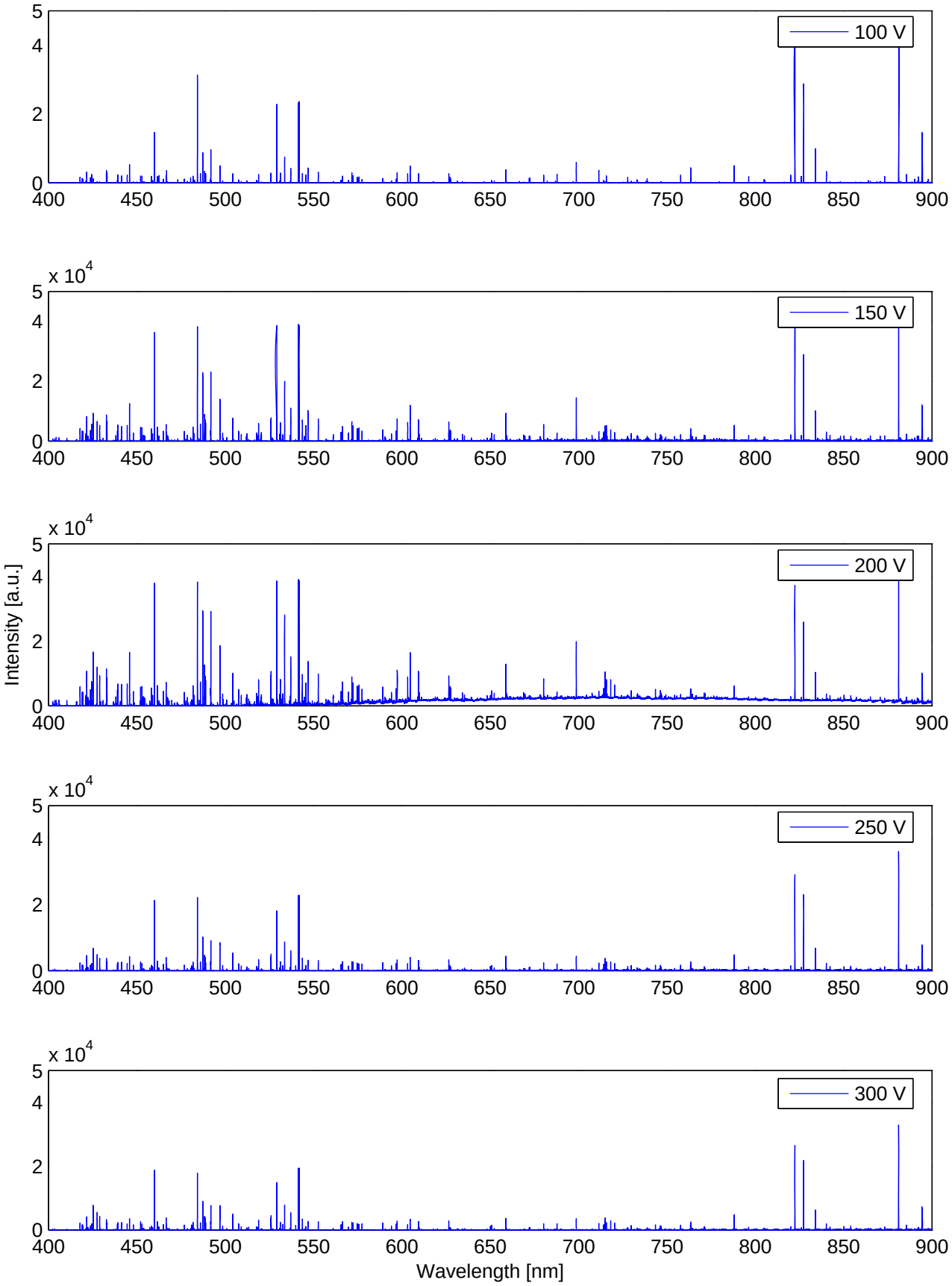

Figure 4-3: Comparison of the MHT-9 spectra for varying discharge voltages: 100V-300V

4.4.1 Discharge Voltage Scan

In order to determine the effect of the discharge voltage on the emission spectrum of the MHT-9 Hall thruster, the thruster discharge voltage was varied from 100V to 300V with 50V increments and the emission spectra were measured. Figure 4-3 shows the obtained spectra for the voltage scan. For the presented spectra, the anode flow rate was 5.5 *sccm* and the cathode flow rate was 1.0 *sccm*.

Unfortunately, for the 150V and 200V cases the prominent emission lines were saturated due to their high intensity for the given CCD exposure time. However, from the unsaturated line intensities, it is observed that the highest emission occurs for the 200V discharge voltage case. This is especially true for the Xenon ion emission lines.

Figure 4-4 shows the trends in the emission line intensity of Xenon neutral lines at 788.74nm and 834.68nm, and Xenon single ion lines at 609.76nm and 699.09nm as the discharge voltage is varied. All these lines are far from saturation. As seen from the linear plots, for both neutrals and ions, the line emission intensity is highest for 200V. The ion emission however has a stronger discharge voltage dependence. For these selected lines, the emission intensity shows similar behavior for different anode propellant flow rates.

Another interesting observation from the spectral graphs was that for the 200V case, there seems to be higher continuum emission in the wavelength range of observation. Even though the same background removal method is applied to the data, for all three Xenon anode flow rates of 5.5, 6.5 and 7.5 *sccm*, the 200V case spectra have high continuum emission. The reason for this observation is unknown.

4.4.2 Flow Rate Scan

In addition to the discharge voltage scan, in order to determine the effect of the anode propellant flow rate on the emission spectrum of the MHT-9 Hall thruster, spectral measurements were conducted for three different anode flow rates: 5.5, 6.5 and 7.5 *sccm* of Xenon. Figure 4-5 shows the measured spectra for the anode flow rate scan. For the pre-

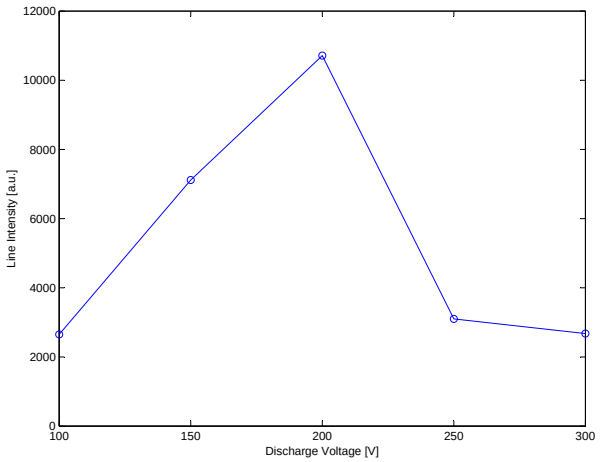

(a) XeII 609.76nm

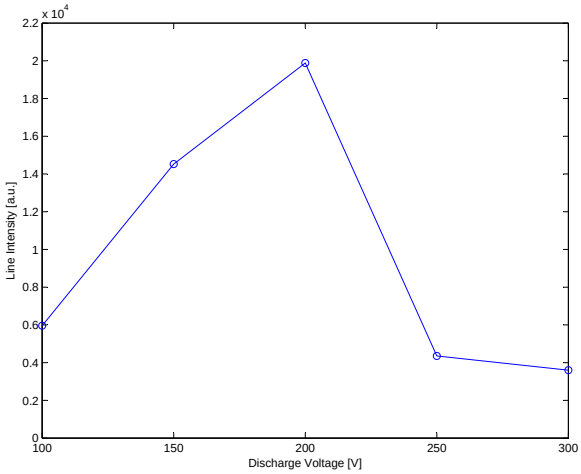

(b) XeII 699.09nm

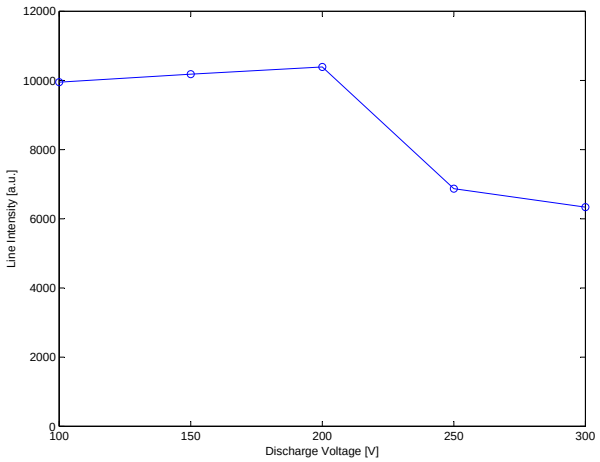

(c) XeI 834.68nm

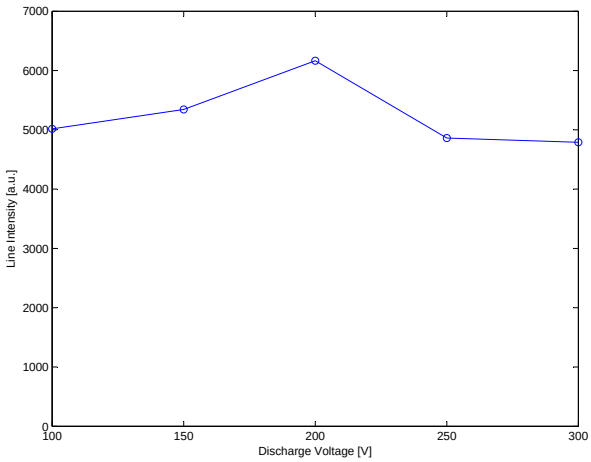

(d) XeI 788.74nm

Figure 4-4: Line emission intensity versus the discharge voltage variation

sented spectra, the discharge voltage was 300V and the cathode flow rate was 1.0 *sccm*. As seen in these graphs, the line emission intensity increases as the propellant flow rate is increased.

Figure 4-6 shows the change in the emission intensity of the Xenon neutral lines at 788.74nm and 834.68nm, and the Xenon single ion lines at 609.76nm and 699.09nm as the anode flow rate is varied. The flow rate increase results in the increase of the emission line intensities for both the neutral and the ion lines. As seen from the presented graphs, the intensity of the neutral lines increase roughly linearly with the increase of the flow rate. However, the intensity of the Xenon single ion emission lines have sharper increase than that of the propellant flow rate. Thus, for the 300V discharge voltage case, as the flow rate is increased

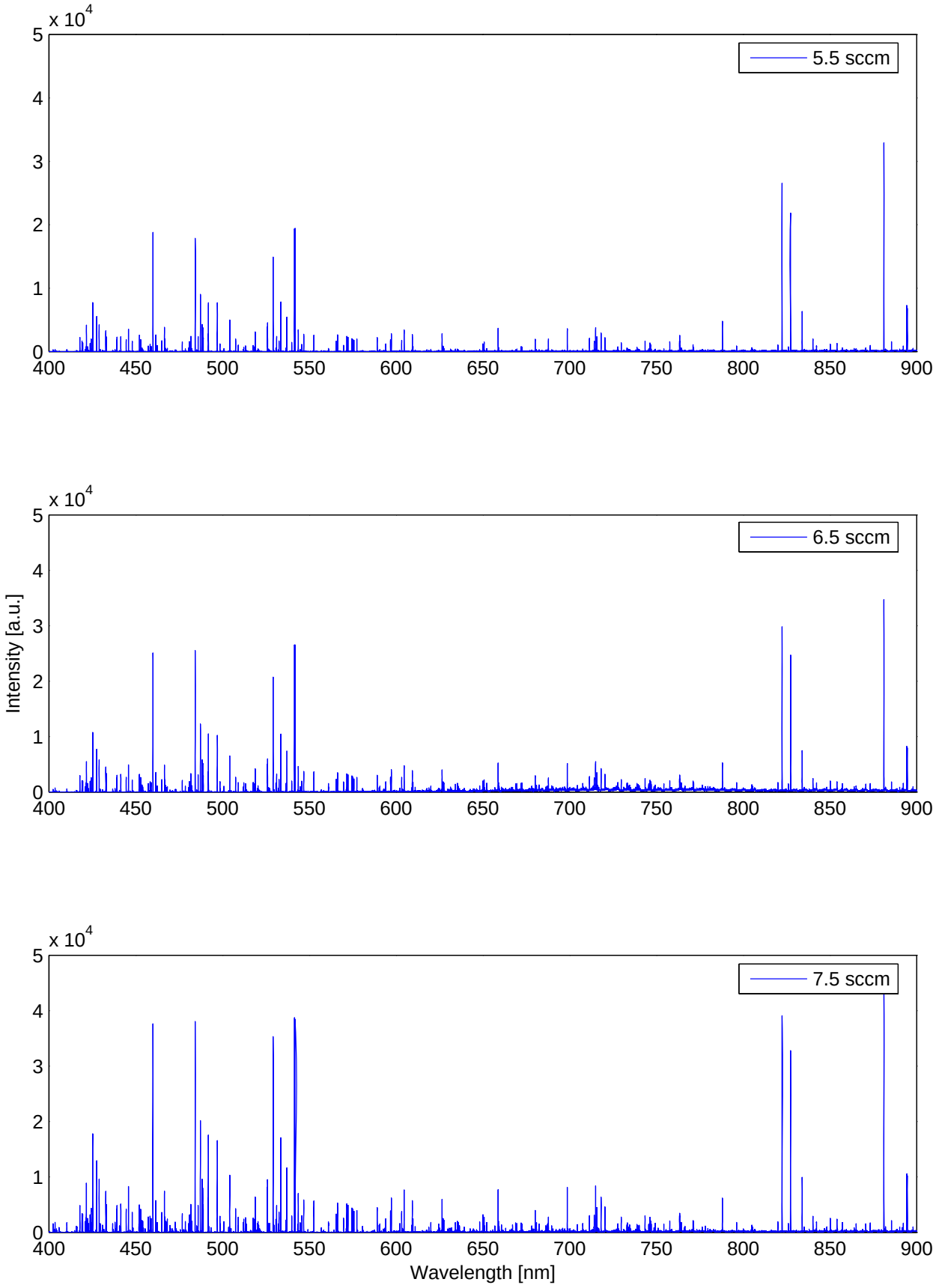

Figure 4-5: Comparison of the MHT-9 spectra for varying anode flow rate: $5.5 - 7.5 sccm$

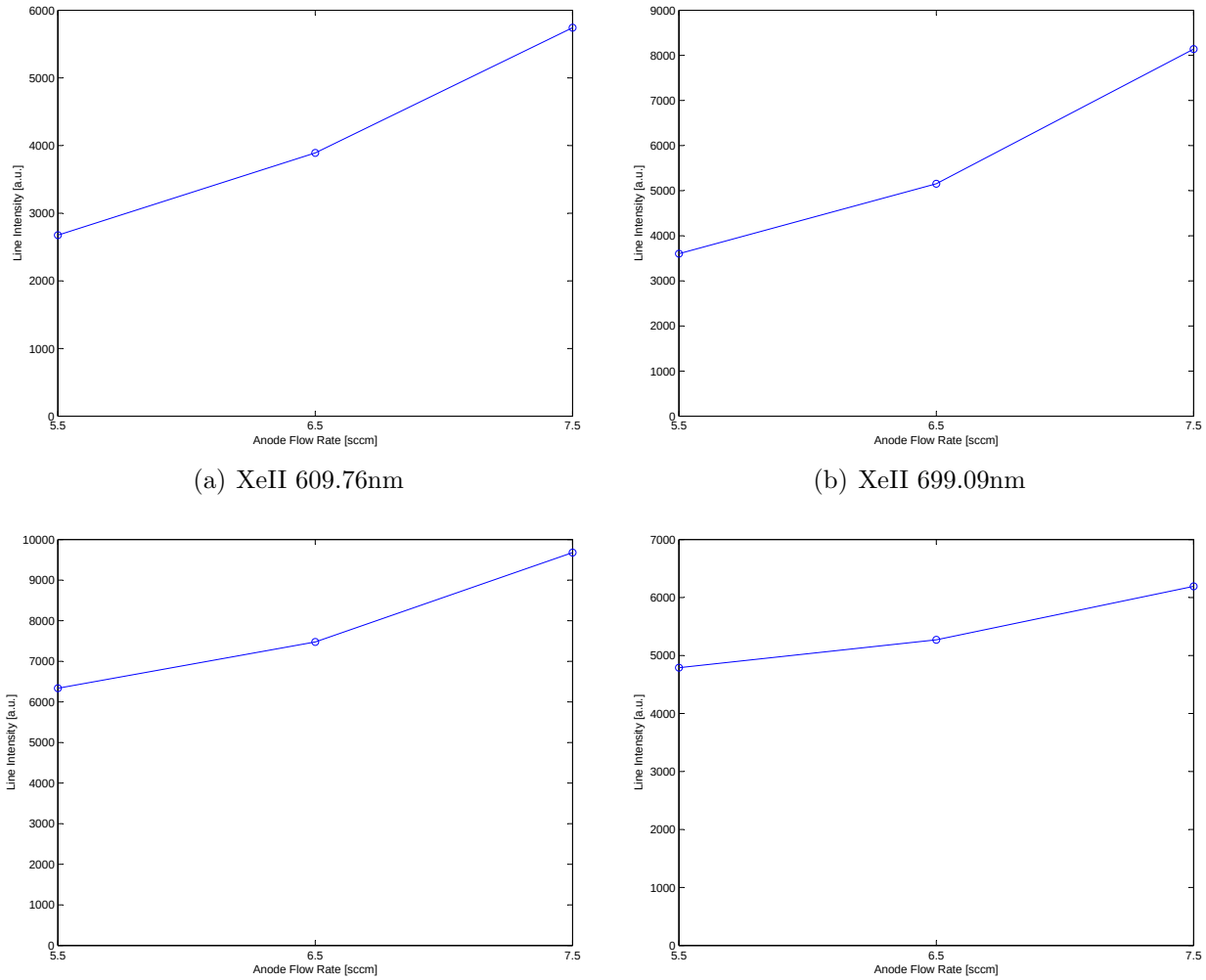

(a) XeII 609.76nm

(b) XeII 699.09nm

(c) XeI 834.68nm

(d) XeI 788.74nm

Figure 4-6: Line emission intensity versus the anode flow rate variation

there is an increase in the degree of ionization of the propellant gas.

4.4.3 Comparison of MHT-9 and BHT-200 Spectra

MHT-9 is a TAL type Hall thruster with a short acceleration layer near the metallic anode, while the BHT-200 is an SPT type Hall thruster with a long ceramic annular channel. Both thrusters were designed to have a nominal operational power of $\sim 200W$. The measured spectra for these two thrusters were compared as shown in figure 4-7. Since the exposure times were different, in the presented spectra, only the relative intensity of the emission lines are compared.

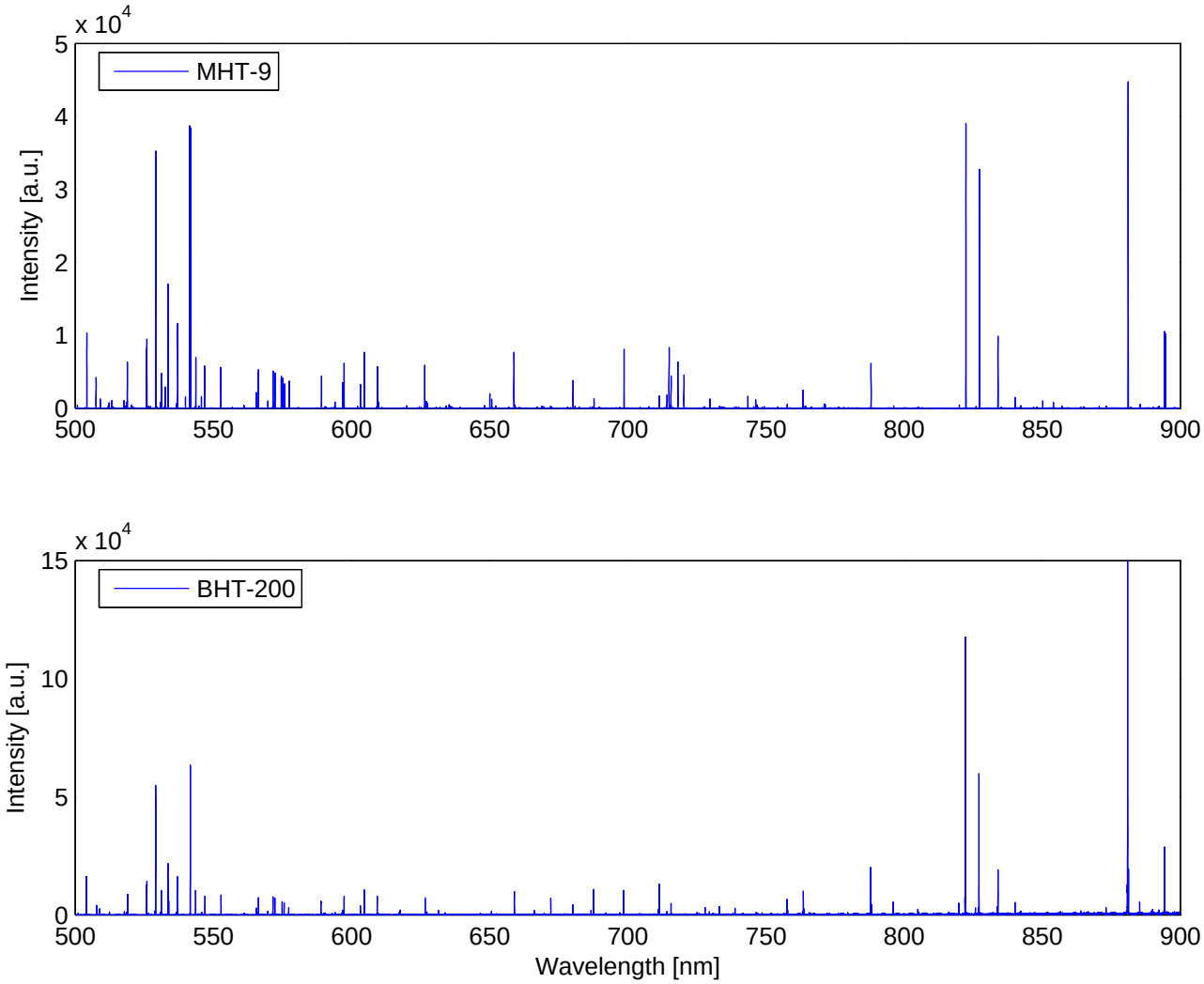

Figure 4-7: Comparison of the MHT-9 and BHT-200 Hall thruster emission spectra

As seen from the comparison of the two spectra, the MHT-9 Hall thruster has higher relative ion emission intensity in comparison to that of the BHT-200 Hall thruster. This might be as a result of the higher plasma density and higher electron temperature for the MHT-9 Hall thruster. Due to its small anode diameter, and since the mass flow rate scales with the diameter instead of the area, the MHT-9 Hall thruster is expected to have much higher plasma density in the thruster exit plane. In addition due to the short acceleration region for the TAL type Hall thrusters, it is expected that MHT-9 has a higher electron temperature.

4.5 Chapter Summary

Spectral measurements of a TAL type laboratory Hall thruster, MHT-9, were performed. The change in emission spectra due to variations in thruster discharge voltage and the anode propellant rate was investigated. It was observed that, the emission intensity is highest for a discharge voltage of 200V. Additionally, for increasing anode flow rate, it was observed that the ion emission intensity increases more than the neutral emission intensity.

The emission spectrum of the MHT-9 Hall thruster was compared with the BHT-200 Hall thruster emission spectrum. It was observed that, the MHT-9 Hall thruster has a higher relative ion to neutral emission intensity. This observation was consistent with the expectation that the TAL type Hall thrusters have higher electron temperature.

Chapter 5

Spectral Measurements of a Helicon Plasma Source

The mini Helicon Thruster Experiment, mHTX, has been built in-house at the MIT Space Propulsion Laboratory in order to assess the possibility of using a helicon plasma source as a propulsive device without a secondary heating or acceleration mechanism [69][8]. Emission spectra of the mHTX helicon plasma were measured [18]. The spectral measurements allowed the determination of the major trends in the degree of ionization of the propellant gas. Various plasma operation parameters such as delivered RF power, propellant mass flow rate, and applied external magnetic field intensity were varied. The measurement results and the accompanying discussion and analysis are presented in this chapter.

Plasma sources employing helicon wave excitation effectively produce uniform, high density plasma [13][24][4]. A helicon source is planned to be used as the primary ionization means for the Variable Specific Impulse Magnetoplasma Rocket (VASIMR) concept [32].

The goal of the mini Helicon Thruster Experiment is to characterize the helicon plasma source in order to gain a deeper understanding of the plasma generation by helical shaped RF antennae, and identify methods by which plasma parameters can be tuned to accelerate the obtained high density plasma to achieve an efficient propulsive system [69].

5.1 Mini Helicon Thruster Experiment (mHTX)

The mini Helicon Thruster Experiment setup consists of a pair of cylindrical electromagnets surrounding a long 2-cm diameter cylindrical quartz tube where the propellant gas flows through. A metallic helical antenna is placed over the quartz tube between the electromagnets. This setup is placed inside the vacuum tank on a metal platform as shown in figure 5-1.

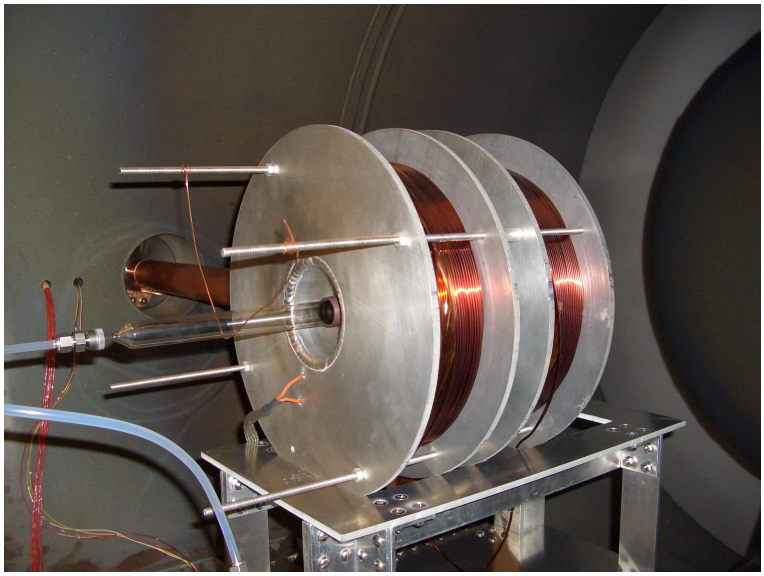

Figure 5-1: Helicon Plasma Source Setup placed inside the MIT-SPL vacuum facility

One end of the quartz tube is attached to a propellant gas flow line, and the other is open to the vacuum of the chamber. The gas flow is controlled by a digital flow meter located outside of the vacuum chamber. Most of the experiments were conducted using Argon gas as the propellant. However, Nitrogen, Xenon and air discharges were also observed and studied.

The helical antenna is powered by a 1.2kW RF power supply, Advanced Energy RFPP-10, operating at 13.56 MHz [69]. The antenna is connected to the RF power supply by an in-house built coaxial transmission line located inside the chamber, a 13.56 MHz vacuum RF power feedthrough, and an impedance-matching network attached to the vacuum port on the outside of the chamber. The impedance-matching network has a classic L-network circuit structure that employs two adjustable vacuum capacitors [69].

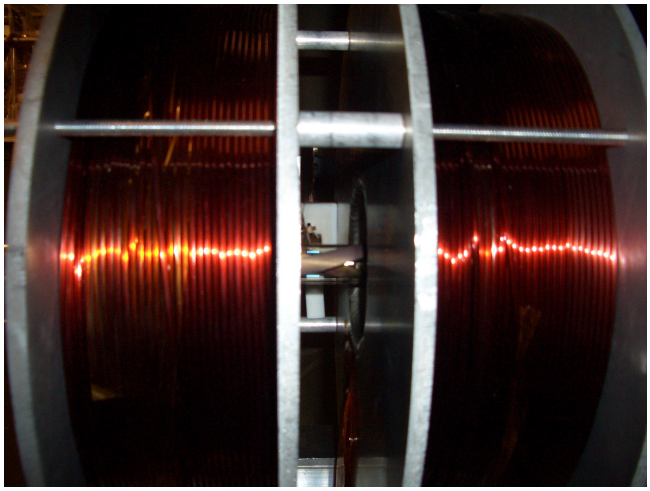

Figure 5-2: Helical antenna placed around the quartz tube between the Helmholtz pair of electromagnets

In order to produce the helicon discharge, the external magnetic field is generated through the use of a pair of electromagnets in Helmholtz configuration. The electromagnets are wound from 10 AWG square, insulated magnet wire [69]. A current of up to 35A is supplied to each electromagnet coils by two 35A-350V power supplies. The magnet system produces a maximum axial magnetic field intensity of 2000 Gauss at the center, axial region between the electromagnets for 35A current to each coil. The helicon antenna is located in this high, axial magnetic field region. Figure 5-2 shows a picture of the antenna located between the electromagnet coils. During the experiments the magnet current is modified for the desired magnetic field intensity. Since the magnets have no cooling pipes, two thermocouple sensors were placed in each magnet in order to monitor the temperature, thus preventing overheating of the magnets [69].

For most of the measurements a $9.86cm$ long $2cm$ diameter helical antenna made of copper was used. However, a longer $13.94cm$ copper antenna and a $9.86cm$ stainless steel antenna were also tested to study the effects of antenna length and material on plasma density. Figure 5-3 shows the picture of the copper antenna, placed between the Helmholtz coils, used for most of our measurements. The figure also shows a picture of the stainless steel antenna of the same length.

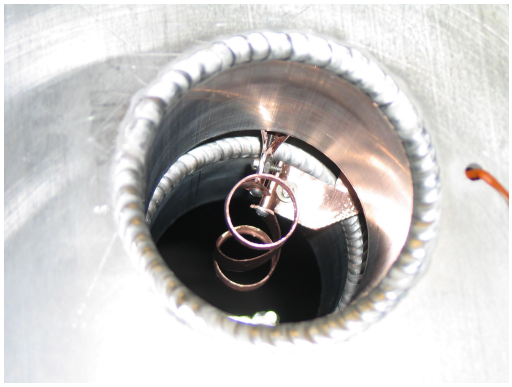

(a) Copper Antenna

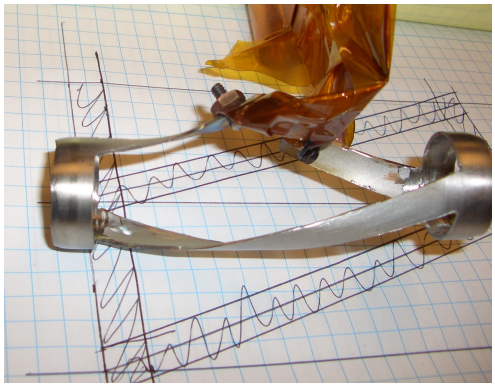

(b) Stainless Steel Antenna

Figure 5-3: Pictures of the helical RF antennas used in the Helicon plasma source experiments

5.2 Experimental Setup

The spectral measurements were performed at the MIT Space Propulsion Laboratory. The vacuum tank was described in section 3.2. A schematic of the MIT-SPL vacuum tank and the helicon plasma source inside can be seen in figure 5-4. The plasma source was located in the center of the vacuum tank, and the antenna region aligned with one of the side windows. The light collection system was placed on a metal shelf that was attached to the glass window port of the vacuum tank.

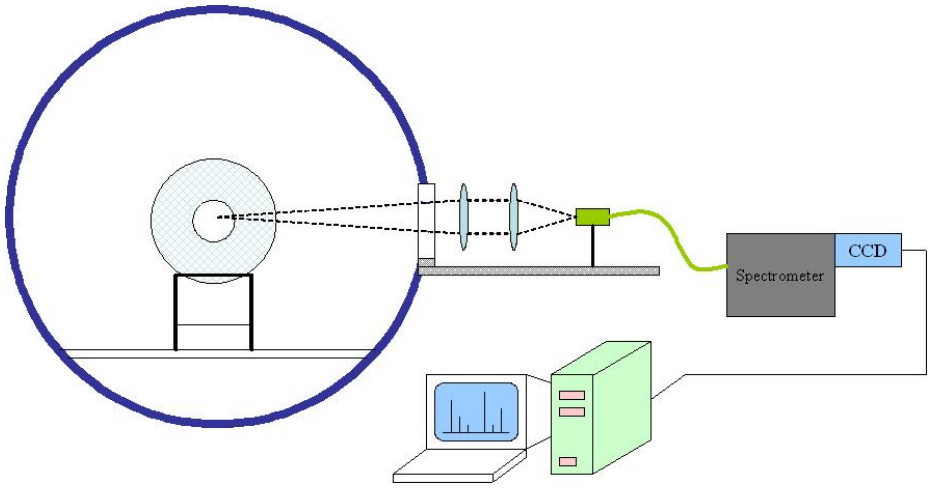

Figure 5-4: Illustration of the experimental setup for spectroscopic measurements

5.2.1 Radiation Collection and Transmission

A collimating-focusing lens system is used to collect the light from the plasma region of interest. The whole optical setup is placed on a metal shelf attached to the vacuum tank window as shown in figure 5-5. As described in more detail in section 3.2.1, the radiation collection is accomplished by a pair of 1 inch diameter collimating-focusing lenses with 1000mm and 100mm focal lengths, respectively. The end of a 36 inch long Oriel fiber bundle is placed at the focal point of the focusing lens. In order to reduce the stray light from inside the vacuum tank, the window is covered with a black optical card board with a $\sim$1 inch hole cut in the middle, in line with the lens axis. A mechanical diaphragm is placed before the collimating lens in order to adjust the intensity of the collected light. The shelf is covered with an optically opaque black cloth during the data acquisition. Mechanical translation stages were used to adjust the exact location and the proper alignment of the optical components. A fiber adapter is used to hold the fiber bundle directly at the entrance slit of the spectrometer.

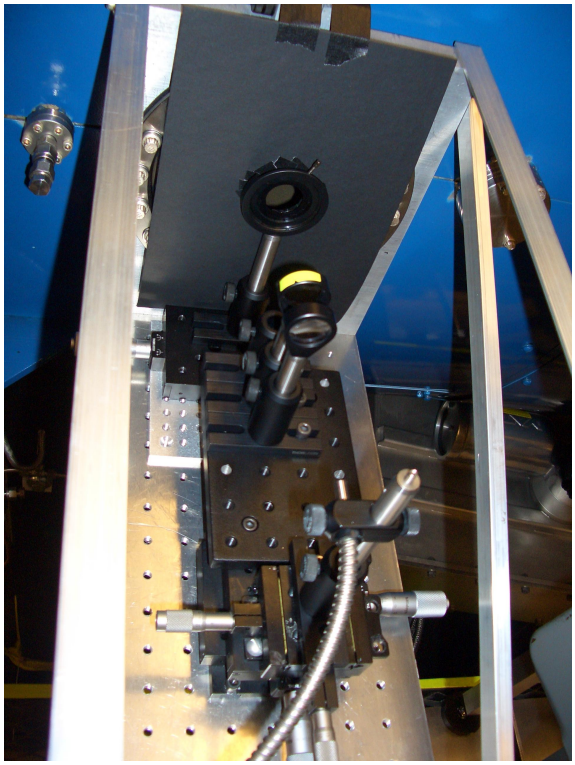

Figure 5-5: Collimating-focusing lens system on the optical shelf attached to the MIT-SPL vacuum tank window port

5.2.2 Radiation Dispersion

A Thermo Jarrel Ash Monospec-18 spectrometer was used as the dispersive instrument. This 156mm focal length, f/3.8 aperture Czerny turner type spectrometer provides a resolution of ∼0.7nm for 1200 g/mm grating. A mechanical dial is adjusted for the desired grating angle. The dial setting was changed to rotate the grating turret between the measurements in order to measure different wavelength regions. Figure 5-6 shows a picture of the spectrometer used in the measurements.

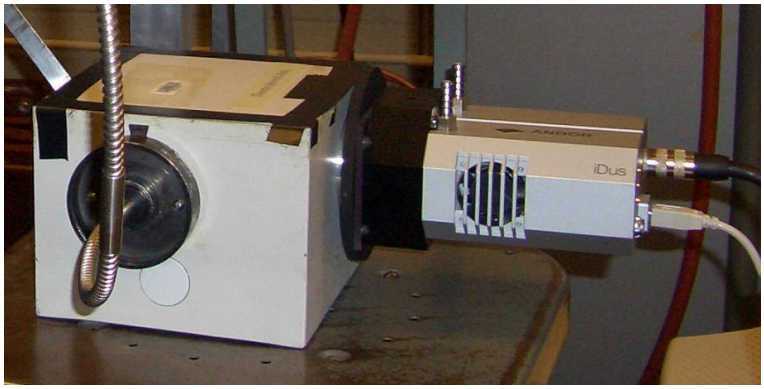

Figure 5-6: Jarrel Ash MonoSpec-18 Spectrometer and Andor iDus DU420A CCD Detector

For the helicon plasma spectral measurements 3 different gratings were used. A grating with 300 grooves/mm blazed at 500nm was used to obtain broad range spectrum. For this short focal length spectrometer, this 300 g/mm grating allowed the detection of a ∼350nm wavelength range for a given spectrometer dial setting. The second grating at 1200 grooves/mm blazed at 600nm was widely used due to its better wavelength range at relatively good resolution. This grating allowed ∼120nm wavelength range for a given dial setting. The high resolution grating at 1800 grooves/mm blazed again at 500nm provided highest resolution spectrum with a small wavelength range. The resolution for this grating was ∼0.5nm and it had a wavelength range of ∼80nm for a given dial setting. In addition to changing the gratings, the inlet slit size was also modified. Three different size inlet slits were available at $25\mu m$, $50\mu m$ and $250\mu m$. Figure 5-7 shows pictures of manually changeable gratings and slits for the spectrometer.

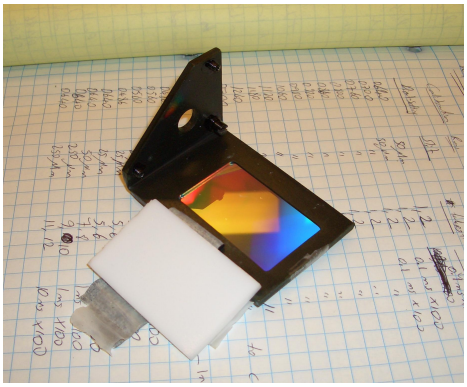

(a) Diffraction Grating

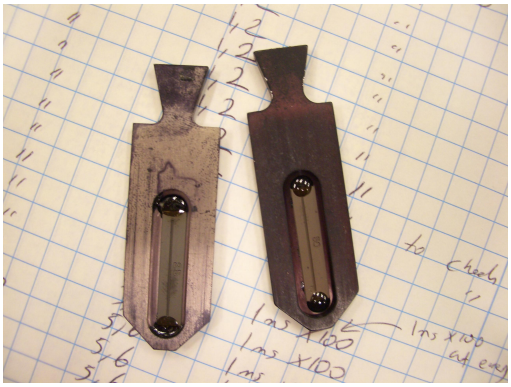

(b) Inlet Slits

Figure 5-7: Manually changeable gratings and slits for MonoSpec18 spectrometer

5.2.3 Radiation Detection

A CCD detector, Andor iDus DU420A, was attached to the exit port of the spectrometer. The CCD has 1024×256 pixels with a pixel size of 26 × 26-μm. This detector can be cooled down to -70 ^{o}C by thermoelectric cooling. It has good quantum efficiency in the visible wavelength range. A picture of this CCD camera attached to the spectrometer is shown in figure 5-6.

5.2.4 Intensity Calibration

The intensity calibration of the measured data was achieved by using a tungsten lamp with measured continuum emission intensity. The tungsten lamp was placed in the same location as that of the helicon plasma source inside the vacuum chamber. The emission intensity produced by the tungsten lamp was measured with the same optical path and exposure time for each spectrometer dial setting that a helicon plasma emission data was taken. Figure 5-8 shows the measured tungsten lamp emission spectrum using the 1800 g/mm grating blazed at 500nm. The complete spectrum for 400 to 850nm was constructed by varying the dial settings for the wavelength range.

The ratio −of the measured continuum emission intensity to the expected theoretical black-body emission intensity calculated using Planck's formula− was used to calibrate the wave-length dependence of the intensity of the measured data. Since the continuum light source

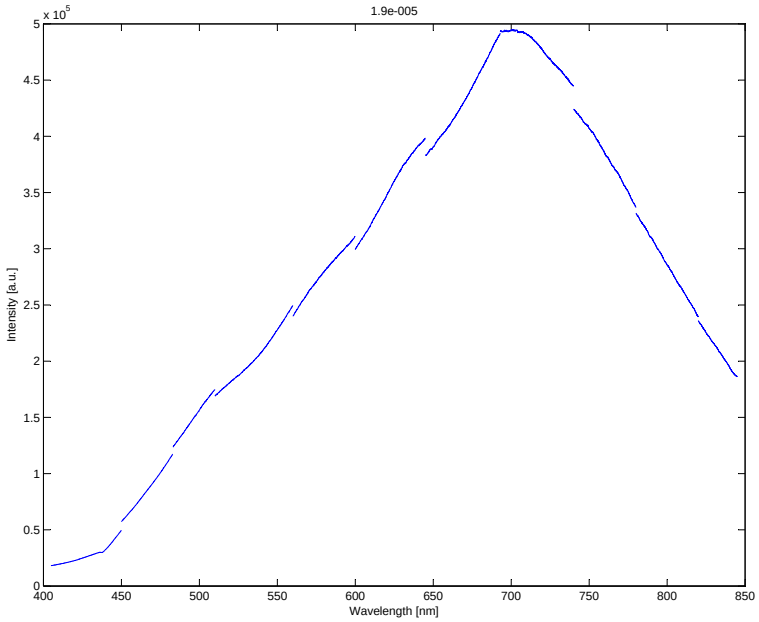

Figure 5-8: Measured emission spectrum of the tungsten intensity calibration lamp

was placed at the location of the observed plasma, the calibration takes into account the effects of the optical path such as the wavelength dependent transmissivity of the vacuum chamber window, the collimating/focusing lenses, and the optical fiber bundle. In addition, the wavelength dependence of the CCD detector quantum efficiency factor and the grating dispersive efficiency factor were all accounted for in the measured spectrum.

5.3 Helicon Plasma Source Spectral Measurements

The data presented in this section were taken in December 2005. A vacuum pressure level of 1.2×10^{-7} Torr was obtained before the plasma source started operating. First, the propellant flow was turned on by digitally setting the flow rate on the flow-meter located outside of the vacuum chamber. For 20sccm of Argon flow rate, the background pressure inside the vacuum tank stabilized around 3×10^{-5} Torr. Second, the magnet power supplies were turned on and currents of up to 30A were delivered to the electromagnet coils to create the desired magnetic field intensity in the antenna region between the electromagnets. Next, the RF power supply was turned on and was set to a desired power level up to the maximum $1200W$. As the RF power was delivered to the antenna, a plasma discharge was observed.

The capacitance of the impedance-matching network circuit was adjusted by changing the dial settings on the two capacitors until the best impedance match for the plasma discharge was obtained. The best impedance-match was obtained by monitoring the total RF power delivered to the plasma on the RF power supply display. The match was also confirmed by visibly observing the brightness and stability of the obtained plasma from a vacuum window port. Spectral measurements were then taken for varying operational parameters.

During the spectral measurements, several operational parameters were varied and the plasma emission spectra were recorded. Several propellant species were tested. Among the tested propellants were Argon (Ar), Xenon (Xe), Nitrogen (N_2), and air. The RF power delivered to the plasma was varied from $400W$ to $1200W$. The magnet currents were varied from 0 to 35A. Thus, an axial magnetic field intensity of up to 2000 Gauss in the antenna region was obtained. For Argon propellant, the gas flow rate was varied from 10 to 100sccm.

The helical antenna length and the antenna material were also studied. In addition to the $9.86cm$ long copper antenna that was used for most of the testing, a $9.86cm$ long stainless steel antenna and a $13.94cm$ long copper antenna were also tested. Aside from taking spectral measurements of the antenna region discharge plasma emission, radiation emission from the plume region of the plasma source was also measured. In order to do these measurements, the direction of the optical lens system located on the side window port was tilted to look in the direction of the plume. Additionally, the entire optical setup was placed on the back window port of the vacuum chamber and the plume region was observed from the back window. This became possible by attaching the mobile optical shelf to the other standard 8 inch window port located at the back of the vacuum chamber.

Several spectrometer settings were changed to vary the spectral resolution and the wavelength region of observation. Data were taken for the wavelength range of 350-850nm as this was the sensitivity range for the available CCD detector. The dial settings were adjusted for each small portion of the spectrum measured. The exposure time of the CCD detector was varied and the spectra were obtained by taking the average of 100 exposures per measurement to increase the signal to noise ratio without saturating the CCD pixels. In addition, in order to demonstrate the capability, a narrow band optical filter was used to

isolate ionic emission lines of interest.

As mentioned, the measurements were conducted in the wavelength range of 350 to 850nm. Table 5.1 lists the prominent Argon neutral and single ion emission lines in the 300-1000nm wavelength region [3]. As observed from this table, the spectrum is dominated by the ion lines in the 400-550nm region, however in the 700-900nm region all the prominent lines are those of the neutral Argon atom.

Prominent Argon Neutral and Single Ion Emission Lines in 300-1000nm Region									
Ar II	303.3508	Ar II	413.1724	Ar II	440.0986	Ar II	514.5308	Ar I	751.4652
Ar II	309.3402	Ar I	415.859	Ar II	442.6001	Ar I	591.2085	Ar I	763.5106
Ar II	347.6747	Ar I	419.0713	Ar II	443.0189	Ar I	603.2127	Ar I	772.3761
Ar II	349.1244	Ar I	419.8317	Ar II	447.4759	Ar II	611.4923	Ar I	772.4207
Ar II	349.1536	Ar I	420.0674	Ar II	448.1811	Ar II	617.2278	Ar I	794.8176
Ar II	350.9778	Ar II	422.8158	Ar I	451.0733	Ar I	641.6307	Ar I	800.6157
Ar II	351.4388	Ar II	423.722	Ar II	454.5052	Ar II	664.3698	Ar I	801.4786
Ar II	354.5596	Ar I	425.9362	Ar II	457.935	Ar I	667.7282	Ar I	810.3693
Ar II	354.5845	Ar I	426.6286	Ar II	458.9898	Ar I	675.2834	Ar I	811.5311
Ar II	355.9508	Ar II	426.6527	Ar II	460.9567	Ar I	687.1289	Ar I	826.4522
Ar II	356.103	Ar I	427.2169	Ar II	465.7901	Ar I	693.7664	Ar I	840.821
Ar II	357.6616	Ar II	427.7528	Ar II	472.6868	Ar I	696.5431	Ar I	842.4648
Ar II	358.8441	Ar I	430.0101	Ar II	473.5906	Ar I	703.0251	Ar I	852.1442
Ar II	372.9309	Ar II	430.9239	Ar II	476.4865	Ar I	706.7218	Ar I	866.7944
Ar II	376.527	Ar II	433.12	Ar II	480.602	Ar I	706.8736	Ar I	884.991
Ar II	385.0581	Ar II	433.203	Ar II	484.781	Ar I	714.7042	Ar I	912.2967
Ar II	394.6097	Ar I	433.3561	Ar II	487.9864	Ar I	720.698	Ar I	919.4638
Ar II	404.2894	Ar II	434.8064	Ar II	488.9042	Ar I	727.2936	Ar I	922.4499
Ar II	405.2921	Ar II	437.0753	Ar II	496.508	Ar I	735.3293	Ar I	929.1531
Ar II	407.2005	Ar II	437.1329	Ar II	501.7163	Ar I	737.2118	Ar I	935.422
Ar II	407.2385	Ar II	437.9667	Ar II	506.2037	Ar I	738.398	Ar I	965.7786
Ar II	410.3912	Ar II	440.0097	Ar II	514.1783	Ar I	750.3869	Ar I	978.4503

Table 5.1: List of Prominent ArI and ArII Lines in 300-1000nm Wavelength Region [3]

5.3.1 Broad-spectrum Results

From the visual observation of the plasma, the increased magnetic field makes a significant difference in the color and the intensity of the radiation emanating from the discharge. Also, for the case with no magnetic field, which is called Inductively Coupled Plasma (ICP) mode, there was no visible plume coming from the plasma source. However, for the high magnetic

field case, which is called the Helicon mode, there was a very bright plume formed at the open end of the quartz tube. One of the earliest spectral measurements conducted was done with the 300 g/mm grating in order to understand the broad range spectrum of the Argon emission. Figure 5-9 shows the comparison of the measured spectra for the ICP and Helicon modes. Prominent Argon neutral and single ion emission lines are identified. In the figure, a picture of the ICP discharge is shown on the left. The picture on the right shows the bright Helicon discharge. As seen from the picture for the Helicon mode a plume is visible.

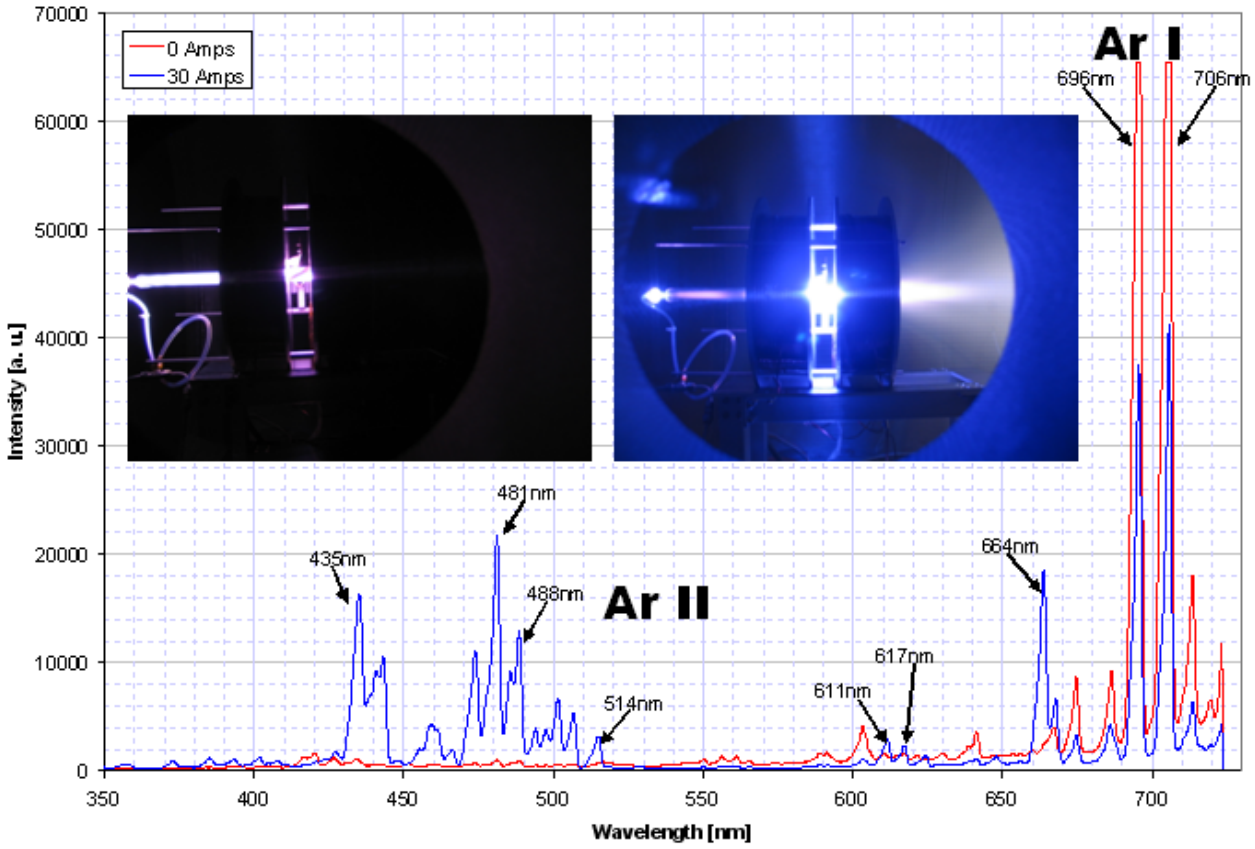

Figure 5-9: Broadband spectra comparison for the ICP and Helicon discharge plasmas

As seen in figure 5-9, for the ICP mode with zero magnet current, the emission is due to neutral Argon atoms, as visible from the high emission intensity of the 696.54nm and 706.72nm Ar-I emission lines. For the Helicon mode, the current to the electromagnets was set at 30A. In the Helicon mode, the neutral emission intensity seems to drop, as the Argon ion emission lines in the 400-500nm wavelength range become visible. This also explains why the helicon discharge plasma looks bright blue as opposed to reddish ICP plasma for the Argon gas.

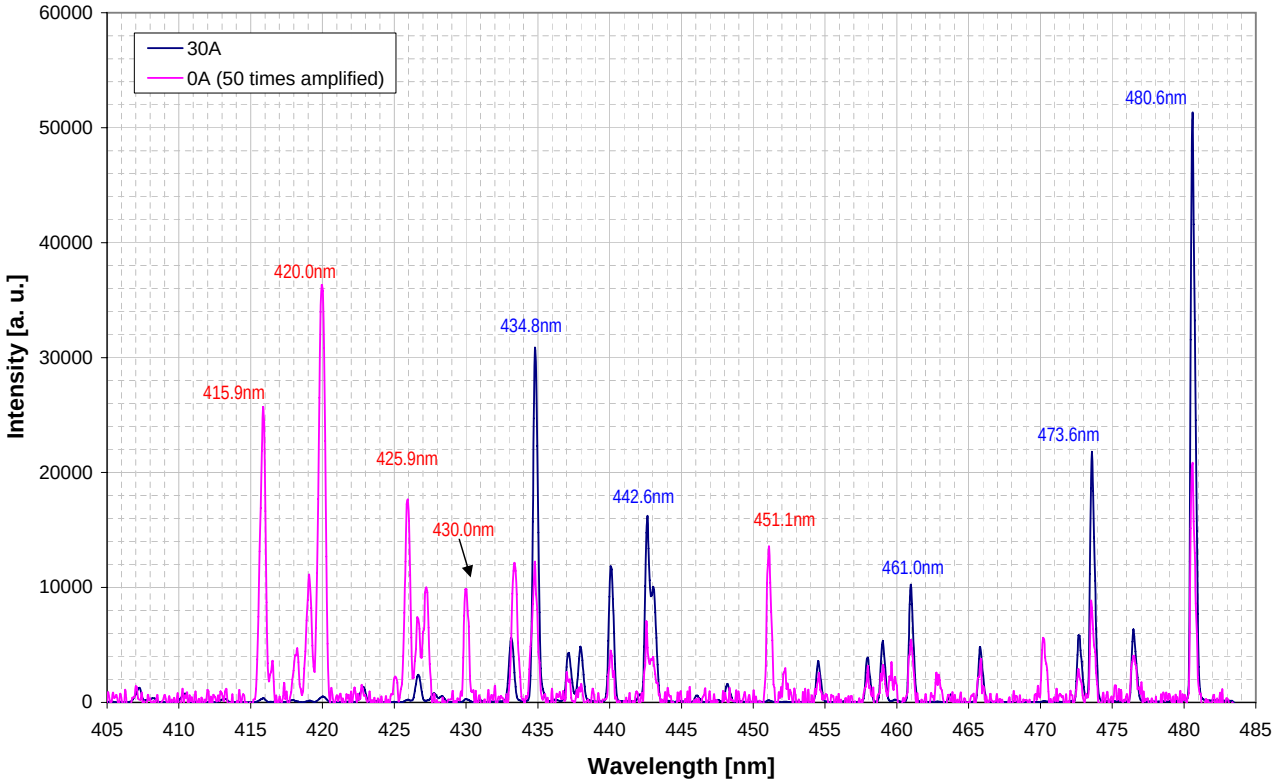

Figure 5-10: Comparison of the ICP and the Helicon discharge plasma in the 405-485nm region. The ICP spectrum is amplified 50 times in comparison to the Helicon spectrum.

5.3.2 ICP vs. Helicon Regimes

As discussed in the previous section, the magnetic field effects on the discharge are profound. Higher resolution measurements of the antenna region emission spectrum using the highest groove density grating are presented in figure 5-10 for the blue portion of the spectrum.

In figure 5-10, the ICP emission intensity is 50 times amplified to make the comparison of the spectrum with that of the helicon discharge emission more clear. A few prominent Argon neutral and single ion emission lines are identified with red and blue labels, respectively. As observed from the presented spectra, prominent Argon ion lines appear in the helicon mode of operation. In the ICP mode of operation the emission due to Argon neutral lines dominate. As observed from the spectra, the emission intensity of the prominent Argon ion emission lines at 434.81nm, 473.59nm, and 480.60nm increases by roughly 120 times, as the magnetic field is turned on, indicating a sharp increase in the ionization fraction of the propellant gas.

Figure 5-11 shows the comparison of the high resolution emission spectra for the helicon and ICP modes of operation for the Argon discharge in the 400-850nm wavelength range. The compared spectra were taken with the same exposure time and spectrometer dial settings, and no amplification to the ICP spectrum is applied. Once again, it is clear that after the magnetic field is turned on the intensity of the plasma ionic emission lines increases as observed from the increase of the emission intensity in the blue portion of the spectrum.

Focusing only on the 800-850nm portion of the spectrum where there are only strong Argon neutral emission lines, figure 5-12 shows the comparison of helicon versus ICP spectrum. As observed from this spectral graph, the neutral emission intensity is reduced by two thirds as the mode changes from ICP to Helicon.

The decrease in the neutral emission can be associated with the increase in the ionization fraction of the gas due to the much more efficient heating of the electrons through wave-particle interactions of the Helicon mode.

5.3.3 Power Scan

The plasma emission spectrum was measured as the RF power delivered to the plasma by the helical antenna was varied from 400W to 1200W in 100W increments. The emission spectra were measured for the antenna region where the discharge occurs. For these measurements the Argon flow rate was kept at 20sccm and the magnet current was set at 30A corresponding to an axial magnetic field intensity of $\sim$1800 Gauss in the antenna region. The measured spectra for the 400-480nm wavelength range are presented in figure 5-13.

The overlap of the spectral graphs in figure 5-13 makes the interpretation difficult. Therefore, in order to visualize the trends better, the emission intensity of the Argon ion emission line at 434.8nm is studied. Figure 5-14 shows the variation in the ArI 434.8nm line intensity as the delivered RF power is varied.

The linear plot of the RF power delivered versus the 434.8nm line emission intensity is presented in figure 5-15. As seen in the graph, the intensity of the line increases linearly

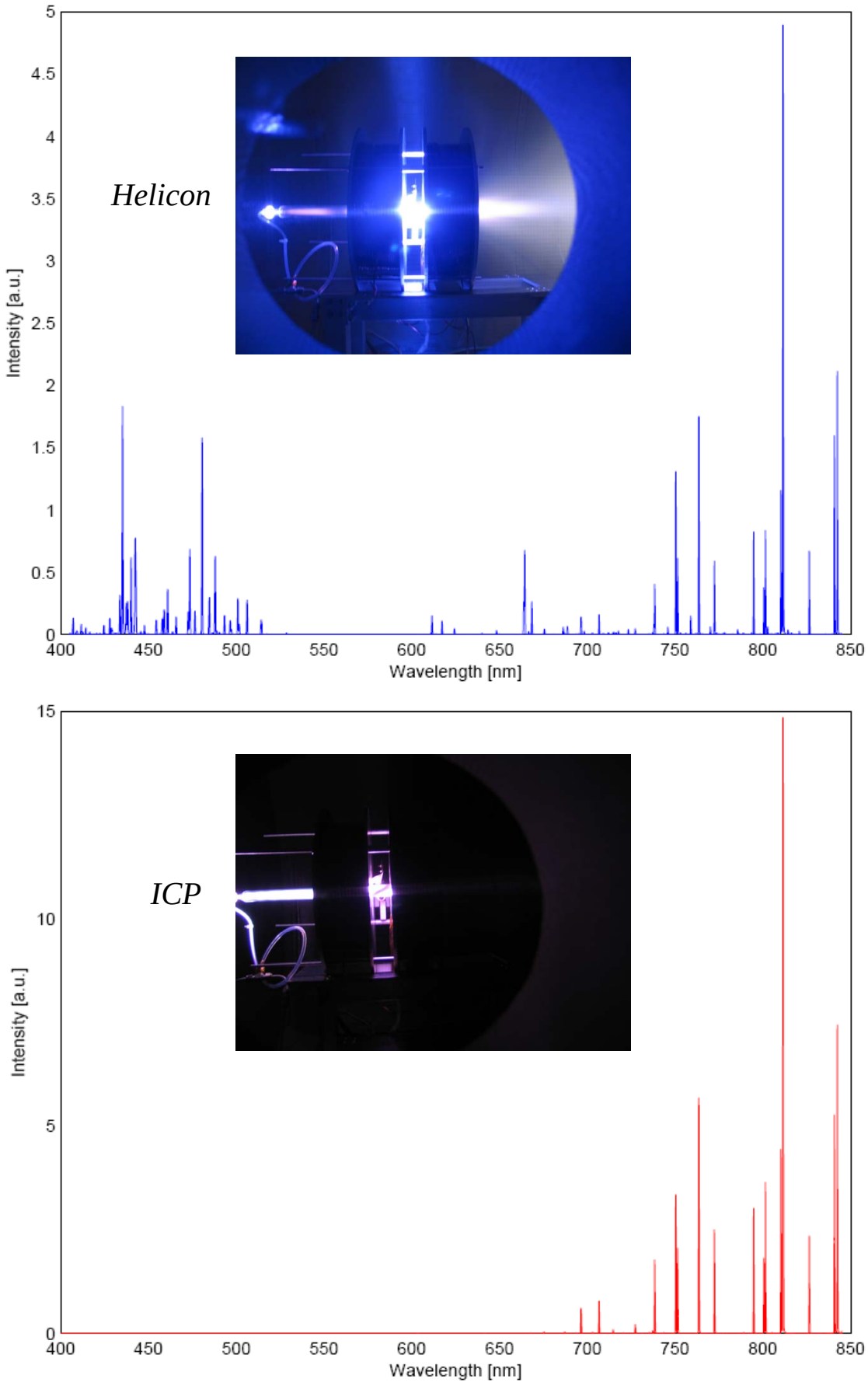

Figure 5-11: Comparison of the Argon Plasma Spectra for Helicon and ICP modes of operation

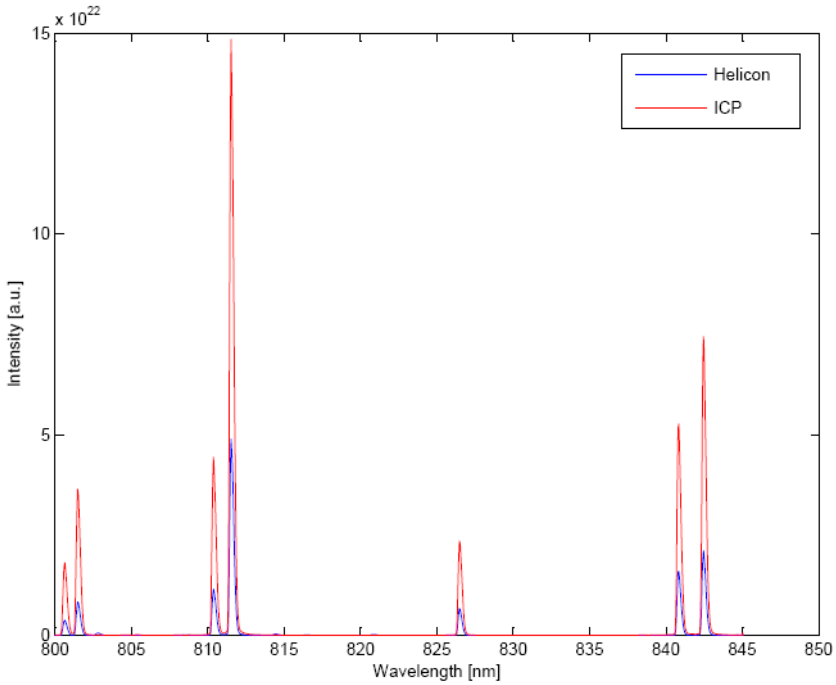

Figure 5-12: Comparison of the Argon Plasma Spectra for Helicon and ICP modes of operation in 800-850nm region

with the power delivered to the antenna. Thus, the ionization fraction linearly increases as the RF power delivered to the Argon propellant gas is increased.

5.3.4 Flow Rate Scan

The Argon propellant flow rate was varied between 10*sccm* and 100*sccm* and the plasma emission spectra from the antenna region were measured. In these measurements, the RF power delivered was kept constant at 1000W and the magnet current was set at 30A corresponding to a maximum axial magnetic field intensity of 1800 Gauss in the antenna region. Argon ion emission line at 434.8nm was studied to obtain the trends of the discharge strength as presented in figure 5-16.

The linear plot of Argon flow rate versus 434.8nm ion line emission intensity is presented in figure 5-17. As seen from the figure, when the mass flow rate is varied the ion emission intensity first increases up to a flow rate of 25sccm and then decreases for higher flow rates. So, for the given power level and magnetic field configuration, there is an optimum

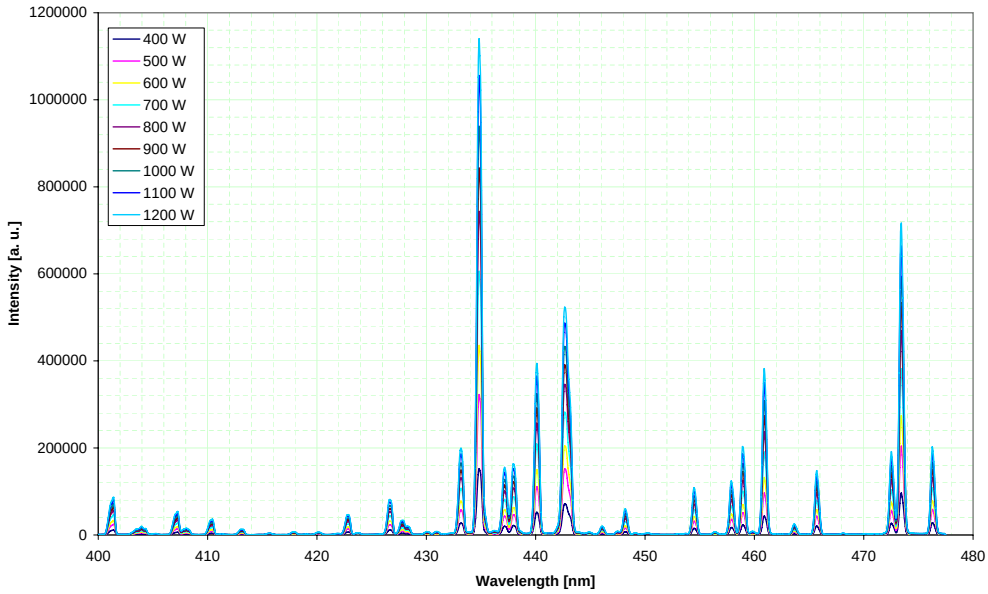

Figure 5-13: Argon discharge antenna region spectrum for varying delivered power

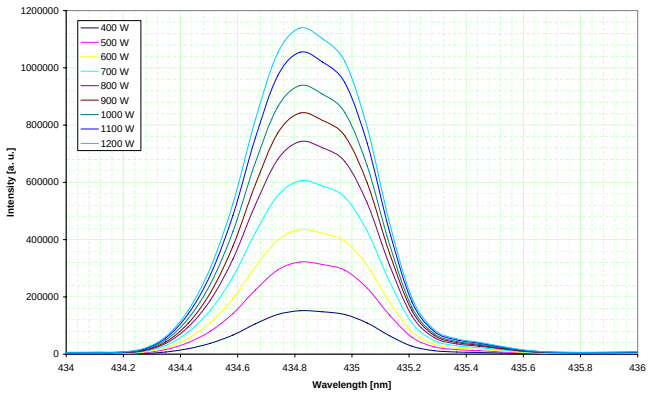

Figure 5-14: Argon ion 434.8nm line emission as RF power delivered is varied

propellant flow rate that maximizes ion line emission intensity. Thus, the ionization rate is limited at high flow rates, as very high background neutral gas density increases the electron energy loses. This leads to reduced electron temperature and increases the energy cost of electron-ion production.

5.3.5 Magnetic Field Intensity Scan

The magnetic field intensity in the antenna region is varied by changing the current supplied to the electromagnets. The plasma emission spectra from the antenna region were recorded for a delivered RF power of 1000W and Argon flow rate of 20sccm. Figure 5-18 shows

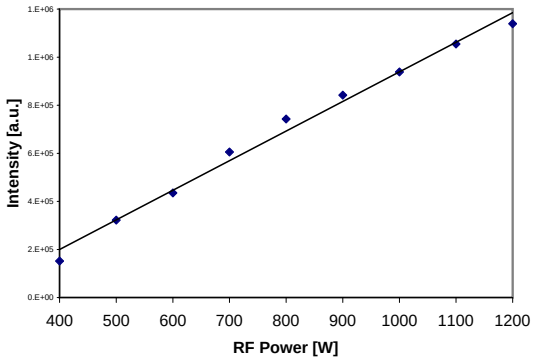

Figure 5-15: Argon ion 434.8nm line emission intensity versus RF power delivered

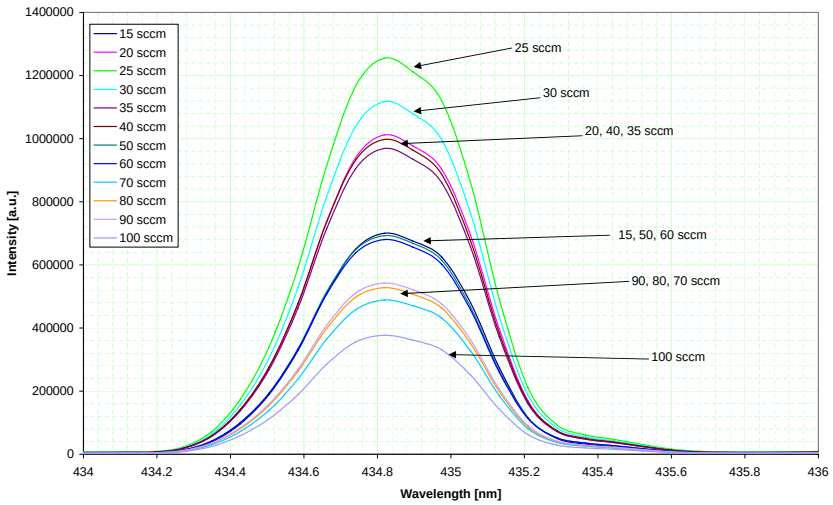

Figure 5-16: Argon ion 434.8nm line emission intensity as Argon flow rate is varied

the measured emission intensity of Argon ion line at 434.8nm for varying current to the electromagnet coils.

A linear plot of the 434.8nm ion line emission intensity versus the magnet current is shown in figure 5-19. As seen from the figure, for magnet current of ∼25A corresponding to an axial magnetic field intensity of ∼1500 Gauss, the ion line emission intensity is the highest. Thus, for the given power level and the flow rate conditions, there is an optimum magnetic field intensity.

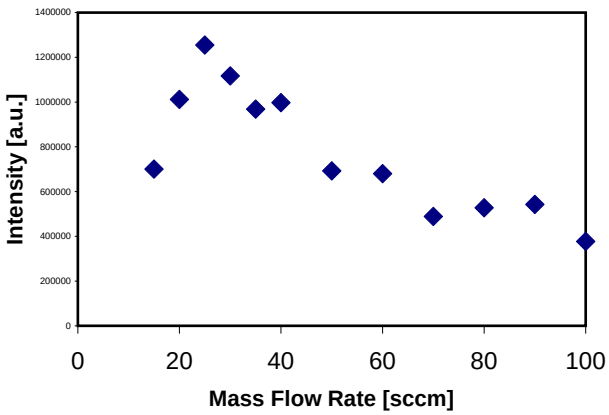

Figure 5-17: Argon ion 434.8nm line emission intensity versus Argon propellant flow rate

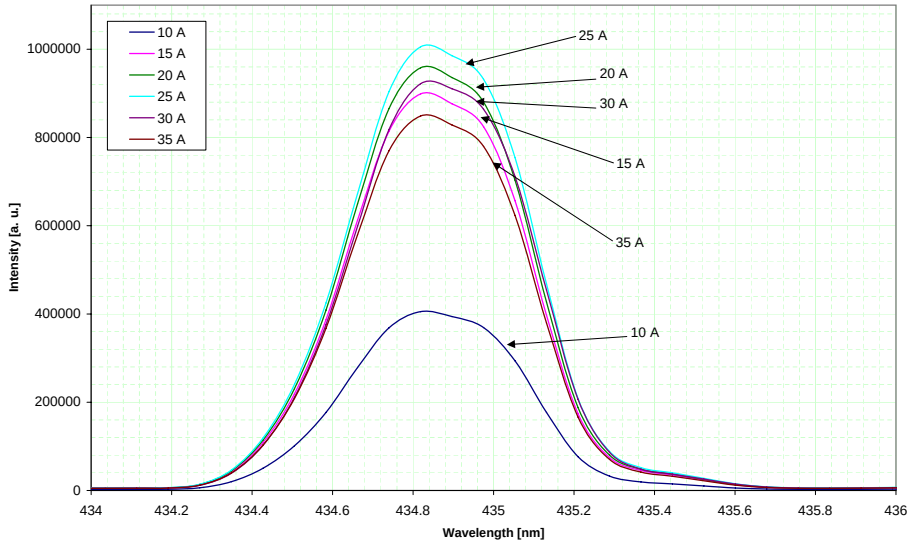

Figure 5-18: Argon ion 434.8nm line emission intensity as the magnetic field intensity is varied

5.3.6 Short vs. Long Antenna

The length of the antenna, 9.86cm, for the mini Helicon Thruster Experiment (mHTX) was chosen to be the half wavelength of the 13.56MHz frequency m=1 Helicon waves in a plasma of 10^{14} cm^{-3} in density for 20eV electron energy [69]. A longer, 13.94cm, antenna corresponding to electron energy of 40eV was tested. The antenna region plasma emission spectra for the two antennae are compared. Figure 5-20 shows the emission spectra for the long and short copper antennae.

For both of the observed spectra shown in figure 5-20, the RF power delivered to the antennas was 1000W, the Argon flow rate was kept at 20sccm, and the magnet current was set at 30A

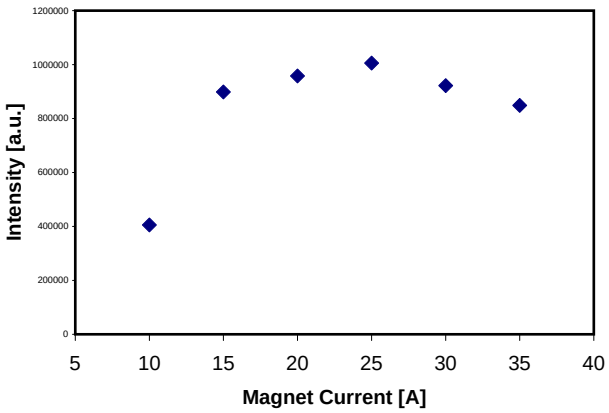

Figure 5-19: Argon ion 434.8nm line emission intensity versus Magnet current

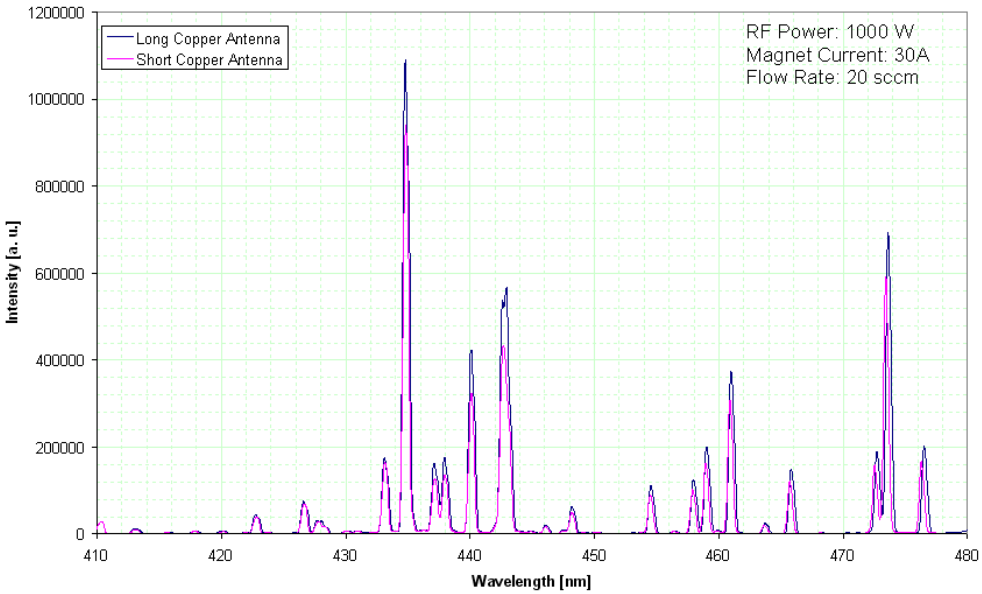

Figure 5-20: Comparison of the emission spectra for short and long copper antennae

corresponding to an axial maximum magnetic field intensity of 1800 Gauss in the antenna region. As seen from the graph, the emission intensity is about 20 percent higher for the longer antenna, possibly indicating a higher electron temperature.

5.3.7 Copper vs. Steel Antenna

In order to study the effects of the antenna material, a copper and a stainless steel antenna were tested. The plasma emission spectra for the two equal sized helical antennae of length of 9.86cm were measured. Figure 5-21 shows the plasma emission in the antenna region for

the 400-480nm portion of the visible spectrum.

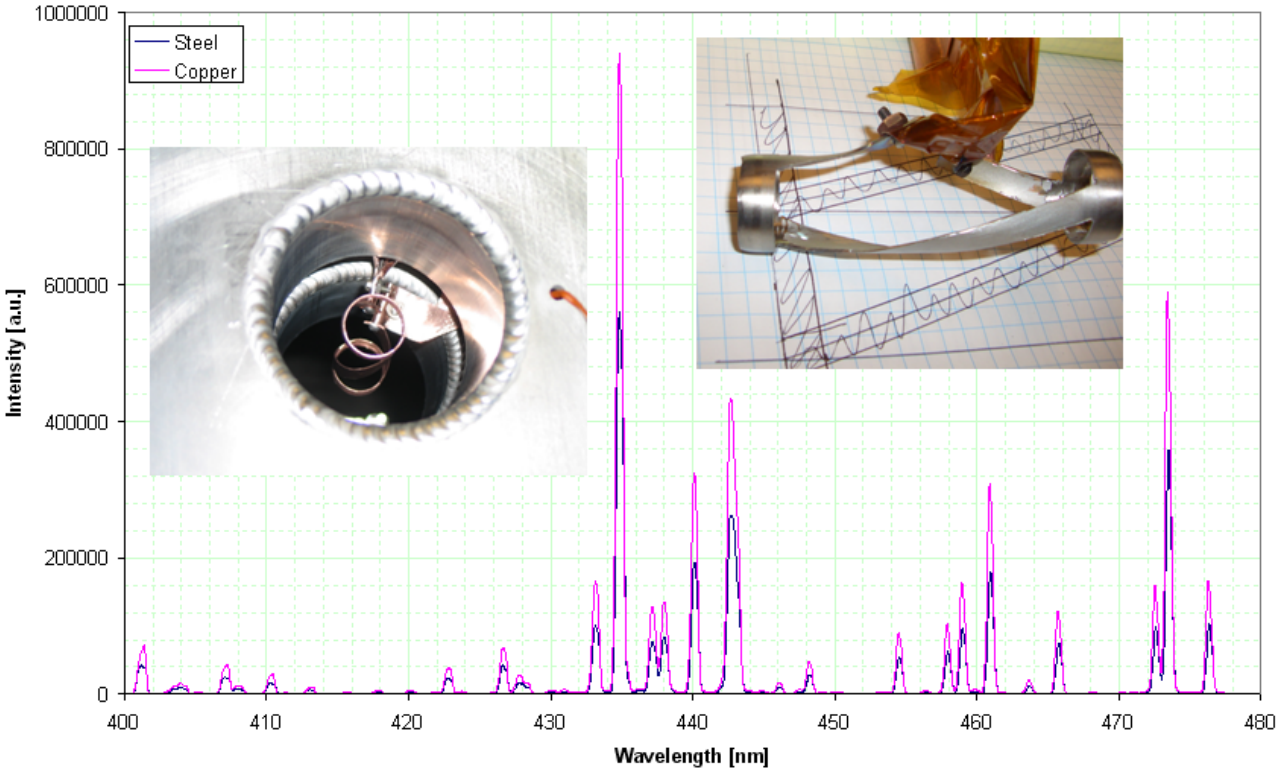

Figure 5-21: Comparison of the emission spectra for Steel and Copper antennas

For both of the measured spectra shown in figure 5-21, the RF power delivered was at 1000W, Argon mass flow rate was kept at 20sccm, and magnet current was 30A corresponding to a magnetic filed intensity of ∼1800 Gauss in the antenna region. From the emission intensity comparison, for the same delivered power the plasma of the copper antenna has about 50 percent higher emission. It is not clear what causes this large difference, but the higher electrical resistance of steel might be a factor. It is however important to point out that due to the heating of the antenna, both the copper and steel antennae materials became softer after testing, and this poses a concern for the lifetime of a possible propulsion system.

5.3.8 Antenna vs. Plume Region

In order to understand the species in the plume region as opposed to the antenna region, the emission spectra of the antenna and plume regions were compared. To achieve, the optical collection system was tilted to allow the viewing of the plume region as depicted in the inset

drawing in figure 5-22.

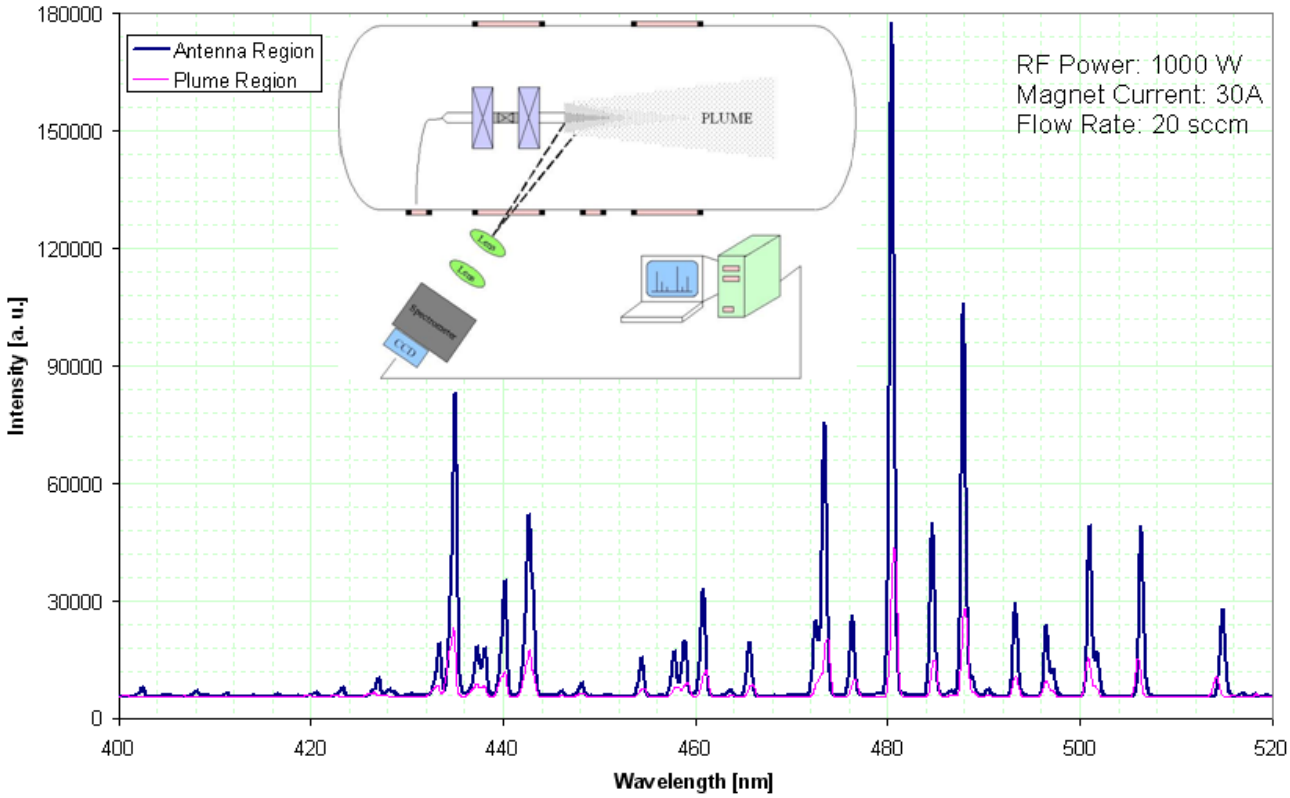

Figure 5-22: Comparison of the emission spectra for antenna and plume regions

The two measured spectra presented in figure 5-22 look similar. The plume region spectrum has the Argon ion emission lines, indicating that the ions are leaving the quartz tube into the vacuum chamber. However, the antenna region has higher emission intensity as expected due to higher plasma density.

5.3.9 Side Window vs. Back Window

In order to measure the emission spectrum from the direction of the opening of the quartz tube, the optical shelf was removed from the side viewing port of the vacuum chamber and mounted on the the back window port. Figure 5-23 shows the measured spectra for the two configurations depicted in the inset drawings in this figure.

As can be observed from the spectra comparison, Argon neutral emission lines are stronger for the back window port measurements. Specifically, Argon neutral emission lines at

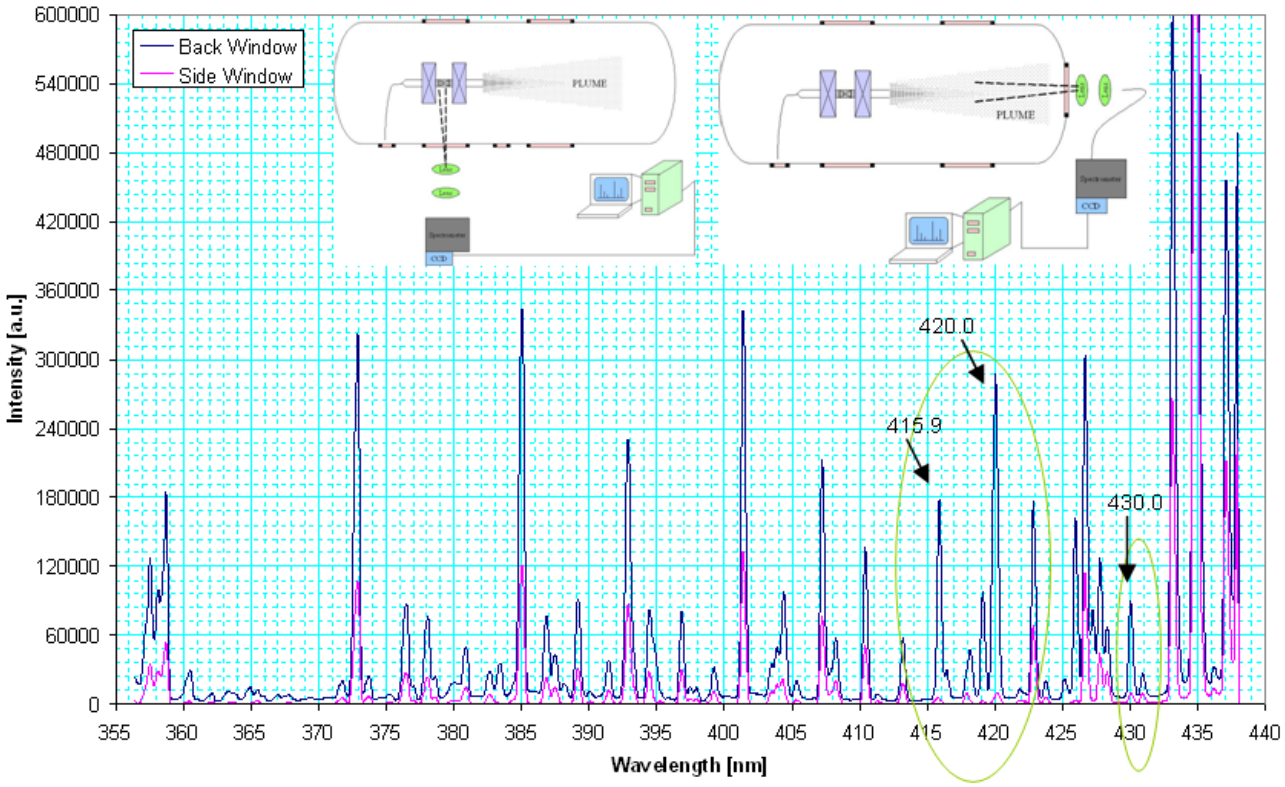

Figure 5-23: Comparison of the emission spectra for side and back window observations

415.86nm, 420.07nm and 430.01nm lines are clearly visible in the spectrum obtained from the back window port. Due to the difficulty of pinpointing the exact region of observation with the optical collection setup, it is difficult to explain why the emission spectrum for the back window has higher neutral emission components. However, one explanation is that the collection optics placed at the back window collects radiation emission from not only the propellant after it is ionized, but before the antenna region deep inside the quartz tube. In addition, the vacuum tank has a higher Argon neutral population due to the operation of the Helicon plasma source, and this might increase ion induced excitation collisions resulting in the background Argon neutral gas radiation emission.

5.3.10 Narrow band-pass filter Measurement

Narrow band-pass filters can be used to allow only the light within a narrow wavelength band to enter the spectrometer/detector system. In order to demonstrate the capability to limit the detection of emission due to a given emission line, thus limiting detection from a

given species only, a narrow band-pass filter was placed in front of the collimating-focusing lens system. The bottom plot in figure 5-24 shows the antenna region emission spectrum measured using an Oriel 53855 narrow band-pass filter. The filter used has a full-width-at-half-maximum (FWHM) of 9nm centered around 489.5nm wavelength. For comparison, the spectrum taken without the filter is shown in the top plot of the same figure. The observed prominent lines are identified. As seen in the figure, the filter blocks out all the emission apart from a narrow band around 489.5nm thus isolating the Argon ionic emission lines in that region. This would allow the imaging of the plasma with appropriate optics and imaging CCDs.

5.4 Chapter Summary

The emission spectra for a laboratory helicon plasma source were measured for various operational parameters. A good qualitative understanding of the strength of the plasma ionization was obtained. According to the spectral measurements, the intensity of the ion emission line increases as the power delivered to the RF antenna, thus to the plasma, is increased. For a set RF power, and fixed magnetic field intensity, there is an optimum mass flow rate for the highest ion line emission intensity. Similarly, for a set RF power, and constant Argon propellant flow rate, there is an optimum axial magnetic field intensity in the antenna region that provides the highest ion emission intensity. Use of a narrow-band filter allows the detection of emission due to only Argon ion lines, thus providing a capability to obtain contour plots of ion emission intensity for a high spatial resolution optical collection system and an imaging CCD detector.

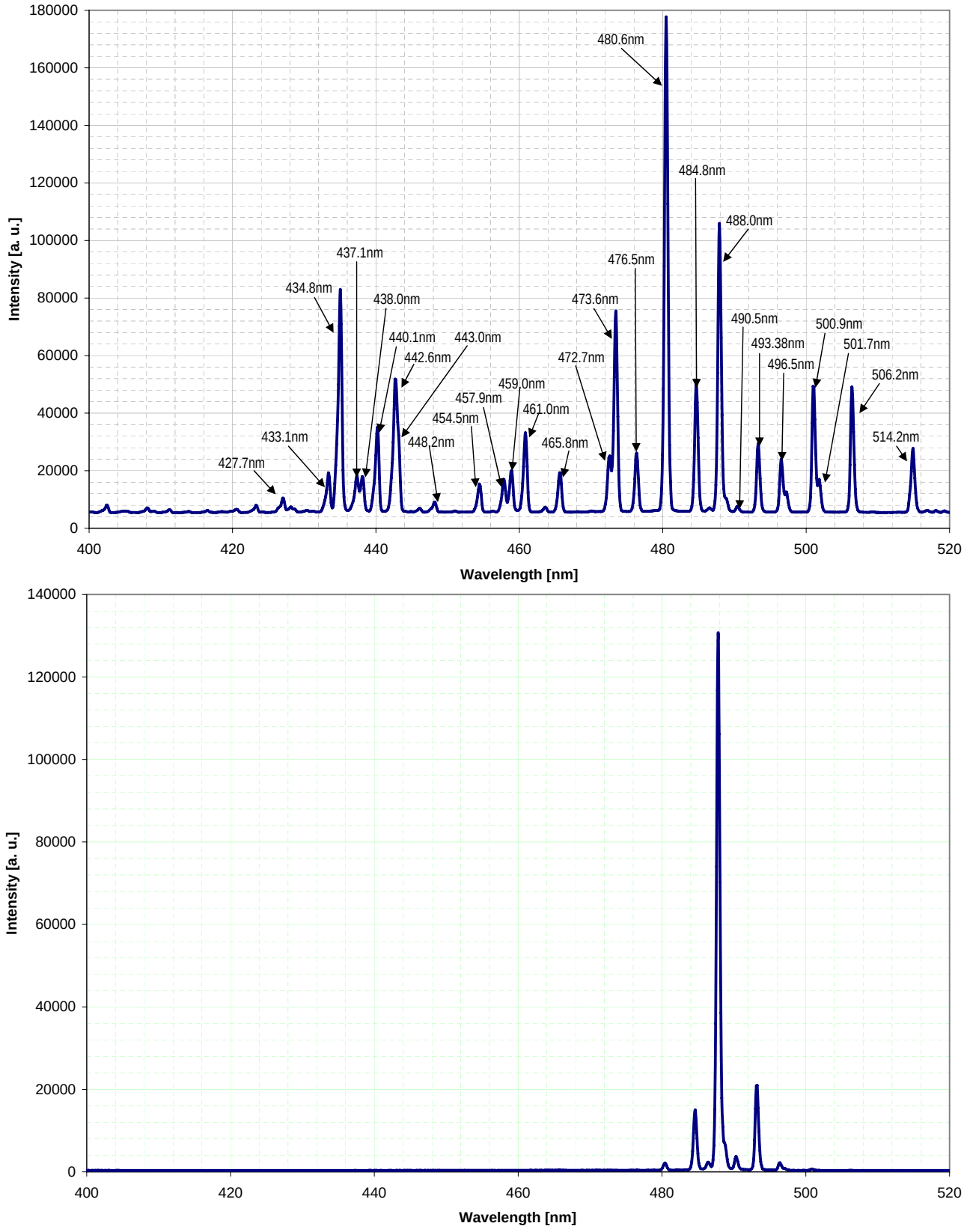

Figure 5-24: Comparison of the emission spectra for with (bottom) and without (top) a narrow band filter centered at 489.5nm with a 9nm FWHM

Chapter 6

Argon Collisional-Radiative Model

A collisional-radiative (C-R) model for Argon plasma has been developed. The model provides the simulated emission spectrum for given plasma parameters. The modeled radiation emission spectra have been compared with the experimental spectral measurement results for the Argon plasma of the MIT mini Helicon thruster experiment described in chapter 5.

This chapter includes the discussions regarding the C-R Model for Argon plasma and presents the simulation results. The purpose of the C-R Model is to predict the intensity of major emission lines for given plasma conditions that are expected in an Argon gas discharge. Major assumptions of the model as well as its possible shortcomings are presented in the following sections.

The C-R Model is developed for low temperature Argon plasma composed of argon atoms, single ions and electrons as the plasma species. In the C-R Model various excitation and de-excitation processes are simulated in order to determine the population densities of the electronic energy levels of Argon atoms and single ions. In terms of the upward transitions, the modeled processes include electron induced excitation and ionization collisions from ground and excited levels. In terms of the downward transitions, the modeled processes include the spontaneous de-excitation of electrons and electron induced de-excitation (quenching) collisions.

In the model a set of parameters such as electron temperature, electron density and neutral density are varied to obtain the emission spectra observed in experimental measurements. The plasma is assumed to be optically thin, thus the optical escape factor is assumed to be unity for all wavelengths.

The Argon C-R Model calculates the electron population densities for the lowest 149 Ar and 123 Ar^+ energy levels. The model gives the simulated intensity values for 148 Ar-I and 127 Ar-II emission lines. Preliminary results show good correlation with the observed spectrum for the given conditions.

6.1 Collisional Radiative Modeling

Collisional radiative models, first introduced by Bates et al. [6][7], have been extensively used in calculating population distribution of energy states as well as obtaining information about the relative significance of the various physical processes.

In C-R models, rate equations are written for the modeled energy levels of atoms or ions, and various processes that populate and de-populate the electron number density of the modeled levels are simulated. Usually, the excited states are grouped into lumped sets in order to reduce the total number of levels being modeled. Thus, in C-R models the population densities of the ground state and the modeled excited states are calculated along with the free electron density [72]. However, in this study, the energy levels were not grouped into lumped sets, but rather all the energy levels up to a maximum level were modeled.

Figure 6-1 shows a schematic of the energy level diagram of a typical atom or ion. The ground state, E_1 is defined at $0eV$. The first excited state is at energy E_2. The ionization energy level, E_i, is depicted by the dashed line. Electrons that have higher energy levels than E_i are part of the continuum.

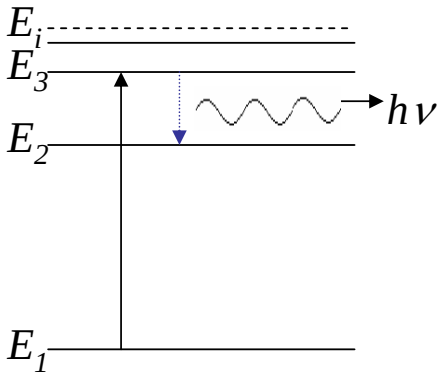

Figure 6-1: Schematic of the electronic energy levels of an atom or an ion

6.1.1 Discussion about the Corona Model Assumption

When considering the population (gain) and de-population (loss) mechanisms that determine the population density of an excited state, it is observed that the gain term is dominated by the electron excitation collisions from ground and meta-stable states. This is due to the fact that other states are much less populated compared to the ground state or meta-stable energy states [66]. Similarly, radiative gain from upper levels, also called cascade emission, is also small because those upper levels have low population densities. The loss term is dominated by the radiative de-excitation, because for most electric propulsion thruster plasma even in the discharge region the pressure is low enough to neglect to first order the collisional de-excitation (quenching) processes. Thus, in the corona model assumption, it is assumed that the excited levels are populated by electron induced excitation collisions and are depopulated by spontaneous radiative de-excitation of the electrons. However, due to the high density nature of the Argon Helicon plasma, in this study a full collisional-radiative model is developed.

6.2 Important Processes

There are numerous processes that determine the population density of the energy levels. Since it is almost impossible to accurately take into account all these processes, the prominent processes have to be identified and taken into consideration in the C-R model. The

following sections provide a discussion on the various processes to be considered for the Argon C-R model.

6.2.1 Electron Induced Excitation Collisions

In electron induced excitation collisions, an electron collides with an atom (or ion) and loses some of its initial energy that goes into the excitation of one of the bound electrons of the atom (or ion) to a higher energy level.

In the presented C-R model, electron induced excitation collisions are the main population mechanism for the energy states. In the *Corona Model* assumption, only the collisional excitation from the ground state are considered important due to the fact that the ground state population density is orders of magnitude higher than the population density of the excited levels. This represents the following reactions from the ground states for Argon neutral and ion respectively.

$$\begin{aligned} Ar(1) + e^- &\rightarrow Ar(k) + e^- \\ Ar^+(1) + e^- &\rightarrow Ar^+(k) + e^- \end{aligned}$$

In these processes, the free electron loses some of its energy that goes into the excitation of one of the bound electrons from ground state, 1, to an excited energy state, k.

Even though the population densities of the excited levels are small, due to much smaller energy differences between the excited levels, the electron induced excitation collisions between the excited levels are found to be important. Electron collisions cause the bound electron to move from a lower excited level i to a higher excited energy level j.

$$\begin{aligned} Ar(i) + e^- &\rightarrow Ar(j) + e^- \\ Ar^+(i) + e^- &\rightarrow Ar^+(j) + e^- \end{aligned}$$

For a given volume V, the number of excitation collisions from a lower energy level i to a

higher energy level j per unit time will be given by:

$$n_e n_{Ar(i)} < v_e Q_{e-Ar}^{i-j} > V \tag{6.1}$$

$$n_e n_{Ar^+(i)} < v_e Q_{e-Ar^+}^{i-j} > V \tag{6.2}$$

where n_e is the electron number density, $n_{Ar(i)}$ and $n_{Ar^+(i)}$are the ith level Ar and Ar^+ densities respectively, v_e is the electron velocity, and Q_{e-Ar}^{i-j} and $Q_{e-Ar^+}^{i-j}$ are the cross-sections for the electron excitation collision from level i to level j for Ar and Ar^+ species. The expression $< v_e Q_{e-Ar}^{i-j} >$ gives the excitation collision rate function, C_{e-Ar}^{i-j}. Assuming a normalized Maxwellian energy distribution for the electrons:

$$f_e(E_e) = \frac{2}{\sqrt{\pi}} \sqrt{\frac{E_e}{(kT_e)^3}} e^{-\frac{E_e}{kT_e}} \tag{6.3}$$

the excitation collision rate function is calculated by the integral:

$$C_{e-Ar}^{i-j} =< v_e Q_{e-Ar}^{i-j} >= \int_0^\infty f_e(E_e) Q_{e-Ar}^{i-j} \sqrt{\frac{2E_e}{m_e}}\, dE_e = \int_0^\infty 2E_e \sqrt{\frac{2}{\pi (kT_e)^3 m_e}} e^{-\frac{E_e}{kT_e}} Q_{e-Ar}^{i-j}\, dE_e \tag{6.4}$$

where m_e and E_e are the electron mass and energy respectively, and $\sqrt{\frac{2E_e}{m_e}}$ is the electron velocity. From the expression it can be seen that the excitation collision rate is a function of electron temperature, T_e, only.

Only those electrons in the tail region of the distribution will have enough energy to cause excitation from the ground state, however much lower energies are required to further excite electrons already at an excited energy level. Thus, despite the fact that the excited level electron densities are small, the excitation collision rate would be large.

In order to model such collisional interactions between electrons and heavy particles (Ar, Ar^+), cross section values for a given excitation collision process are needed. The collision cross-section information for electron induced excitation processes can be obtained from experimental results published in the literature. However, few such experimental data are available. Thus, analytical models are employed for this study.

Cross-Section Calculations

Drawin [34] proposed analytical formulas for the electron induced cross section for excitation of an atom in a lower energy level, i to a higher energy level, j. The analytical forms proposed by Drawin are adapted by many researchers [5][43][74][16]. Bultel et. al. [16] discussed the variations of forms for allowed and forbidden transitions to be adapted in a C-R model.

Collisions Between Allowed Energy Levels

Not all transitions to lower energy levels proceed by spontaneous emission [45]. The selection rules determine the allowed transitions. Transitions not permitted by selection rules are called *forbidden* transitions. Forbidden transitions are not truly forbidden in a literal sense, but occur with a much lower probability. The allowed transitions are those that satisfy the selection rules [45].

For optically allowed transitions the Drawin's formula for the excitation cross-section is [64]:

$$\sigma_{ij}(U_{ij}) = 4\pi a_o^2 \left(\frac{E_{ion}^H}{E_{ij}}\right)^2 \alpha_{ij} f_{ij} \times \frac{U_{ij}-1}{U_{ij}^2} ln(1.25\beta_{ij}U_{ij}) \tag{6.5}$$

where E_{ij} is the energy difference between the higher level j and the lower level i such that $E_{ij} = E_j - E_i$, U_{ij} is the normalized electron energy, $U_{ij} = E_e/E_{ij}$, a_o is the Bohr radius, f_{ij} is the oscillator strength, and α_{ij} and β_{ij} are collision cross section parameters which are of the order of unity [64]. The experimental collision cross-section data can then be used to adjust the appropriate collision cross section parameters in Drawin's analytical formula.

Collisions Between Forbidden Energy Levels

For optically forbidden transitions without change in spin ($\Delta l \neq \pm 1$), Bultel et. al. [16] report the following Drawin's formula for the corresponding cross-section

$$\sigma_{ij}(U_{ij}) = 4\pi a_o^2 \alpha_{ij} \times \frac{U_{ij}-1}{U_{ij}^2} \tag{6.6}$$

and for the optically-forbidden transition with change in spin ($\Delta J \neq 0, \pm 1$), the cross-section

has the analytical form:

$$\sigma_{ij}(U_{ij}) = 4\pi a_o^2 \alpha_{ij} \times \frac{U_{ij} - 1}{U_{ij}^5} \tag{6.7}$$

The parameters α and β are adapted in accordance with the recent experimental results compiled by Vlcek [74] and Bultel et al. [16]. However, for the transitions that did not have the α and β values reported, $\alpha = 0.01$ and $\beta = 4$ values are adapted for equation 6.5.

6.2.2 Electron Induced Ionization Collisions

In electron induced ionization collisions, free electron collisions with atoms (or ions) result in a bound electron to be freed and the atom to be ionized. Such ionization processes will result in the change of the population density of the energy levels from where the bound electron is knocked out. Ionization processes occur from the highly populated ground state as well as the excited states. Similarly to excitation processes, the ionization collisions would require less energy from highly excited energy levels as those levels are energetically much closer to the continuum. The ionization process for a neutral Argon atom from an energy level k (including the ground state) to the continuum can be represented by the following reaction:

$$Ar(k) + e^- \quad \rightarrow \quad Ar^+ + 2e^-$$

A similar reaction would occur for the singly charged Argon ions. However, since the doubly charged Argon ions are neglected in this model, ionization of Argon single ions has not been modeled.

For ionization from excited energy levels of Argon neutrals, Drawin proposed an analytical form for the calculation of the necessary cross section values [74]:

$$\sigma_{k-ion}(U_k) = 4\pi a_o^2 \left(\frac{E_{ion}^H}{E_{k-ion}}\right)^2 g_k \alpha_{k-ion} \times \frac{U_k - 1}{U_k^2} ln(1.25\beta_{k-ion} U_k) \tag{6.8}$$

where E_{k-ion} is the energy difference between the level k and the ionization energy E_{ion},

such that $E_{k-ion} = E_{ion} - E_k$, g_k is the degeneracy of level k, U_k is the normalized electron energy: $U_k = E_e/E_{k-ion}$, a_o is the Bohr radius, and α_{k-ion} and β_{k-ion} are ionization collision cross-section parameters that depend on the specific transition. Values for α_{k-ion} are taken from Vlcek [74], and β_{k-ion} is assumed to be 4.00 for up to level 12 and 1.00 for higher levels [74].

6.2.3 Heavy Particle Induced Excitation and Ionization Collisions

Inelastic collisions between the atoms or ions result in the loss of some of the kinetic energy of the colliding particles. This energy goes to a bound electron, causing the bound electron to excite to a higher bound energy state or move into the continuum. Thus, such inelastic collisions between the atoms or ions result in the change of the electron population densities of the corresponding energy levels. There are various combinations of such excitation processes occurring. A few of such possible excitation processes are provided below:

$$\begin{aligned} Ar(i) + Ar(1) &\rightarrow Ar(j) + Ar(1) \\ Ar(i) + Ar^+(1) &\rightarrow Ar(j) + Ar^+(1) \\ Ar^+(i) + Ar(1) &\rightarrow Ar^+(j) + Ar(1) \\ Ar^+(i) + Ar^+(1) &\rightarrow Ar^+(j) + Ar^+(1) \end{aligned}$$

where $j > i$. Such inelastic collisions can also result in the ionization of the neutral Argon atom.

$$\begin{aligned} Ar(i) + Ar(1) &\rightarrow Ar^+(k) + Ar(1) + e^- \\ Ar(i) + Ar^+(1) &\rightarrow Ar^+(k) + Ar^+(1) + e^- \end{aligned}$$

These reactions can in principle occur between two excited species. However since the population densities of excited species are much smaller than those of Argon neutral and ion populations at ground states, such processes can be neglected.

Available experimental collision cross sections for inelastic heavy particle collision processes

are not complete or adequate for the current modeling purposes. Considering the fact that the current model does not take into account the particle kinetics, all heavy particle induced excitation/ionization collisions are neglected.

6.2.4 Spontaneous Radiative De-excitation

Spontaneous de-excitation of electrons from higher energy levels to lower energy levels results in the emission of photons with energies corresponding to the difference in the energy levels. The frequency of the occurrence of such spontaneous de-excitation processes depends on the relevant Einstein's transition coefficients, A_{ij} for the given upper, j, and lower, i, energy states. Einstein's transition coefficient values can be calculated using analytic formulas for simple atomic systems such as the Hydrogen atom. But for more complicated atoms, available experimental or theoretical values are to be collected from the literature. For Argon neutral and single ion species, Einstein transition coefficients are published at the online National Institute of Standards and Technology (NIST) atomic spectra database [3].

The number of de-excitation processes that occur per unit time from level j to level i is given by the expression:

$$n_{Ar(j)} A_{ij} V \tag{6.9}$$

where A_{ij} is the Einstein transition coefficient for the transition from level j to level i, and V is the plasma volume.

If the thin plasma assumption is valid, then self-absorption of this radiation is negligible. Thus, the emission intensity of a given line can be determined by just recording the total number of de-excitation events as prescribed by equation 6.9.

6.2.5 Electron Induced De-excitation Collisions

In addition to the spontaneous radiative de-excitation of the electrons from higher energy levels to lower energy levels, electron induced collisions can also result in electrons to de-

excite to lower energy levels. This process is also called *quenching* collision. Such processes can be very significant in dense plasmas where collisional effects dominate. In electric thruster plasmas, very closely spaced upper energy levels will have significant collisional de-excitation that will provide the equilibration between those states.

In order to calculate the appropriate quenching collision rates, micro-reversibility, also called the method of detailed balance, can be used. According to micro-reversibility, in equilibrium conditions every forward process has to be balanced by its reverse process. Thus, in thermodynamic equilibrium, the electron induced quenching collision rate has to be equal to the electron induced excitation rate for each transition.

The net excitation rate, including quenching, can be given by:

$$\dot{N}_{ij} = n_i n_e C_{ij}(T_e) - n_j n_e C_{ji}(T_e) \tag{6.10}$$

where $\dot{N}_{ij}$ is the rate of the event ij, n_i and n_j are the population densities for levels i and j ($j > i$), n_e is the electron density. $C_{ij}(T_e) =< \sigma_{ij} v_e >$ and $C_{ji}(T_e) =< \sigma_{ji} v_e >$ are the electron excitation and de-excitation collision rate functions. In equilibrium $\dot{N}_{ij} = 0$, so that

$$0 = n_i^* n_e C_{ij}(T_e) - n_j^* n_e C_{ji}(T_e) \tag{6.11}$$

where $n_i = n_i^*$ and $n_j = n_j^*$ such that the levels assume the equilibrium level density given by Boltzmann relation. Thus, in equilibrium

$$C_{ji}(T_e) = \frac{n_i^*}{n_j^*} C_{ij}(T_e) \tag{6.12}$$

and the Botzmann equilibrium density ratio is given by

$$\frac{n_j^*}{n_i^*} = \frac{g_j}{g_i} e^{-\frac{E_j - E_i}{kT_e}} \tag{6.13}$$

where g_i and g_j are the degeneracies of levels i and j [64]. Thus, the quenching collision rate function can be obtained from the electron induced collision rate function:

$$C_{ji}(T_e) = \frac{g_i}{g_j} e^{\frac{E_j - E_i}{kT_e}} C_{ij}(T_e) \tag{6.14}$$

6.2.6 Radiative Recombination of Electrons

In a radiative recombination process, an electron recombines with an ion, producing a neutral (or an ion with a lower degree of ionization). This results in radiation emission corresponding to the difference in the energy of the free electron and the energy of the bound energy state. This process can be represented as the following reaction:

$$Ar^{+}(i) + e^{-} \quad \rightarrow \quad Ar(k) + h\nu$$

where h is the Planck's constant, ν is the frequency of the radiation emitted. Thus, the energy of the radiation emitted corresponds to the energy lost by the recombining electron.

Radiative recombination cross sections have an n^3 dependence where n is the effective principal quantum number for the energy level of the recombined electron [50]. Bultel et al. [16] lists the photo-ionization cross section for a few energy levels of Argon neutral. Due to the very small cross-section for this processes, radiative recombination processes are neglected in the C-R modeling.

6.2.7 Photo-absorption, Stimulated Emission and Photo-ionization

In the photo absorption process, a photon of the right frequency is absorbed by the atom, causing an electron to transition to a higher energy state. In a stimulated emission process, an electron at a higher energy level is induced to decay to a lower energy state by the presence of electromagnetic radiation at a frequency corresponding to the transition energy. In photo-ionization, the absorption of radiation results in the ionization of the atom (or ion). In all such processes, the energy density of the electromagnetic radiation has to be high and the gas has to be relatively dense. For the current C-R model, an optically thin plasma is assumed. Thus, the radiation emitted from the plasma leaves the plasma volume without being reabsorbed. Hence, in the current C-R model, photo-absorbtion, stimulated emission and photo-ionization processes are neglected.

6.3 Discussion of the Argon C-R Model

Argon neutrals and ions have complicated energy level structures. Modeling of the radiation emission from Argon plasma is a daunting task. The Argon C-R model described in this chapter calculates the electron population densities for the lowest 149 Ar and 123 Ar^+ energy levels. The model gives the simulated emission intensity values for 148 Ar-I and 127 Ar-II emission lines. A list of modeled Argon lines is presented in Appendix D. The emission lines are selected such that all the Argon neutral and single ion emission lines in the wavelength range of 0 to 1000nm that are reported as *observed* in the NIST Atomic Spectra Database [3] are simulated. Thus, the reported Ritz wavelengths, which are derived from the level energies, are not simulated in this C-R model.

Since experimental measurements showed no emission lines from highly ionized Argon ions, only singly charged Argon ions are assumed in this model. As a first assumption the ionization fraction of the plasma does not change. Thus, the total population density of neutrals, and singly charged ions remains constant as their energy level population energy densities change according to the physical processes simulated in the C-R model.

6.3.1 Modeling Assumptions

Few major assumptions were made in order to simulate the Argon plasma. Major assumptions dealt with the state of the plasma being modeled, as well as the optical transparency of the plasma. In addition, it is assumed that the cross-section and spontaneous de-excitation values collected from the literature are adequately accurate.

Uniformity of the Plasma

The most significant assumption for the presented C-R model is that the plasma conditions are assumed to be known and the plasma is assumed to be uniform in the volume space of interest. What is being modeled is *the radiation coming from a uniform plasma of a given*

volume with given neutral density, electron density, and electron temperature.

Thus, other particle kinetics such as convection or diffusion are not modeled. This assumption is valid as long as the time to reach a steady state level population density is shorter than the flow-induced evolution time for the moving plasma volume. As presented later in this chapter, the level population densities reach a steady state value in $\sim 10^{-6}$ seconds with the current processes simulated in this C-R model. For typical electric thruster plasma, the accelerated ions move with velocities on the order of a few tens of thousands of meters per second in the near plume region, and the velocities are smaller in the discharge zone. Thus, the ion residence time in a few centimeters long region is on the order of few microseconds to hundreds of microseconds. Thus, for the discharge region of the Argon Helicon plasma, the uniform plasma assumption is a valid one. This condition also allows the implementation of the C-R model in more complicated Particle in Cell (PIC) kinetic plasma models. Such implementation is presented as a recommendation for future work.

Opacity of the Plasma

The plasma is assumed to be *optically thin* [44]. Thus, any radiation created within the plasma volume in question, will leave without being absorbed by other particles in the plasma. This assumption prompts the analysis of the time scales for radiation absorption, which requires the order of magnitude comparison of the radiation absorption mean free path with the size of the plasma. In the case of the Helicon plasma source, the length in question would be the diameter of the quartz tube where the Helicon plasma is being generated.

Quasi-neutrality of the Plasma

The plasma is assumed to be quasi-neutral. The model simulates Argon neutral, Argon single ion and electrons as the species existing in the volume of computation. Given the total particle number density, ionization fraction information and the quasi-neutrality assumptions, the number density of electrons, ions and neutrals are determined.

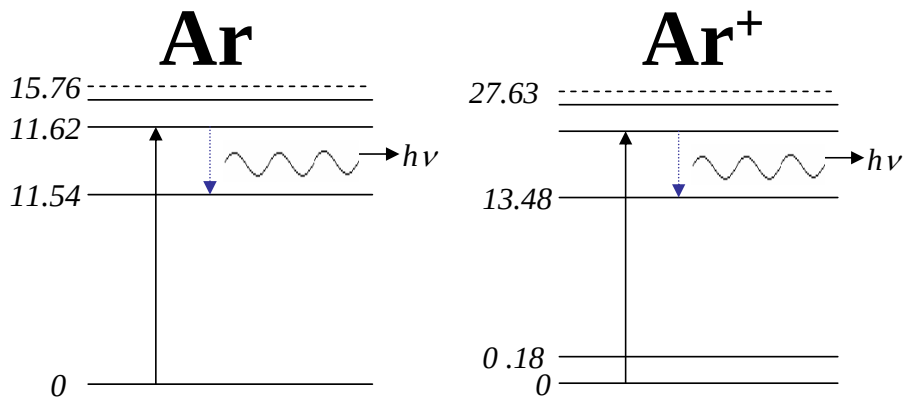

Figure 6-2: Argon neutral and single ion energy levels

Electron Distribution Function

In the C-R model, a normalized Maxwellian energy distribution is assumed for the electrons. A Maxwellian energy distribution assumption requires that the electrons are equilibrated amongst themselves by collisional interactions [72]. For high density plasma observed in the Argon Helicon discharge, this assumption is likely to be valid.

6.3.2 Time Dependent Equation for the Level Population Density

Figure 6-2 shows the graphic representation of Argon neutral and ion energy levels. The model simulates the electron impact collisional excitation, de-excitation, and ionization processes and radiative de-excitation processes between all the levels of interest for Argon neutral and Argon single ion species. In the model the population densities for every energy level are calculated by solving the following time dependent system of differential equations:

$$\frac{dn_m}{dt} = \overbrace{\sum_{j<m} n_j n_e < \sigma_{jm} v > - \sum_{k>m} n_m n_e < \sigma_{mk} v >}^{Collisional\ Excitation} + \overbrace{\sum_{k>m} A_{km} n_k - \sum_{j<m} A_{mj} n_m}^{Spontaneous\ Emission} + \underbrace{\sum_{k>m} n_k n_e < \sigma_{km} v > - \sum_{j<m} n_m n_e < \sigma_{mj} v >}_{Collisional\ De-excitation} - \underbrace{n_m n_e < \sigma_{m-ion} v >}_{Ionization} \quad (6.15)$$

In this equation n_m is the population density of level m, n_e is the plasma electron density,

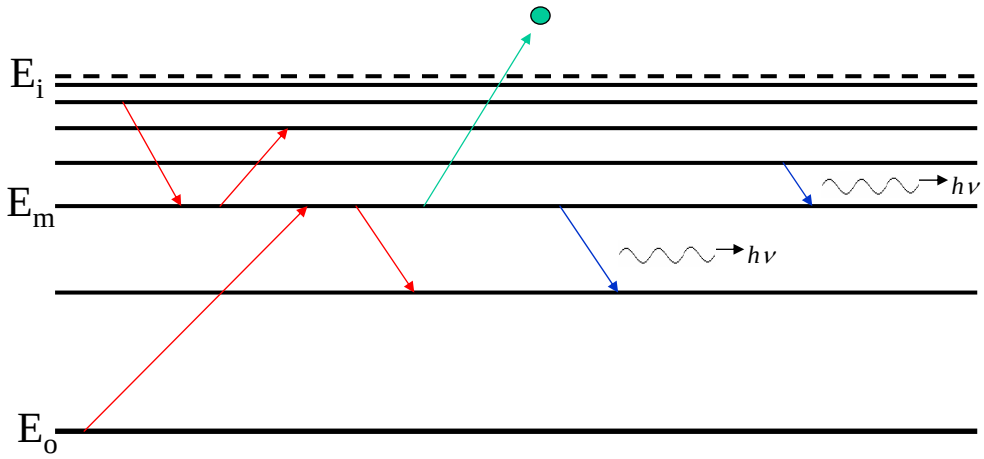

Figure 6-3: Illustration of the processes simulated in the Argon C-R model

σ_{ij} is the excitation collision cross-section from level i to j, A_{ij} is the Einstein's transition coefficient for spontaneous de-excitation from level j to i, σ_{ji} is the de-excitation collision cross section from level j to i, σ_{k-ion} is the ionization collision cross section from level k, and v is the electron velocity. An illustration of all the processes simulated in the current Argon C-R model is shown in figure 6-3.

Since electron recombination processes are not modeled, the electron impact ionization process is a net loss process for Argon neutrals. The inclusion of the ionization process results in a decrease in the total number of Argon neutral particle density. Thus, for calculating the steady state population densities, only the collisional excitation, de-excitation and spontaneous emission processes are considered.

6.3.3 Calculation of the Excitation Collision Rate Function

The electron impact excitation collision rate function C_{ij} is given by:

$$C_{ij} = \langle \sigma_{ij} v \rangle = \int_0^\infty f_e(E_e) \sigma_{ij} \sqrt{\frac{2E_e}{m_e}}\, dE_e \tag{6.16}$$

where m_e is electron mass, v is the electron velocity such that $v = \sqrt{\frac{2E_e}{m_e}}$, $f_e(E_e)$ is the normalized electron energy distribution function, and σ_{ij} is the electron impact excitation cross-section from level i to j. For a Maxwellian energy distribution function for the elec-

trons, this equation takes the form:

$$C_{ij} = \int_0^\infty 2E_e \sqrt{\frac{2}{\pi (kT_e)^3 m_e}} e^{-\frac{E_e}{kT_e}} \sigma_{ij}\, dE_e \tag{6.17}$$

where T_e is the plasma electron temperature.

6.3.4 Calculation of the De-excitation Collision Rate Function

As discussed in section 6.2.5, the micro-reversibility argument gives the relationship between the electron impact excitation and de-excitation collision rate functions. Thus, the de-excitation collision rate function, C_{ji}, can be calculated using the following relation:

$$C_{ji} = \frac{g_i}{g_j} e^{\frac{E_j - E_i}{kT_e}} C_{ij} \tag{6.18}$$

where g_i and g_j are the degeneracies of levels i and j respectively, and C_{ij} is the electron impact collision rate function given by equation 6.17.

6.3.5 Calculation of the Ionization Collision Rate Function

Calculation of the electron impact ionization collision rate function, C_{k-ion}, is similar to the calculation of the excitation rate function, C_{ij}. Thus, for a Maxwellian electron energy distribution function C_{k-ion} can be calculated using the following equation:

$$C_{k-ion} = \int_0^\infty 2E_e \sqrt{\frac{2}{\pi (kT_e)^3 m_e}} e^{-\frac{E_e}{kT_e}} \sigma_{k-ion}\, dE_e \tag{6.19}$$

6.4 C-R Model Flow Chart and Description

The C-R model refers to the tables constructed using data values collected from the literature, primarily from the online NIST atomic spectra database [3], as well as collision rate functions calculated using analytical forms for the cross-sections.

First, the assumed plasma condition is initialized. The following plasma parameters are input to the model: electron temperature, T_e, in eV, electron number density, n_e, in m^{-3} and neutral atom number density, n_n, in m^{-3}. Since, quasi-neutrality is assumed, the single ion density, n_i, is equal to the electron number density, n_e.

Next, code operation parameters are initialized. The maximum number of energy levels to be simulated for Argon neutral and Argon single ion are entered. The computational time step, Δt, is assigned, and the maximum computational time, t_{max}, is input. The maximum number of energy levels can be reduced in order to accelerate the computation. Thus, the radiation emission lines that have higher upper energy levels than the maximum energy level are not modeled. This reduces the total number of line transitions simulated. The computational time step, Δt, is assigned such that it is shorter than the fastest process being modeled. Since, some of the resonant spontaneous radiative de-excitation processes have very short life-times on the order of nanoseconds, the time step has to be very small, $\sim 10^{-10}\, s$. The maximum computation time has to be long enough to assure that the energy level population densities reach a steady state. This time step has to be longer than the slowest process being modeled. Thus, t_{max} is limited by the spontaneous excitation processes with long residence times, on the order of $\sim 10^{-5}\, s$, or the smallest collision rate.

After initializing the necessary plasma and computational parameters, the matrices of parameters needed by the model are created. These matrices are for species energy levels, level degeneracies, level energy difference, emission lines, oscillator strengths, spontaneous emission coefficients, collision rate functions, and collision cross section parameters.

6.4.1 Energy Levels and Corresponding Degeneracy

The first matrix to be created is a single column array for the energies of the simulated levels in eV. The data are obtained from NIST atomic spectra database [3]. A depiction of the array for Argon neutral energy levels is presented in 6.20.

$$\text{Argon Neutral Energy Levels} = \begin{bmatrix} 0 \\ 11.5483537 \\ 11.623592 \\ \vdots \\ 15.502922 \end{bmatrix} \tag{6.20}$$

After the creation of the level energy array, a square matrix for the level energy difference, $E_{ij} = E_j - E_i$, is created. Additionally, a single column array similar to that of the energy levels is created for the degeneracy of each energy level.

6.4.2 Emission Lines

Arrays for the modeled emission lines are created. The arrays have 4 columns. The first column has the modeled emission line, λ_{ij} in nm. The second column has the corresponding spontaneous transition coefficient, A_{ij}. The third column has the lower level energy, E_i, and the fourth column has the upper level energy, E_j, for the corresponding radiative transition of wavelength λ_{ij}.

6.4.3 Einstein's Spontaneous Emission Coefficients

A matrix for the Einstein's spontaneous emission coefficient, A_{ij}, is created. This matrix is a square matrix with a size of the maximum number of energy levels modeled. However, not all of the transitions occur within the 0 to 1000nm spectral range. Furthermore, since most radiative transitions are *forbidden*, this matrix is a very sparsely populated matrix.

Only those elements where the emission lines are modeled are filled, while the rest are set to zero. Thus, for Argon neutral the A_{ij} matrix has only 148 elements filled and similarly for the Argon single ion 127 elements are filled. The matrix is automatically populated using a list of data imported to the code from a spread sheet. The data are obtained from the NIST atomic spectra database [3]. A depiction of the array for the spontaneous emission coefficient matrix is shown in 6.21

$$A_{ij} = \begin{bmatrix} 0 & A_{1-2} & A_{1-3} & A_{1-4} & \dots & A_{1-149} \\ 0 & 0 & A_{2-3} & A_{2-4} & \dots & A_{2-149} \\ 0 & 0 & 0 & A_{3-4} & \dots & A_{3-149} \\ 0 & 0 & 0 & 0 & \dots & A_{4-149} \\ \vdots & \vdots & \vdots & \vdots & \ddots & \vdots \\ 0 & 0 & 0 & 0 & 0 & 0 \end{bmatrix} \tag{6.21}$$

Unlike most literature where A_{ij} notation has the upper energy level as the first subscript, in this study A_{ij} spontaneous emission coefficient represents a radiative transition from a higher energy level j to a lower energy level i.

6.4.4 Oscillator Strength

A matrix for the absorbtion oscillator strengths, f_{ij}, is created. In order to create this matrix the following relationship relating the oscillator strength, f_{ij}, to the Einstein's spontaneous emission coefficient, A_{ij}, is used [50]:

$$f_{ij} = \frac{\epsilon_o c m_e}{2\pi e^2} \frac{g_i}{g_j} \lambda_{ij}^2 A_{ij} \tag{6.22}$$

where $\frac{\epsilon_o c m_e}{2\pi e^2} = 1.49919 \times 10^{-14}\ nm^{-2}s$ [33].

6.4.5 Collision Rate Functions and Relevant Collision Coefficients

Matrices for the collision rate functions are created. First, a matrix that represents the electron induced excitation collision rate between all the relevant levels, $C_{ij} = \langle \sigma_{ij} v \rangle$ is created. In calculating C_{ij}, the Drawin formula discussed in section 6.2.1 is used to determine the collision cross section. In Drawin's formula, there are three parameters that have to be implemented externally. The first one is the oscillator strength, f_{ij}. The matrix for oscillator strengths is used for importing this parameter. The other parameters α and β have to be obtained from experimental data. In this model α values were stored in a square matrix of size of the maximum energy level modeled and are used in the calculation of the cross sections. The α parameters for Argon neutrals were obtained from Bultel et. al. [16]. Since, there are no experimental data available for the α parameters for Argon single ions, the values for the neutrals are used for the similar energy levels of the ions. The β parameter is taken to be 4 for both neutral and single ion Argon cross section calculations. Since the β parameter appears inside the logarithm, its effect is more on the shape of the cross section, rather than the magnitude. Thus, its effect is smaller than that of α.

In order the calculate the collision rate, the integral:

$$C_{ij} = \int_0^\infty 2E_e \sqrt{\frac{2}{\pi (kT_e)^3 m_e}} e^{-\frac{E_e}{kT_e}} \sigma_{ij} \, dE_e \tag{6.23}$$

is evaluated numerically within the energy range of 0 to $10T_e$ with an energy step of $0.01T_e$. In the current model, the C_{ij} matrix is calculated only once for the input electron temperature and the assumed electron energy distribution function. In all of the simulations, the electron energy distribution function is assumed to be Maxwellian, but this can be easily changed to any other normalized distribution function without significantly effecting the computational complexity. If the C_{ij} value for the same distribution function and plasma temperature had been calculated in a previous run, that matrix can be readily imported without the need to recalculate it. A depiction of the matrix for the electron induced collisional excitation rate function is shown in 6.24.

$$C_{ij} = \begin{bmatrix} 0 & C_{1-2} & C_{1-3} & C_{1-4} & \dots & C_{1-149} \\ 0 & 0 & C_{2-3} & C_{2-4} & \dots & C_{2-149} \\ 0 & 0 & 0 & C_{3-4} & \dots & C_{3-149} \\ 0 & 0 & 0 & 0 & \dots & C_{4-149} \\ \vdots & \vdots & \vdots & \vdots & \ddots & \vdots \\ 0 & 0 & 0 & 0 & 0 & 0 \end{bmatrix} \tag{6.24}$$

The electron induced de-excitation collision rate, C_{ji}, matrix is then created by using the simple algebraic relationship between C_{ij} and C_{ji} (equation 6.18).

$$C_{ji} = \begin{bmatrix} 0 & 0 & 0 & 0 & \dots & 0 \\ C_{2-1} & 0 & 0 & 0 & \dots & 0 \\ C_{3-1} & C_{3-2} & 0 & 0 & \dots & 0 \\ C_{4-1} & C_{4-2} & C_{4-3} & 0 & \dots & 0 \\ \vdots & \vdots & \vdots & \vdots & \ddots & \vdots \\ C_{149-1} & C_{149-2} & C_{149-3} & C_{149-4} & \dots & 0 \end{bmatrix} \tag{6.25}$$

The electron induced ionization rate, C_{k-ion}, single column array is created by calculating the following integral numerically in the energy range between 0 to $10T_e$ with an energy step of $0.01T_e$.

$$C_{k-ion} = \int_0^\infty 2E_e \sqrt{\frac{2}{\pi (kT_e)^3 m_e}} e^{-\frac{E_e}{kT_e}} \sigma_{k-ion}\, dE_e \tag{6.26}$$

6.4.6 Initialization of the Level Population Densities

Next, population number densities of all the energy states are initialized. It is assumed that at the beginning of the computation, all the neutrals and the ions are in their ground states. Thus, the neutral ground state density is set to the neutral density, n_n, and all the excited state densities of the neutral atom are set to zero. Similarly, assuming quasi-neutrality, ion

ground state density is set to the electron density, n_e, and all the excited state densities of the singly charged ion are set to zero.

6.4.7 Time Loop: Calculation of the Level Population Densities

The energy level population number densities are calculated within a time loop. The time is increased from $t = 0$ to the prescribed maximum time ($\sim\ 10\mu s$) with a prescribed time step increment ($\sim\ 0.1ns$). For every time step the population densities of all the energy levels are calculated.

In calculating the level population density, the values from a previous iteration are used. From the ground state to a prescribed highest energy level, *maxlevel*, all necessary population *gain* and *loss* values are calculated and stored in single column arrays.

In order to calculate the population density of all the levels, the time dependent population density equation is solved for individual energy levels. The differential equation that determines the change in the state population density of any level m is given by:

$$\begin{aligned}\frac{dn_m}{dt} &= \sum_{j<m} n_j n_e C_{jm} - \sum_{k>m} n_m n_e C_{mk} + \sum_{k>m} A_{km} n_k - \sum_{j<m} A_{mj} n_m \\ &\quad + \sum_{k>m} n_k n_e C_{km} - \sum_{j<m} n_m n_e C_{mj} - n_m n_e C_{m-ion} \end{aligned} \tag{6.27}$$

where collisional excitation, de-excitation and ionization and radiative de-excitation processes are considered.

This equation requires the population densities to be non-negative at all times. Once the gain and loss terms are all calculated separately, the change in the number density of the given state is determined. Then, the electron population density is calculated for that level. The loop continues and the population state densities for both the neutral and the ion energy levels are updated.

For the case where the electron impact ionization is neglected, the neutral and ion densities do not vary with time. Then, the the sum of the state population densities for given species remain constant:

$$\sum_{k=1}^{maxlevel_{Ar}} n_{Ar}(k) = constant = n_n \tag{6.28}$$

$$\sum_{k=1}^{maxlevel_{Ar^+}} n_{Ar^+}(k) = constant = n_e \tag{6.29}$$

where n_n and n_e are neutral and electron densities respectively. Thus, for the case where ionization and recombination processes are neglected, steady state population densities for the energy levels can be determined.

As a first order, the population density of level m is determined by using the simple Eulerian approach such that the value of the density from the previous step is used with an addition from the current step which involves the rate times the time step, such that:

$$n_m^{new} = n_m^{old} + \delta t \frac{dn_m}{dt} \tag{6.30}$$

where $\frac{dn_m}{dt}$ is calculated using equation 6.27 with state number density values of the previous iteration.

In order to improve the smoothness of the change in the population density as well as to allow larger time steps, the 4th order Runge-Kutta method is implemented [23]. In the Runge-Kutta method, the density of a state is calculated by taking a smoother prediction using the values at a full time step and a half time step prior, plus an intermediate updating of the latter.

6.4.8 Reaching Steady State Level Population Density

For the simulations where only electron induced collisional excitation, de-excitation processes and the radiative spontaneous processes are simulated, a steady state is reached for every energy level modeled. Examples of the code reaching steady state population densities for the energy levels are shown in figure 6-4 for the case of a plasma with an electron

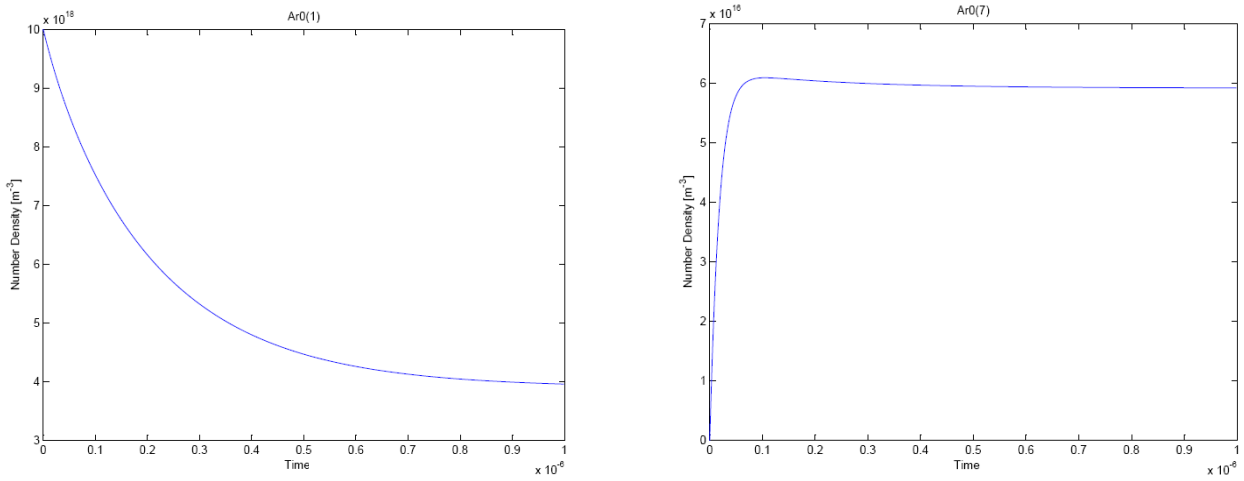

(a) Argon Neutral Ground Level

(b) Argon Neutral Level 7

Figure 6-4: Simulated population density of Argon neutral atom energy levels

temperature of 30eV, electron density of 10^{19} m^{-3}, and neutral density of 10^{19} m^{-3}. The figure shows the change in the population densities of Argon neutral ground state (level 1) and the 6th excited state (level 7) as a function of time as calculated by the C-R model. As seen from the figure, the population density of the levels reaches a steady state value after about ~ 1 μs.

For the cases where the electron-impact ionization collisions for Argon neutral atom are modeled, due to the lack of a reverse process, no steady state is reached, as expected. In theses cases, the level population densities keep decreasing monotonically due to the ionization of electrons from these levels.

Figure 6-5 shows the steady state population density for the modeled energy levels of Argon neutral atoms for the case of a plasma with an electron temperature of 30eV, electron density of 10^{19} m^{-3}, and neutral density of 10^{19} m^{-3}. As seen in this logarithmic scale plot, the level population density drops sharply after the ground level, as expected.

6.4.9 Obtaining Simulated Emission Spectra

When the steady state energy level population densities are achieved, the expected emission line intensities are calculated for all the lines being modeled. As discussed earlier, for

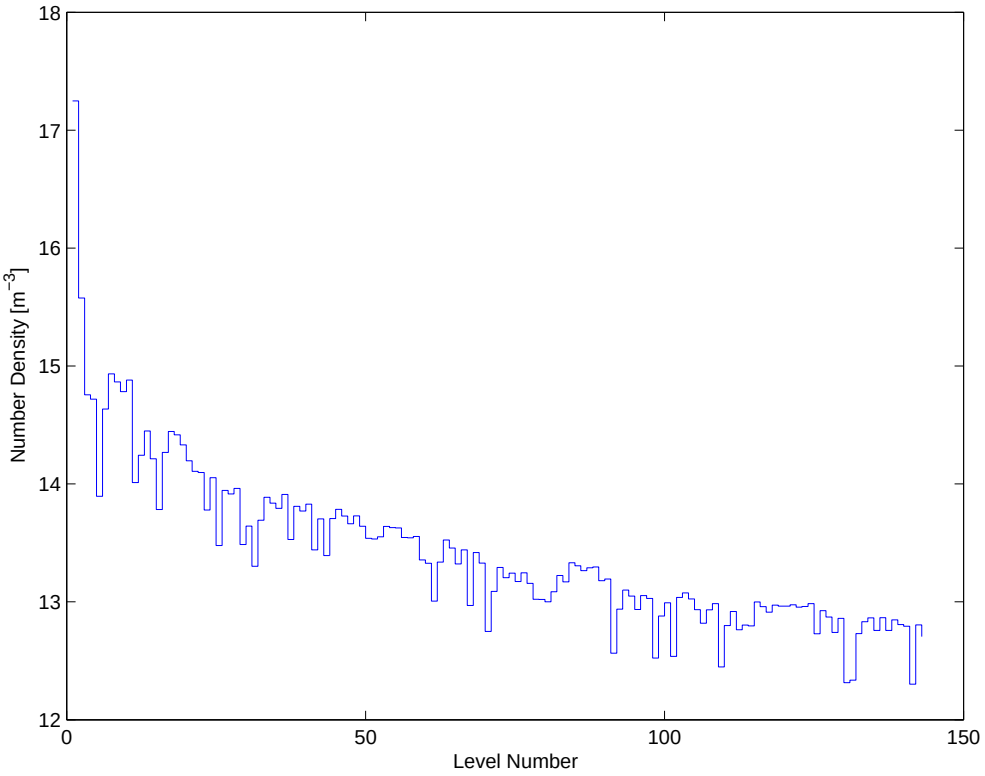

Figure 6-5: Simulated Argon neutral steady state energy level electron population density

optically thin plasmas any radiation created within the plasma leaves the plasma volume without significant absorption by the plasma. Thus, the line intensities can be calculated by simply determining the number of spontaneous radiative de-excitation processes occurring for the steady state conditions. This is done by using equation 6.31 for the line $\lambda_{ij} = \frac{hc}{E_j - E_i}$ that corresponds to the transition between the higher energy level j and the lower energy level i. Once all of the emission intensities, I_{ij}, are calculated, the plots of wavelength versus calculated intensities are produced for the lines being simulated by the C-R model:

$$I_{ij} = n_j A_{ij} \tag{6.31}$$

Experimentally measured spectral lines, such as the ones presented in chapter 5, have a broadening mainly due to the effects of the optical system being used, such as the spectrometer, slit size, etc. The measured line width can also be due to the thermal broadening effects. However, in the reported experimental measurements, the instrumental effects dominate over the thermal broadening effects. Thus, in order to be able to compare the

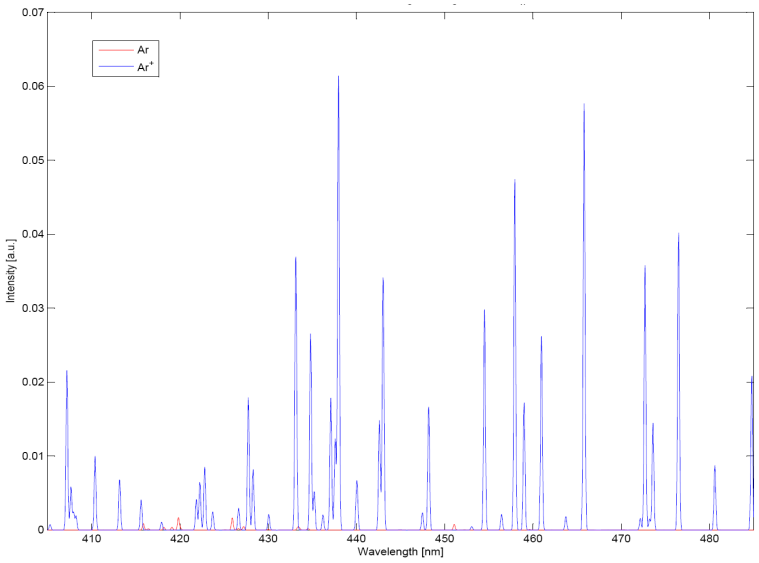

Figure 6-6: Simulation of the line widening by using a Gaussian form-factor

simulation results with the experimental measurements, it would be desirable to introduce appropriate artificial broadening to the presented simulated line emission results.

The broadening of the emission lines can be modeled by assuming a Gaussian shape centered around given simulated line, λ_{ij}:

$$I_{ij}^{G}(\lambda) = I_{ij}\frac{1}{\sigma\sqrt{2\pi}}e^{-\frac{(\lambda-\lambda_{ij})^2}{2\sigma^2}} \tag{6.32}$$

where I_{ij} is the emission intensity calculated by using equation 6.31, σ^2 is the variance for the Gaussian function, and I_{ij}^{G} is the Gaussian profile for the line emission. The variance, σ^2, employed in the Gaussian function should be chosen such that the instrumental broadening effects observed in the measured spectra are mimicked. Figure 6-6 shows an example of the simulated spectrum where the emission lines are widened appropriately in order to simulate the instrumental effects on the measured spectrum.

6.5 Simulation Results and Discussion

Figure 6-7 shows the measured emission spectrum for the Argon plasma of the MIT mini Helicon Thruster Experiment described in chapter 5. The C-R model plasma parameters

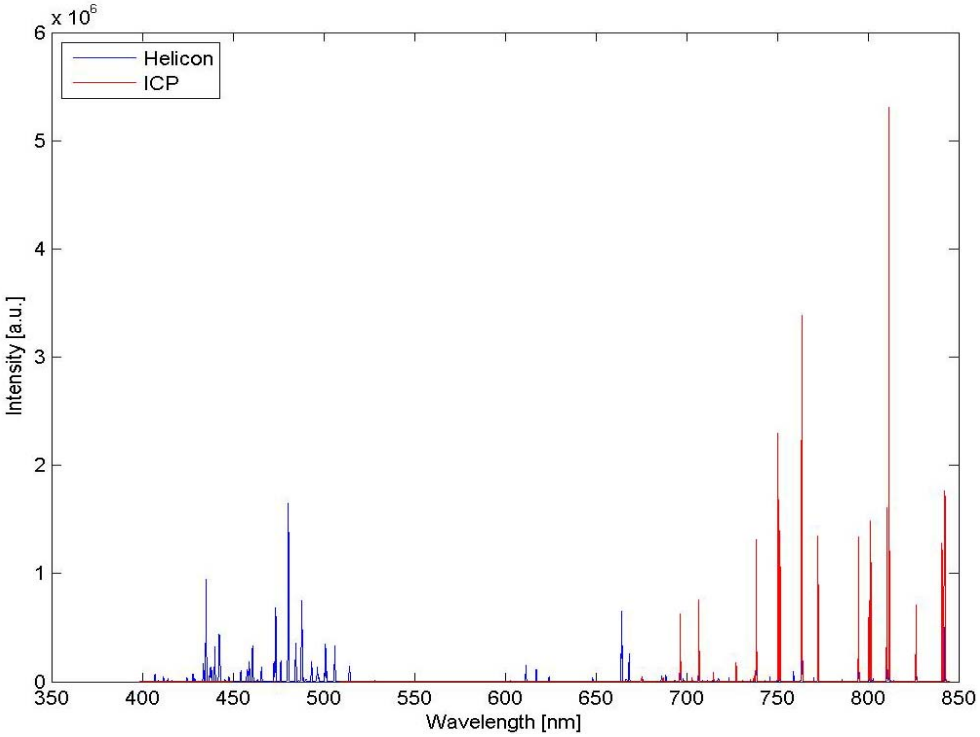

Figure 6-7: Experimental Spectra of Helicon and ICP modes of Argon Plasma

such as electron temperature T_e, electron density n_e and neutral density n_n are varied to obtain a spectrum that matches the measured experimental spectrum.

The best matching spectrum is obtained for input plasma electron temperature of 30eV, electron density of 10^{19} m^{-3} and neutral density of 10^{19} m^{-3}. Figure 6-8 shows the comparison of the experimental and simulation spectra for the wavelength range of 400 to 850nm. The line intensities are in arbitrary units, as the experimental line intensities do not have an absolute calibration. It is observed that for the given plasma parameters, the simulated spectrum matched well the experimental broad-spectrum measurements.

Figures 6-9 and 6-10 show respectively the 750-800nm and 800-850nm region spectra comparison in more detail. This portion of the spectrum is dominated by Argon neutral emission lines. As can be seen from the two spectral graphs, the simulated spectrum relative line intensities show good match with the experimental spectrum relative line intensities for the most part of the spectral interval. There are a few differences in the compared spectra. For example, the relative line intensities of Argon neutral emission lines at 750.39nm and 751.47nm are different for the measured and simulated spectra. The discrepancy can be

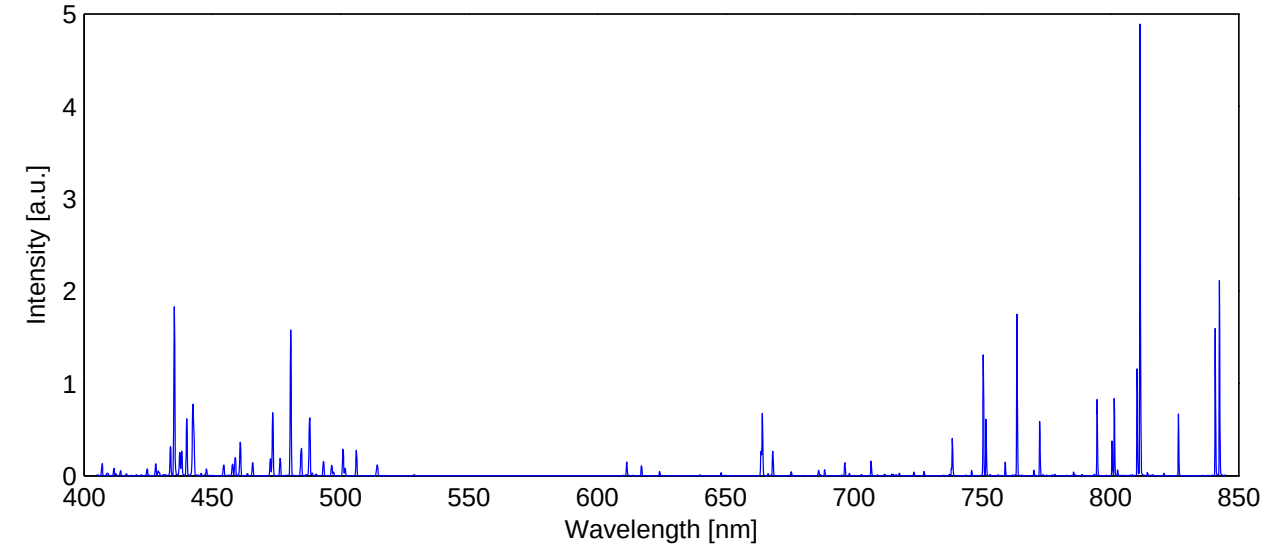

(a) Experimental Helicon Spectrum (RF Power: 1000W, Magnetic Field: 1800 Gauss, Mass Flow Rate: 20sccm)

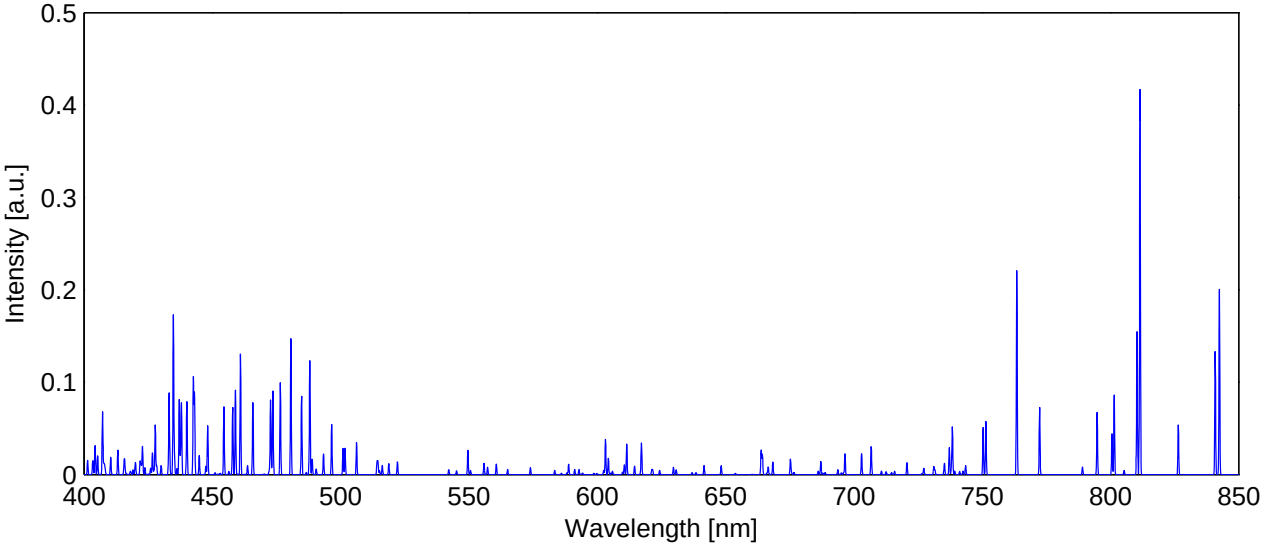

(b) Simulated Spectrum ($T_e = 30eV$, $n_e = 10^{19}\ m^{-3}$, $n_n = 10^{19}\ m^{-3}$)

Figure 6-8: Comparison of Experimental and Simulated Argon emission Spectra of 400-850nm Region

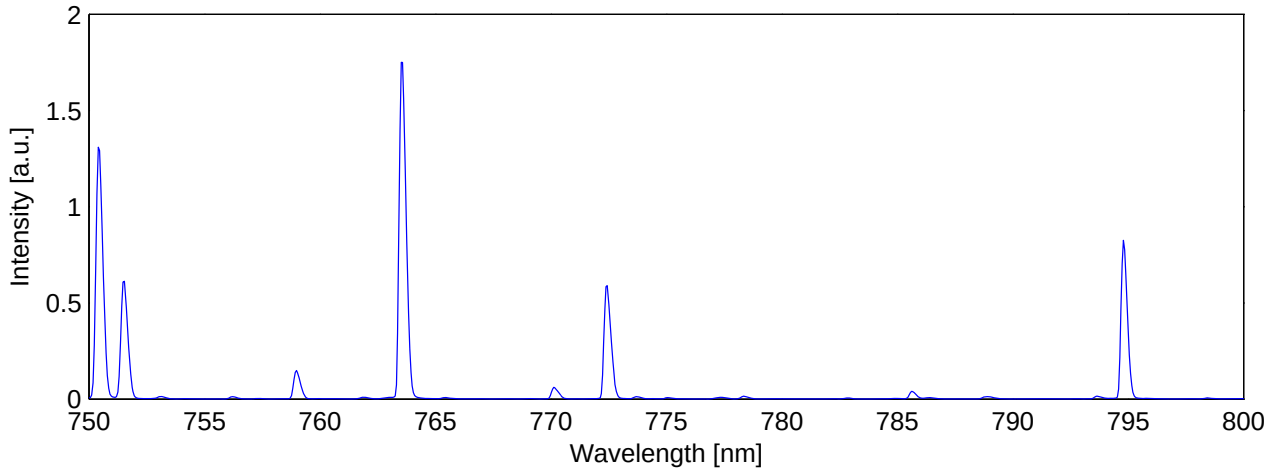

(a) Experimental Helicon Spectrum (RF Power: 1000W, Magnetic Field: 1800 Gauss, Mass Flow Rate: 20sccm)

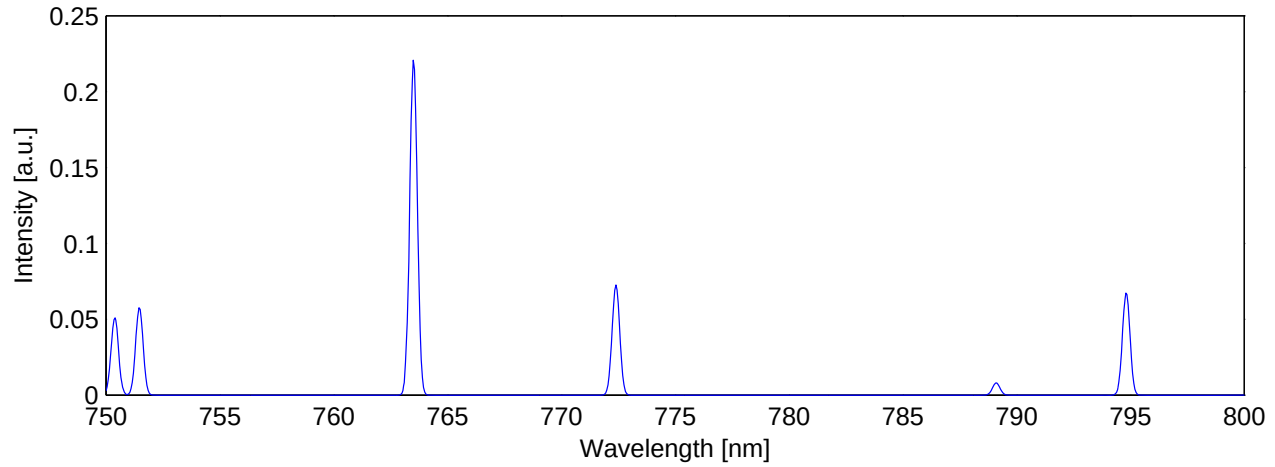

(b) Simulated Spectrum ($T_e = 30eV$, $n_e = 10^{19}\ m^{-3}$, $n_n = 10^{19}\ m^{-3}$)

Figure 6-9: Comparison of Experimental and Simulated Argon emission Spectra of 750-800nm Region

attributed to the uncertainty in the excitation cross-section collision parameters.

Figure 6-11 shows the 450-500nm region spectra comparison in more detail. This portion of the spectrum is dominated by Argon ion emission lines as presented in table 5.1. As seen from these spectral graphs, the simulated spectrum matches moderately well the experimental spectrum. Even though the Argon ion line at 480.6nm is the line with highest intensity in both spectral graphs, the experimentally measured relative intensity is much higher compared to that predicted by the C-R model. The uncertainty in the excitation collision cross-section is again a major factor for the difference between the measured and simulated spectra.

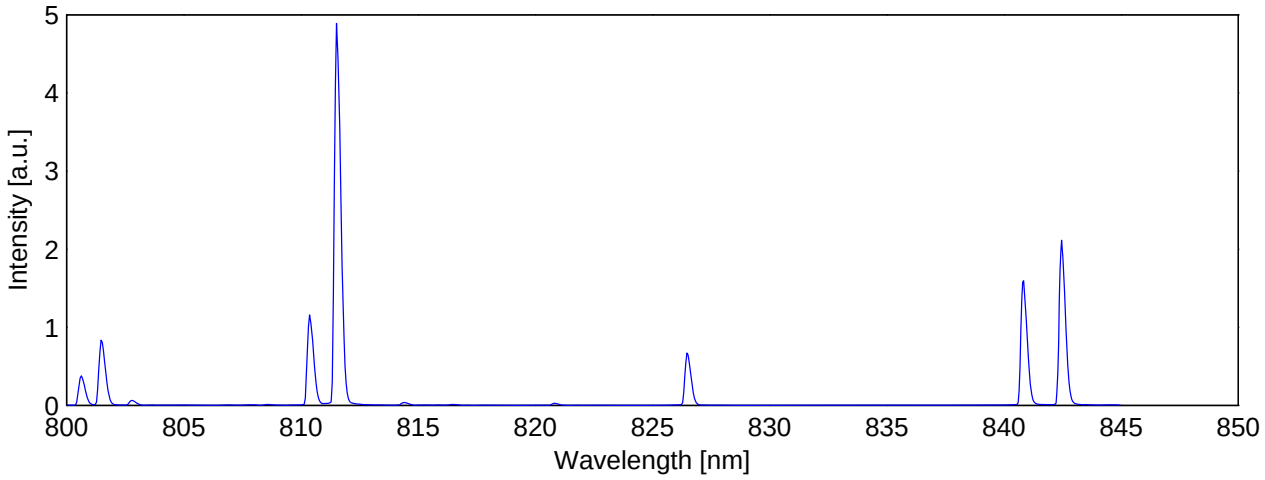

(a) Experimental Helicon Spectrum (RF Power: 1000W, Magnetic Field: 1800 Gauss, Mass Flow Rate: 20sccm)

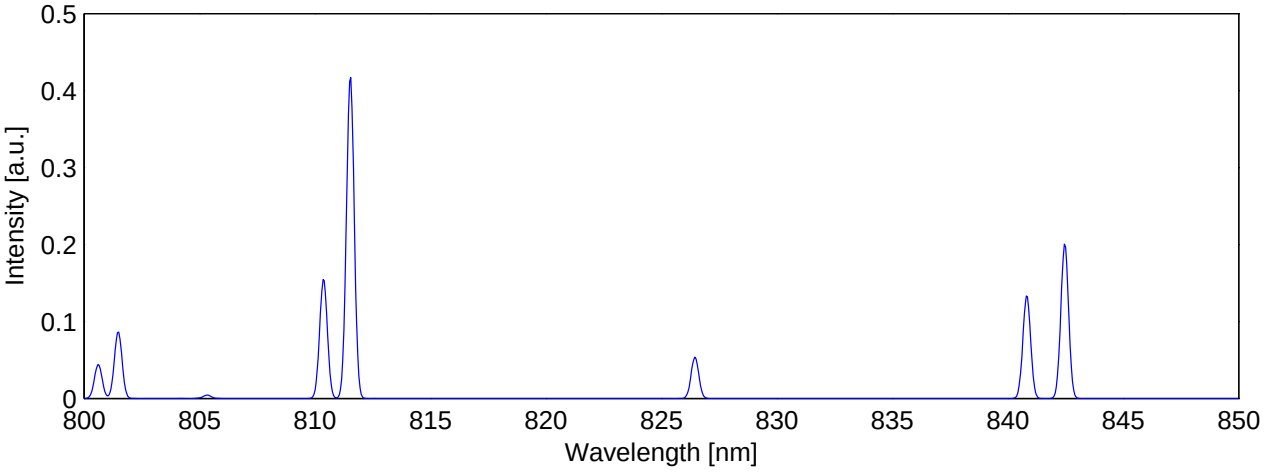

(b) Simulated Spectrum ($T_e = 30eV$, $n_e = 10^{19}\ m^{-3}$, $n_n = 10^{19}\ m^{-3}$)

Figure 6-10: Comparison of Experimental and Simulated Argon emission Spectra of 800-850nm Region

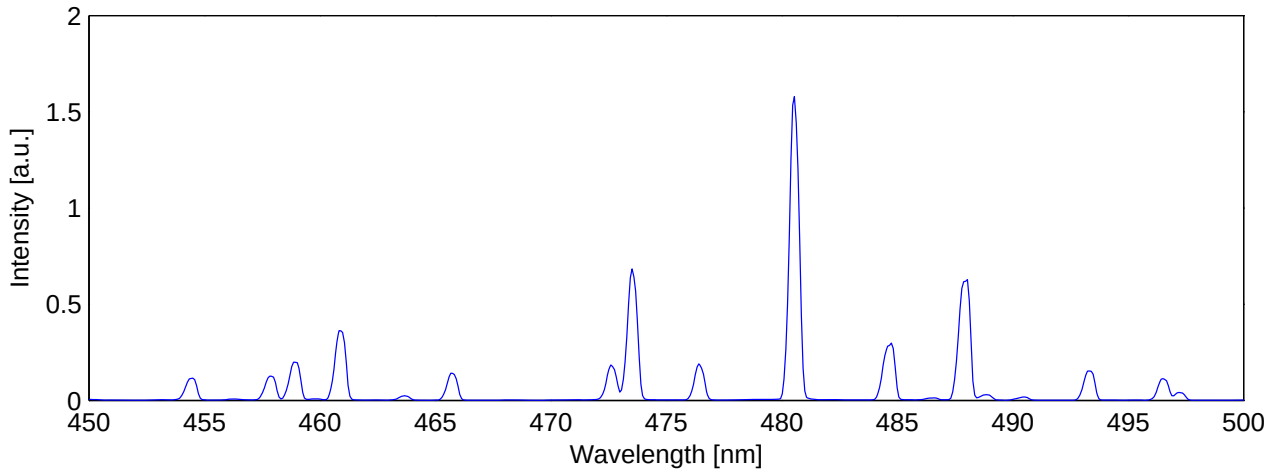

(a) Experimental Helicon Spectrum (RF Power: 1000W, Magnetic Field: 1800 Gauss, Mass Flow Rate: 20sccm)

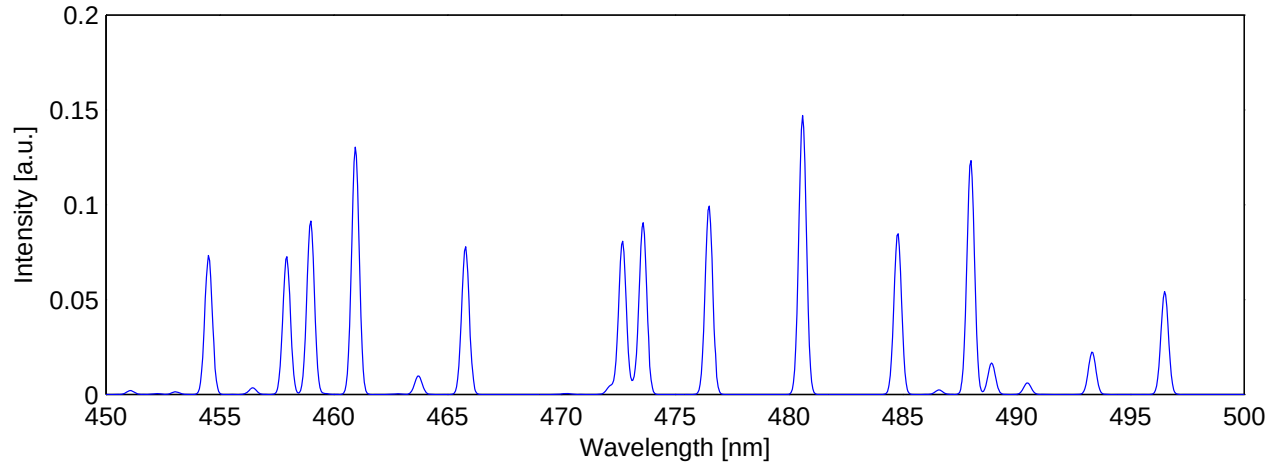

(b) Simulated Spectrum ($T_e = 30eV$, $n_e = 10^{19}\ m^{-3}$, $n_n = 10^{19}\ m^{-3}$)

Figure 6-11: Comparison of Experimental and Simulated Argon emission Spectra of 450-500nm Region

6.6 Chapter Summary

A collisional radiative-model for Argon plasma is developed. The model calculates the steady state electron population densities of Argon neutral and Argon single ion energy levels, and provides simulated emission spectra for the input plasma parameters. The simulated spectral graphs agree reasonably well with the experimental spectra.

The accuracy of the results obtained using the C-R Model depends on the extent of the processes modeled as well as the availability of data for the modeled collisional and radiative processes. The lack of experimental cross-section data for electron impact excitation, de-excitation and ionization processes limits the modeling effort to theoretical formulas. In addition, the lack of cross-section data for the heavy particle induced excitation and ionization processes also limits the accuracy.

The C-R model is not implemented as part of a kinetic model, thus there is no information about the particle kinetics, such as particle energies, velocities, etc. The model also neglects continuum processes such as radiative electron recombination, Bremsstrahlung, etc., which might be important for other plasmas.

Chapter 7

Xenon Collisional Radiative Model

A collisional-radiative model for Xenon plasma has been developed. Simulated emission spectra for Xenon are obtained using this C-R model. The modeled radiation emission spectra have been compared with the experimental spectral measurement results of the BHT-200 Hall thruster discussed in chapter 3.

The C-R model calculates the electron population densities for the lowest 114 Xe and 123 Xe^+ energy levels. The model gives the simulated emission intensity values for the most prominent 39 XeI and 23 XeII emission lines. Preliminary results show good agreement with the experimentally observed emission spectra.

A detailed discussion about the collisional-radiative modeling, and important processes to be considered are discussed in chapter 6. Thus, those discussions will not be repeated here. Similarly, same modeling assumptions made for the Argon C-R model described in section 6.3.1 are made for the Xenon C-R model.

7.1 Description of the Xenon Collisional-Radiative Model

Similar to the Argon C-R model, the Xenon model simulates the electron induced excitation and de-excitation, and radiative spontaneous emission processes. Since there are much

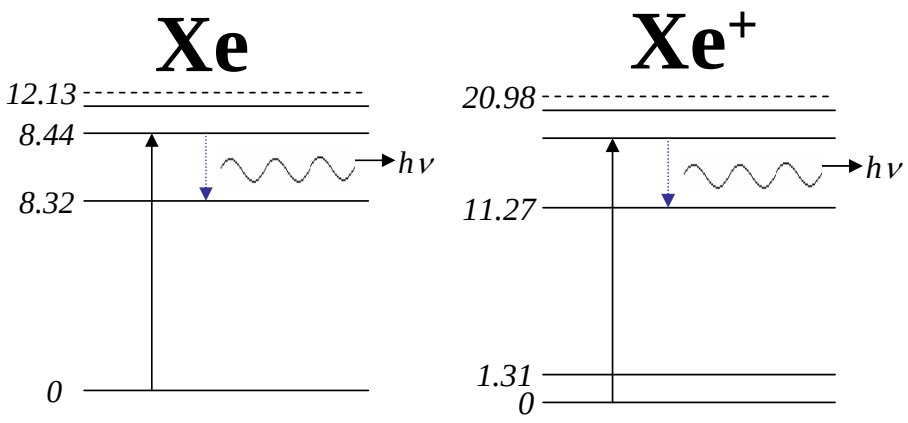

Figure 7-1: Xenon neutral and single ion energy levels

fewer spontaneous emission coefficient data available for Xenon, fewer energy levels and much fewer emission lines are simulated. Thus, unlike the Argon C-R model where all the prominent emission lines in the 0 to 1000nm wavelength range have been simulated, the Xenon C-R model includes the simulation of only a fraction of the hundreds of possible radiative transitions.

Figure 7-1 shows the graphic illustration of Xenon neutral and single ion energy levels. Compared to Argon, Xenon has lower ionization and first excitation energies. The numerical model developed here allows the investigation of the mechanisms that populate/de-populate the atomic and ionic energy levels. In the model, a set of plasma parameters such as electron temperature, electron density, and neutral density are varied to obtain the simulated emission spectrum. The simulated spectra are then compared with the experimental measurements. Since the plasma is assumed to be optically thin, the optical escape factor for all the wavelengths is assumed to be unity.

7.1.1 Calculation of the Excitation Collision Rate Function

Due to lack of a complete set of data on electron impact excitation collision cross sections, analytical expressions proposed by Drawin [35] are used for the collision rate calculations. For optically allowed transitions Drawin formula for the excitation cross section, σ_{ij}, between

levels i and j is:

$$\sigma_{ij}(U_{ij}) = 4\pi a_o^2 \left(\frac{E_{ion}^H}{E_{ij}}\right)^2 \alpha_{ij} f_{ij} \times \frac{U_{ij}-1}{U_{ij}^2} ln(1.25\beta_{ij}U_{ij}) \tag{7.1}$$

where E_{ij} is the energy difference between the higher level j and the lower level i such that $E_{ij} = E_j - E_i$, U_{ij} is the normalized electron energy, $U_{ij} = E_e/E_{ij}$, E_{ion}^H is the ionization energy for Hydrogen, a_o is the Bohr radius, f_{ij} is the oscillator strength, and α_{ij} and β_{ij} are collision cross section parameters.

In literature, there are few data available for electron impact collision excitation cross-section for Xenon. Most relevantly, Fons et. al. [38] present electron impact excitation cross-sections into the $5p^5 6p$ levels of Xenon for ten radiative transitions to the lower energy levels. In another paper by Chiu et. al. [27], the authors present a set of Xenon apparent emission excitation cross section data for 12 visible (4 Xe-I and 8 Xe-II lines) and 8 Xe-I near-infrared lines for electron energies ranging from 10 to 70 eV. The data presented by Chiu et. al. [27] is used in determining the Drawin collision parameters, α and β, for electron impact excitation collisions from ground state to the upper energy level of the relevant emission lines. An example of such a fit for the Chiu et al. data for 467.12nm line is shown in figure 7-2.

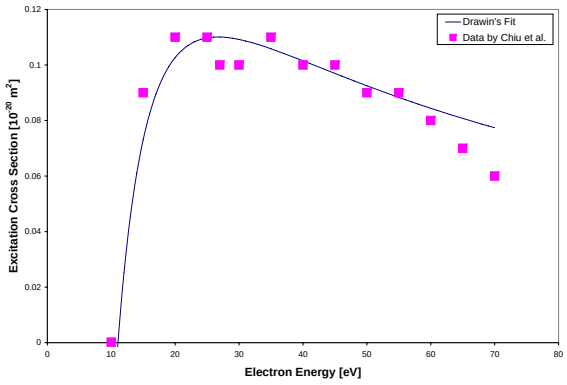

Figure 7-2: Drawin's fit for the apparent electron impact excitation collision data for Xe-I 473.12nm line [27]

In order the calculate the collision rate, the integral:

$$C_{ij} = \int_0^\infty 2E_e \sqrt{\frac{2}{\pi(kT_e)^3 m_e}} e^{-\frac{E_e}{kT_e}} \sigma_{ij}\, dE_e \tag{7.2}$$

is evaluated numerically within the energy range of 0 to $10T_e$ with an energy step of $0.01T_e$. In all of the simulations, the electron energy distribution function is assumed to be Maxwellian.

As discussed in section 6.2.5, micro-reversibility argument gives the relationship between the electron impact excitation and de-excitation collision rate functions. Thus, the de-excitation collision rate function, C_{ji}, is calculated using the following relation:

$$C_{ji} = \frac{g_i}{g_j} e^{\frac{E_j - E_i}{kT_e}} C_{ij} \tag{7.3}$$

where g_i and g_j are the degeneracies of levels i and j respectively, and the excitation rate, C_{ij}, is calculated using equation 7.2.

7.1.2 Einstein's Spontaneous Emission Coefficients

Compared to the Argon data, there are much less spontaneous emission coefficient data available for Xenon. Unlike Argon neutral and single ions, the NIST Atomic Spectral Database [3] presents the spontaneous emission coefficients for only a few Xenon neutral and single ion emission lines. The Einstein's coefficient values used in the Xenon C-R model are compiled from NIST Atomic Spectra Database [3], from Pfrommer [68], and from Malovic et. al. [59]. The spontaneous emission coefficient values used in the Xenon C-R model are presented in Appendix E.

7.1.3 Calculation of Level Population Densities

The C-R model simulates the electron impact collisional excitation, de-excitation and radiative de-excitation processes between all the levels of interest for Xenon neutral and Xenon single ion species. In the model the population densities for every energy level are calculated

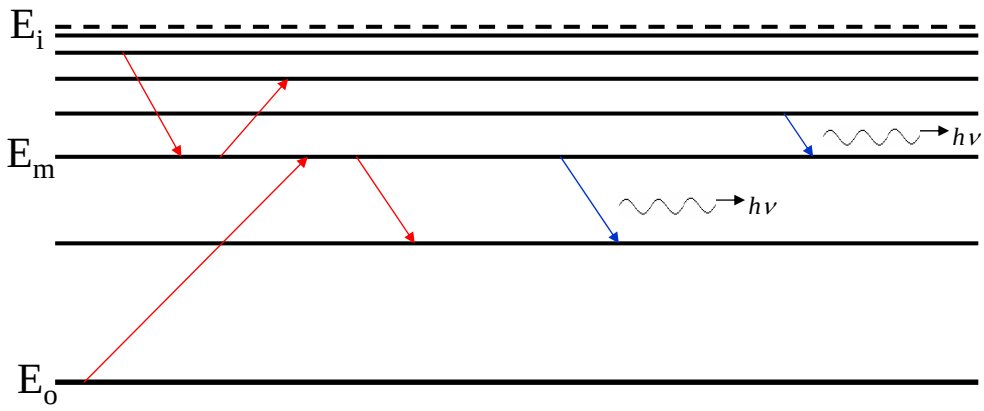

Figure 7-3: Illustration of the processes simulated in the Xenon C-R model

by solving the following coupled system of differential equations:

$$\frac{dn_m}{dt} = \overbrace{\sum_{j<m} n_j n_e < \sigma_{jm} v > - \sum_{k>m} n_m n_e < \sigma_{mk} v >}^{Collisional\ Excitation} + \overbrace{\sum_{k>m} A_{km} n_k - \sum_{j<m} A_{mj} n_m}^{Spontaneous\ Emission} + \underbrace{\sum_{k>m} n_k n_e < \sigma_{km} v > - \sum_{j<m} n_m n_e < \sigma_{mj} v >}_{Collisional\ De-excitation} \tag{7.4}$$

In this equation n_m is the population density of level m, n_e is the plasma electron density, σ_{ij} is the excitation collision cross-section from level i to j, A_{ij} is the Einstein's transition coefficient for spontaneous de-excitation from level j to i, σ_{ji} is the de-excitation collision cross section from level j to i, and v is the electron velocity. An illustration of all the processes simulated in the current Xenon C-R model is shown in figure 7-3.

The Xenon C-R model flow chart and description is similar to that of the Argon C-R model described in section 6.4. First, necessary plasma parameters such as the plasma temperature, density and neutral density values are entered. Second, code operation parameters such as maximum number of energy levels to be simulated, computational time-step and the maximum computation time are initialized. Then, all the necessary matrices to be used by the model are created. Next, the energy level population densities are initialized such that at the beginning of the time iterations all electrons are at the ground energy level of respective species. The time evolution of the level population densities are then iteratively calculated by using equation 7.4. After steady state population densities for the energy levels are achieved, the line radiation emission intensities are calculated and a Gaussian

spread is introduced to reproduce the instrumental line broadening effects. The simulated spectral graphs are then produced and analyzed.

7.2 Simulation Results and Discussion

The simulated Xenon emission spectra are compared with the experimental emission spectra for the BHT-200 Hall thruster. Figure 7-4 shows the comparison of the measured emission spectrum for the Xenon plasma of the BHT-200 Hall thruster 33mm plume region with the simulated Xenon spectrum. For the simulation, the input plasma electron temperature is 5eV, the electron density is 10^{18} m^{-3} and neutral density is 10^{18} m^{-3}. The measured spectrum is calibrated using the quantum efficiency of the CCD detector in the 800-1000nm wavelength region. For the presented wavelength range, the simulated spectrum shows good agreement with the measured spectrum. However, since some of the emission lines such as the Xe neutral emission lines at 951.34nm and 992.32nm are not simulated, those lines do not appear in the simulated spectrum.

7.3 Chapter Summary

A collisional radiative-model for Xenon plasma is developed. The model calculates the steady state electron population densities of Xenon neutral and single ion energy levels, and provides simulated emission spectra for the given plasma parameters. The simulated spectral graphs are compared with the experimental measurements of BHT-200 Hall thruster plasma. The simulated spectra shows reasonably well match with the experimental spectra in the near-infrared region of the spectrum where the neutral Xenon atom emission is prominent.

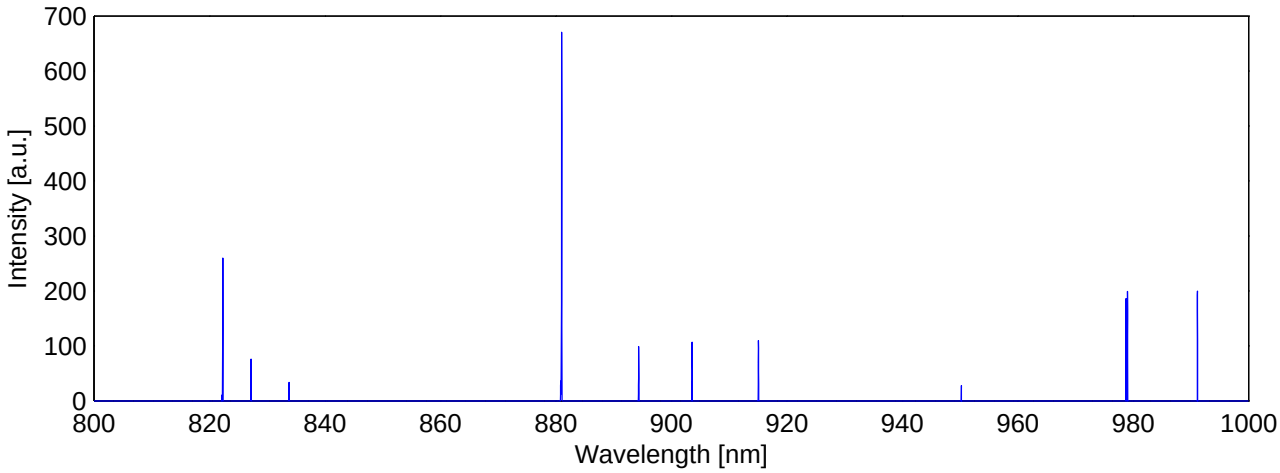

(a) Experimental BHT-200 Hall Truster Spectrum for the 33mm Plume Region

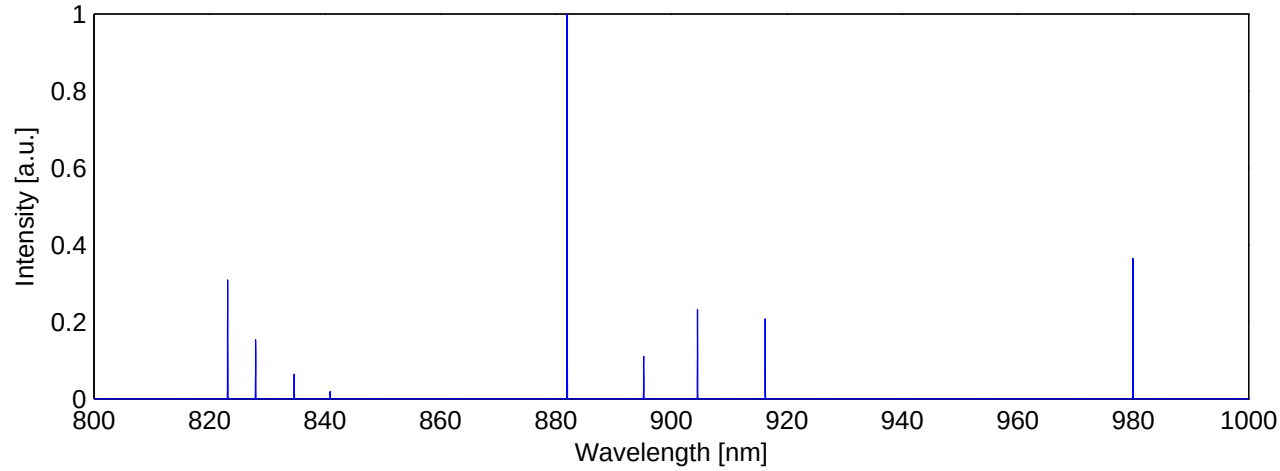

(b) Simulated Spectrum ($T_e = 5eV$, $n_e = 10^{18}\ m^{-3}$, $n_n = 10^{18}\ m^{-3}$)

Figure 7-4: Comparison of the Experimental and Simulated Xenon emission Spectra for the 800-1000nm Wavelength Region

Chapter 8

Optical Diagnostics of the BHT-200 Hall Thruster Surface Erosion

SPT type Hall effect thrusters have concentric annular walls made of dielectric ceramic material. Erosion of these ceramic walls due to impact of high energy ions is one of the major life limiting factors for these thrusters.

The impulse obtained from a Hall thruster is provided by the acceleration of the ionized propellant due to the potential drop between the anode located at the end of the annular acceleration channel and the cathode located outside the thruster. The ion flux directed out of the annular channel produces the thrust. However, some of the high energy ions, $E_i > 100eV$, hit the channel walls, causing sputtering of the ceramic insulator material.

Erosion of the thruster ceramic walls results in plasma impurities in the discharge and the plume regions due to the eroded products entering the plasma. The detection of radiation emission due to these erosion products is a promising method in determining the erosion rate of the thruster components, and subsequently of the thruster operational lifetime. Optical emission spectroscopy is considered an ideal method in evaluating the erosion rate, as such measurements do not disturb the plasma as well as provide real time data acquisition capability.

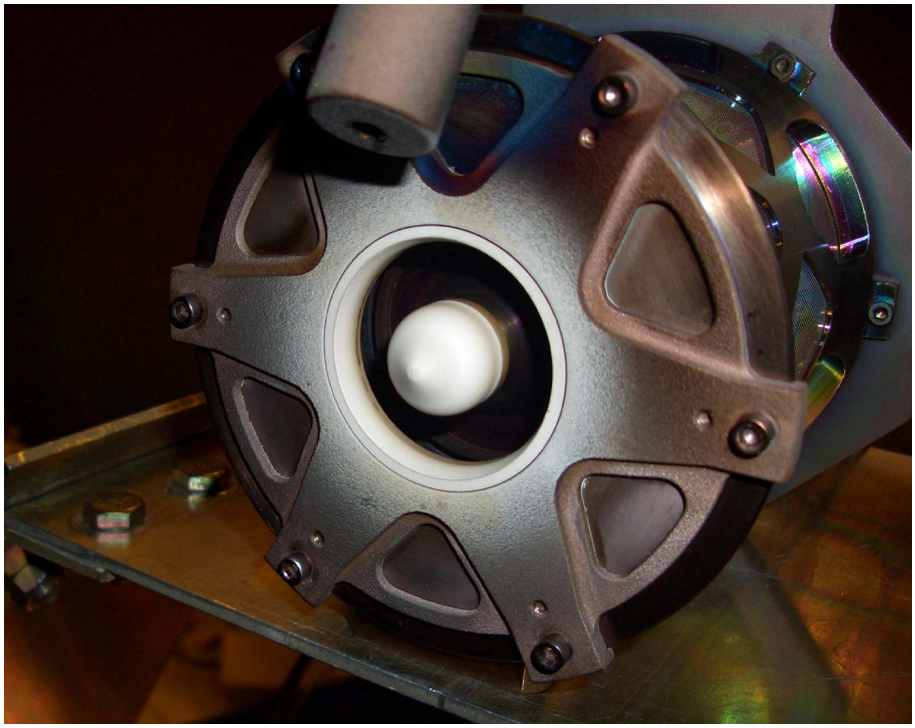

Figure 8-1: BHT-200 Hall thruster ceramic annular walls made of Boron-Nitride

As discussed in chapter 3, the BHT-200 Hall thruster is an SPT type Hall thruster. It has insulator ceramic annular walls made of Boron-Nitride (BN). A picture of the BHT-200 Hall thruster annular channel is shown in figure 8-1. Optical emission spectroscopy can be used to identify the regimes of operation that cause high thruster wall erosion by measuring the radiation emission of erosion products. Even though an absolute material loss correlation to the emission data is difficult to obtain, these emission data can be directly used to study the relative effect of various changes in operating parameters on erosion, in real time. Radiation emission due to excited Boron atoms is expected to be detected in BHT-200 Hall thruster plume plasmas, because of the ion sputtering of the thruster's wall material made out of BN ceramic. In this chapter, spectral measurements of Boron neutral emission lines at 249.677nm and 249.773nm are presented for varying thruster operational parameters.

Determination of the ceramic erosion rate is traditionally conducted by operating the thruster for long durations (several weeks to months) inside vacuum chambers, and measuring the change in the wall thickness before and after the testing. However, such experiments are long and expensive, and often require the destruction of the thruster. In addition, the analysis of the findings is difficult due to the uncertainty in the deposition rates and other

vacuum tank effects, as well as the difficulties in establishing a non-varying reference for surface geometry measurements.

There have been a few computational models developed to simulate the erosion of the Hall thruster ceramic walls [26][82][73][39][81]. Most relevantly, Cheng [25] modeled the erosion of the ceramic nose cone of the BHT-200 Hall thruster using a hybrid-PIC Hall thruster discharge plasma simulation code. The models use experimental and analytical sputtering coefficients for Xenon ions hitting Boron-Nitride walls. However an accurate modeling of the erosion is difficult due to the uncertainties in predicting the plasma properties, electric field strengths (or sheath potential drops), and wall thermal conditions inside the Hall thruster discharge channel.

In previous studies, optical emission spectroscopy has been proposed as a means to diagnose the erosion rate of the ceramic walls of Hall thrusters [60][66][53][36]. In Hall thrusters, optical emission spectroscopy provides emission lines due to mainly the propellant plasma particles such as Xenon neutrals and single ions as discussed in chapters 3 and 4. Measurements of line emission due to the Xenon double ions are also reported [60]. In addition, radiation emission lines due to the thruster ceramic wall materials such as Boron and Silicon were also detected [66][48][53] as further discussed in the next section.

8.1 Literature Review

As a first stage of the research, one should identify the lines of erosion products expected to be detected in the electric thruster plasma emission spectrum. In experiments by Karabadzhak et al. [53], samples of materials commonly used by electric thrusters were placed in the thruster plume region and were exposed to the energetic ion beam leaving the thruster. The emission spectrum in the impingement region was recorded. The spectrum was analyzed to identify the emission lines, and those lines were compared with the plume spectrum. Lines that can be easily separated from Xenon emission lines were selected to be those to be used in erosion rate analysis. The authors identified lines for Cr, Fe, Co, Ni, Si and B elements. The Boron neutral (BI) lines at 249.68 and 249.77 were identified as the

lines to be analyzed for BN ceramic wall erosion.

In another paper by Pagnon et al. [66], the emission by the propellant plasma (Xe, Xe^+) and the BN-SiO_2 ceramic erosion products (B and Si) have been used to analyze the wall erosion of an SPT type Hall thruster. In that analysis, a high resolution (0.15nm in UV) spectrum was investigated for radiative emission of the excited states of Xe, Xe^+, neutral Boron and Silicon species. The authors measured the 245-255nm wavelength region spectrum for the erosion product analysis due to the existence of strong Xe-II, B-I (∼250nm) and Si-I (∼252nm) emission lines. In the paper, along with the Boron line emission at 249.77nm, Xe neutral emission line at 828.01nm and Xenon single ion emission line at 484.43nm were used to predict Boron number density in the plume. To accomplish this the ratio, $R = I_{Boron} \times \frac{I_{Xe}}{I_{Xe^+}}$, was plotted. It is claimed that this ratio is proportional to the density of Boron. According to the authors, the ceramic erosion rate is proportional to the thruster operational power.

In the paper by Bugrova et al. [15], the erosion of an SPT type Hall thruster wall insulator material was investigated using optical emission spectroscopy. Boron neutral emission line at 249.77nm was measured. A simple corona model assumption is used to deduce the Boron number density from the measured emission intensity. The values for the electron temperature and density were obtained with the help of electrostatic probes. Gryzinski's formula [46] was used to calculate the electron impact excitation cross section from the ground state to the upper energy state of the corresponding radiative process.

According to Crofton [31] along with the Boron atoms, Boron Nitride (BN) molecules are also expected to be detected in the plume due to the sputtering of condensed Boron-Nitride. The author points out that the detection of BN, however, can be much harder.

In the most relevant study, Hargus et al. [48] looked at the the ceramic erosion rate of the BHT-200 Hall thruster. The authors measured emission in the vacuum ultraviolet (VUV) portion of the spectrum. In that study the optics were focused on the Boron-Nitride ceramic nose cone of the BHT-200 Hall thruster center pole as seen in figure 8-1. Specifically, the Boron neutral resonant line at 137.9nm was measured and analyzed in order to determine the effect of various operating conditions on the Boron emission intensity. The authors claim

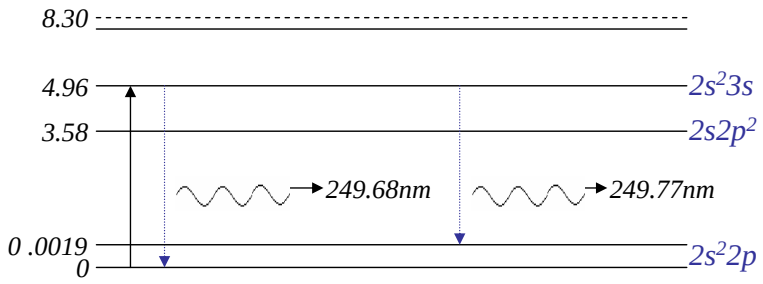

Figure 8-2: Illustration of the neutral Boron energy levels and the 249.68 and 249.77nm resonant emission lines

that the VUV portion of the spectrum is chosen due to the wide spacing of the emission lines in that region, along with the fact that most transitions in the VUV region of the spectrum are to the ground state and thus are a better indication of the Boron density in comparison to the transitions between the excited levels.

In our study, we decided to focus on the $\sim 250nm$ portion of the UV spectrum, due to the limitations of doing measurements in vacuum conditions. Yet, the respective Boron lines are resonant lines to the ground state, whereas the nearby Xenon emission lines are lines between the excited states.

8.2 Discussion of the Erosion Rate Calculation

Boron has a doublet transition at 249.68nm and 249.77nm. These are the longest wavelength resonant transitions for Boron [31]. The excited state lifetimes are $\sim$ 8ns and $\sim$ 4ns respectively, due to the large oscillator strengths of the transitions [31][3]. Figure 8-2 shows the graphic illustration of the Boron atomic energy levels, in eV, and the 249.68nm and 249.77nm resonant emission lines.

Measurement of these resonant Boron lines will be used to obtain the thruster erosion rate trends. However, it is difficult to relate the intensity of the spectral emission with number density of the eroded products, and in general one needs a complicated Collisional-Radiative Model to understand the processes resulting in radiation emission. Additionally, relating the number density of the erosion products to the actual erosion rate is another challenge.

However, if one assumes that both the eroded species and the propellant species (ie. Xe, Xe^{+}, Xe^{++}) are induced only by the electron impact excitation collisions, the variations in emission intensity can be related to the variations in the species densities by taking into account the relevant cross section and spatial/temporal plasma electron temperature and density values. Moreover, one can assume direct proportionality between the thruster erosion rate and eroded species number density.

For optically thin plasma, assuming corona equilibrium, the intensity, I_{ij}, of an emission line λ_{ij} corresponding to a radiative transition from the energy level j to level i will be given by:

$$I_{ij} = \frac{A_{ij}}{\sum_{k<j} A_{kj}} n_e n_1 < \sigma v_e >_{1j} \tag{8.1}$$

where n_e is the electron density, n_1 is the ground state atom density, A_{ij} is the spontaneous emission transition coefficient from level j to level i, $\sum_{k<j} A_{kj}$ is the reciprocal of the lifetime, τ, of level j, and $< \sigma v_e >_{1j}$ is the electron impact excitation collision rate from the ground state to level j.

The values of electron temperature and density can be obtained from other intrusive diagnostics measurements such as using Langmuir probes. The experimental measurement of the Boron neutral emission lines at λ=249.677nm corresponding to the transition between the levels $2p^2\ P^0_{1/2}$ at ground state (0eV) and $3s^2\ S_{1/2}$ energy level at 4.964eV and at λ=249.773nm corresponding to the transition between the levels $2p^2\ P^0_{3/2}$ at 0.00189 eV and $3s^2\ S_{1/2}$ energy level at 4.964eV can be used in order to deduce the erosion rate of insulator material. Gryzinski's formula [46] has been used by other researchers to calculate the electron excitation cross section from the ground state to the 4.964eV state [15].

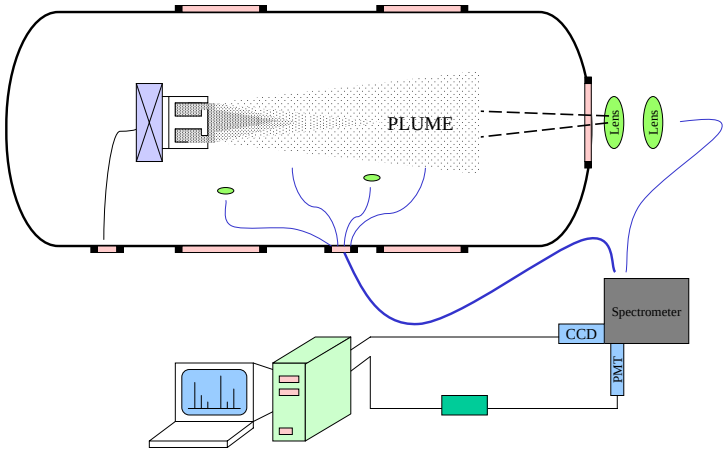

Figure 8-3: Schematic of the Thruster Erosion Rate Spectral Measurement Setup

8.3 Experimental Setup

The BHT-200 Hall thruster erosion rate spectral measurements were performed in the MIT Space Propulsion Laboratory vacuum tank. The base pressure was 7.8×10^{-8} Torr before the thruster operation was began. The chamber pressure during the testing was 3.57×10^{-5} Torr for the nominal operational flow rates for the thruster. The BHT-200 thruster was mounted on top of a metal stand inside the chamber. The thruster was run on Xenon propellant.

For the spectral measurements, the radiation emitted by the thruster plasma as well as the erosion products was collected by a collimating lens located inside the vacuum chamber, and transmitted to the entrance slit of a spectrometer through UV-rated optical fibers. A schematic of the experimental setup is shown in figure 8-3. A picture of the thruster and the collimating lens is shown in figure 8-4.

8.3.1 Radiation Collection and Transmission

A collimating lens was used to collect the light from the plasma region of interest. The Ocean Optics UV-74 lens is 5 mm in diameter and has a focal length of 10mm. It has an SMA connector on the focused end where the optical fiber cable is attached. The lens has good transmissivity in the UV wavelength range. A close-up picture of the lens is shown in

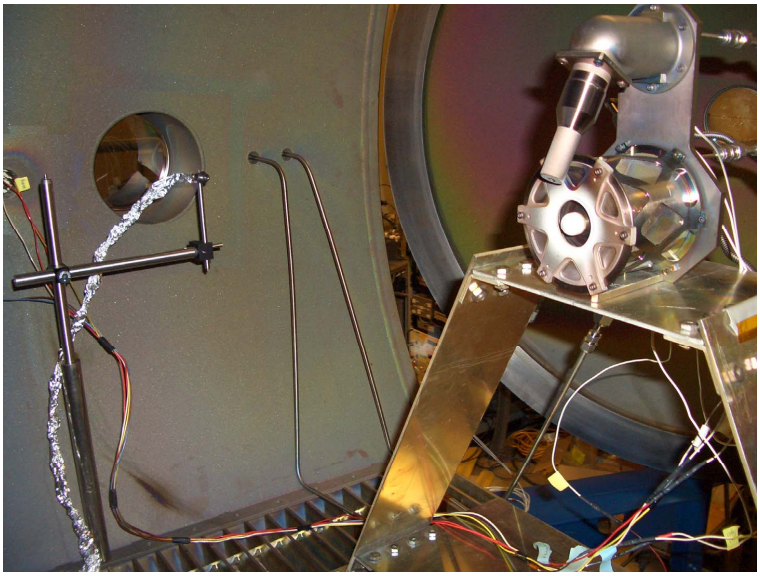

Figure 8-4: Picture of the BHT-200 Hall thruster and the collimating lens/fiber system inside the vacuum chamber

figure 8-5(a).

The collected signal was transmitted from inside the chamber to the outside through a four-channel vacuum-fiber feedthrough. This four-channel vacuum feedthrough has four 200μm diameter UV rated fiber cables. A picture of the vacuum fiber feedthrough is shown in figure 8-5(b). The fiber ends were attached to a 3m long Acton Research LG-456-020 fiber bundle, similar to the one described in section 3.2.1, using an SMA mating adaptor outside of the vacuum tank. The fiber bundle carried the collected signal to the entrance slit of the spectrometer.

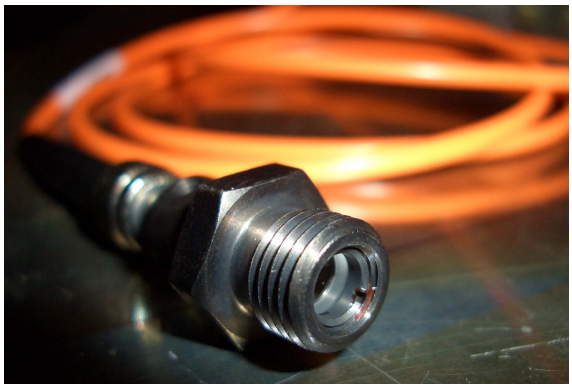

(a) Collimating Lens

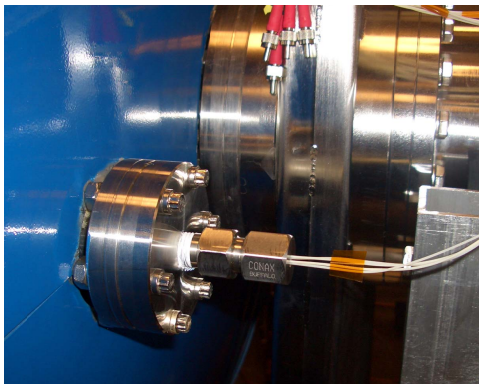

(b) Four-channel Vacuum Fiber Feedthrough

Figure 8-5: Pictures of the collimating lens and the vacuum fiber-feedthrough

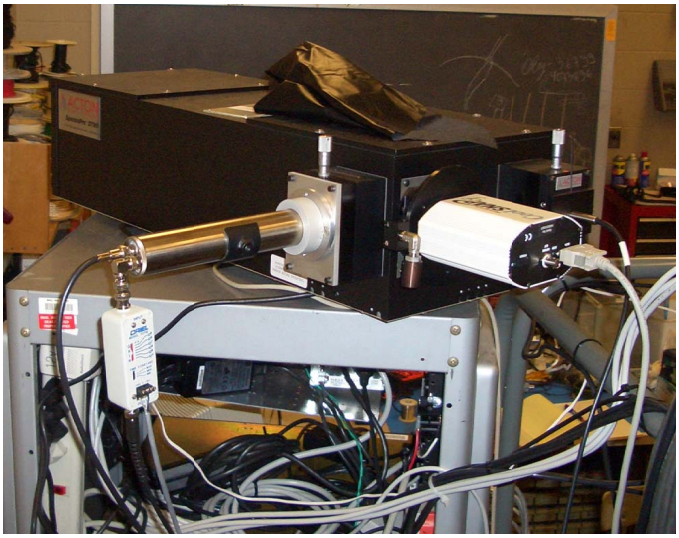

Figure 8-6: Acton Research-750i spectrometer with CCD and PMT detectors attached at the exit ports

8.3.2 Radiation Dispersion

An Acton Research SpectraPro-750i spectrometer was used as the dispersive instrument. This 750mm focal length, f/6.5 aperture Czerny-Turner type spectrometer provides a resolution of $\sim 0.01nm$ at 435nm using 1800 g/mm grating. The inlet port was equipped with an adjustable slit assembly. The spectrometer has a triple-grating turret, and was equipped with 3 different diffraction gratings. The grating with 300 grooves/mm blazed at 500nm was used to obtain broader range spectrum. The second grating at 1800 grooves/mm blazed at 500nm was widely used due to its better wavelength range with relatively good resolution. The high resolution UV optimized holographic grating of 3600 grooves/mm provided a high resolution spectrum, $\sim 0.007nm$ with small wavelength range of only ~ 3 nm. A picture of the spectrometer is shown in figure 8-6.

8.3.3 Radiation Detection

A CCD camera, Roper Scientific Photometrics K4, was attached to the axial exit port of the spectrometer. The CCD has 2048×2048 pixels with a pixel size of 7.4 × 7.4-μm. This thermoelectric cooled detector has good quantum efficiency in the visible wavelength range as well as in the UV portion of the spectrum. A Photo-multiplier-tube (PMT) detector was

Figure 8-7: Region of the BHT-200 Hall thruster where the collimating lens was pointed

attached to the side exit port of the spectrometer. The PMT is sensitive in the 190nm to 850nm wavelength range. It is located in an Oriel PMT housing. The PMT bias voltage is provided by a Bertran-230 high voltage power supply. For the measurements, the power supply potential was set at $-1000V$. Figure 8-6 shows the Acton SectraPro-750i spectrometer with the CCD and PMT detectors attached at the two exit ports.

8.4 Measurement Results

For the spectral measurements, the BHT-200 Hall thruster was placed in the center of the MIT-SPL vacuum chamber on a metal stand. Unless specified otherwise, the thruster was run at the nominal operational parameters of 250V discharge potential, 8.0sccm Xenon propellant flow rate to the anode. The cathode Xenon propellant flow rate was kept constant at 1.0sccm and the magnet current was kept constant at 1.0A for all runs. The collimating lens, located inside the vacuum chamber, was pointed at the nose cone of the thruster. As seen in figure 8-7, when a laser pointer is shone into the fiber cable end on the outside the vacuum chamber, the collimating lens projects the light beam on the nose cone of the thruster as a $\sim 1cm$ diameter red dot, indicating the cylindrical region of radiation collection for the spectral measurements. For the measurement results presented in this section, the 1800 g/mm grating blazed at 500nm was used. The spectral resolution in the

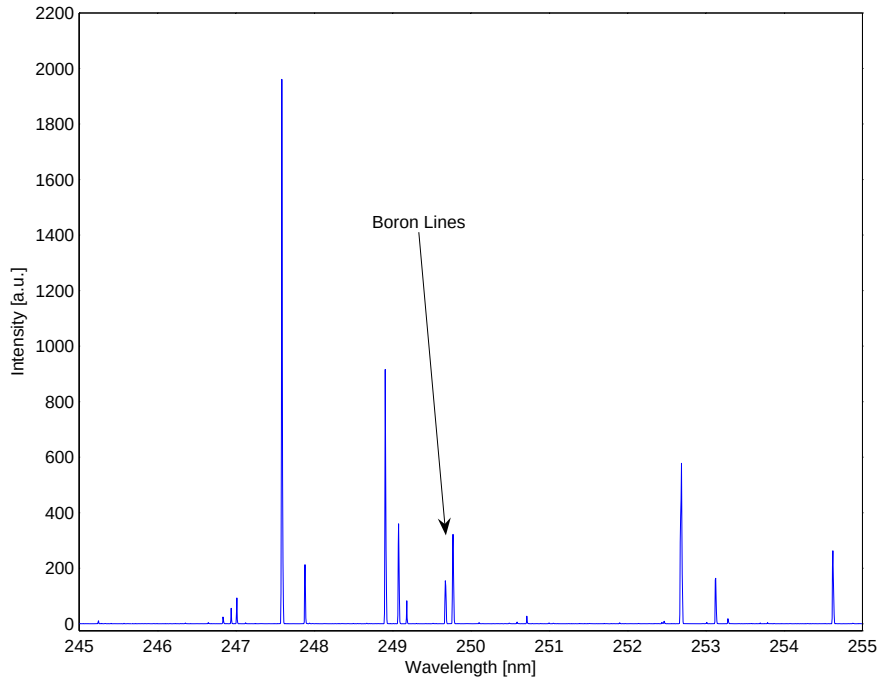

Figure 8-8: BHT-200 Hall thruster measured spectrum of 245-255nm wavelength region

region of observation was $\sim$ 0.012nm. For all the measurements presented in this section, an exposure time of 250s were used.

In order to detect the line emission due to the erosion products, a spectral range where significant Boron emission lines exists was chosen. The wavelength range between 245-255nm has strong Boron neutral emission lines at 249.677nm and 249.773nm as discussed in earlier sections. Thus this wavelength region was chosen for the spectral measurements. Figure 8-8 shows the measured spectrum in 245-255nm region for nominal operating conditions of the thruster. The two Boron neutral emission lines are identified.

Figure 8-9 shows the spectrum of the 247-250nm region where all the detected lines are identified. As seen in this figure, the region has lines only due to Xenon single ions and Boron neutrals. The Boron line at 249.677nm has a spontaneous emission transition coefficient of $1.2 \times 10^8\ s^{-1}$ and the line at 249.773nm has a spontaneous emission transition coefficient of $2.4 \times 10^8\ s^{-1}$ [3]. The observed line ratio for these two transitions from the $3s^2\ S_{1/2}$ energy level at 4.964eV shows the validity of equation 8.1. Thus, if the local electron temperature and density are known, and if the absolute emission intensity can be determined, the integrated area under these two lines can be used to obtain the local Boron neutral density.

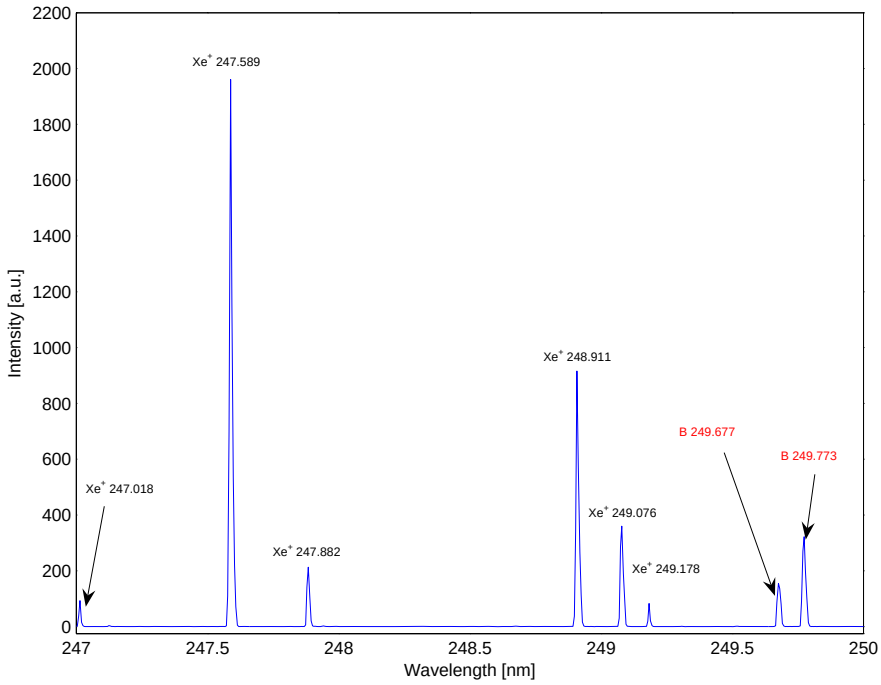

Figure 8-9: BHT-200 Hall thruster measured spectrum of 247-250nm wavelength region

Such measurements and analysis are reserved for future work.

8.4.1 Voltage Scan

In order to observe the variation in the emission intensity of the Boron lines, the thruster discharge voltage was varied from 175V to 300V with 25V increments and the emission spectra in the 245-255nm wavelength region were measured. Figure 8-10 shows the measured Boron 249.677nm and 249.773nm line emission as the discharge voltage is varied. As seen from the figure, the line emission intensities increase as the voltage is increased.

Figure 8-11 shows the variation in the integrated emission intensity for the two Boron lines for varying discharge voltage. As the discharge current does not show significant variation for the scanned voltage range, the variation of the integrated emission intensity of the Boron lines as a function of thruster power show a similar trend, as presented in figure 8-12.

From figures 8-11 and 8-12, it is observed that as the discharge voltage (and the thruster power) is increased the Boron emission intensity increases. The increase is more significant

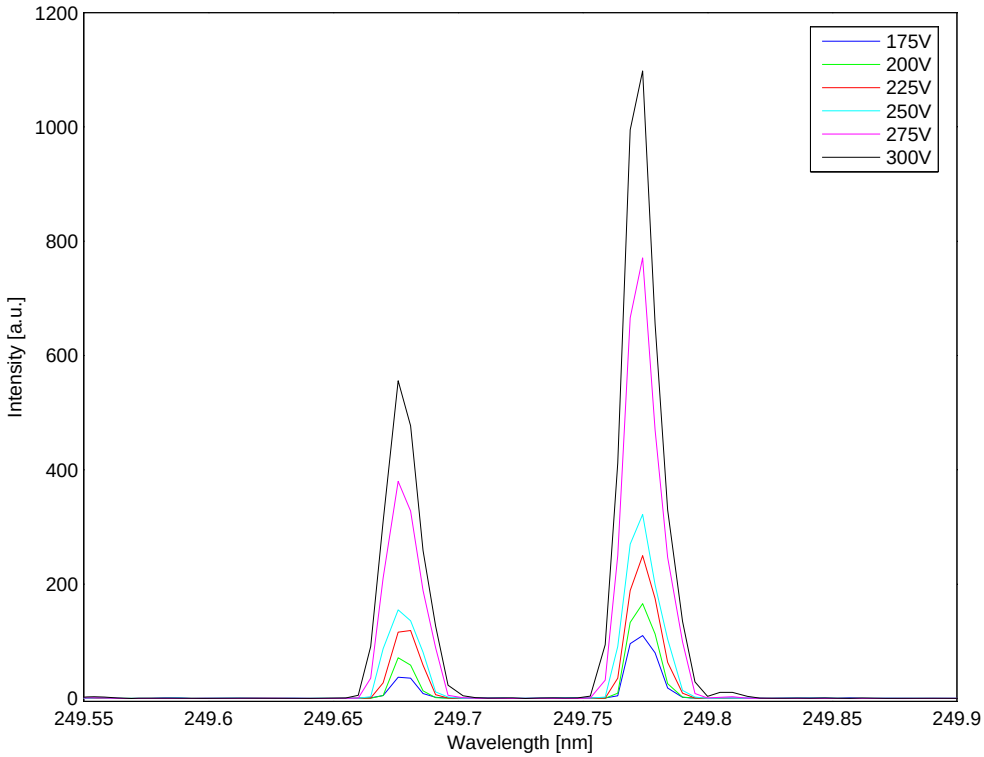

Figure 8-10: Boron 249.677nm and 249.773nm line emission as the discharge voltage is varied

for higher discharge voltages. Thus, assuming the emission intensity is linearly proportional to the Boron density, the observation indicates that the erosion rate increases for increasing discharge voltage (and power).

Figure 8-13 shows the comparison of the integrated emission intensities of the Xenon single ion line at 248.911nm and the two neutral Boron lines for varying discharge voltages. As seen from the figure, unlike what has been observed for the discharge region ion emission intensity, for the measured region the Xenon single ion emission intensity varies. In section 3.3.2, it was presented that for the discharge region, the ion emission intensity remained roughly constant for varying discharge voltage. The comparison in figure 8-13 shows that the Boron emission intensity increases monotonically as the voltage is increased, however the Xenon single ion intensity variation is much smaller and non-monotonic.

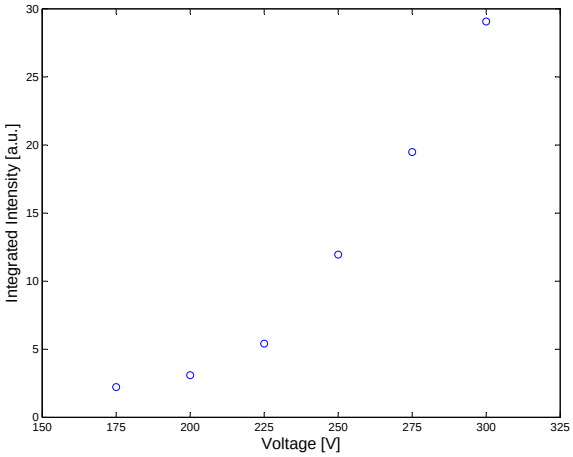

Figure 8-11: Boron 249.677nm and 249.773nm emission lines total integrated intensity for varying discharge voltage

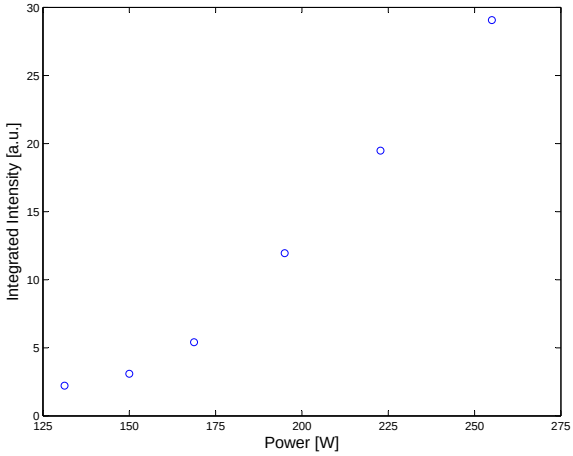

Figure 8-12: Boron 249.677nm and 249.773nm emission lines total integrated intensity for varying thruster power

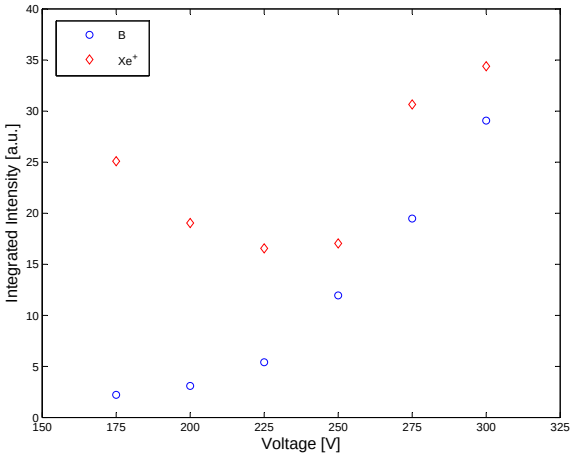

Figure 8-13: Comparison of neutral Boron and singly charged ion emission lines total integrated intensities for varying discharge voltage

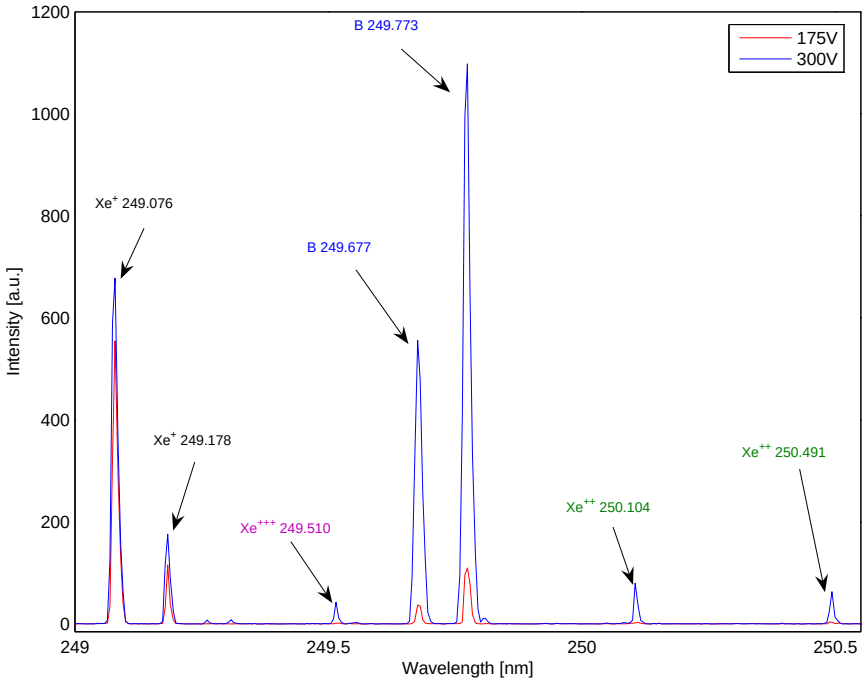

Figure 8-14: BHT-200 Hall thruster measured spectra comparison for the 175V and 300V discharge voltages in the 249.0-250.55nm wavelength region

Xe^{++} and Xe^{+++} Emission Lines

BHT-200 Hall thruster emission spectral measurements conducted in the visible and near-infrared regions of the electromagnetic spectrum were discussed in chapter 3. In those measurements, no lines due to highly charged Xenon ions were measured. In the high resolution, high exposure time, UV spectral measurements conducted for determining the ceramic erosion rate, we were able to detect emission from the Xe^{++} and Xe^{+++} species.

Figure 8-14 shows the comparison of the emission spectra for the 175V and 300V discharge voltage cases in the 249.0nm to 250.55nm wavelength region. For the 300V case, the discharge current was 0.85A and for the 175V case the discharge current was 0.75V. The anode and cathode propellant flow rates were 8.0 and 1.0 sccm, respectively. The magnet current was kept at 1.0A for the two spectra. As shown in this portion of the measured spectrum, in addition to the Xenon single ion and Boron neutral lines, the emission lines due to the Xe^{++} and Xe^{+++} species are visible for the 300V discharge voltage.

As observed from figure 8-14, for the 175V discharge voltage case, the Xe^{++} and Xe^{+++}

lines are not visible. However, for the 300V case, line emission from these species are clearly observed. In addition, in comparison to the 175V case, the 300V case has dramatically higher Boron line emission intensities. As seen from the presented portion of the spectrum, for the 300V case, the Boron emission lines become the dominant lines. This indicates a dramatic increase in the Boron number density in the region of radiation collection. Thus indicating a significant increase in the wall erosion. One other observation is that the intensities of the Xe^+ emission lines do not show significant variation as the discharge voltage is varied from 175V to 300V.

8.4.2 Anode Propellant Flow Rate Scan

In order to observe the variation in the emission intensity of the Boron lines, the anode propellant flow rate was varied from 7.5sccm to 10.0sccm with 0.5sccm increments and the emission spectra in the 245-255nm wavelength region were measured. Figure 8-15 shows the variation in the integrated emission intensity for the two Boron lines for varying Xenon propellant flow rate to the anode. The cathode flow rate was kept constant at 1.0sccm. As seen from the figure, for the given thruster operational parameters, the Boron emission intensity first drops sharply as the anode flow rate is increased from 7.5sccm to 8.5sccm. The minimum emission intensity occurs at 8.5sccm. Then, as the flow rate is increased the Boron emission intensity linearly increase with the increase in the propellant flow rate.

Figure 8-16 shows the comparison of the integrated emission intensities of Xenon single ion line at 248.911nm and two neutral Boron lines for varying anode flow rates. As seen from the figure, the Boron neutral and Xenon single ion emission line intensities vary in a similar fashion as the flow rate is increased. Similar to the Boron intensity, the Xenon single ion emission intensity is minimum for an anode flow rate of 8.5sccm. However, for Xe^+ emission line both the drop in emission intensity from 7.5 to 8.5sccm and the increase in emission intensity from 8.5 to 10.0sccm flow rates are steeper. The ratio of the Xenon ion and Boron emission line intensities shown in figure 8-16 remain constant to within %5. The reduction in the ion emission intensity in the region of observation around the thruster ceramic nose cone can explain the reduction in the Boron emission lines. Since the ion

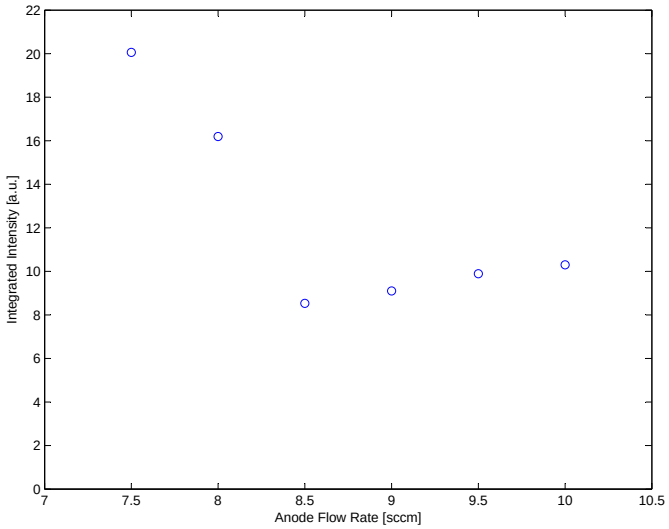

Figure 8-15: Boron 249.677nm and 249.773nm emission lines total integrated intensity for varying anode propellant flow rate

emission intensity is proportional to the ion density in the nose cone region, a reduction in ion emission implies a reduction in ion density in the nose cone region, thus a reduction in the number of ions causing the sputtering of Boron-Nitride ceramic material, thus a reduction in the Boron emission intensity. However, the ion emission intensity also depends on the local electron temperature, thus the effects of the anode propellant flow rate on the plasma electron temperature need to be better understood.

8.5 Chapter Summary

The BHT-200 Hall thruster has insulator annular walls made of Boron-Nitride (BN) ceramic material. The erosion of the walls is a major life limiting factor for Hall effect thruster. In order to asses the effect of the BHT-200 Hall thruster operational parameters on the ceramic wall erosion rate, spectral measurements of the neutral Boron atom emission lines at 249.677nm and 249.773nm are conducted. The measured spectra in the 245-255nm wavelength region are presented.

The thruster discharge voltage was varied and the emission intensity of the Boron lines were recorded. The trends showed that as the discharge voltage was increased, the Boron emission line intensity increased. Especially for higher voltages than the nominal operational voltage

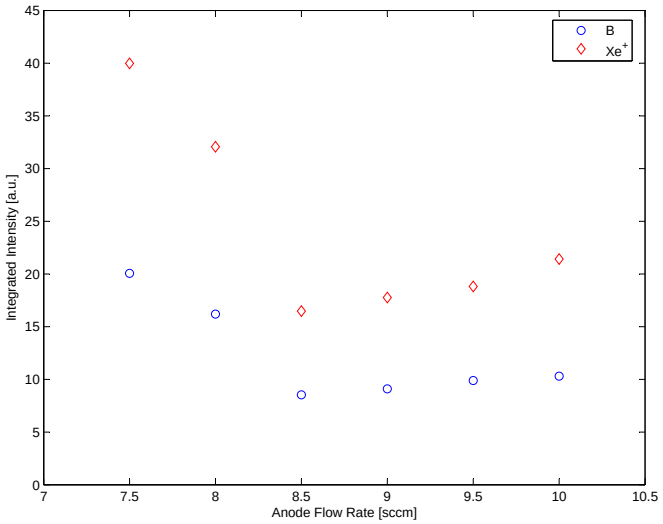

Figure 8-16: Comparison of neutral Boron and singly charged Xenon ion emission lines total integrated intensities for varying anode propellant flowrate

of 250V, the erosion rate seems to increase dramatically. This could be due to the increase in the energies of the ions hitting the wall as a result of the increased potential drop between the anode and the cathode. The effect of increased wall temperature is another factor for high voltage operational regime. Consequently, the erosion of the wall ceramic material increases for increased thruster power.

In addition, the thruster anode propellant flow rate was varied and the emission spectrum of the 245-255nm wavelength region was measured. The results show that the Boron emission intensity is lowest for an anode flow rate of 8.5sccm. For lower flow rates the Boron emission intensity increased sharply. For higher flow rates, the Boron emission intensity slightly increased with a linear rate. In the region of observation around the thruster nose cone, the Xenon single ion emission intensity showed similar behavior to the Boron emission intensity for the flow rate variation. The Boron line behavior is therefore clearly driven by that of the Xe^{+} population, but the non-monotonic variation of the later has not been explained. But the fact that, for this thruster, the magnetic field geometry is optimized for 8.5sccm anode flow rate seems to be the most likely explanation.

The high resolution, very long exposure time nature of these measurements allowed the detection of the radiation emission from Xe^{++} and Xe^{+++} species for high discharge voltage cases. In a spectral graph covering the 249.0nm to 250.55nm wavelength region, emission

lines due to Boron, Xe^{+}, Xe^{++} and Xe^{+++} species were presented.

Chapter 9

Conclusions and Recommendations

The purpose of this thesis is to conduct non-intrusive diagnostics of electric thruster plasmas through emission spectroscopy and to provide computational means to analyze data obtained by the spectral measurements. The thesis work increased the understanding of the radiation emission from electric thruster plasmas.

Electric propulsion thruster diagnostics is commonly done through intrusive plasma probes that disturb the plasma and the thruster operation. Emission spectroscopy provides an alternative means of diagnostics as it is a non-invasive, fast and economical diagnostic method of plasmas. Emission spectroscopy allows access to hard to reach locations, and provides unique capabilities such as remote diagnostics of the plasma parameters.

9.1 Summary and Contributions

This thesis had experimental, theoretical and computational components. On the experimental side, radiation emission of three different electric propulsion thrusters and plasma sources were measured in the visible and near-infrared regions of the electromagnetic spectrum. In addition ultraviolet spectral measurements were conducted on the BHT-200 Hall thruster. On the theoretical side collisional-radiative models were developed for Argon and

Xenon plasmas with neutral, single charged ion and electron species. On the computational side, numerical codes were created for the Argon and Xenon C-R models and simulations were performed.

9.1.1 Experimental Study

In order to conduct visible and near-infrared measurements, a versatile and portable spectral measurement setup was designed and constructed. For this setup, a portable optical shelf that can be attached to any standard 8 inch vacuum window port was built. Use of optical lenses and fiber cables allowed the collection of radiation emission signal of the plasma regions of interest from outside the vacuum chamber.

Radiation emission of a commercial Hall thruster, BHT-200, was studied. For the study, spectral measurements of the radiation emission from 10 different regions around the thruster were conducted. The measured regional spectra were compared. It was observed that cathode region has emission only due to the Xenon neutral gas. The comparison of the discharge and the plume region spectra indicated a significantly higher relative ion emission intensity in the discharge region. Additionally, spectral measurements of the thruster discharge region were conducted for varying discharge potential. The spectral measurements showed that for increasing discharge voltage, the neutral Xenon emission intensity falls, whereas the ionic emission intensity remains fairly constant.

Spectral measurements of a TAL type laboratory Hall thruster, MHT-9, were conducted during the thruster's preliminary testing. The effects of the discharge voltage and anode propellant flow rate on the emission spectrum were studied. It was observed that for the the MHT-9 Hall thruster, 200V discharge voltage has the highest ionic emission intensity. The anode propellant flow rate scan showed that as the flow rate is increased, the ionic emission intensity increased faster than the neutral emission intensity. The measured MHT-9 spectrum was compared with the spectrum of a similar power level SPT type Hall thruster, BHT-200. The spectral comparison showed that the MHT-9 Hall thruster has higher relative ionic emission intensity, indicating a higher electron temperature for this thruster in

comparison to the BHT-200 Hall thruster.

Spectral measurements of an experimental Helicon plasma source were conducted for Argon gas. Trends in the plasma ionization fraction for various operational parameters were obtained. Measurements of the Helicon plasma emission spectrum showed that as the input RF power was increased, the ionization fraction increased linearly. For the Helicon plasma generation, there is an optimum axial magnetic field intensity that provides the highest ion line emission intensity, thus the highest propellant ionization fraction. It was also observed that for a given input RF power, and a given magnetic field intensity, there is an optimum gas flow rate for which the ionization rate is maximum.

Since the vacuum chamber window material does not transmit in the ultraviolet portion of the electromagnetic spectrum, a UV spectral measurement setups was designed and constructed. For this setup, a four channel fiber feedthrough was attached to a standard vacuum port with an NPT connector. UV rated lenses were used to collect the radiation emission from inside the vacuum chamber and UV rated fiber cables were used to bring the signal to the entrance slit of a spectrometer located outside the vacuum chamber. Such a setup also allowed a better spatial resolution. A 750mm focal length spectrometer was purchased and it was equipped with UV rated CCD and PMT detectors. Thus a high spectral and spatial resolution spectoscopy setup was built.

In order to asses the effect of the operational parameters on the BHT-200 Hall thruster ceramic wall erosion rate, spectral measurements of the Boron atom emission lines at 249.677nm and 249.773nm were conducted. It was determined that the thruster wall ceramic material erosion increases with increased discharge voltage. In addition, it was observed that BHT-200 Hall thruster has an optimum anode propellant rate for the minimum wall erosion rate for a given magnetic field geometry. The measurements demonstrated that optical emission spectroscopy is a powerful tool in diagnosing thruster erosion rate.

9.1.2 Theoretical and Computational Study

Collisional-radiative models have been developed for Argon and Xenon plasmas. Major ultraviolet, visible and near-infrared emission lines were identified. Collisional excitation cross-section data and a comprehensive set of spontaneous emission coefficients data were collected for both species.

Two numerical codes were written for the collisional-radiative models of Argon and Xenon gas discharges simulating neutral, single charged ion and electron species. Using the numerical codes, steady state energy level population densities of the simulated plasma species were determined. Predicted emission spectrum was obtained. The experimental spectral measurement results were analyzed with the computational codes. The simulated spectra showed good match with the experimental measurements.

9.2 Recommended Future Work

9.2.1 Experimental Measurements

The experimental setup designed for the spectral measurements both from the inside and the outside the vacuum tank can be used in further spectroscopic studies. As described in Chapters 3, 4, 5 and 8, the light collection from the thruster plasma is done either by an optical shelf located on the outside of the vacuum chamber, or through the use of fibers that brought the signal from inside to outside. The optical setups used in this study were designed to be modular and mobile. Thus, conducting further studies on electric propulsion plasma sources operating in the SPL or other vacuum tank facilities can be done relatively easily. The optical shelf can be attached to any standard 8 inch vacuum port. Similarly, the vacuum fiber feed through can be used in any vacuum tank with standard ports.

Improvement of the spatial resolution of the spectral measurements would be the first step in further experimental studies. Use of a collimating lens attached to a motorized translation stage inside the vacuum tank will allow accurate measurements of specific locations. Such

a setup will allow collection of data that can be Abel inverted to obtain spatial information for cylindrically symmetric radiation sources such electric thruster plume plasmas.

In chapter 8, it was demonstrated that optical emission spectroscopy provides valuable, real time information about the thruster wall erosion through detection of the radiation emission due to the erosion products. Simultaneous electrostatic probe and spectral measurements, however, will allow the necessary information to determine the erosion rate.

Since the constructed spectral measurement setup, with the 750mm focal length spectrometer with 3600 g/mm holographic grating and small pixel size CCD detector, provide very high spectral resolution ($\sim 0.007nm$), Doppler shift flow velocity measurements can be conducted. In addition, a Fabry-Perot interferometer can be used for the analysis of line broadening.

9.2.2 Theoretical and Computational Work

Understanding the radiative processes in electric thruster plasmas requires understanding thousands of radiative and collisional processes. Most electric propulsion systems use high atomic mass nobel gasses such as Xenon or Argon. These atoms and their ions have very complicated electronic energy structures. Thus, there are hundreds of energy levels with a correspondingly large number of possible electronic transitions, resulting in hundreds of emission lines. There are limited experimental data on the collisional excitation and ionization processes. Additionally, the radiative transition coefficients have to be measured or calculated.

Since electronic transitions for species such as Xenon and Argon are important to the broad electric propulsion community, a database for collision cross sections, and spontaneous emission, absorption and stimulated emission transition coefficients has to be compiled and maintained. Only after a comprehensive database is compiled and the uncertainties in the data are understood, an accurate and complete modeling of the collisional-radiative processes can be attempted.

The C-R model developed for this thesis is designed in such a way that additional processes, such as electron three-body or radiative recombination transitions, or heavy particle collisional excitation transitions can be easily implemented. Additionally, the major assumptions in the model can be easily modified for improvement. For example, the electron energy distribution function can be changed to any other normalized energy distribution function, the optically thin plasma assumption can be changed to allow absorption processes by introducing a wavelength and density dependent absorbtion coefficient. Furthermore, since all the data are stored in matrices, allowing the user to modify the content to a more up-to-date collision cross section or transition coefficient values, the model can be improved as new and more accurate data become available.

Implementation of the C-R Model in a Kinetic Code for Plasmas

One of the most important assumptions of the C-R model is that, it models the radiation emission from a uniform plasma of known density and temperature. Implementing the C-R model into a complicated kinetic code for plasmas and using local electron and neutral density values and the local electron temperature will improve the accuracy of the simulated spectrum obtained by the C-R model.

Particle-in-Cell (PIC) computational codes have been extensively used to simulate electric thruster plasmas. In PIC simulations, plasma particles are simulated as collections of macro-particles where each simulated macro-particle represent a large number of real particles. The computational domain is divided into small computational elements. The model determines the local plasma parameters, such as the density and plasma temperature, and calculates the forces acting on the simulated macro-particles, and moves the particles according to the forces acting on them. The model provides a quasi-steady state plasma properties after a long iteration run. For example, AQUILA is a hybrid-PIC plasma simulation code that was developed at MIT Space Propulsion Laboratory to simulate electric thruster plume plasmas [22][70]. AQUILA runs on tetrahedral volume elements. The code simulates collisions using Monte Carlo Collisions (MCC) or Direct Simulation Monte Carlo (DSMC) collision algorithms. A C-R model can be implemented as a post-processing step for such

a kinetic model. Since the PIC or hybrid-PIC plasma simulation codes would provide the time averaged particle densities and the plasma temperature values in each computational element, the C-R model can be run for every computational element (or a cluster of neighboring computational elements) and the radiation emission from the volume element can be calculated. A simulated collection optics located on a window port of the vacuum tank can be used to simulate the collection optics. Such a virtual collection optics model has already been developed earlier for AQUILA plume simulation model [21][20]. Thus, after the determination of the steady state plasma properties (neutral and ion densities and local electron temperature values), the C-R model can be used to calculate the plasma emission from every computational element and calculate the percentage of the radiation collected by the collection optics. Thus, this technique will remove the inherent assumption of the C-R model by introducing the non-uniformity to the plasma being modeled. Despite the fact that local elements are assumed to have uniform plasma, the cumulative effects will be revealed by the combination of the PIC and C-R models. Such an implementation will be the first of its kind, and will be an important tool for better analysis of the experimentally measured spectra.

Appendix A

BHT-200 Hall Thruster Measured Spectral Graphs

In this section the measured spectral graphs for the BHT-200 Hall Thruster running on Xenon propellant are presented. The spectral measurements were conducted on March 29, 2006. The discharge voltage and current were 250V and 0.81A respectively. The anode propellant rate was kept constant at 8.0 sccm whereas the cathode flow rate was at 1.0 sccm of Xenon. The tests were conducted in the MIT Space Propulsion Laboratory vacuum tank. The vacuum pressure was 3.56×10^{-5} Torr when the thruster was in operation. The thruster was placed in the central axis of the cylindrical chamber aligned with the window port. However, in order to allow viewing of the discharge region, the thruster was placed at angle of ~ 6 degrees from the axis. For the spectral graphs presented here, the optical system was pointed at Region-I as shown in figure 3-5 in chapter 3.

In all of the spectral measurements an Acton SpectraPro 500i spectrometer and Roper Scientific Cascade Photometrics Cascade:650 CCD detector were used. The CCD detector had 572×1024 pixels with a pixel size of $7.4\mu m \times 7.4\mu m$. The presented spectral graphs are not intensity calibrated.

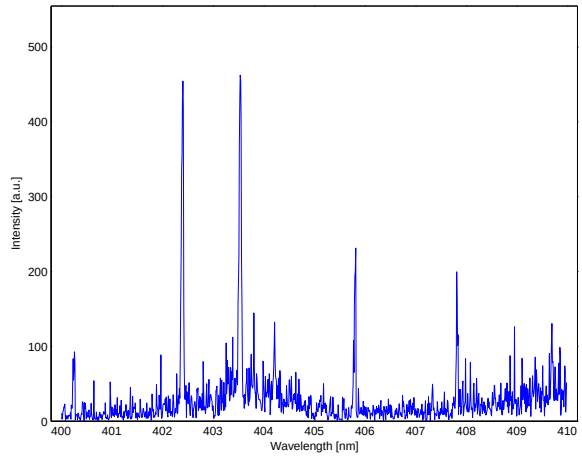

(a) Discharge 400nm

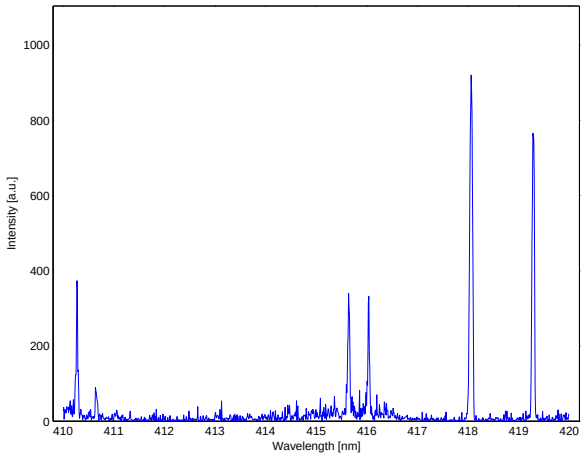

(b) Discharge 410nm

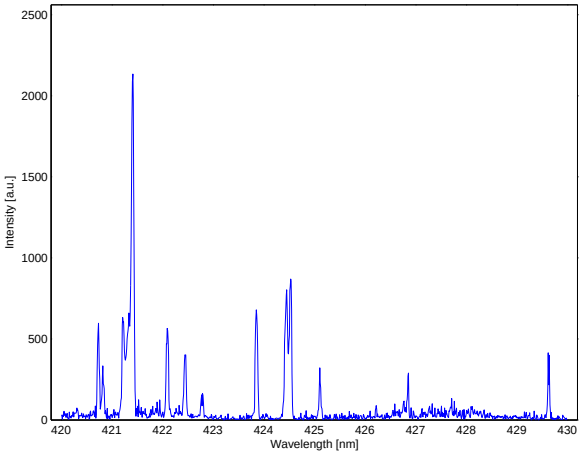

(c) Discharge 420nm

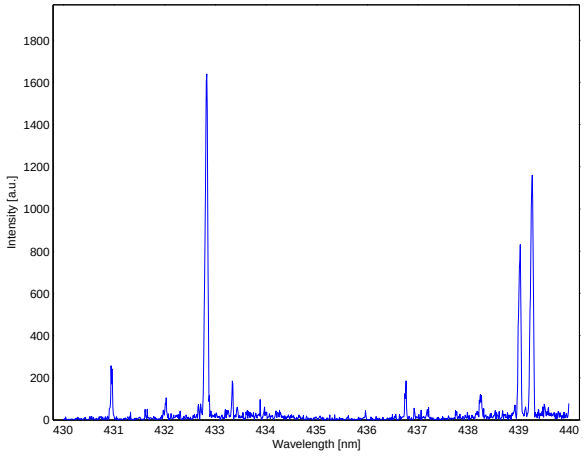

(d) Discharge 430nm

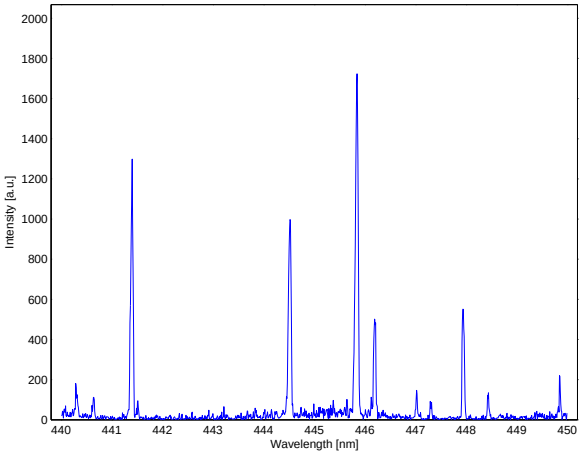

(e) Discharge 440nm

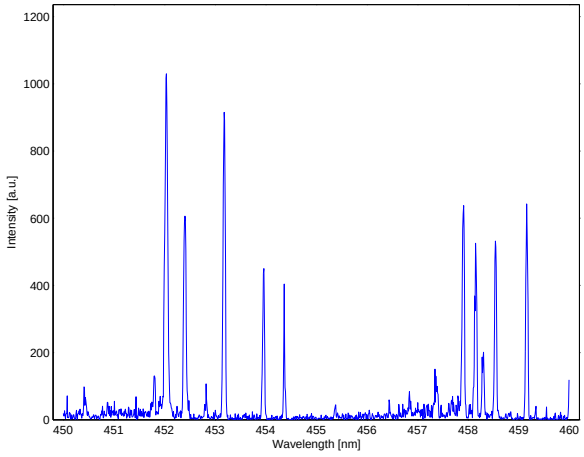

(f) Discharge 450nm

Figure A-1: BHT-200 Hall Thruster Discharge Region Emission Spectra 400-460nm

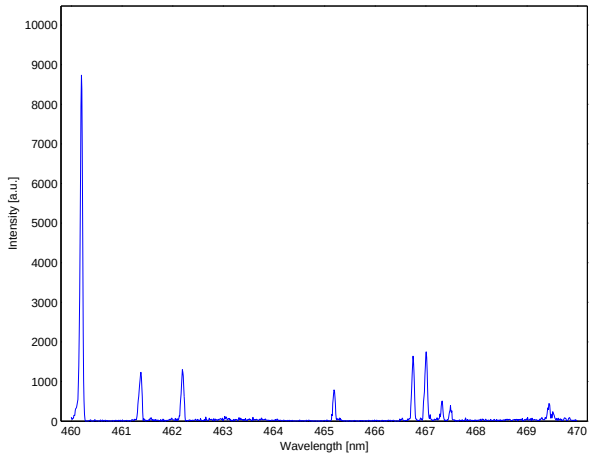

(a) Discharge 460nm

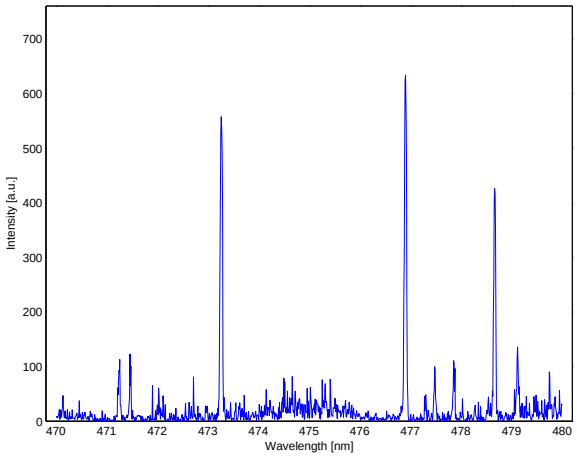

(b) Discharge 470nm

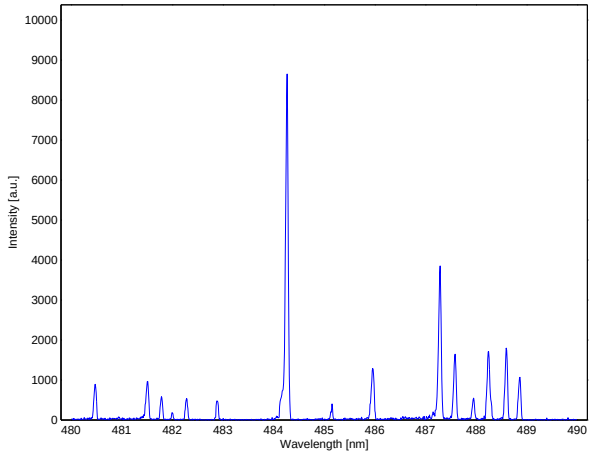

(c) Discharge 480nm

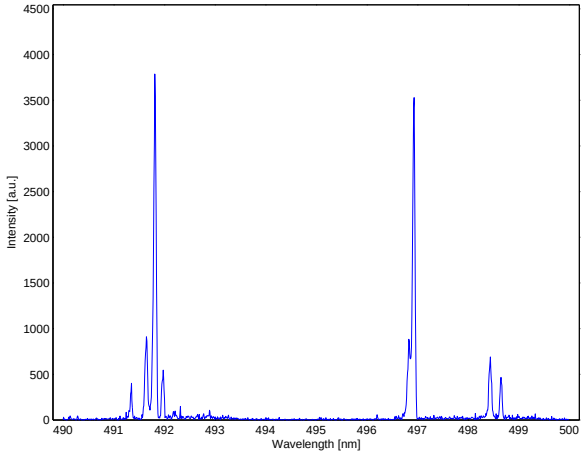

(d) Discharge 490nm

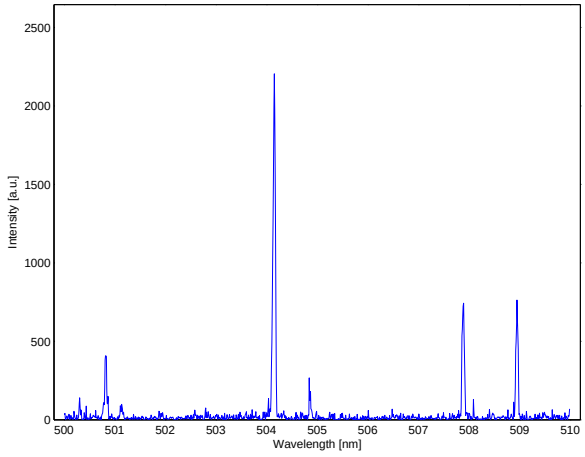

(e) Discharge 500nm

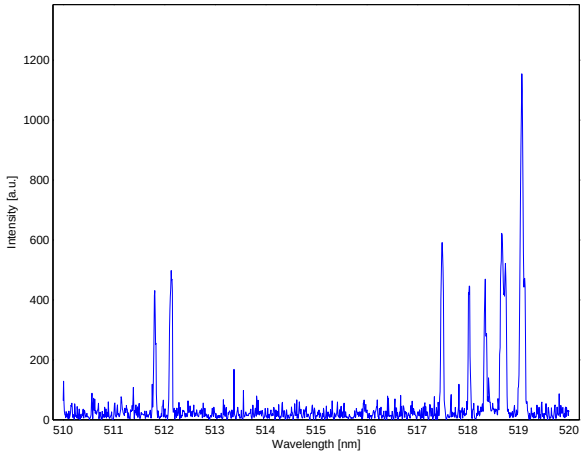

(f) Discharge 510nm

Figure A-2: BHT-200 Hall Thruster Discharge Region Emission Spectra 460-520nm

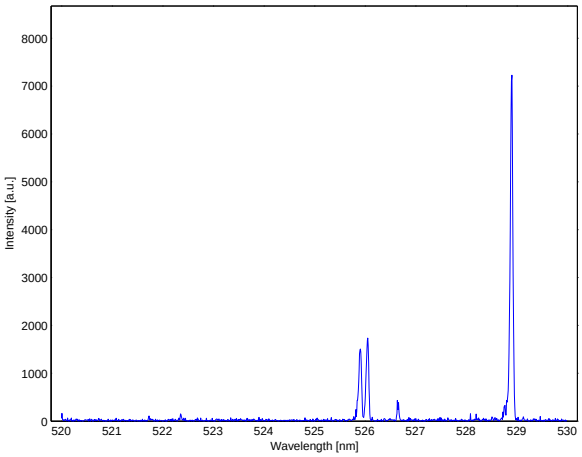

(a) Discharge 520nm

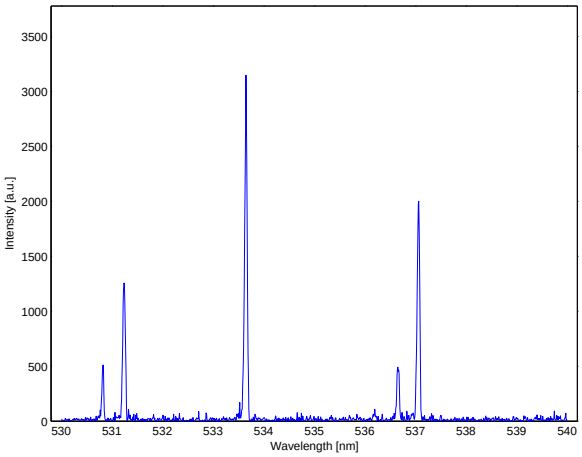

(b) Discharge 530nm

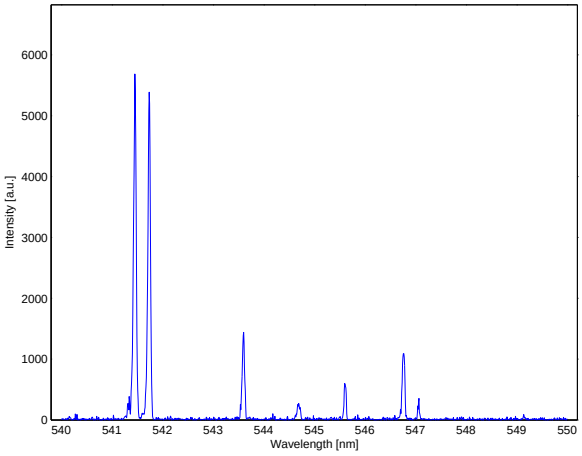

(c) Discharge 540nm

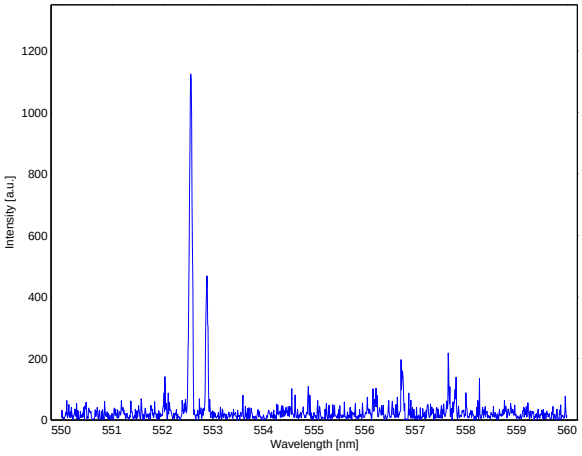

(d) Discharge 550nm

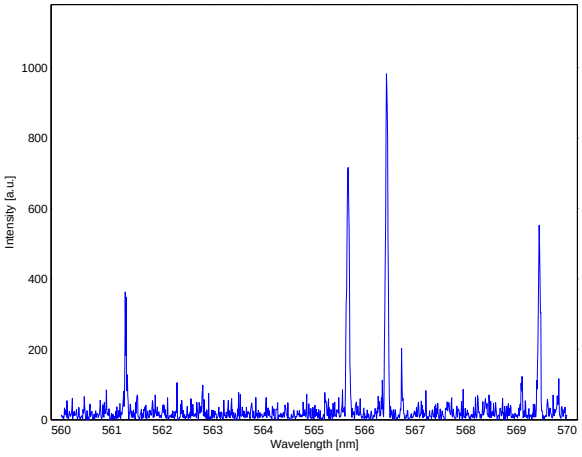

(e) Discharge 560nm

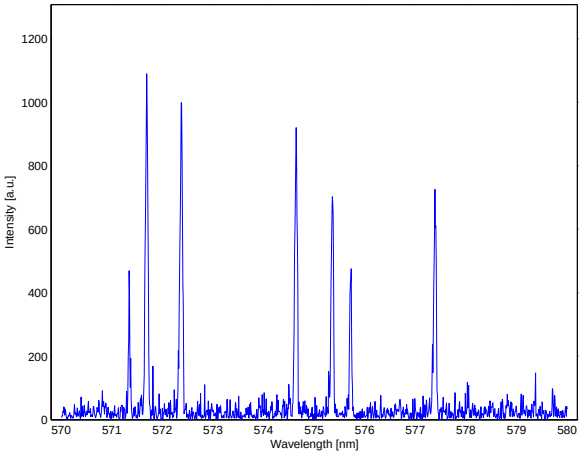

(f) Discharge 570nm

Figure A-3: BHT-200 Hall Thruster Discharge Region Emission Spectra 520-580nm

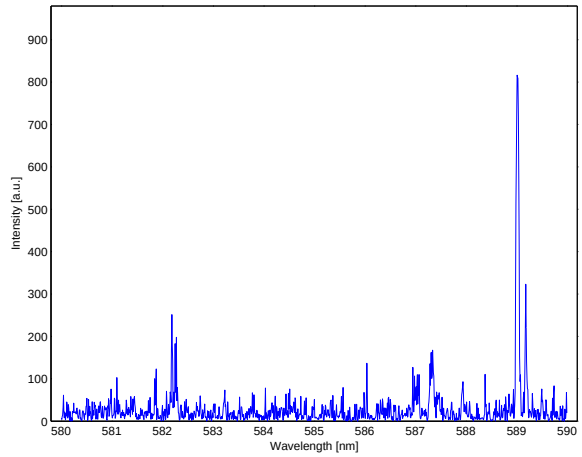

(a) Discharge 580nm

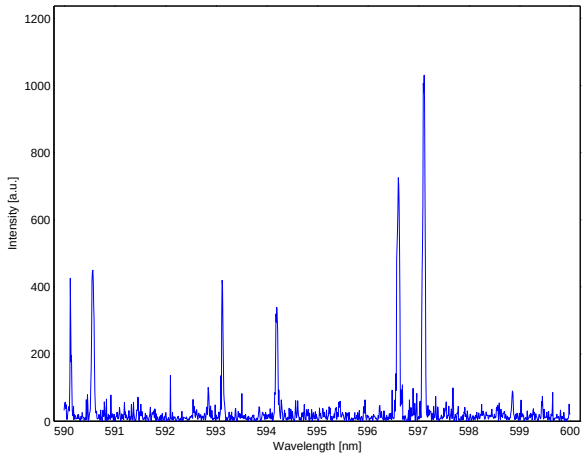

(b) Discharge 590nm

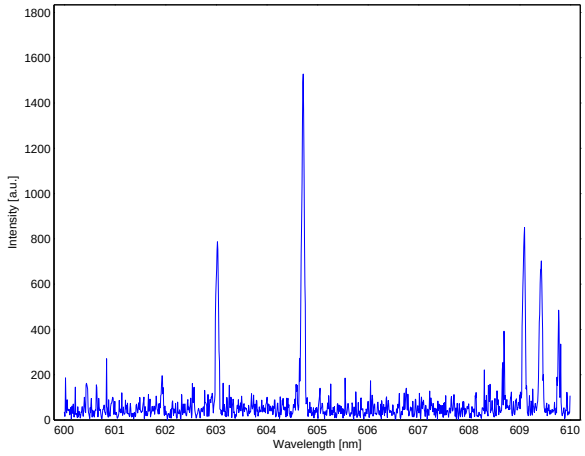

(c) Discharge 600nm

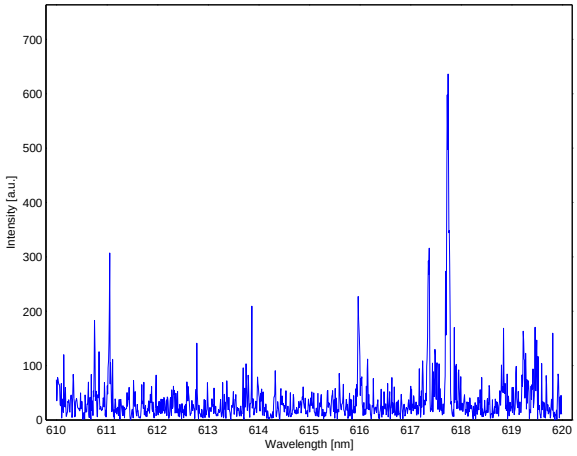

(d) Discharge 610nm

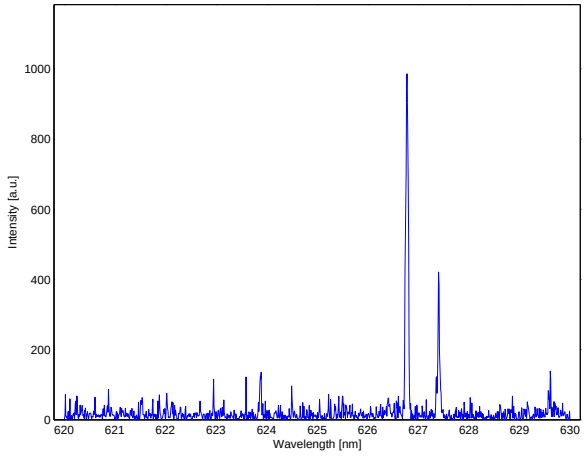

(e) Discharge 620nm

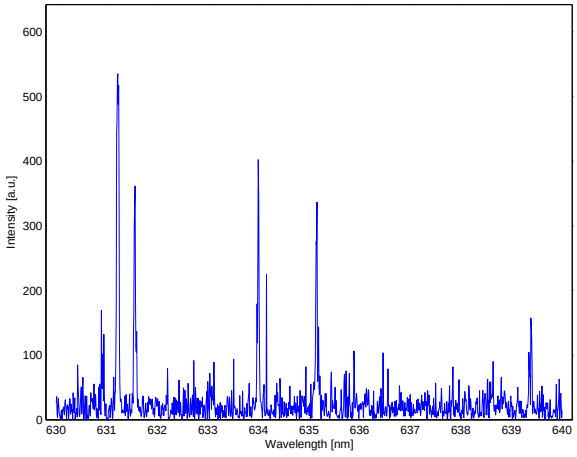

(f) Discharge 630nm

Figure A-4: BHT-200 Hall Thruster Discharge Region Emission Spectra 580-640nm

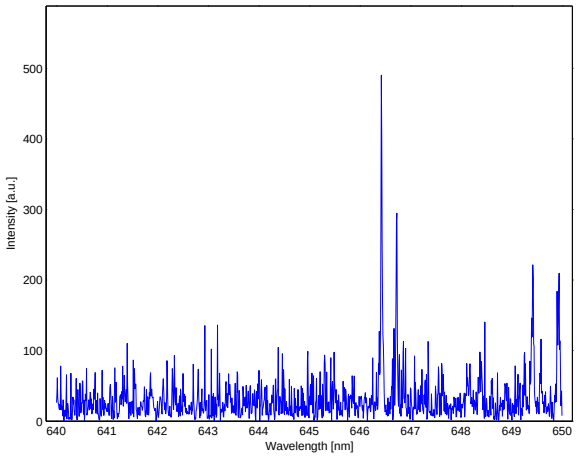

(a) Discharge 640nm

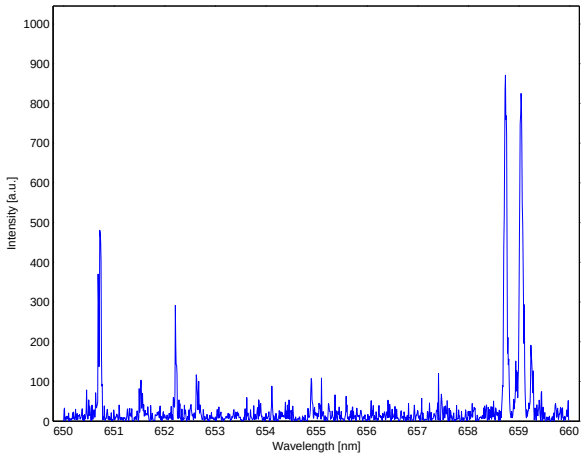

(b) Discharge 650nm

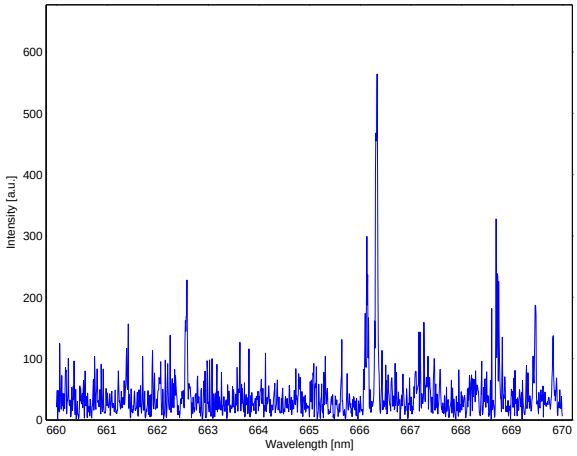

(c) Discharge 660nm

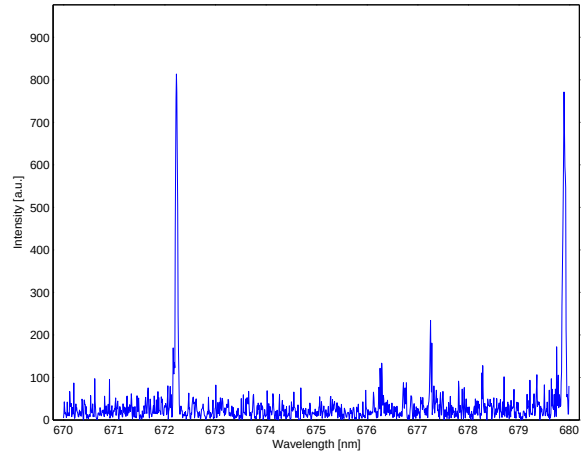

(d) Discharge 670nm

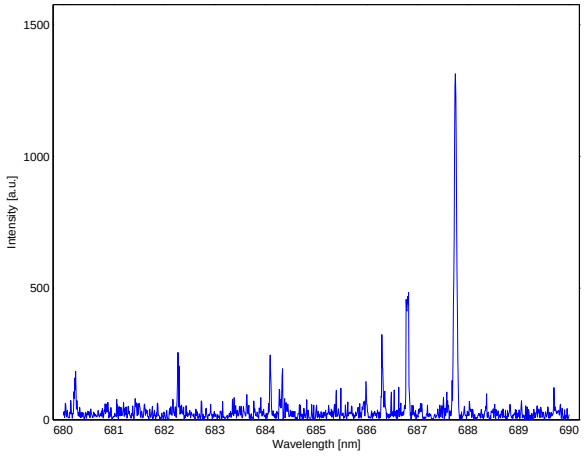

(e) Discharge 680nm

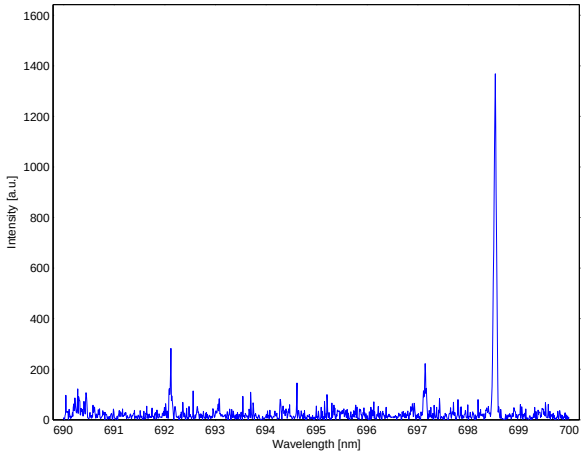

(f) Discharge 690nm

Figure A-5: BHT-200 Hall Thruster Discharge Region Emission Spectra 640-700nm

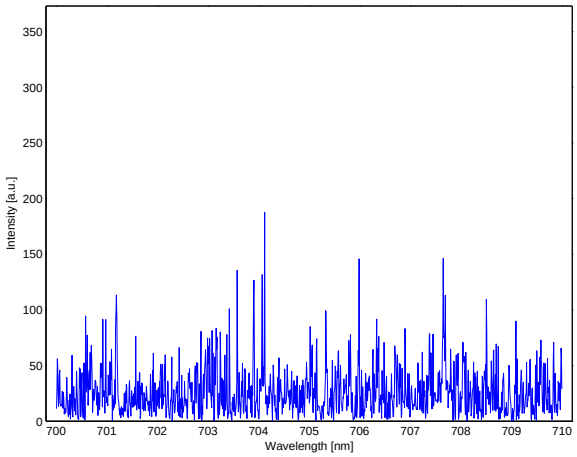

(a) Discharge 700nm

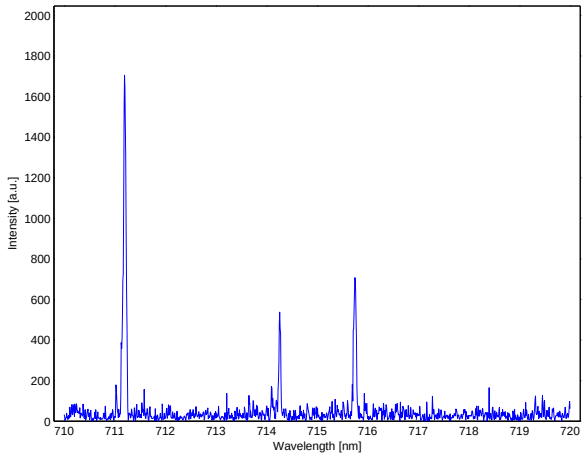

(b) Discharge 710nm

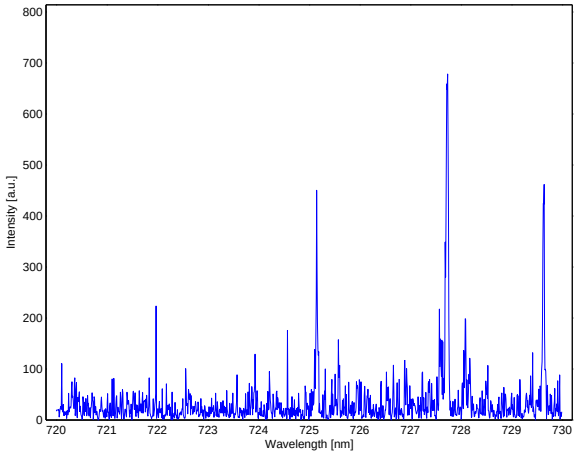

(c) Discharge 720nm

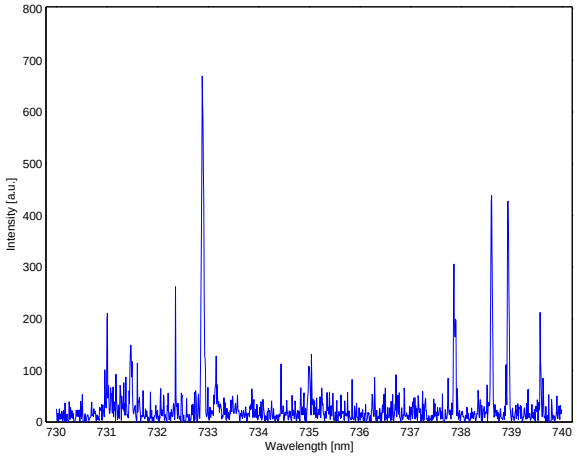

(d) Discharge 730nm

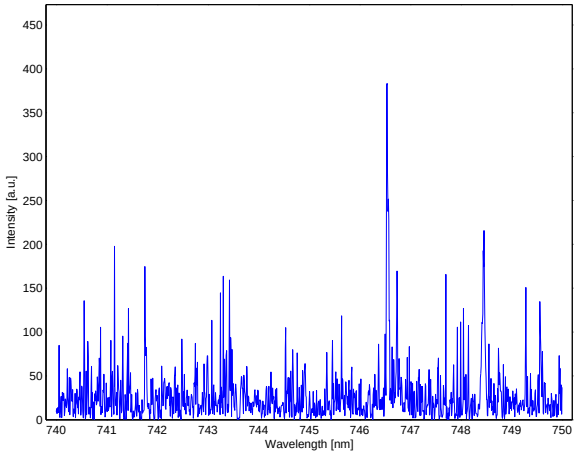

(e) Discharge 740nm

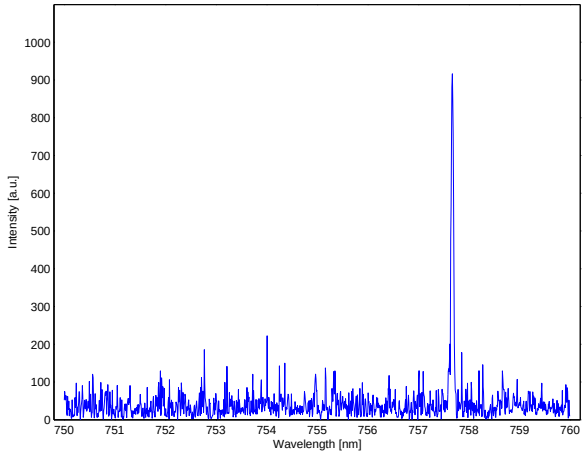

(f) Discharge 750nm

Figure A-6: BHT-200 Hall Thruster Discharge Region Emission Spectra 700-760nm

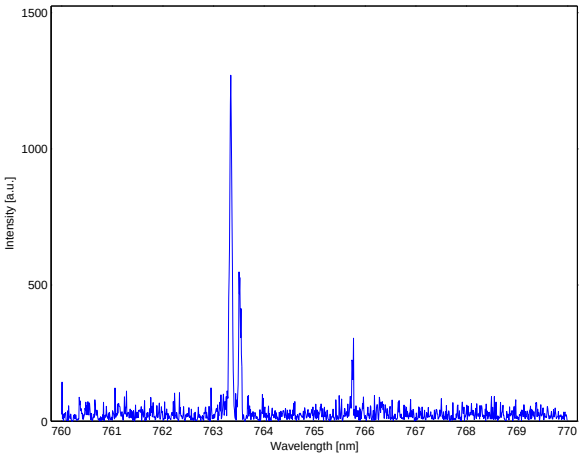

(a) Discharge 760nm

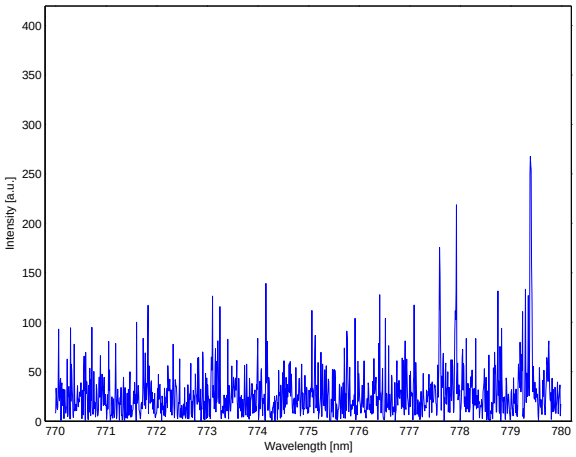

(b) Discharge 770nm

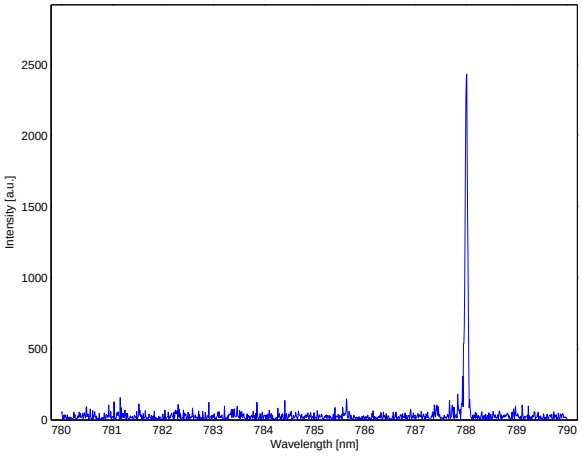

(c) Discharge 780nm

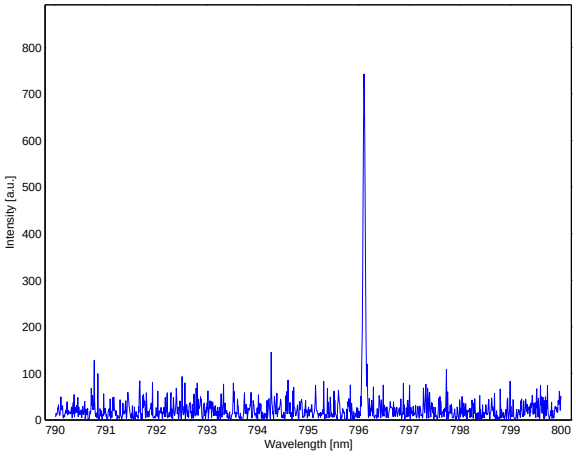

(d) Discharge 790nm

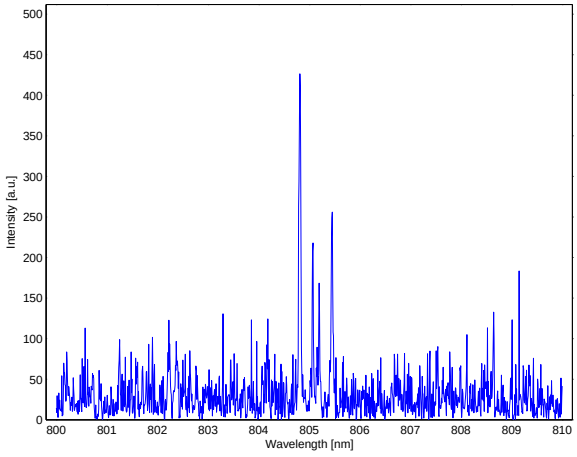

(e) Discharge 800nm

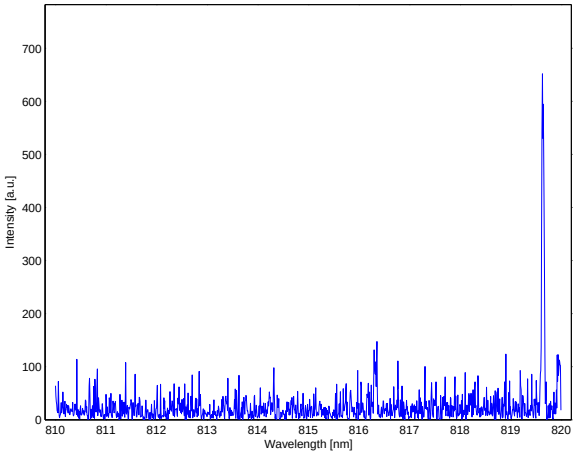

(f) Discharge 810nm

Figure A-7: BHT-200 Hall Thruster Discharge Region Emission Spectra 760-820nm

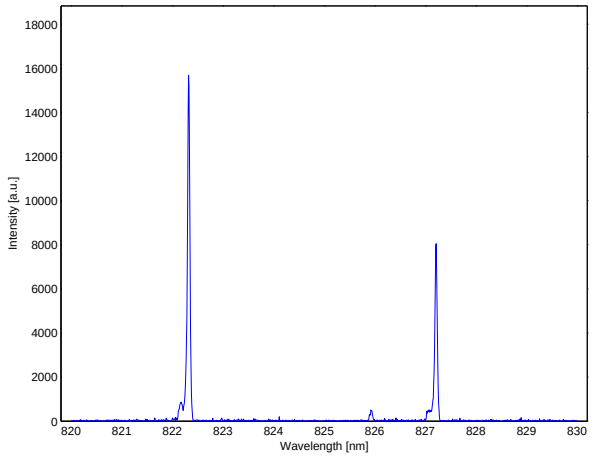

(a) Discharge 820nm

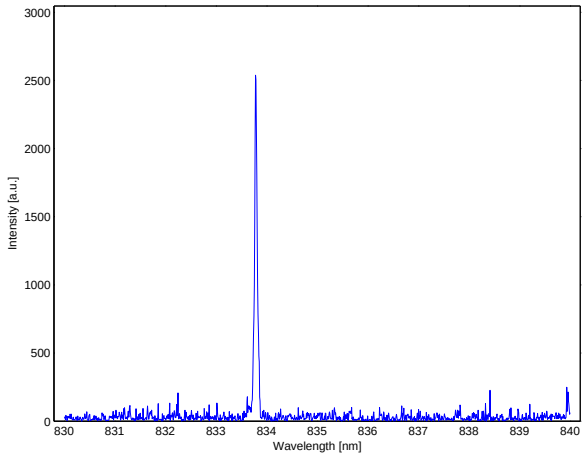

(b) Discharge 830nm

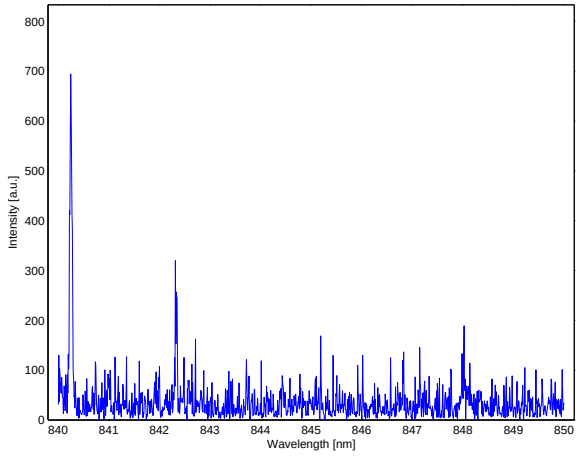

(c) Discharge 840nm

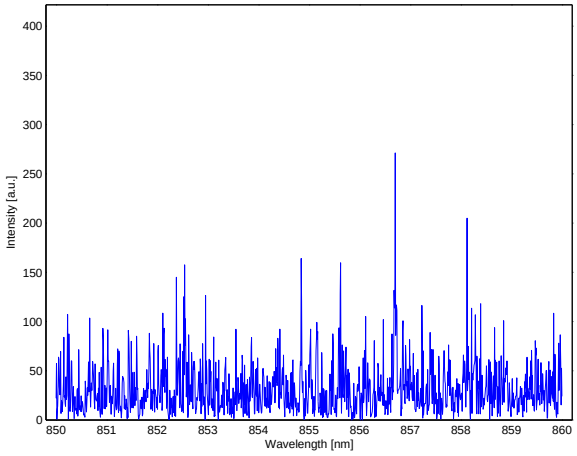

(d) Discharge 850nm

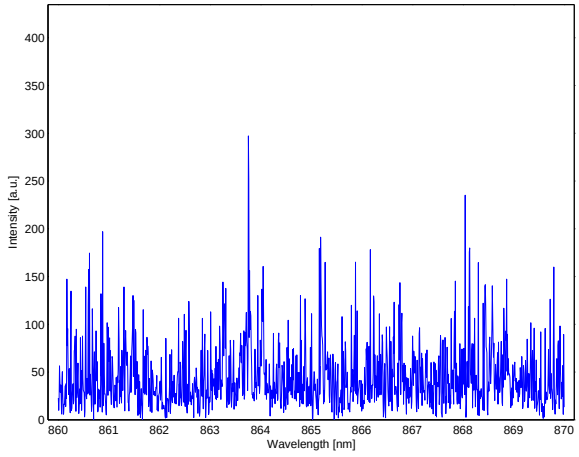

(e) Discharge 860nm

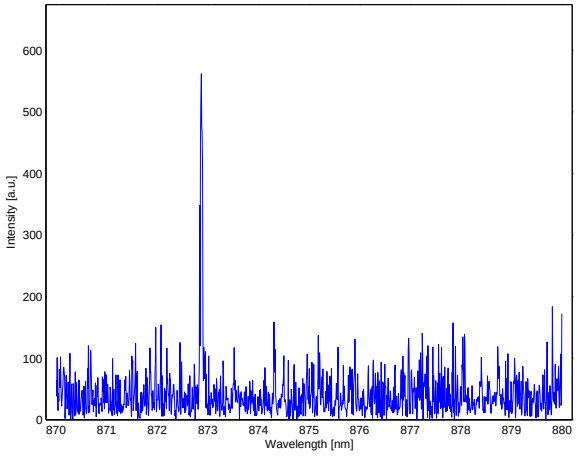

(f) Discharge 870nm

Figure A-8: BHT-200 Hall Thruster Discharge Region Emission Spectra 820-880nm

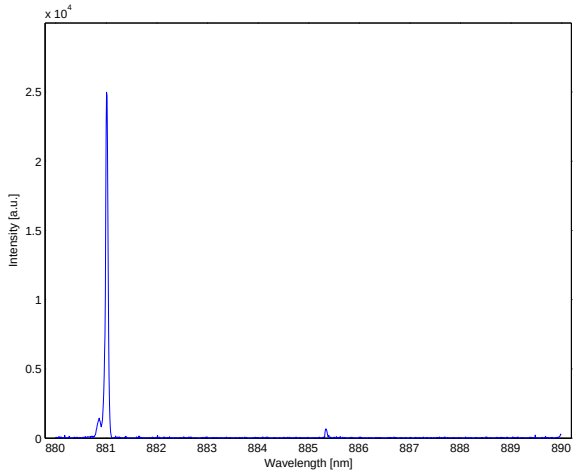

(a) Discharge 880nm

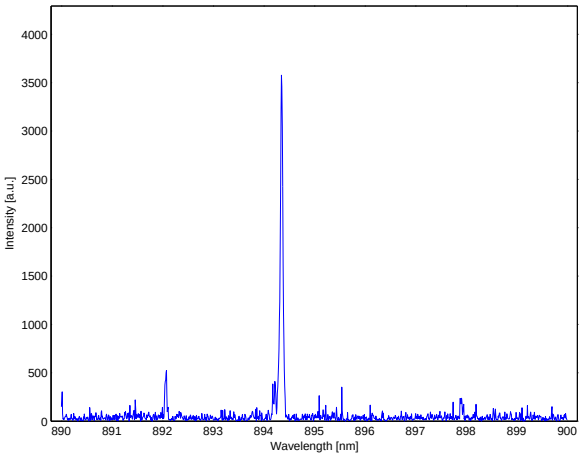

(b) Discharge 890nm

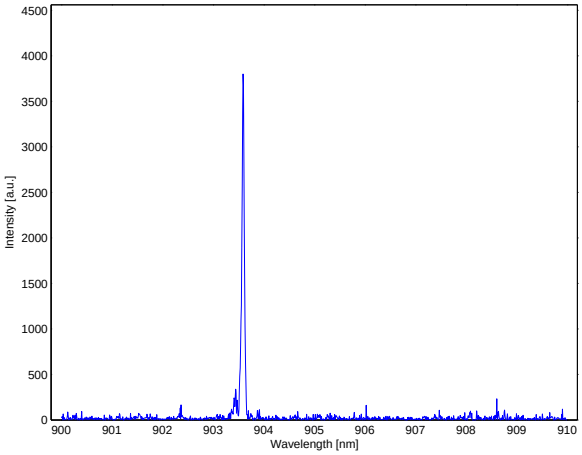

(c) Discharge 900nm

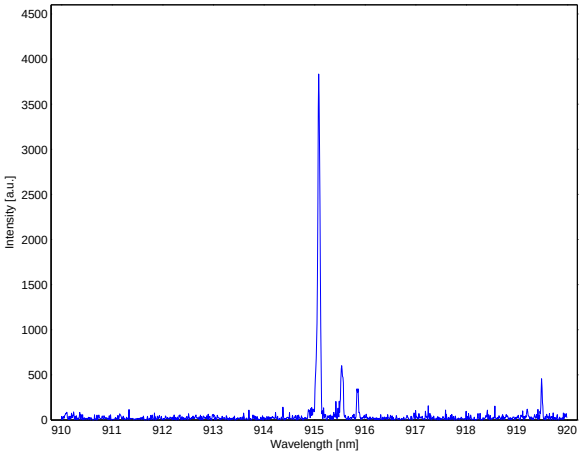

(d) Discharge 910nm

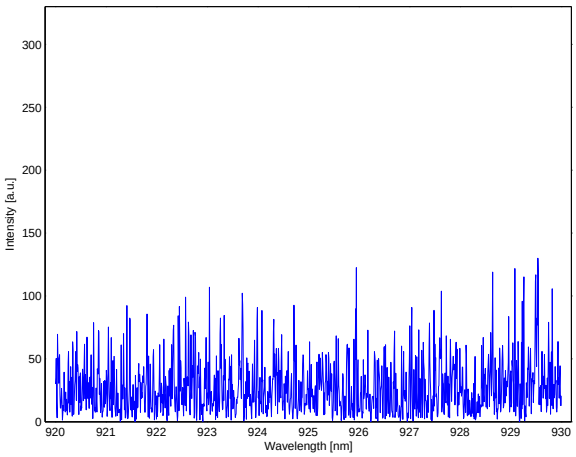

(e) Discharge 920nm

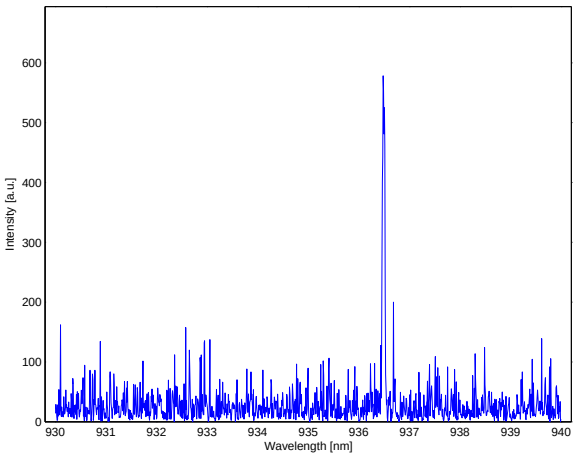

(f) Discharge 930nm

Figure A-9: BHT-200 Hall Thruster Discharge Region Emission Spectra 880-940nm

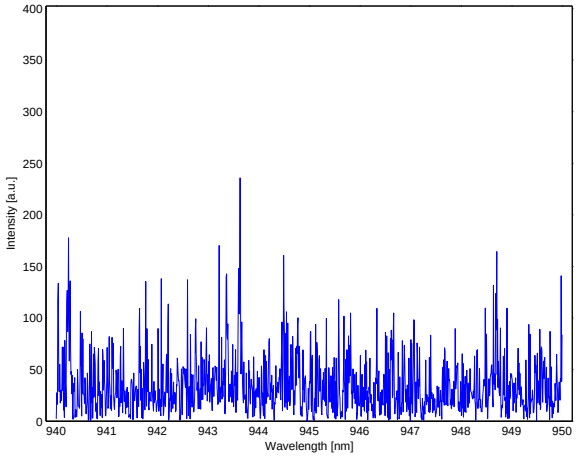

(a) Discharge 940nm

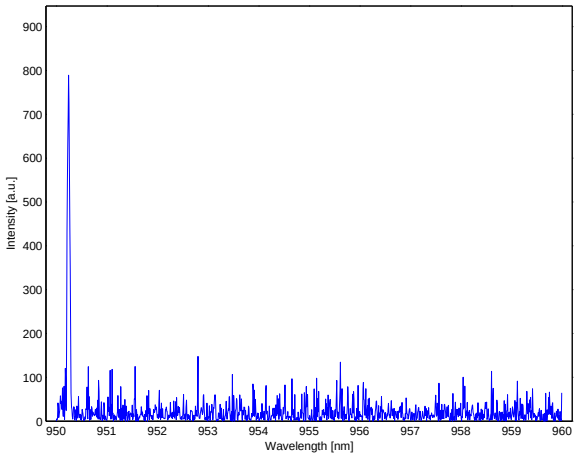

(b) Discharge 950nm

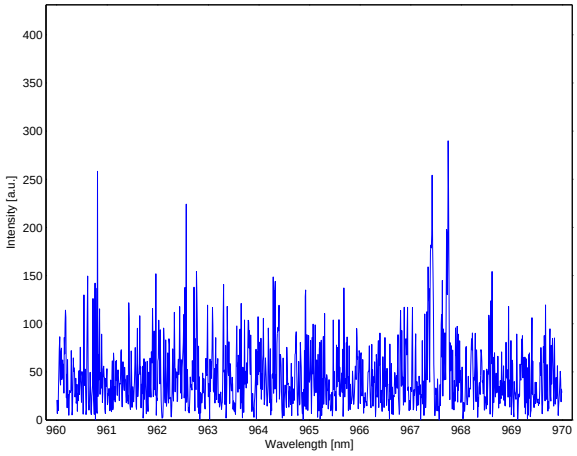

(c) Discharge 960nm

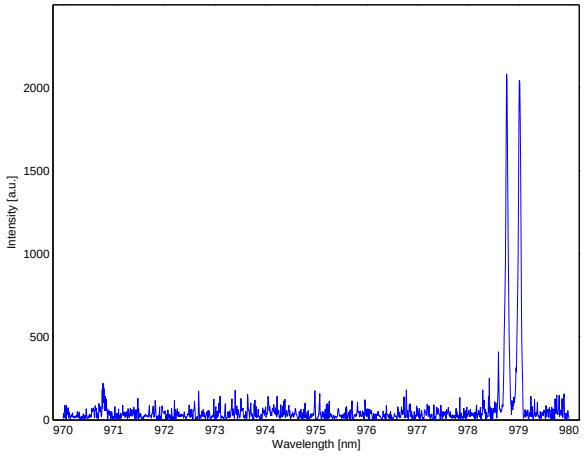

(d) Discharge 970nm

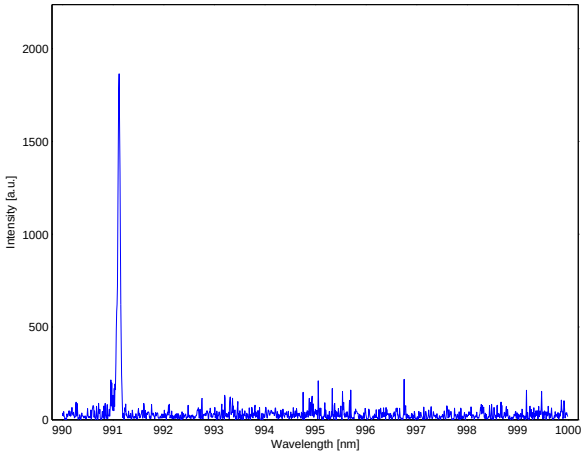

(e) Discharge 980nm

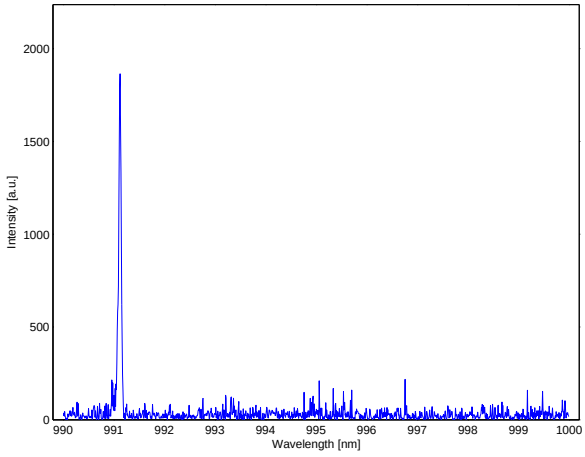

(f) Discharge 990nm

Figure A-10: BHT-200 Hall Thruster Discharge Region Emission Spectra 940-1000nm

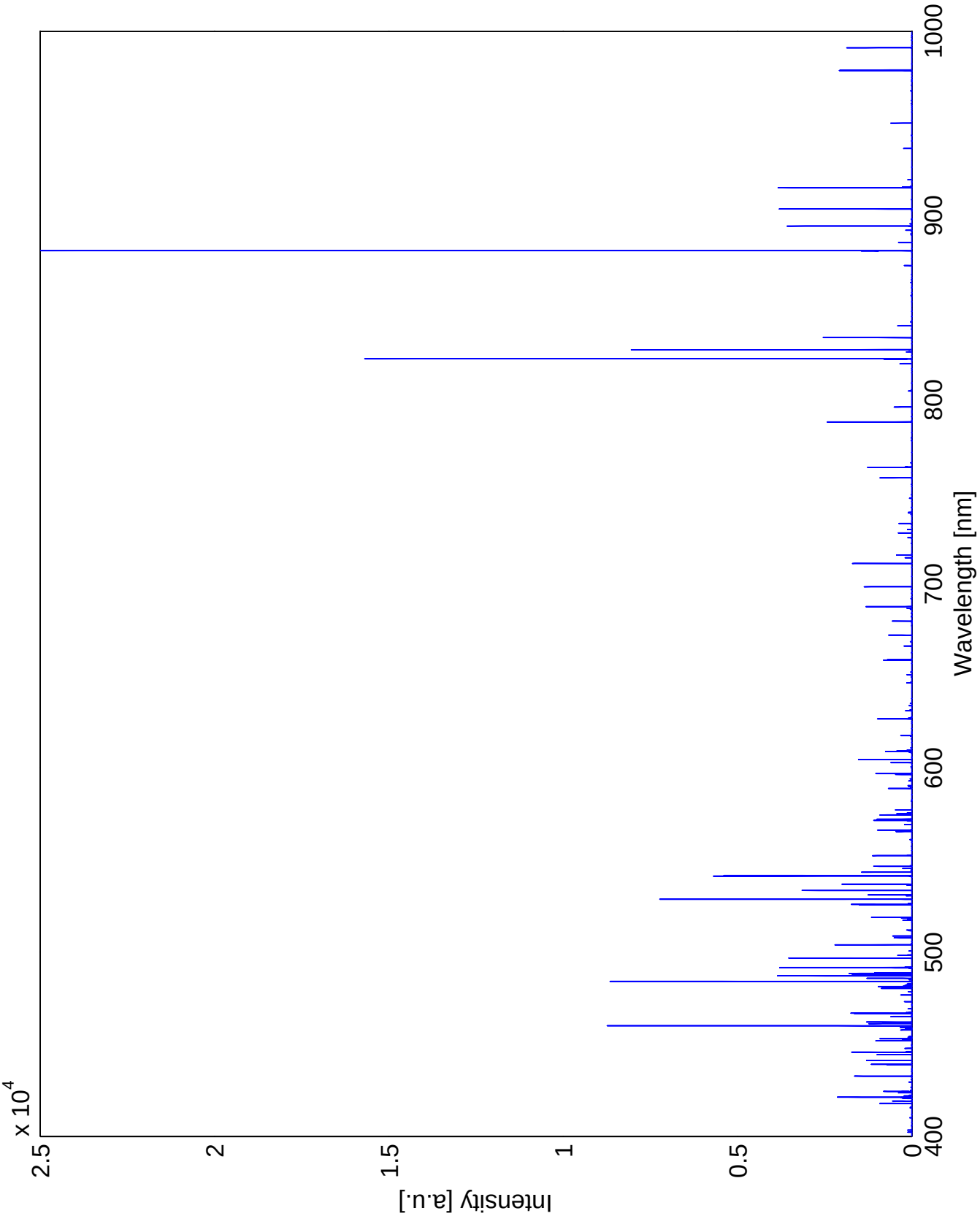

Figure A-11: BHT-200 Hall Thruster Discharge Region Emission Spectrum 400-1000nm

Appendix B

MHT-9 Hall Thruster Measured Spectral Graphs

In this section the measured spectral graphs for the MHT-9 Hall thruster are presented. The spectral measurements were conducted on June 22, 2006 during the thruster's initial characterization tests. For the presented results the discharge voltage and current were 300V and 0.78A respectively. The anode propellant flow rate was 6.5 *sccm* and the cathode flow rate was 1 *sccm* of Xenon. The tests were conducted in the MIT Space Propulsion Laboratory vacuum tank. The vacuum pressure was 3.5×10^{-5} Torr when the thruster was in operation. The thruster was placed on top of metal stand in the central axis of the cylindrical chamber aligned with the window port. The thruster firing direction was aligned with the vacuum tank cylindrical axis.

In all of the spectral measurements an Acton SpectraPro 500i spectrometer and Roper Scientific Cascade Photometrics Cascade:650 CCD detector were used. The CCD detector had 572×1024 pixels with a pixel size of $7.4\mu m \times 7.4\mu m$. The presented spectral graphs are not intensity calibrated.

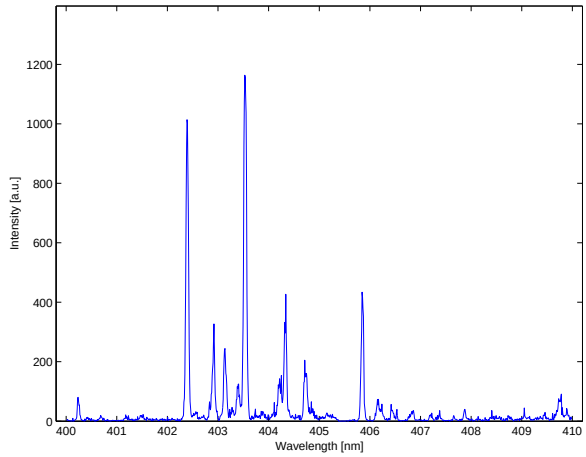

(a) Discharge 400nm

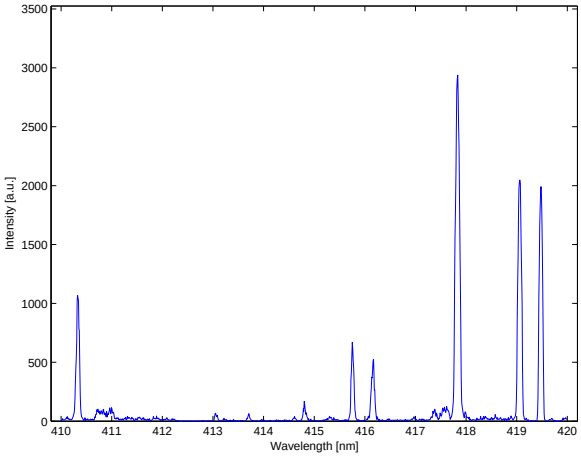

(b) Discharge 410nm

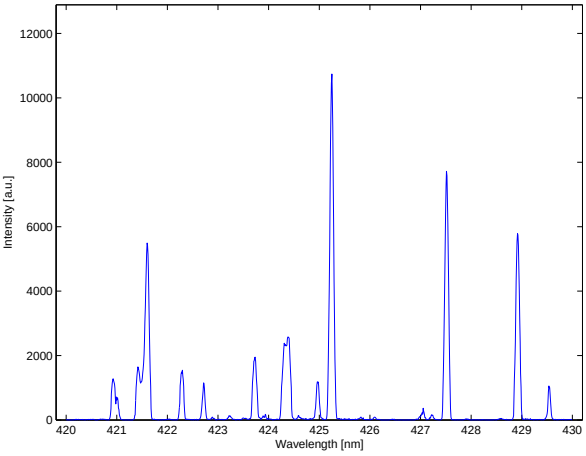

(c) Discharge 420nm

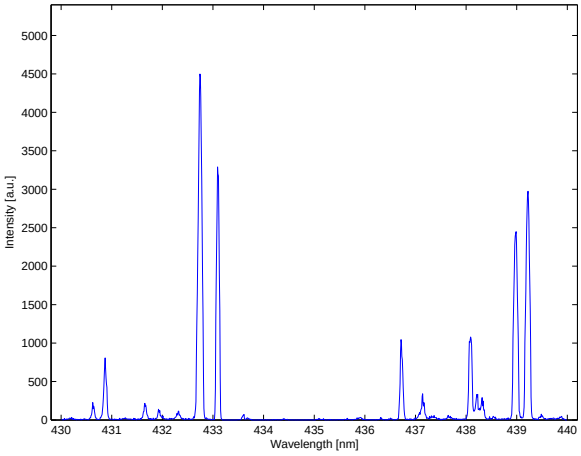

(d) Discharge 430nm

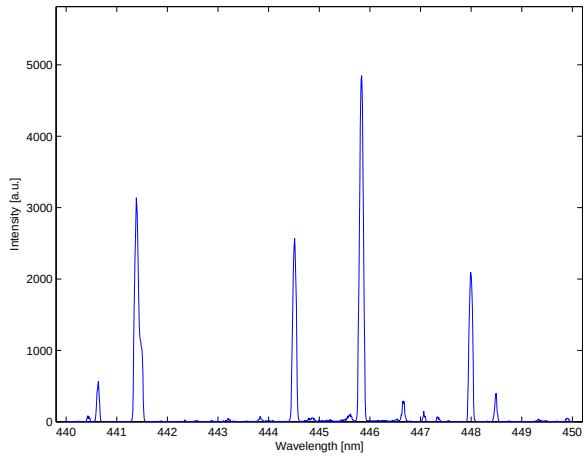

(e) Discharge 440nm

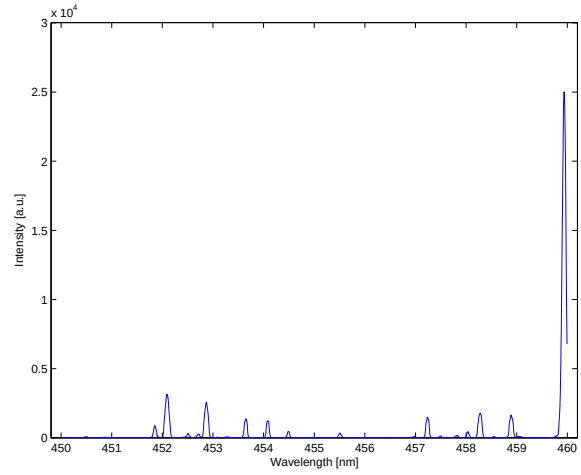

(f) Discharge 450nm

Figure B-1: MHT-9 Hall Thruster Discharge Region Emission Spectra 400-460nm

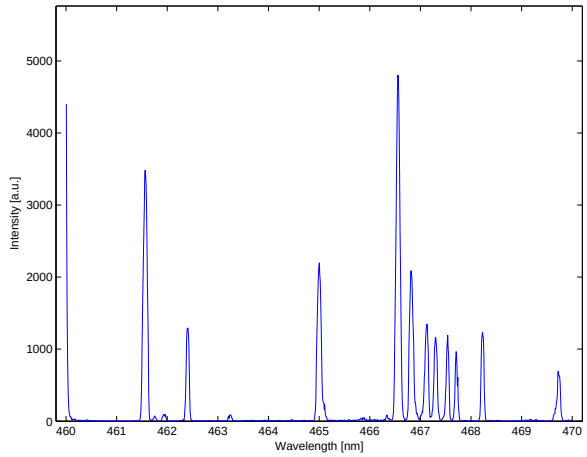

(a) Discharge 460nm

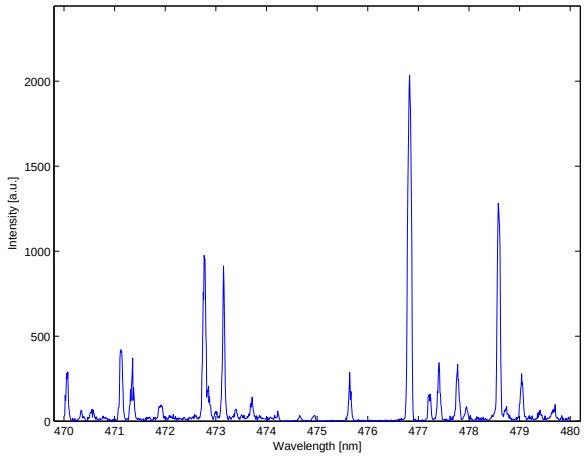

(b) Discharge 470nm

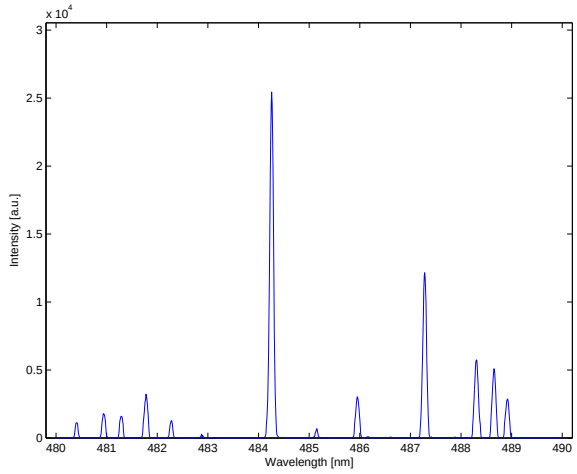

(c) Discharge 480nm

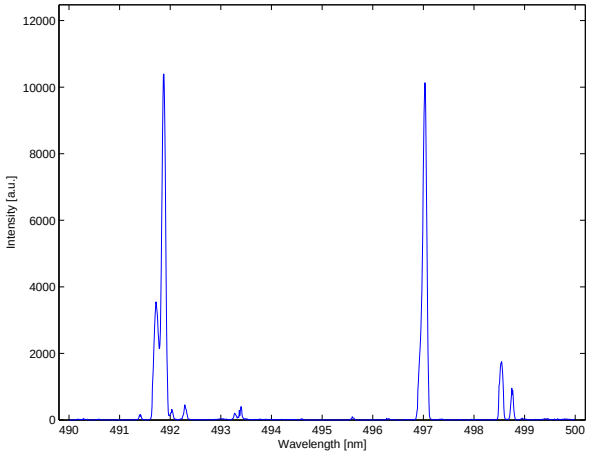

(d) Discharge 490nm

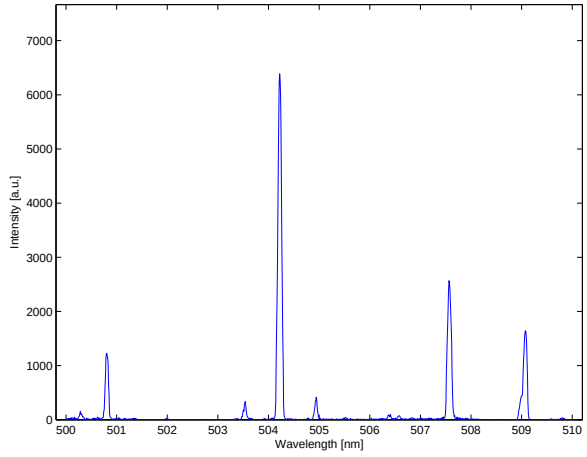

(e) Discharge 500nm

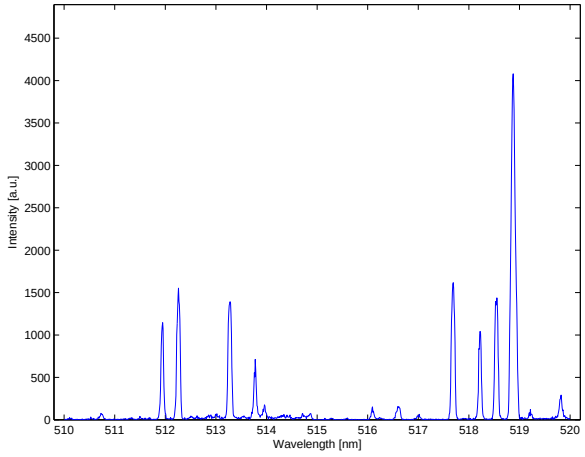

(f) Discharge 510nm

Figure B-2: MHT-9 Hall Thruster Discharge Region Emission Spectra 460-520nm

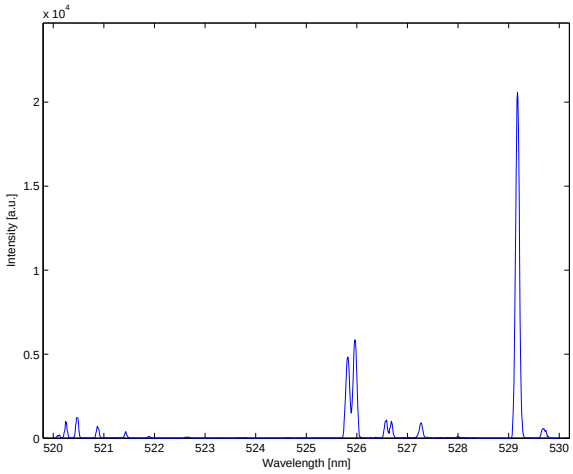

(a) Discharge 520nm

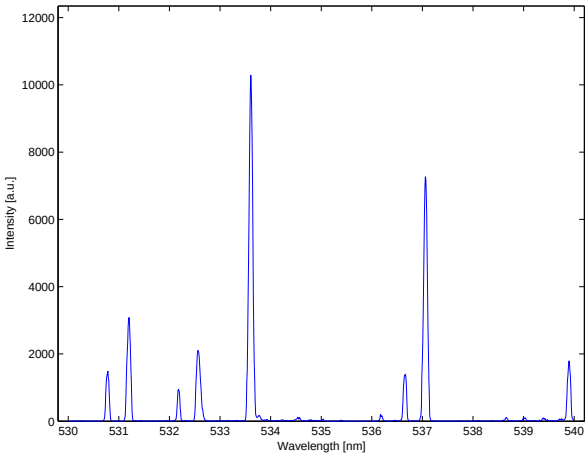

(b) Discharge 530nm

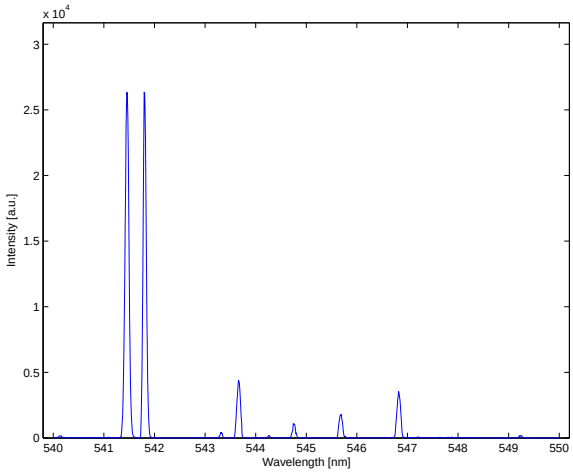

(c) Discharge 540nm

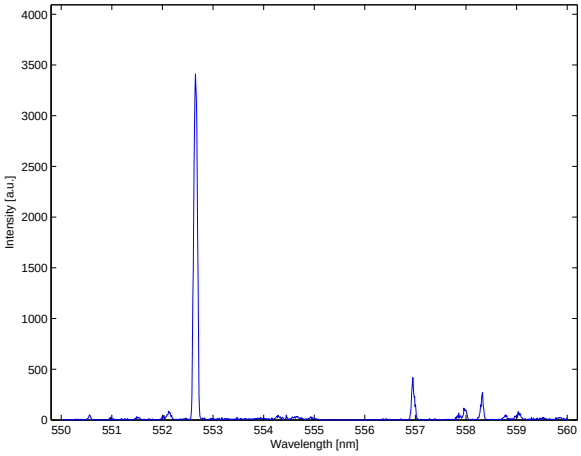

(d) Discharge 550nm

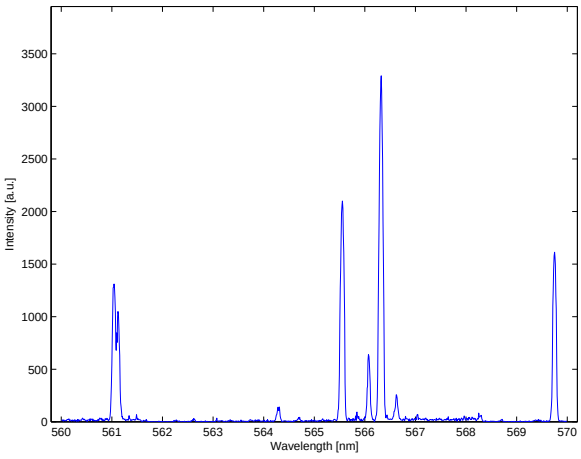

(e) Discharge 560nm

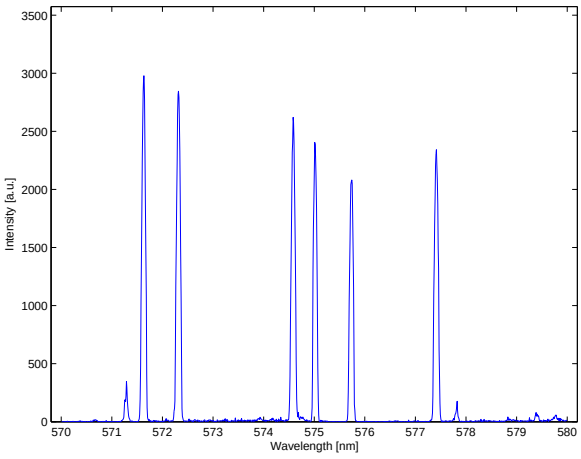

(f) Discharge 570nm

Figure B-3: MHT-9 Hall Thruster Discharge Region Emission Spectra 520-580nm

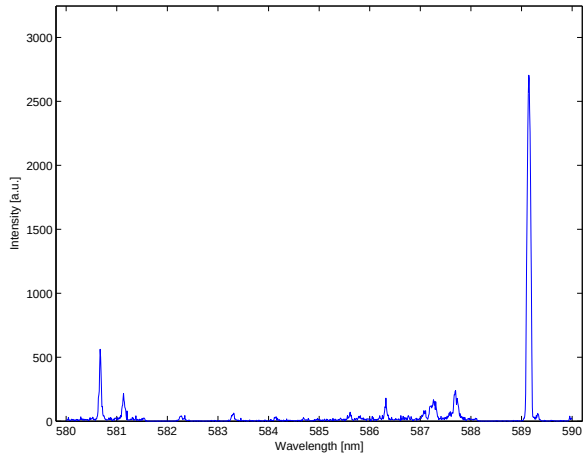

(a) Discharge 580nm

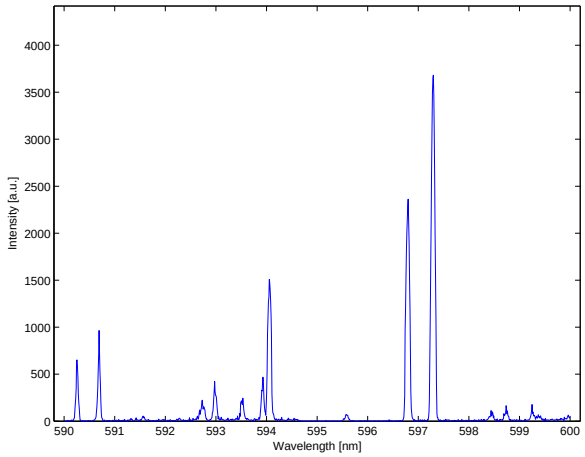

(b) Discharge 590nm

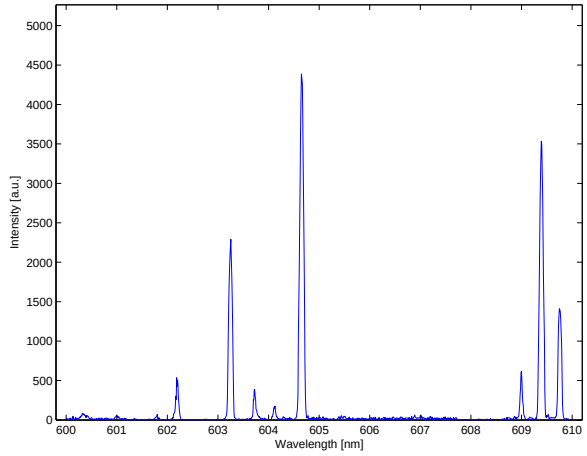

(c) Discharge 600nm

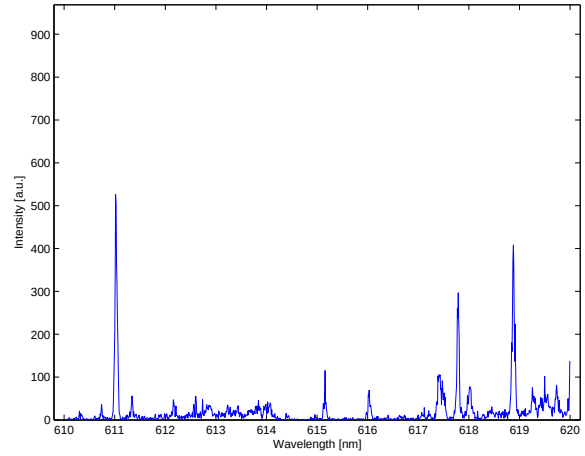

(d) Discharge 610nm

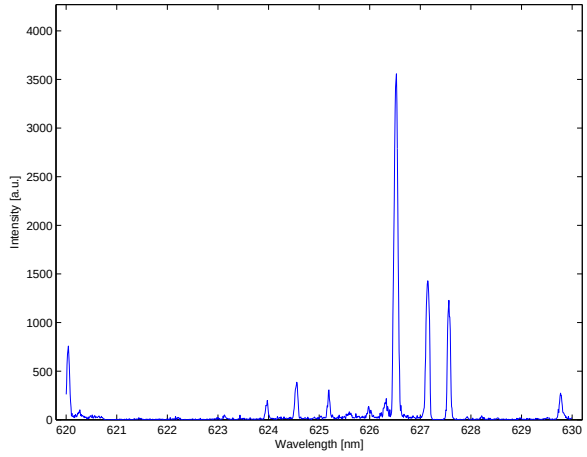

(e) Discharge 620nm

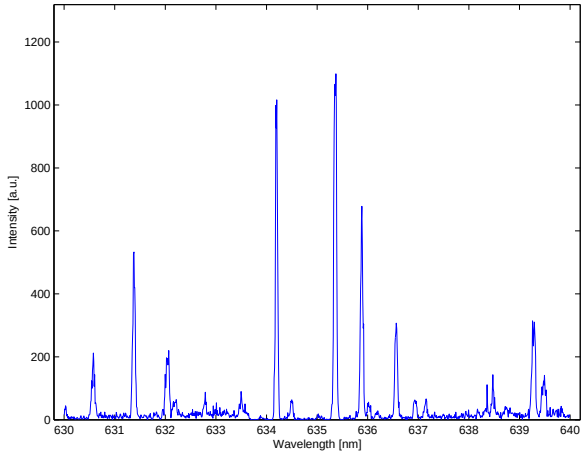

(f) Discharge 630nm

Figure B-4: MHT-9 Hall Thruster Discharge Region Emission Spectra 580-640nm

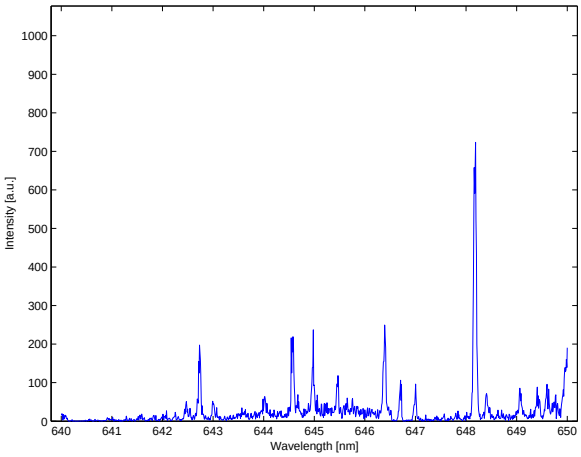

(a) Discharge 640nm

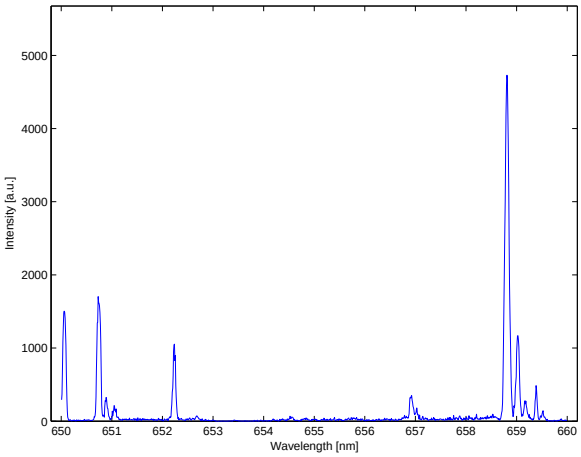

(b) Discharge 650nm

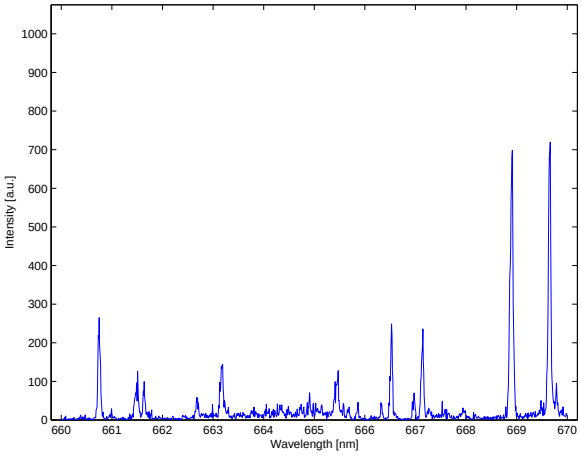

(c) Discharge 660nm

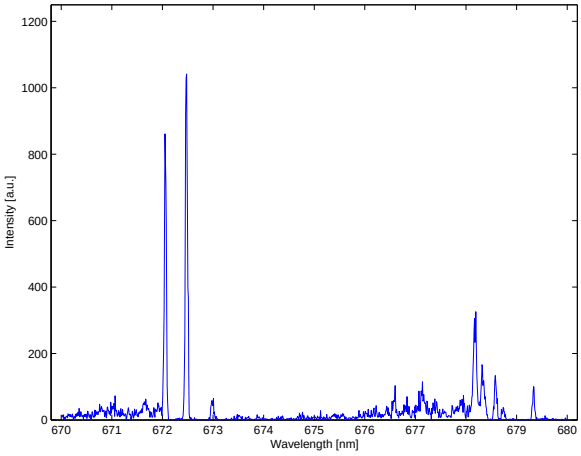

(d) Discharge 670nm

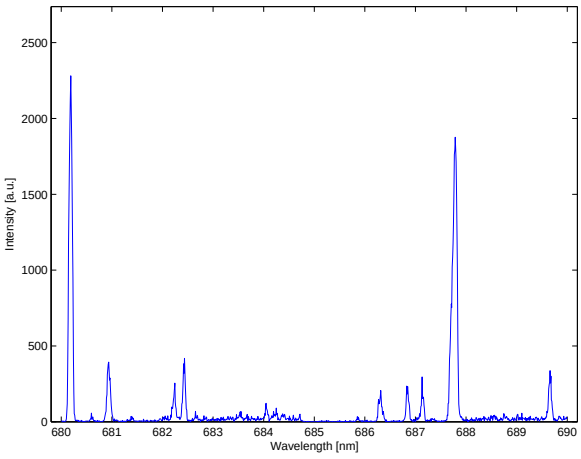

(e) Discharge 680nm

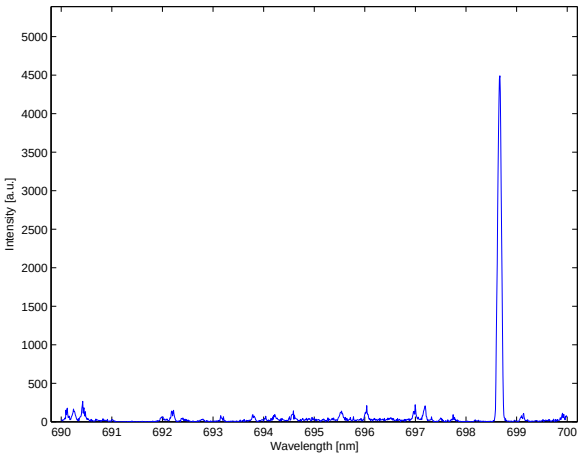

(f) Discharge 690nm

Figure B-5: MHT-9 Hall Thruster Discharge Region Emission Spectra 640-700nm

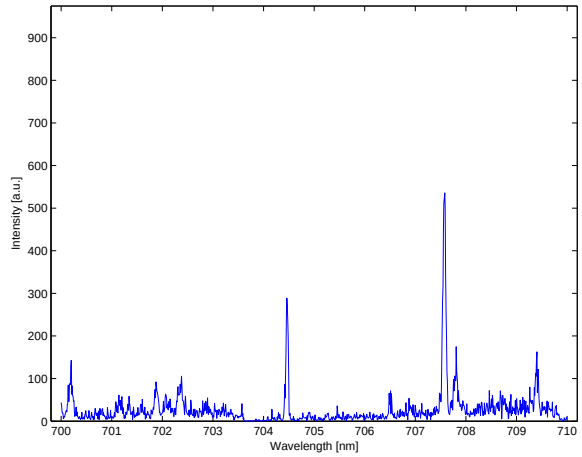

(a) Discharge 700nm

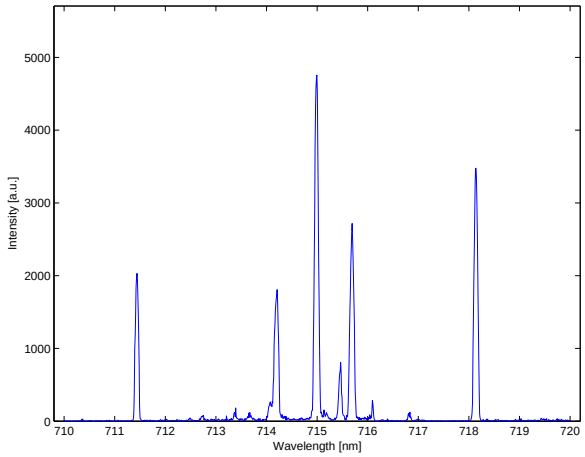

(b) Discharge 710nm

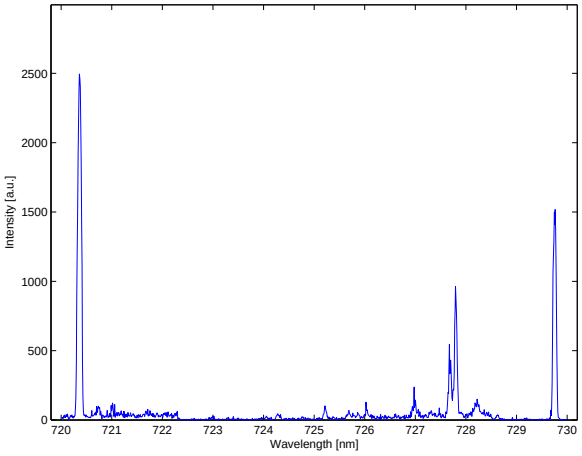

(c) Discharge 720nm

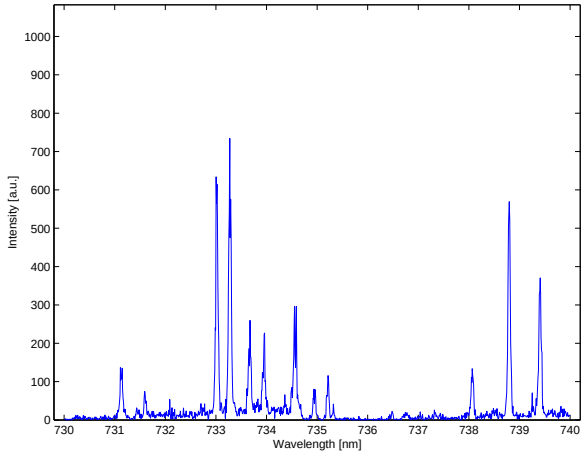

(d) Discharge 730nm

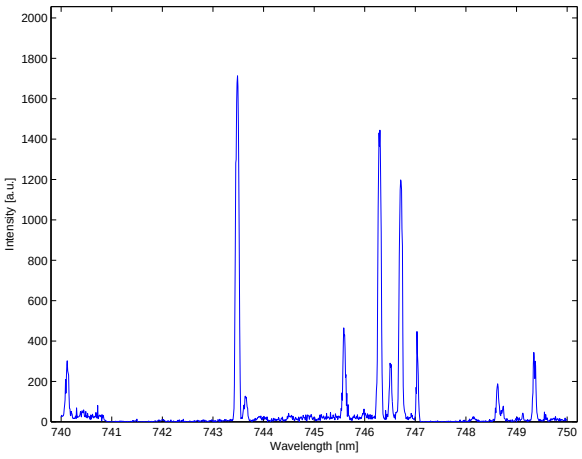

(e) Discharge 740nm

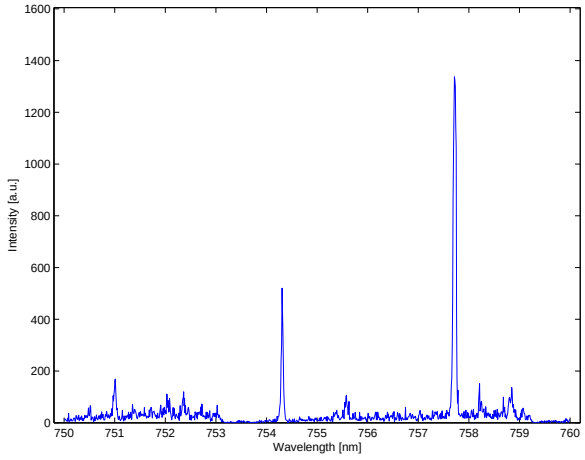

(f) Discharge 750nm

Figure B-6: MHT-9 Hall Thruster Discharge Region Emission Spectra 700-760nm

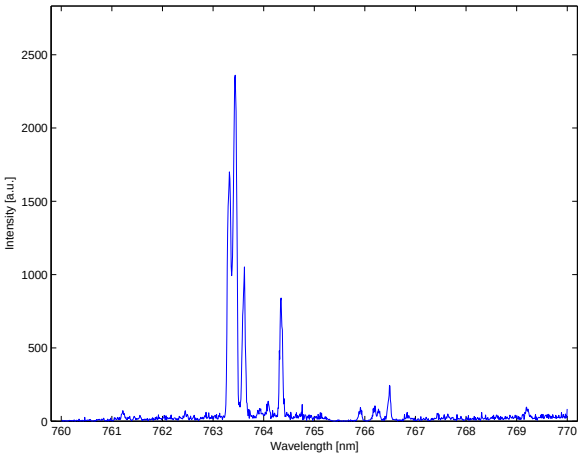

(a) Discharge 760nm

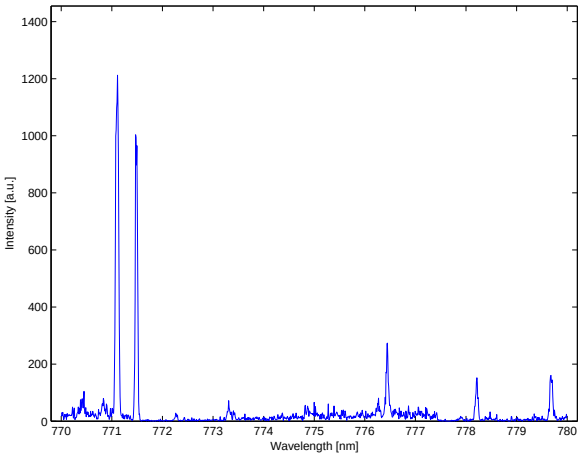

(b) Discharge 770nm

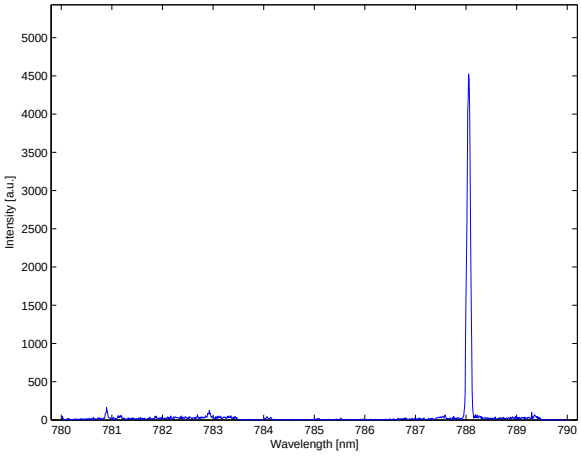

(c) Discharge 780nm

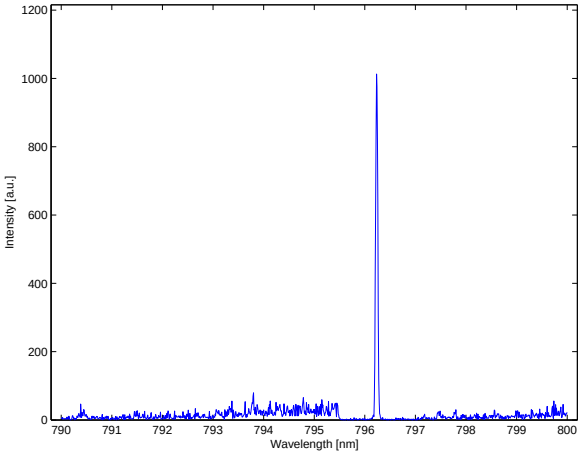

(d) Discharge 790nm

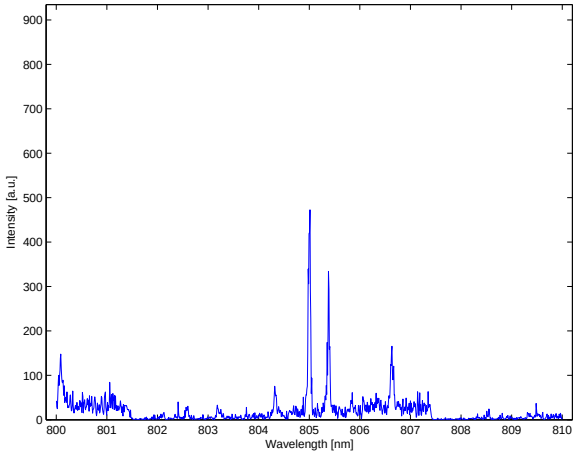

(e) Discharge 800nm

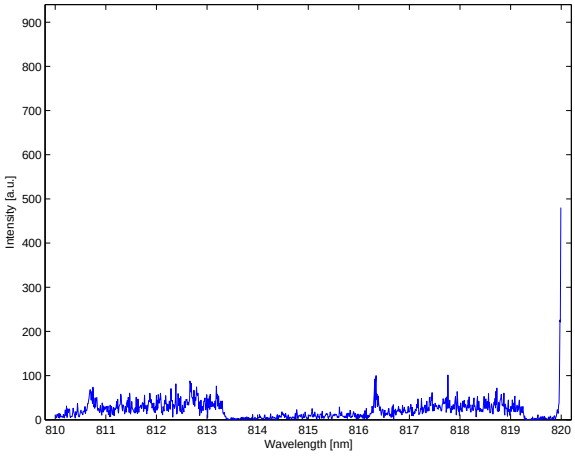

(f) Discharge 810nm

Figure B-7: MHT-9 Hall Thruster Discharge Region Emission Spectra 760-820nm

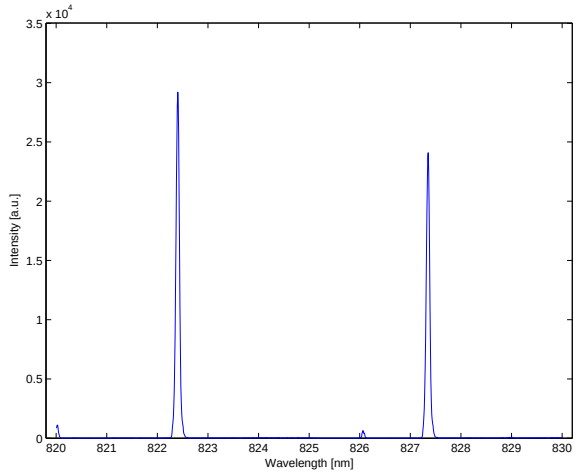

(a) Discharge 820nm

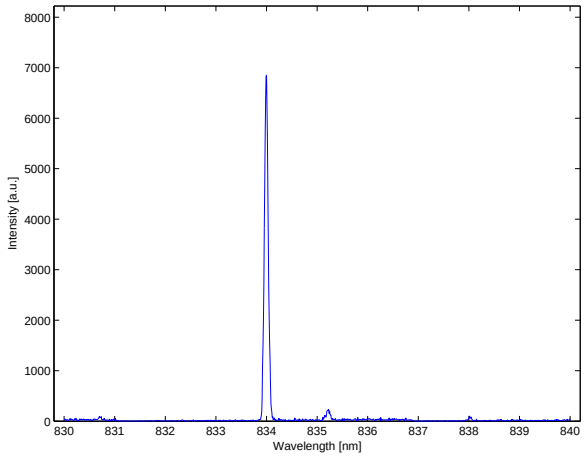

(b) Discharge 830nm

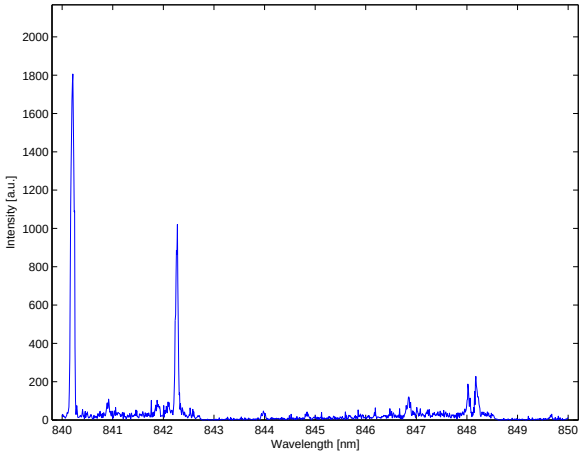

(c) Discharge 840nm

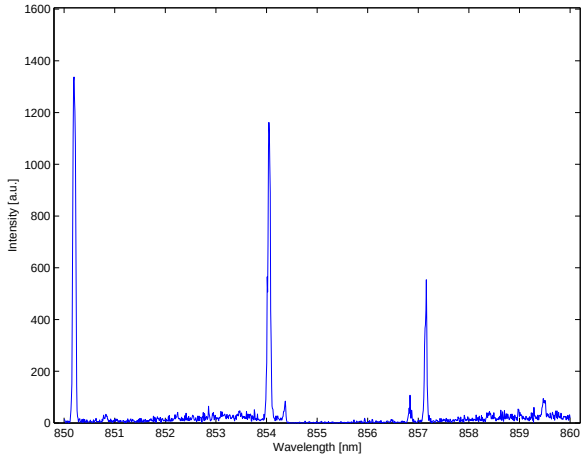

(d) Discharge 850nm

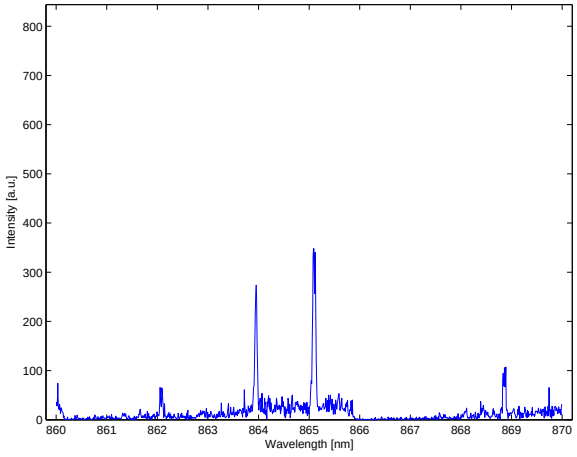

(e) Discharge 860nm

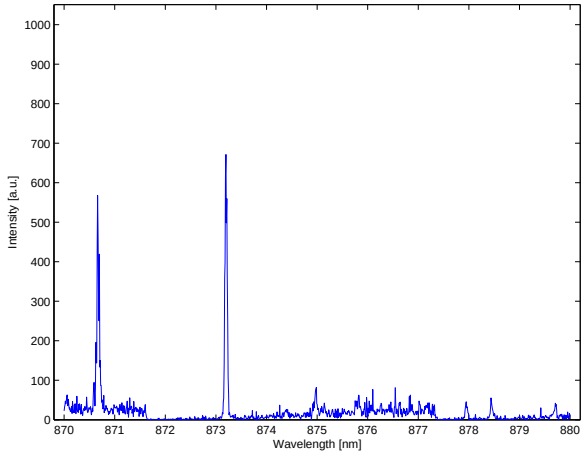

(f) Discharge 870nm

Figure B-8: MHT-9 Hall Thruster Discharge Region Emission Spectra 820-880nm

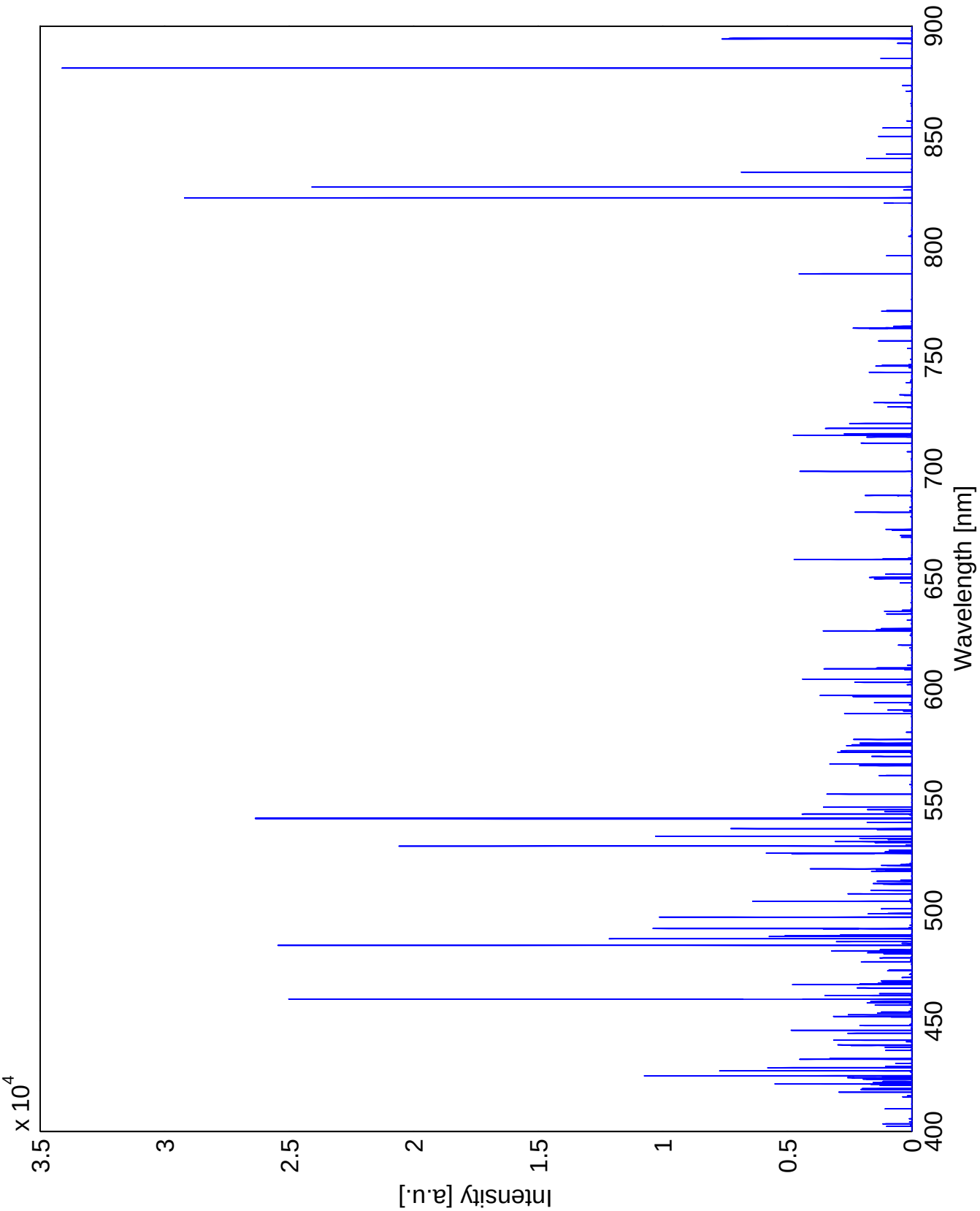

Figure B-9: MHT-9 Hall Thruster Emission Spectrum 400-900nm

Appendix C

mHTX Helicon Plasma Source Measured Spectral Graphs

In this section the measured spectral graphs for the experimental Helicon plasma source running on Argon propellant are presented. Most of the spectral measurements were conducted on December 23, 2005. For the Helicon Mode of operation, the RF power delivered to the antenna was 1000W, the magnet coil current was 30A for both magnets, and the Argon propellant flow rate was 20sccm. For the inductively-coupled-plasma (ICP) mode of operation, the current to the magnet coils was set to zero, and the RF power delivered to the antenna was 400W for the same propellant flow rate of 20sccm of Argon. The tests were conducted in the MIT Space Propulsion Laboratory vacuum tank. The vacuum pressure was 4×10^{-5} Torr when the plasma source was in operation. The Helicon plasma source was placed on top of a metal platform in the central axis of the cylindrical chamber and the antenna region was aligned with the window port. All the measurements represent the emission from the antenna region of the plasma source.

In all of the spectral measurements, a 156mm focal length Jarrel Ash Thermo MonoSpec18 monochromator and an Andor iDus DU420A CCD detector were used. The CCD detector had 1024×256 pixels with a pixel size of $26\mu m \times 26\mu m$. For the measurements presented in this section, the spectrometer inlet slit size was 50 micron, and the acquisition time was 100

microseconds×100. A grating with 1800 grooves/mm was used for all measurements. For the measurements, the dial setting of the Jarrell Ash MonoSpec18 monochromator determined the wavelength range being recorded. The broadband spectra shown in figures C-7 and C-8 were intensity calibrated using a tungsten continuum light source with a black-body emission spectrum corresponding to a temperature of 3025 Kelvin.

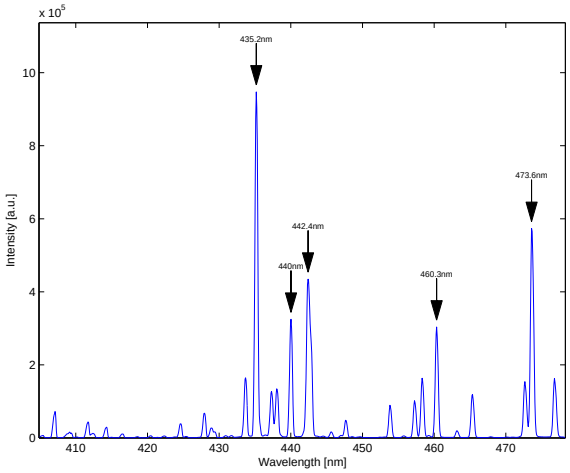

(a) Antenna 400nm

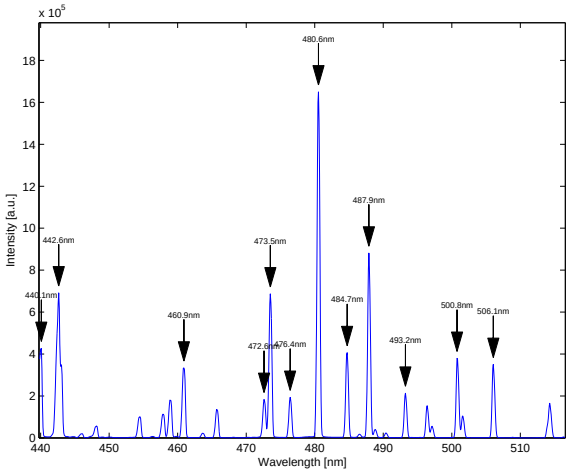

(b) Antenna 445nm

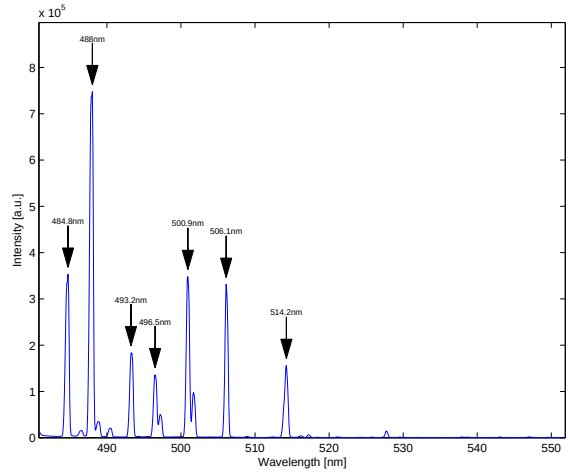

(c) Antenna 480nm

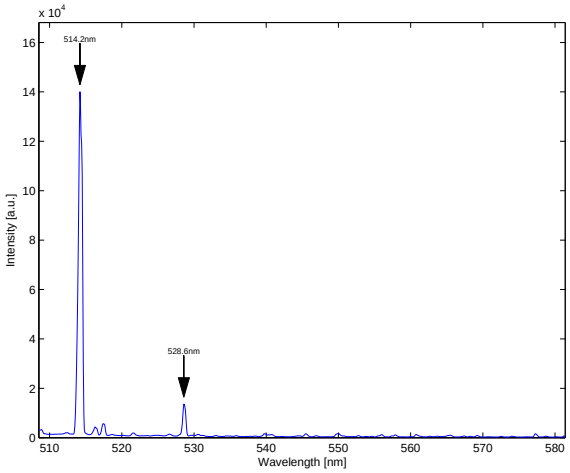

(d) Antenna 510nm

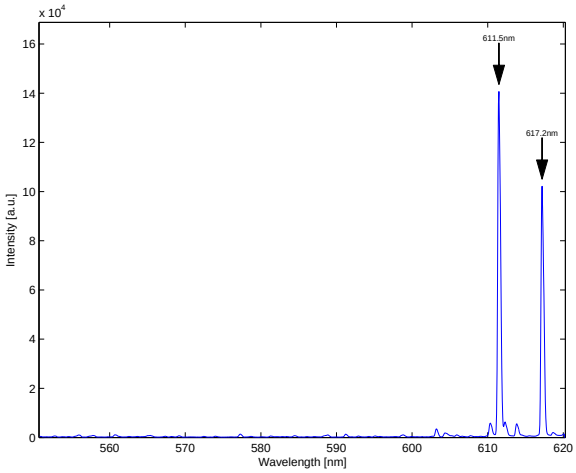

(e) Antenna 550nm

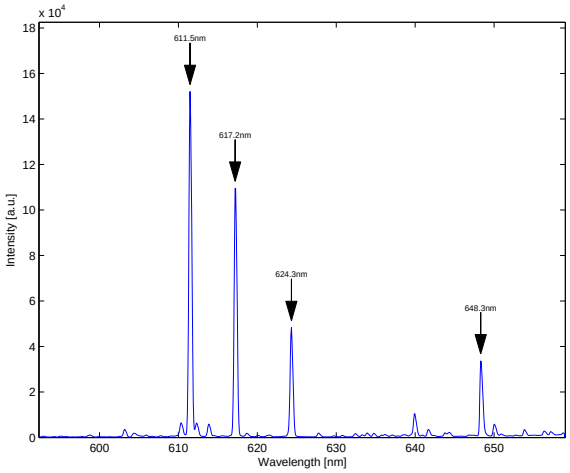

(f) Antenna 595nm

Figure C-1: mHTX Helicon Plasma Source Helicon Mode Emission Spectra of the Antenna Region 400-660nm

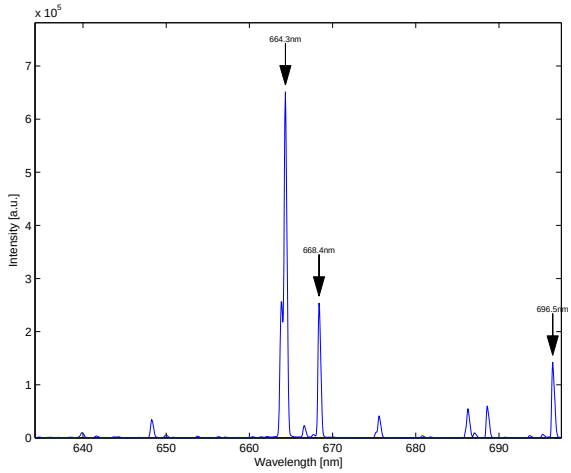

(a) Antenna 635nm

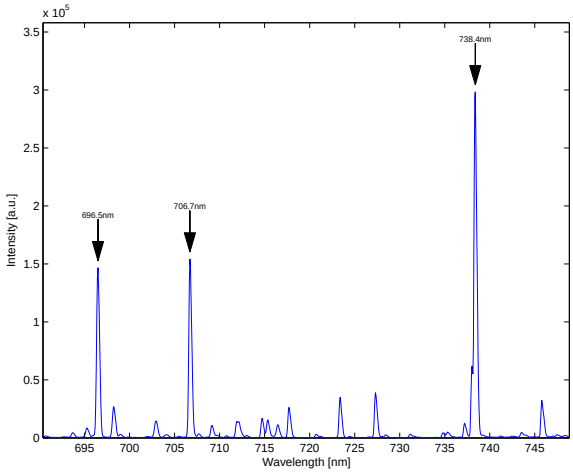

(b) Antenna 690nm

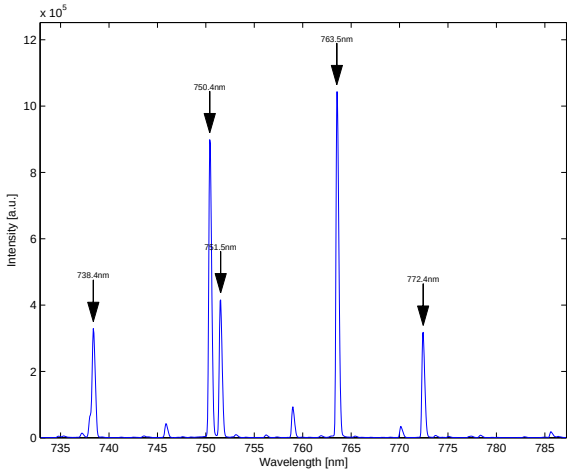

(c) Antenna 735nm

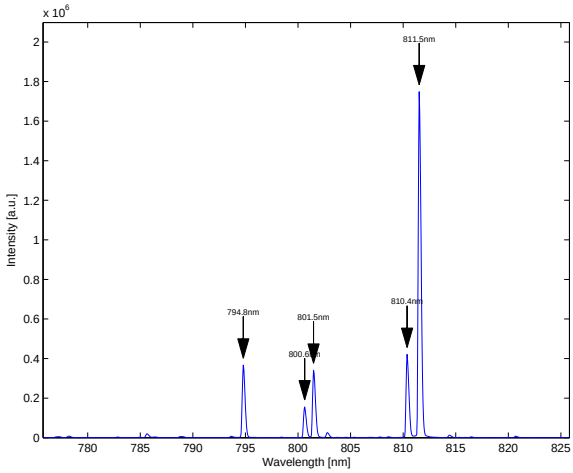

(d) Antenna 775nm

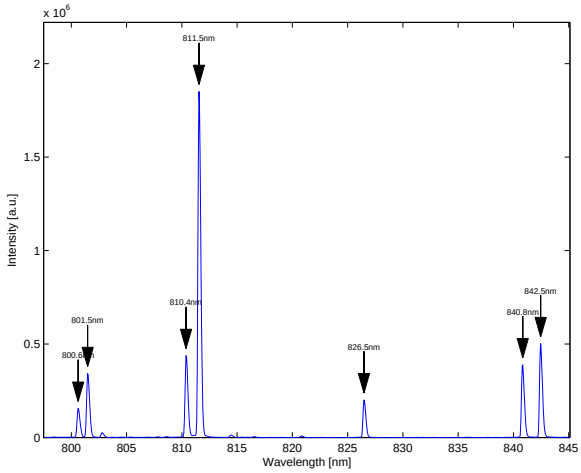

(e) Antenna 800nm

Figure C-2: mHTX Helicon Plasma Source Helicon Mode Emission Spectra of the Antenna Region 635-845nm

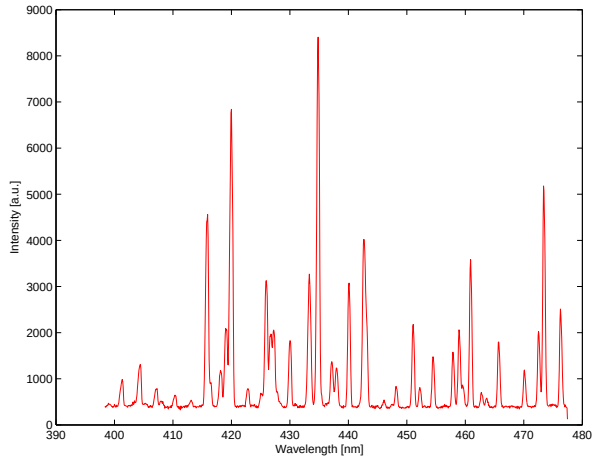

(a) Antenna 400nm

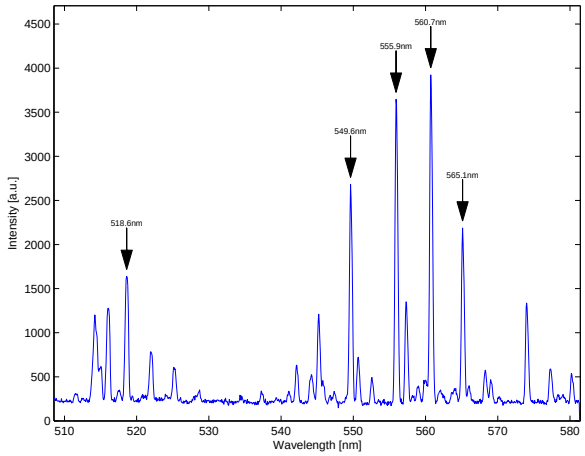

(b) Antenna 510nm

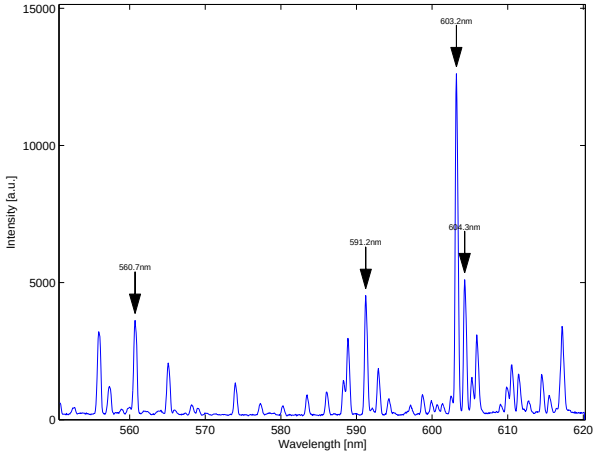

(c) Antenna 550nm

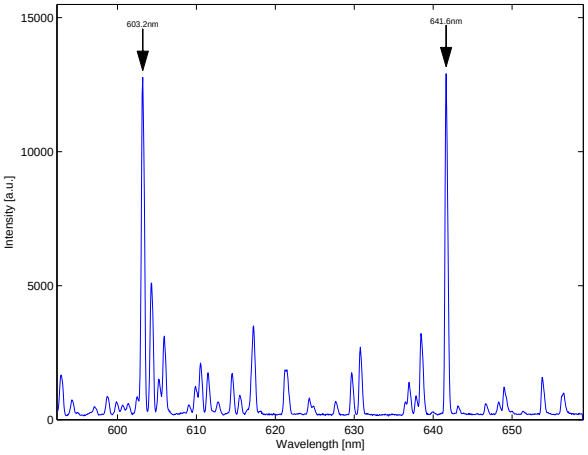

(d) Antenna 595nm

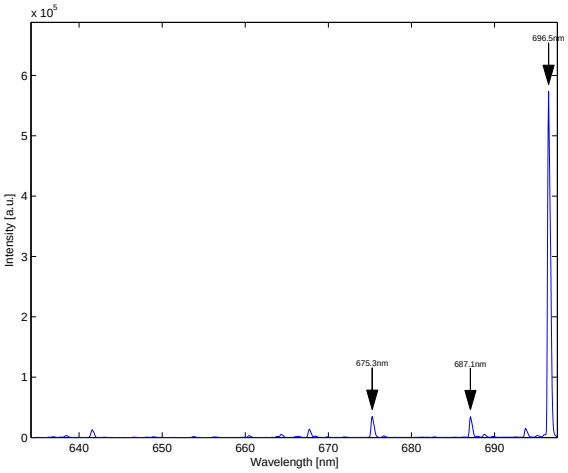

(e) Antenna 635nm

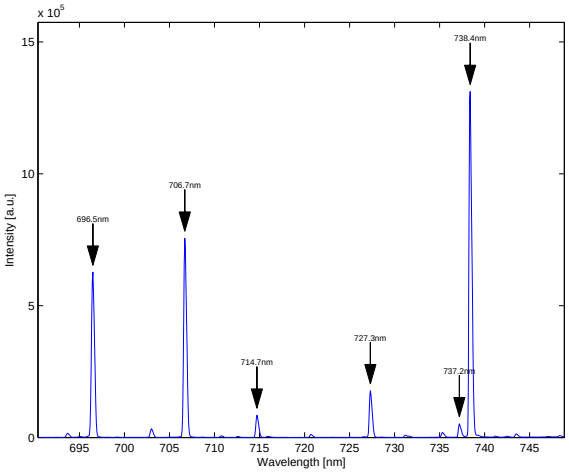

(f) Antenna 690nm

Figure C-3: mHTX Helicon Plasma Source ICP Mode Emission Spectra of the Antenna Region 400-745nm

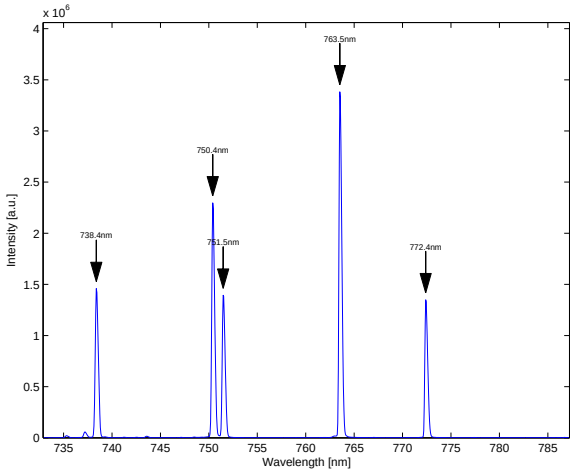

(a) Antenna 735nm

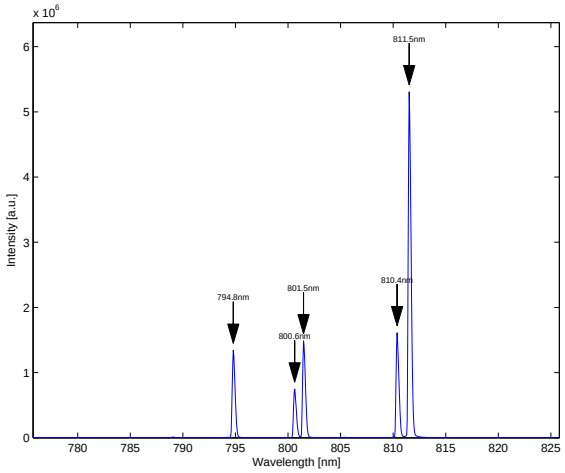

(b) Antenna 775nm

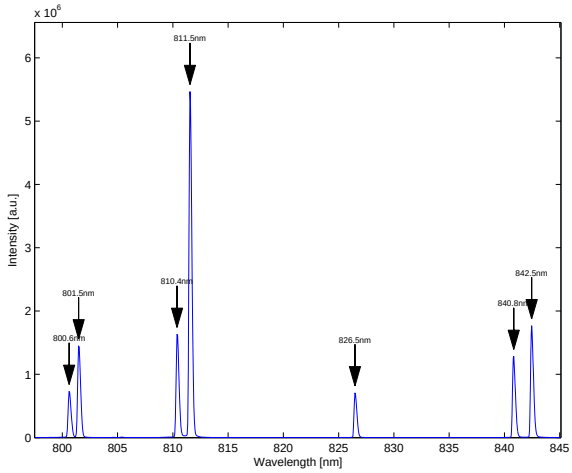

(c) Antenna 800nm

Figure C-4: mHTX Helicon Plasma Source ICP Mode Emission Spectra of the Antenna Region 735-845nm

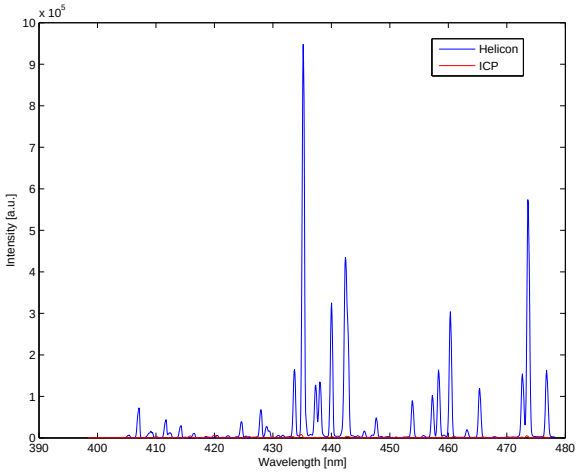

(a) Antenna 400nm

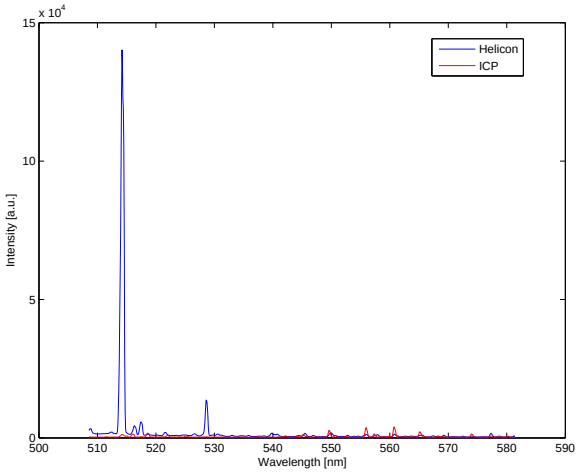

(b) Antenna 510nm

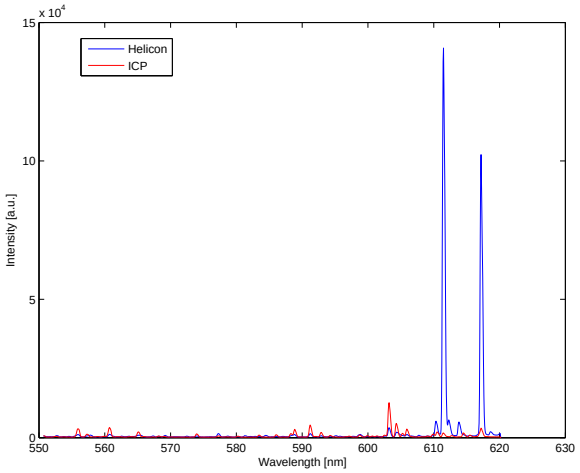

(c) Antenna 550nm

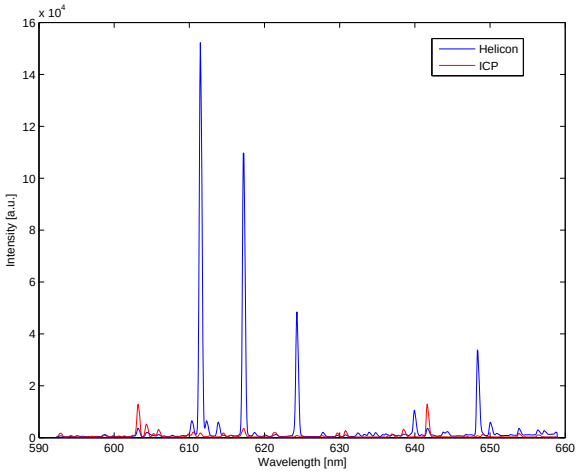

(d) Antenna 595nm

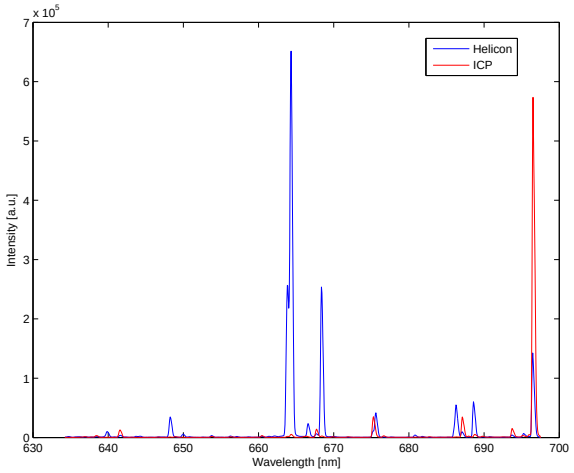

(e) Antenna 635nm

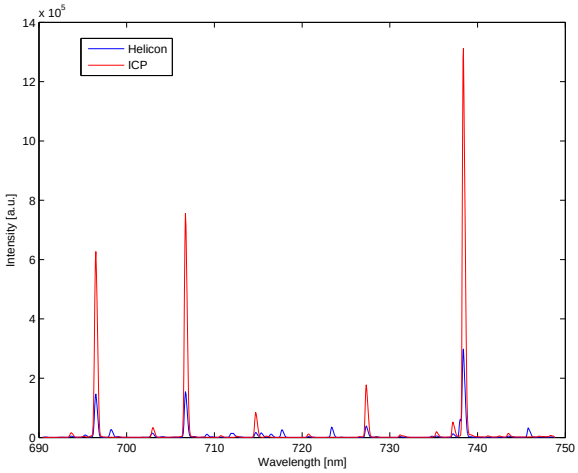

(f) Antenna 690nm

Figure C-5: mHTX Helicon Plasma Source Antenna Region ICP vs. Helicon Modes Emission Spectra Comparison for 400-750nm

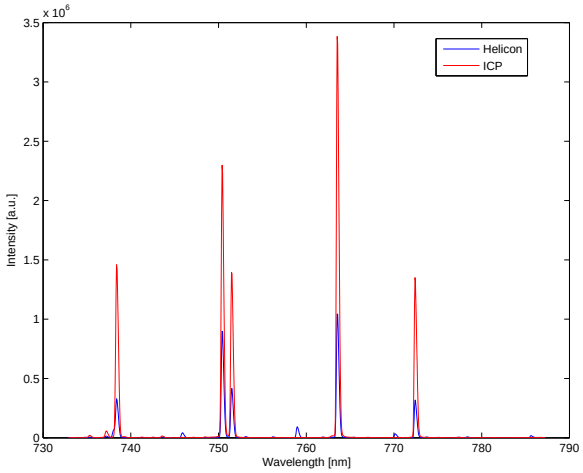

(a) Antenna 735nm

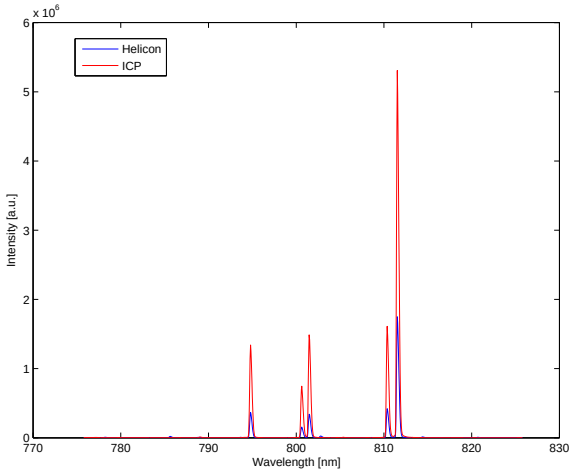

(b) Antenna 775nm

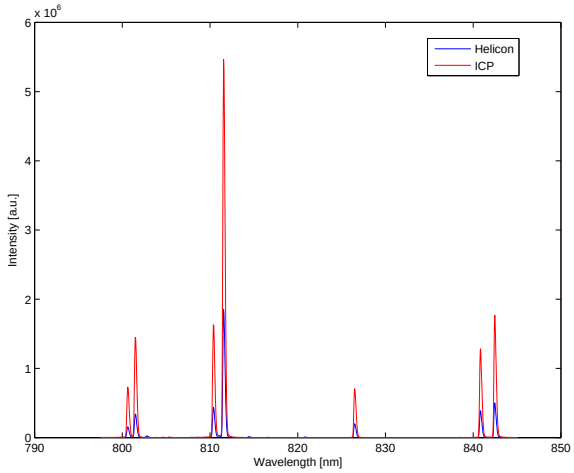

(c) Antenna 800nm

Figure C-6: mHTX Helicon Plasma Source Antenna Region ICP vs. Helicon Modes Emission Spectra Comparison for 735-845nm

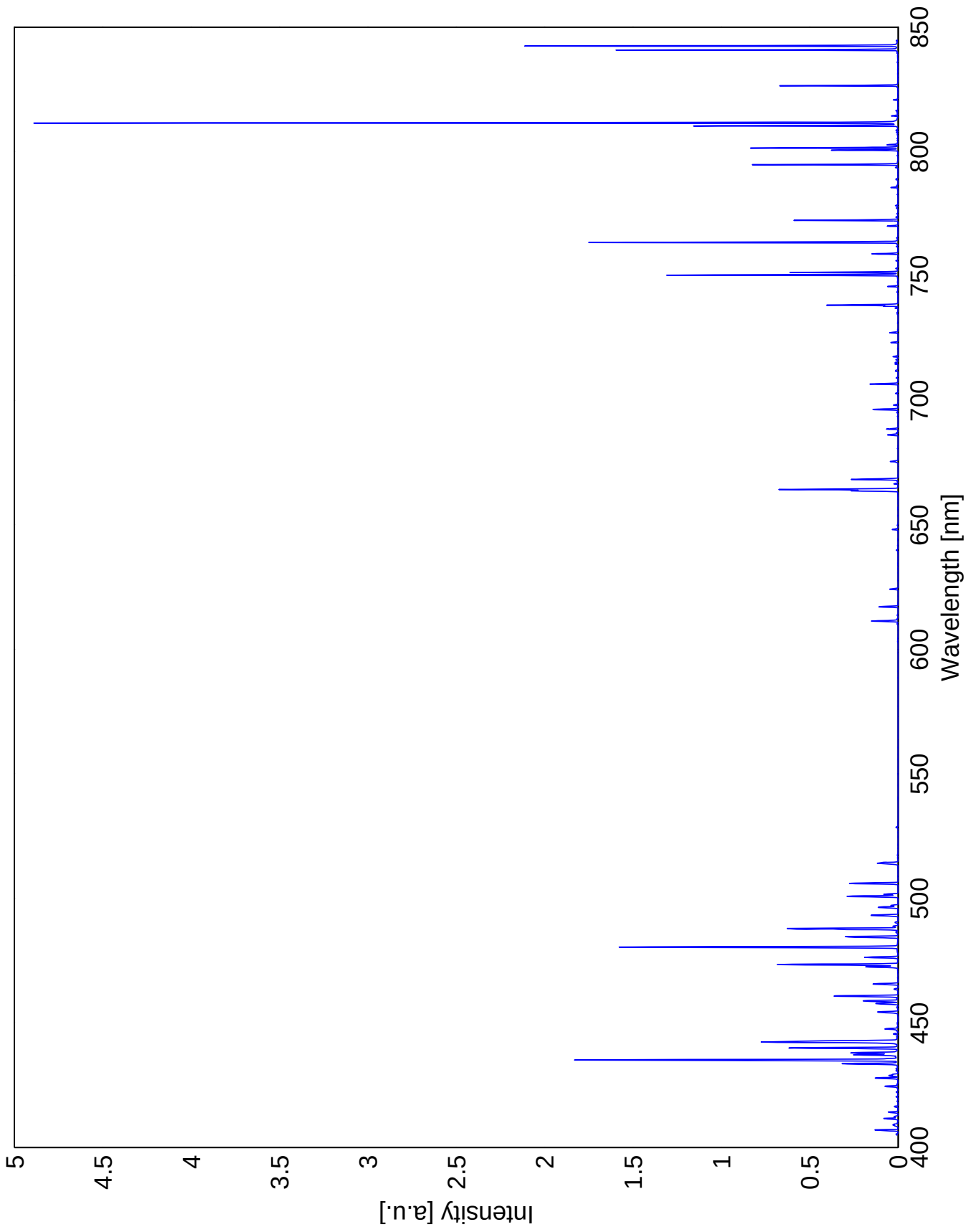

Figure C-7: mHTX Helicon Plasma Source Antenna Region Emission Spectrum for Helicon Mode

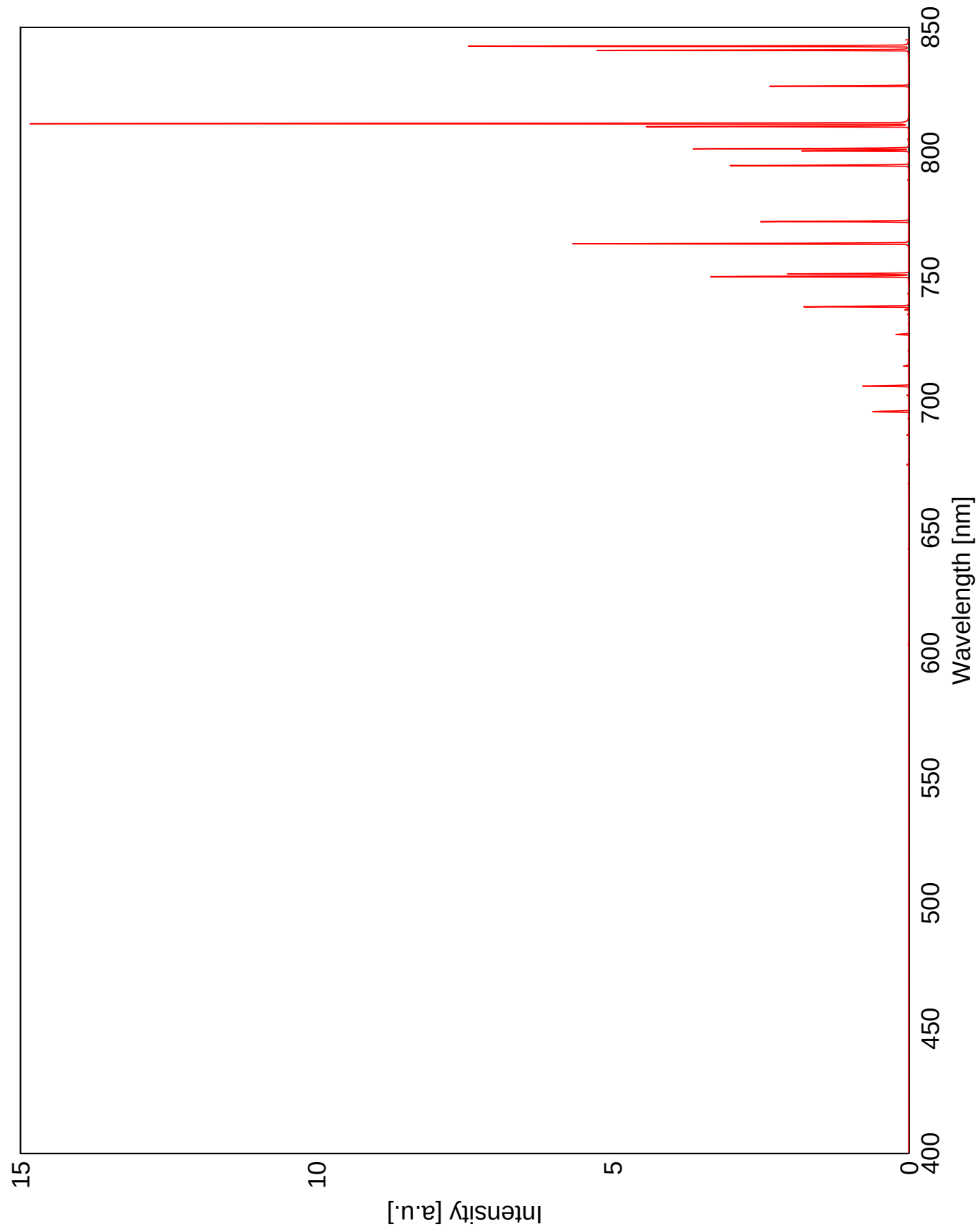

Figure C-8: mHTX Helicon Plasma Source Antenna Region Emission Spectrum for ICP Mode

Appendix D

CRM Simulated Argon Emission Lines

The Argon C-R model simulates the intensity of 148 Argon neutral and 127 Argon single ion emission lines. This section lists the relevant data for all the lines being simulated by the C-R model.

The first column presents the wavelength of the simulated emission line in nm. The second column presents Einstein's spontaneous emission transition coefficient values employed by the C-R model. Columns three and four represent the lower and upper energy levels for the line transition, respectively. Columns five and six present the degeneracies for the lower and upper energy levels, respectively. The listed values are adapted from the online National Institute of Standards and Technology (NIST) Atomic Spectra Database [3]. Column seven presents the corresponding absorbtion oscillator strength values calculated using equation 6.22.

Argon Neutral Lines Simulated						
λ [nm]	A_{ij} [s^{-1}]	E_i [eV]	E_j [eV]	g_i	g_j	f_{ij}
86.68	3.13E+08	0	14.3036675	1	3	0.10577
86.9754	3.50E+07	0	14.2550847	1	3	0.011908
87.6058	2.70E+08	0	14.1525142	1	3	0.093198
87.9947	7.70E+07	0	14.0899676	1	3	0.026815
104.822	5.10E+08	0	11.8280704	1	3	0.25203
106.666	1.19E+08	0	11.623592	1	3	0.060894
340.618	3.90E+05	11.8280704	15.4670036	3	1	0.00022612
346.1078	6.70E+04	11.623592	15.2048079	3	5	0.00020054
355.4305	2.70E+05	11.5483537	15.0356393	5	5	0.00051136
356.3286	1.20E+05	11.7231596	15.2016566	1	3	0.00068527
356.7656	1.10E+05	11.5483537	15.02259	5	7	0.00029386
357.2295	5.10E+05	11.8280704	15.2977948	3	1	0.00032524
360.6522	7.60E+05	11.623592	15.0603891	3	1	0.000494
363.2683	6.60E+04	11.623592	15.0356393	3	5	0.00021762
363.446	1.30E+05	11.623592	15.033971	3	3	0.00025744
364.3116	2.40E+04	11.623592	15.0258678	3	5	7.96E-05
364.9832	8.00E+05	11.8280704	15.2240866	3	1	0.00053256
365.9529	4.40E+04	11.623592	15.0106092	3	3	8.83E-05
367.067	3.10E+04	11.8280704	15.2048079	3	5	0.00010437
367.5235	4.90E+04	11.8280704	15.2006136	3	3	9.92E-05
377.0369	7.00E+04	11.7231596	15.0106092	1	3	0.00044755
383.4678	7.50E+05	11.8280704	15.0603891	3	1	0.00055113
389.466	5.70E+04	11.8280704	15.0106092	3	3	0.00012962
394.7505	5.60E+04	11.5483537	14.6882894	5	5	0.00013082
394.8979	4.55E+05	11.5483537	14.6871173	5	3	0.00063825
404.4418	3.33E+05	11.623592	14.6882894	3	5	0.001361
415.859	1.40E+06	11.5483537	14.5289126	5	5	0.0036298
416.418	2.88E+05	11.5483537	14.5249124	5	3	0.00044922
418.1884	5.61E+05	11.7231596	14.6871173	1	3	0.0044125
419.0713	2.80E+05	11.5483537	14.5060667	5	5	0.00073721

Argon Neutral Lines Simulated						
λ [nm]	A_{ij} [s^{-1}]	E_i [eV]	E_j [eV]	g_i	g_j	f_{ij}
419.1029	5.39E+05	11.7231596	14.6806494	1	3	0.004258
419.8317	2.57E+06	11.623592	14.5759479	3	1	0.0022637
420.0674	9.67E+05	11.5483537	14.4990527	5	7	0.0035814
425.1185	1.11E+05	11.5483537	14.4639949	5	3	0.00018045
425.9362	3.98E+06	11.8280704	14.7381144	3	1	0.0036083
426.6286	3.12E+05	11.623592	14.5289126	3	5	0.0014189
427.2169	7.97E+05	11.623592	14.5249124	3	3	0.0021808
430.0101	3.77E+05	11.623592	14.5060667	3	5	0.0017418
433.3561	5.68E+05	11.8280704	14.6882894	3	5	0.0026653
433.5338	3.87E+05	11.8280704	14.6871173	3	3	0.0010905
434.5168	2.97E+05	11.8280704	14.6806494	3	3	0.00084067
451.0733	1.18E+06	11.8280704	14.5759479	3	1	0.0011998
452.2323	8.98E+04	11.7231596	14.4639949	1	3	0.000826
459.6097	9.47E+04	11.8280704	14.5249124	3	3	0.00029991
462.8441	3.83E+04	11.8280704	14.5060667	3	5	0.00020501
470.2316	1.09E+05	11.8280704	14.4639949	3	3	0.00036133
515.1391	2.39E+06	12.9070145	15.3131543	3	1	0.0031694
516.2285	1.90E+06	12.9070145	15.3080767	3	3	0.0075909
518.7746	1.38E+06	12.9070145	15.2962923	3	5	0.0092799
522.1271	8.80E+05	13.0757149	15.4496521	7	9	0.0046242
542.1352	6.00E+05	13.0757149	15.3620404	7	5	0.0018884
545.1652	4.70E+05	12.9070145	15.1806326	3	5	0.0034903
549.5874	1.69E+06	13.0757149	15.3310391	7	9	0.0098392
550.6113	3.60E+05	13.0948717	15.346002	5	7	0.0022907
555.8702	1.42E+06	12.9070145	15.1368475	3	5	0.010963
557.2541	6.60E+05	13.0948717	15.319167	5	7	0.0043017
560.6733	2.20E+06	12.9070145	15.1177454	3	3	0.010368
565.0704	3.20E+06	12.9070145	15.1005428	3	1	0.0051061
573.952	8.70E+05	13.153143	15.3127282	3	5	0.007161
583.4263	5.20E+05	13.1717769	15.2962923	5	5	0.0026536

Argon Neutral Lines Simulated						
λ [nm]	A_{ij} [s^{-1}]	E_i [eV]	E_j [eV]	g_i	g_j	f_{ij}
586.031	2.85E+05	12.9070145	15.0220874	3	3	0.0014674
588.2624	1.23E+06	12.9070145	15.0140645	3	1	0.0021271
588.8584	1.29E+06	13.0757149	15.1806326	7	5	0.0047901
591.2085	1.05E+06	12.9070145	15.0035649	3	3	0.0055021
592.8813	1.10E+06	13.0948717	15.185507	5	3	0.0034781
594.2669	1.80E+05	13.0948717	15.1806326	5	5	0.000953
598.7302	1.20E+05	13.0757149	15.1459273	7	7	0.00064491
599.8999	1.40E+05	13.0948717	15.1610477	5	5	0.00075534
602.515	9.00E+05	13.3022266	15.3594347	5	3	0.0029389
603.2127	2.46E+06	13.0757149	15.1305434	7	9	0.017253
604.3223	1.47E+06	13.0948717	15.1459273	5	7	0.011268
605.2723	1.90E+05	12.9070145	14.9548511	3	5	0.0017392
605.9372	4.20E+05	12.9070145	14.9526038	3	5	0.0038531
609.8803	5.20E+05	13.153143	15.185507	3	3	0.0028997
610.5635	1.21E+06	13.2826382	15.3127282	3	5	0.011271
614.5441	7.60E+05	13.3022266	15.319167	5	7	0.0060243
617.0174	5.00E+05	13.1717769	15.1806326	5	5	0.0028538
617.3096	6.70E+05	13.153143	15.1610477	3	5	0.0063795
621.2503	3.90E+05	13.1717769	15.1669454	5	7	0.0031592
621.5938	5.70E+05	13.3022266	15.2962923	5	5	0.0033018
629.6872	9.00E+05	13.3278562	15.2962923	3	5	0.0089166
630.7657	6.00E+05	13.1717769	15.1368475	5	5	0.0035789
636.9575	4.20E+05	13.1717769	15.1177454	5	3	0.0015328
638.4717	4.21E+05	12.9070145	14.848368	3	3	0.0025729
641.6307	1.16E+06	12.9070145	14.8388101	3	5	0.011933
653.8112	1.10E+05	13.0757149	14.9715214	7	7	0.00070494
660.4853	1.30E+04	13.0948717	14.9715214	5	7	0.00011903
666.0676	7.80E+05	13.153143	15.0140645	3	1	0.0017293
666.4051	1.50E+05	13.0948717	14.9548511	5	5	0.00099868
667.7282	2.36E+05	11.623592	13.479886	3	1	0.00052583

Argon Neutral Lines Simulated						
λ [nm]	A_{ij} [s^{-1}]	E_i [eV]	E_j [eV]	g_i	g_j	f_{ij}
675.2834	1.93E+06	12.9070145	14.7425399	3	5	0.02199
675.6163	3.60E+05	13.3022266	15.1368475	5	5	0.0024635
676.6612	4.00E+05	13.1717769	15.0035649	5	3	0.0016474
687.1289	2.78E+06	12.9070145	14.7108972	3	3	0.019678
687.9582	1.80E+05	13.153143	14.9548511	3	5	0.0021286
688.8174	2.50E+05	13.153143	14.9526038	3	5	0.0029638
693.7664	3.08E+06	12.9070145	14.6936388	3	1	0.0074082
695.1478	2.20E+05	13.1717769	14.9548511	5	5	0.0015938
696.025	2.40E+05	13.1717769	14.9526038	5	5	0.0017431
696.5431	6.39E+06	11.5483537	13.3278562	5	3	0.027887
703.0251	2.67E+06	13.0757149	14.8388101	7	5	0.014131
706.7218	3.80E+06	11.5483537	13.3022266	5	5	0.028454
706.8736	2.00E+06	13.0948717	14.848368	5	3	0.0089892
710.7478	4.50E+05	13.0948717	14.8388101	5	5	0.003408
712.582	6.00E+05	13.2826382	15.0220874	3	3	0.0045675
714.7042	6.25E+05	11.5483537	13.2826382	5	3	0.0028717
715.8839	2.10E+06	13.2826382	15.0140645	3	1	0.0053782
720.698	2.48E+06	13.3022266	15.0220874	5	3	0.011587
726.5172	1.70E+05	13.153143	14.859229	3	3	0.0013452
727.0664	1.10E+05	13.0757149	14.780511	7	7	0.00087176
727.2936	1.83E+06	11.623592	13.3278562	3	3	0.014512
731.1716	1.70E+06	13.153143	14.848368	3	3	0.013625
731.6005	9.60E+05	13.3278562	15.0220874	3	3	0.0077033
735.0814	1.20E+06	13.3278562	15.0140645	3	1	0.0032403
735.3293	9.60E+05	13.0948717	14.780511	5	7	0.010895
737.2118	1.90E+06	13.0757149	14.7570507	7	9	0.019904
738.398	8.47E+06	11.623592	13.3022266	3	5	0.11539
739.298	7.20E+05	13.1717769	14.848368	5	3	0.0035398
741.2337	3.90E+05	13.2826382	14.9548511	3	5	0.005354
742.5294	3.10E+05	13.3022266	14.9715214	5	7	0.0035873

Argon Neutral Lines Simulated						
λ [nm]	A_{ij} [s^{-1}]	E_i [eV]	E_j [eV]	g_i	g_j	f_{ij}
743.5368	9.00E+05	13.1717769	14.8388101	5	5	0.0074594
743.6297	2.70E+05	13.0757149	14.7425399	7	5	0.0015988
750.3869	4.45E+07	11.8280704	13.479886	3	1	0.12522
751.4652	4.02E+07	11.623592	13.2730373	3	1	0.11344
763.5106	2.45E+07	11.5483537	13.1717769	5	5	0.21412
772.3761	5.18E+06	11.5483537	13.153143	5	3	0.027797
772.4207	1.17E+07	11.7231596	13.3278562	1	3	0.31396
789.1075	9.50E+05	13.1717769	14.7425399	5	5	0.0088686
794.8176	1.86E+07	11.7231596	13.2826382	1	3	0.52848
800.6157	4.90E+06	11.623592	13.1717769	3	5	0.078478
801.4786	9.28E+06	11.5483537	13.0948717	5	5	0.089369
805.3308	8.60E+05	13.1717769	14.7108972	5	3	0.0050171
810.3693	2.50E+07	11.623592	13.153143	3	3	0.24613
811.5311	3.31E+07	11.5483537	13.0757149	5	7	0.45753
826.4522	1.53E+07	11.8280704	13.3278562	3	3	0.15667
840.821	2.23E+07	11.8280704	13.3022266	3	5	0.39393
842.4648	2.15E+07	11.623592	13.0948717	3	5	0.38128
852.1442	1.39E+07	11.8280704	13.2826382	3	3	0.15132
860.5776	1.04E+06	13.3022266	14.7425399	5	5	0.011547
866.7944	2.43E+06	11.7231596	13.153143	1	3	0.082114
907.5394	1.20E+06	13.3278562	14.6936388	3	1	0.0049391
912.2967	1.89E+07	11.5483537	12.9070145	5	3	0.1415
919.4638	1.76E+06	12.9070145	14.2550847	3	3	0.022307
922.4499	5.03E+06	11.8280704	13.1717769	3	5	0.10694
929.1531	3.26E+06	12.9070145	14.2410268	3	1	0.014065
935.422	1.06E+06	11.8280704	13.153143	3	3	0.013905
965.7786	5.43E+06	11.623592	12.9070145	3	3	0.07593
978.4503	1.47E+06	11.8280704	13.0948717	3	5	0.035164

Argon Single Ion Lines Simulated						
λ [nm]	A_{ij} [s^{-1}]	E_i [eV]	E_j [eV]	g_i	g_j	f_{ij}
71.809	9.50E+08	0	17.2658324	4	2	0.03672
72.3361	2.30E+09	0	17.1400263	4	4	0.18042
72.5548	1.90E+09	0.17749367	17.2658324	2	2	0.14995
73.093	4.50E+08	0.17749367	17.1400263	2	4	0.072086
74.0269	3.10E+07	0	16.7485279	4	4	0.0025468
74.5322	7.30E+06	0.17749367	16.8124712	2	2	0.00060795
91.9781	1.40E+08	0	13.479751	4	2	0.0088782
93.2054	6.70E+07	0.17749367	13.479751	2	2	0.008726
289.1612	1.82E+07	17.1400263	21.4264882	4	2	0.011407
294.2893	5.30E+07	17.1400263	21.3517985	4	4	0.068815
297.905	4.16E+07	17.2658324	21.4264882	2	2	0.055348
303.3508	9.90E+06	17.2658324	21.3517985	2	4	0.027316
309.3402	4.40E+08	19.8671558	23.8740138	4	6	0.94683
324.3689	1.06E+08	19.261083	23.0823021	4	2	0.083601
329.364	1.70E+08	19.8671558	23.6304234	4	4	0.27648
330.7228	3.40E+08	19.8010853	23.5488916	2	2	0.55752
335.0924	1.50E+08	21.1270321	24.8259692	6	6	0.25251
337.6436	1.50E+08	21.1430741	24.8140633	8	8	0.25637
338.8531	1.90E+08	19.9725369	23.6304234	2	4	0.65413
347.6747	1.25E+08	19.222901	22.7879777	6	6	0.22652
349.1244	1.79E+08	19.261083	22.811357	4	4	0.32709
349.1536	2.31E+08	19.222901	22.7728782	6	8	0.56291
350.9778	2.55E+08	19.3053437	22.8368703	2	2	0.47093
351.4388	1.36E+08	19.261083	22.7879777	4	6	0.37773
354.5596	3.40E+08	19.7622598	23.2581123	4	6	0.96118
354.5845	3.90E+08	21.1270321	24.6226401	6	8	0.98017
355.9508	2.88E+08	19.6800477	23.1622367	6	8	0.7294
356.103	4.00E+08	21.1430741	24.6237745	8	10	0.95056
357.6616	2.75E+08	19.5490106	23.0145441	6	8	0.70319
358.1608	1.76E+08	19.6425808	23.1032837	2	4	0.67695

Argon Single Ion Lines Simulated						
λ [nm]	A_{ij} [s^{-1}]	E_i [eV]	E_j [eV]	g_i	g_j	f_{ij}
358.2355	2.53E+08	19.6103067	23.0702885	4	6	0.73014
358.8441	3.03E+08	19.4945327	22.9486467	8	10	0.73117
362.2138	6.40E+07	19.261083	22.683064	4	2	0.062941
363.9833	1.40E+08	21.3517985	24.7571439	4	6	0.4171
371.8206	2.00E+08	21.492401	24.8259692	4	6	0.62179
372.9309	4.80E+07	16.6438534	19.9674978	6	4	0.066721
373.7889	2.30E+08	21.4980485	24.8140633	6	8	0.64236
376.527	9.80E+07	19.222901	22.5148025	6	6	0.20829
376.6119	7.40E+06	18.0606387	21.3517985	4	4	0.015735
377.052	4.10E+07	19.3053437	22.5926622	2	4	0.17477
378.084	7.70E+07	19.4945327	22.7728782	8	8	0.16502
380.3172	1.50E+08	21.4980485	24.7571439	6	6	0.32527
380.9456	4.40E+07	19.261083	22.5148025	4	6	0.14359
385.0581	3.87E+07	16.7485279	19.9674978	4	4	0.086024
386.8528	1.40E+08	19.9674978	23.1715343	4	6	0.47116
392.5719	1.40E+08	21.1270321	24.2843928	6	4	0.21564
392.8623	2.44E+07	16.8124712	19.9674978	2	4	0.11292
393.2547	9.30E+07	19.9674978	23.1193767	4	4	0.21562
394.6097	1.40E+08	21.1430741	24.28413	8	6	0.24512
397.9356	9.80E+07	19.9674978	23.0823021	4	2	0.11633
399.4792	1.60E+08	20.7435447	23.8463131	2	2	0.38279
401.3857	1.05E+07	16.4065009	19.4945327	8	8	0.025361
403.3809	9.80E+07	19.6103067	22.683064	4	2	0.11953
403.546	4.40E+06	18.4265479	21.4980485	4	6	0.016113
404.2894	4.06E+07	18.4265479	21.492401	4	4	0.099487
405.2921	6.70E+07	20.7435447	23.8018128	2	4	0.32999
407.2005	5.80E+07	18.4541128	21.4980485	6	6	0.14418
407.6628	8.00E+07	19.6425808	22.683064	2	2	0.19932
407.9574	1.19E+07	18.4541128	21.492401	6	4	0.019794
408.2387	2.90E+06	16.6438534	19.6800477	6	6	0.0072457

Argon Single Ion Lines Simulated						
λ [nm]	A_{ij} [s^{-1}]	E_i [eV]	E_j [eV]	g_i	g_j	f_{ij}
410.3912	1.20E+08	19.4945327	22.5148025	8	6	0.22725
413.1724	8.50E+07	18.4265479	21.4264882	4	2	0.10877
415.6086	3.90E+07	19.6103067	22.5926622	4	4	0.10099
417.9297	1.30E+07	19.5490106	22.5148025	6	6	0.034041
421.8665	3.60E+07	19.7622598	22.7003761	4	4	0.096053
422.2637	6.90E+07	19.8671558	22.8025082	4	2	0.092224
422.6988	4.10E+07	21.3517985	24.28413	4	6	0.16474
422.8158	1.31E+07	16.7485279	19.6800477	4	6	0.052665
423.722	1.12E+07	18.4265479	21.3517985	4	4	0.030146
426.6527	1.64E+07	16.6438534	19.5490106	6	6	0.044756
427.7528	8.00E+07	18.4541128	21.3517985	6	4	0.1463
428.2898	1.32E+07	16.7485279	19.6425808	4	2	0.01815
430.065	5.70E+06	18.6159413	21.4980485	6	6	0.015805
433.12	5.74E+07	16.7485279	19.6103067	4	4	0.16143
433.203	1.92E+07	16.4441135	19.3053437	4	2	0.027009
434.8064	1.17E+08	16.6438534	19.4945327	6	8	0.44215
435.2205	2.12E+07	16.4573768	19.3053437	2	2	0.060202
436.2066	5.50E+06	18.6565198	21.4980485	4	6	0.023534
437.0753	6.60E+07	18.6565198	21.492401	4	4	0.18902
437.1329	2.21E+07	16.4255752	19.261083	6	4	0.042207
437.5954	2.05E+07	17.1400263	19.9725369	4	2	0.029426
437.9667	1.00E+08	16.8124712	19.6425808	2	2	0.28757
440.0097	1.60E+07	16.4441135	19.261083	4	4	0.046441
440.0986	3.04E+07	16.4065009	19.222901	8	6	0.066205
442.6001	8.17E+07	16.7485279	19.5490106	4	6	0.35991
443.0189	5.69E+07	16.8124712	19.6103067	2	4	0.33484
443.0996	1.09E+07	16.4255752	19.222901	6	6	0.032084
444.8879	6.50E+07	21.4980485	24.28413	6	6	0.19287
447.4759	2.90E+07	18.6565198	21.4264882	4	2	0.043528
448.1811	4.55E+07	18.7324382	21.4980485	6	6	0.13702

Argon Single Ion Lines Simulated						
λ [nm]	A_{ij} [s^{-1}]	E_i [eV]	E_j [eV]	g_i	g_j	f_{ij}
453.0552	2.10E+06	18.6159413	21.3517985	6	4	0.0043081
454.5052	4.71E+07	17.1400263	19.8671558	4	4	0.14587
456.4405	2.90E+07	19.9674978	22.683064	4	2	0.045289
457.935	8.00E+07	17.2658324	19.9725369	2	2	0.25151
458.9898	6.64E+07	18.4265479	21.1270321	4	6	0.31457
460.9567	7.89E+07	18.4541128	21.1430741	6	8	0.33511
463.7233	7.10E+06	18.4541128	21.1270321	6	6	0.022889
465.7901	8.92E+07	17.1400263	19.8010853	4	2	0.14507
472.1591	1.50E+07	19.9674978	22.5926622	4	4	0.050133
472.6868	5.88E+07	17.1400263	19.7622598	4	4	0.19696
473.2053	6.70E+06	18.7324382	21.3517985	6	4	0.014995
473.5906	5.80E+07	16.6438534	19.261083	6	4	0.13002
476.4865	6.40E+07	17.2658324	19.8671558	2	4	0.43568
480.602	7.80E+07	16.6438534	19.222901	6	6	0.2701
484.781	8.49E+07	16.7485279	19.3053437	4	2	0.14956
486.591	1.50E+07	19.9674978	22.5148025	4	6	0.079867
487.9864	8.23E+07	17.1400263	19.6800477	4	6	0.44072
488.9042	1.90E+07	17.2658324	19.8010853	2	2	0.068086
490.4752	3.70E+06	18.6159413	21.1430741	6	8	0.017792
493.3209	1.44E+07	16.7485279	19.261083	4	4	0.052539
496.508	3.94E+07	17.2658324	19.7622598	2	4	0.29123
500.9334	1.51E+07	16.7485279	19.222901	4	6	0.085209
501.7163	2.07E+07	18.6565198	21.1270321	4	6	0.11717
506.2037	2.23E+07	16.8124712	19.261083	2	4	0.17133
514.1783	8.10E+06	18.7324382	21.1430741	6	8	0.042806
514.5308	1.06E+07	17.1400263	19.5490106	4	6	0.063107
611.4923	2.00E+07	19.1160678	21.1430741	10	8	0.089693
617.2278	2.00E+07	19.1188611	21.1270321	8	6	0.085672
624.312	3.00E+06	17.6946637	19.6800477	8	6	0.013147
648.3082	1.06E+07	18.0606387	19.9725369	4	2	0.033396

Argon Single Ion Lines Simulated						
λ [nm]	A_{ij} $[s^{-1}]$	E_i [eV]	E_j [eV]	g_i	g_j	f_{ij}
663.8221	1.37E+07	17.7430899	19.6103067	6	4	0.060338
663.974	1.69E+07	17.7757915	19.6425808	4	2	0.055849
664.3698	1.47E+07	17.6288553	19.4945327	10	8	0.077819
666.6359	8.80E+06	17.9417499	19.8010853	2	2	0.05863
668.4293	1.07E+07	17.6946637	19.5490106	8	6	0.053754
686.1269	2.40E+06	18.0606387	19.8671558	4	4	0.016939
738.0426	5.60E+06	18.2880541	19.9674978	4	4	0.045731

Appendix E

CRM Simulated Xenon Emission Lines

The Xenon C-R model simulates the intensity of 39 Xenon neutral and 23 Xenon single ion emission lines. This section lists the relevant data for all the lines being simulated by the C-R model.

The first column presents the wavelength of the simulated emission line in nm. The second column presents Einstein's spontaneous emission transition coefficient values employed by the C-R model. Columns three and four represent the lower and upper energy levels for the line transition, respectively. Columns five and six present the degeneracies for the lower and upper energy levels, respectively. The listed values are adapted from the online National Institute of Standards and Technology (NIST) Atomic Spectra Database [3], from Pfrommer [68], and from Malovic et al. [59]. Column seven presents the corresponding absorbtion oscillator strength values calculated using equation 6.22.

Xenon Neutral Lines Simulated						
λ [nm]	A_{ij} [s^{-1}]	E_i [eV]	E_j [eV]	g_i	g_j	f_{ij}
105.612829	2.45E+08	0	11.739501	1	3	0.12291
106.125564	1.90E+07	0	11.682783	1	3	0.0096244
106.8168	3.99E+08	0	11.60718	1	3	0.20475
108.5441	4.10E+07	0	11.422451	1	3	0.021726
109.9716	4.34E+07	0	11.274184	1	3	0.023606
111.0713	1.50E+08	0	11.162564	1	3	0.083229
112.931	4.40E+06	0	10.978772	1	3	0.0025238
117.0413	1.60E+08	0	10.593211	1	3	0.098577
119.2037	6.20E+08	0	10.40103	1	3	0.39623
125.021	1.40E+07	0	9.9170761	1	3	0.0098417
129.5588	2.46E+08	0	9.5697248	1	3	0.18571
146.961	2.81E+08	0	8.4365236	1	3	0.27295
450.0978	1.44E+06	8.3153155	11.069148	5	3	0.0026241
452.46805	3.50E+05	8.3153155	11.054723	5	5	0.0010742
458.27472	1.31E+06	8.4365236	11.141221	3	1	0.0013749
462.42756	1.28E+06	8.3153155	10.995724	5	5	0.0041035
467.12258	3.16E+06	8.3153155	10.968784	5	7	0.014472
473.41518	1.11E+06	8.4365236	11.054723	3	5	0.006216
480.7019	3.29E+06	8.4365236	11.015035	3	1	0.0037991
482.9708	1.29E+06	8.4365236	11.002922	3	3	0.0045112
581.4505	9.30E+05	9.6856199	11.817355	5	5	0.0047137
619.826	6.60E+05	9.5801524	11.579907	3	5	0.0063356
631.8062	2.70E+06	9.7207401	11.682574	7	9	0.020775
684.6613	2.60E+06	9.6856199	11.496004	5	5	0.018272
688.2155	6.12E+06	9.6856199	11.486655	5	7	0.060839
711.9598	8.39E+06	9.7207401	11.461709	7	9	0.081974
728.5301	4.09E+06	9.7892996	11.490671	3	5	0.054241
739.3793	4.89E+06	9.8210934	11.4975	5	7	0.056108

Xenon Neutral Lines Simulated						
λ [nm]	A_{ij} [s^{-1}]	E_i [eV]	E_j [eV]	g_i	g_j	f_{ij}
788.7393	2.37E+07	9.5697248	11.141221	3	1	0.07368
796.7342	4.21E+06	9.4471945	11.002922	1	3	0.1202
823.16336	2.48E+07	8.3153155	9.8210934	5	5	0.25193
828.01162	3.70E+07	8.4365236	9.9334847	3	1	0.12677
834.68217	2.78E+07	9.5697248	11.054723	3	5	0.48394
840.91894	2.39E+06	8.3153155	9.7892996	5	3	0.015202
881.94106	3.22E+07	8.3153155	9.7207401	5	7	0.52568
895.22509	8.98E+06	8.4365236	9.8210934	3	5	0.17982
904.54466	1.12E+07	8.3153155	9.6856199	5	5	0.13738
916.2652	2.65E+07	8.4365236	9.7892996	3	3	0.33354
979.9697	2.69E+07	8.3153155	9.5801524	5	3	0.23237

Xenon Single Ion Lines Simulated						
λ [nm]	A_{ij} [s^{-1}]	E_i [eV]	E_j [eV]	g_i	g_j	f_{ij}
433.052	1.40E+08	14.073738	16.935969	6	8	0.52481
441.484	1.00E+08	13.584097	16.391672	6	6	0.2922
460.303	8.20E+07	11.78648	14.479257	4	4	0.26047
484.433	1.10E+08	11.53902	14.097672	6	8	0.51601
487.65	6.30E+07	13.584097	16.125875	6	8	0.29947
526.044	2.20E+07	12.925359	15.281622	2	4	0.18254
526.195	8.50E+07	14.000895	16.356464	4	4	0.35283
529.222	8.90E+07	11.53902	13.881132	6	6	0.3737
533.933	1.88E+08	11.53902	13.860462	6	4	0.53567
537.239	7.10E+07	11.78648	14.093641	4	2	0.15361
541.915	6.20E+07	11.78648	14.073738	4	6	0.40945
543.896	7.40E+07	12.745459	15.024379	4	2	0.16409
547.261	9.90E+06	11.83276	14.097672	8	8	0.044451
553.107	8.80E+06	11.83276	14.073738	8	6	0.03027
571.961	6.10E+06	11.90663	14.073738	4	6	0.044876
597.646	2.80E+07	11.78648	13.860462	4	4	0.14993
603.62	7.50E+06	11.82769	13.881132	6	6	0.040968
605.115	1.70E+07	11.83276	13.881132	8	6	0.069991
609.759	2.60E+07	11.82769	13.860462	6	4	0.096617
627.082	1.80E+07	14.000895	15.977495	4	6	0.15917
627.754	3.60E+06	11.90663	13.881132	4	6	0.031903
680.574	6.10E+06	13.442747	15.264009	8	6	0.031769
699.088	2.70E+07	12.32465	14.097672	10	8	0.15826

Bibliography

[1] Charged coupled device (CCD) image sensors. Eastman Kodak Company, Iamge Sensor Solutions, Rochester, NY, 2001.

[2] *Photomultiplier Tubes, Basics and Applications, 3rd Edition*. Hamamatsu Photonics, Hamamatsu City, Japan, 2006.

[3] NIST atomic spectra database, V.3.1.0. Available from http://www.physics.nist.gov/PhysRefData/ASD/index.html, 2007.

[4] D. Arnush and F. F. Chen. Generalized theory of helicon waves. II. excitation and absorption. *Physics of Plasmas*, 5(5), 1998.

[5] J. Bacri and A. M. Gomes. Influence of atom-atom collisions on thermal equilibrium in argon arc discharges at atmospheric pressure. *Journal of Physics, D: Applied Physics*, 11, 1978.

[6] D. R. Bates, A. E. Kingston, and R. W. P. McWhirter. Recombination between electrons and atomic ions. I. optically thin plasmas. *Proceedings of Royal Society of London*, (1330), 1962.

[7] D. R. Bates, A. E. Kingston, and R. W. P. McWhirter. Recombination between electrons and atomic ions. II. optically thick plasmas. *Proceedings of Royal Society of London*, (1341), 1962.

[8] O. Batishchev, J. Pucci, N. Sinenian, Z. LaBry, M. Celik, and M. Martinez-Sanchez. Mini-helicon thruster experiment at MIT. In 48^{th} *Annual Meeting of the Division of Plasma Physics*, Philadelphia, PA, October 2006. Bulletin APS, 51 (7) 224.

[9] B. E. Beal, A. D. Gallimore, J. M. Haas, and W. A. Hargus. Plasma properties in the plume of a hall thruster cluster. *Journal of Propulsion and Power*, 20(6):985–991, 2004.

[10] B. E. Beal, A. D. Gallimore, and W. A. Hargus. Plasma properties downstream of a low-power hall thruster. *Physics of Plasmas*, 12(123503), 2005.

[11] V. Blateau, M. Martinez-Sanchez, O. Batishchev, and J. Szabo. PIC simulation of high specific impulse hall effect thruster. In 27^{th} *International Electric Propulsion Conference*, Pasadena, CA, October 2001. also IEPC–01–037.

[12] A. Bogaerts, R. Gijbels, and J. Vlcek. Collisional-radiative model for an argon glow discharge. *Journal of Applied Physics*, 84(1):121–135, 1998.

[13] R. W. Boswell and Francis F. Chen. Helicon - the early years. *IEEE Transactions on Plasma Science*, 25(6):1229–1244, 1997.

[14] I. D. Boyd and J. T. Yim. Modeling of the near field plume of a hall thruster. *Journal of Applied Physics*, 95(9):4575–4584, 2004.

[15] A. I. Bugrova, A. M. Bishaev, A. V. Desyatskov, and M. V. Kozintseva. Spectral investigation of SPT MAG insulator erosion. In 29^{th} *International Electric Propulsion Conference*, Princeton, NJ, November 2005. also IEPC–2005–167.

[16] A. Bultel, B. van Ootegem, A. Bourdon, and P. Vervisch. Influence of Ar_2^+ in argon collisional-radiative model. *Physical Review E*, 65, 2002.

[17] C. Cai, I. D. Boyd, and Q. Sun. Three-dimensional particle simulation of plume flows from hall thrusters. In 29^{th} *International Electric Propulsion Conference*, Princeton, NJ, November 2005. also IEPC–2005–048.

[18] M. Celik, O. Batishchev, and M. Martinez-Sanchez. Application of spectroscopic measurements to electrical propulsion. In 48^{th} *Annual Meeting of the Division of Plasma Physics*, Philadelphia, PA, October 2006. Bulletin APS, 51 (7) 328.

[19] M. Celik and M. Martinez-Sanchez. Numerical simulation of the electric thruster plume environment around the TPF spacecraft. In 41^{st} *Joint Propulsion Conference and Exhibit*, Tucson, AZ, July 2005. also AIAA–2005–4046.

[20] M. Celik and M. Martinez-Sanchez. Plume effects on radiation detection by spacecraft. In 29^{th} *International Electric Propulsion Conference*, Princeton, NJ, November 2005. also IEPC–2005–193.

[21] M. Celik and T. D. Pigeon M. Martinez-Sanchez. Studies on the interaction of the terrestrial planet finder spacecraft with thruster plumes. In 40^{th} *Joint Propulsion Conference and Exhibit*, Forth Lauderdale, FL, July 2004. also AIAA–2004–3637.

[22] M. Celik, M. M. Santi, S. Y. Cheng, M. Martinez-Sanchez, and J. Peraire. Hybrid-PIC simulation of a hall thruster plume on an unstructured grid with DSMC collisions. In 28^{th} *International Electric Propulsion Conference*, Toulouse, France, March 2003. also IEPC–03–134.

[23] S. C. Chapra and R. P. Canale. *Numerical Methods for Engineers, Fourth Edition*. McGraw Hill, 2002.

[24] F. F. Chen and D. Arnush. Generalized theory of helicon waves. I. normal modes. *Physics of Plasmas*, 4(9), 1997.

[25] Shannon Yun-Ming Cheng. Modeling of hall thruster lifetime and erosion mechanisms. Ph.D. Thesis, Massachusetts Institute of Technology, Cambridge, MA, *in preperation*.

[26] Shannon Yun-Ming Cheng. Computational modeling of a hall thruster plasma plume in a vacuum tank. M.S. Thesis, Massachusetts Institute of Technology, Cambridge, MA, 2002.

[27] Y. Chiu, B. L. Austin, S. Williams, R. A. Dressler, and G. F. Karabadzhak. Passive optical diagnostics of Xe-propelled Hall thrusters. I. emission cross sections. *Journal of Applied Physics*, 99(113304), 2006.

[28] E. Y. Choueiri. Fundamental difference between the two hall thruster variants. *Physics of Plasmas*, 2001.

[29] E. Y. Choueiri and R. G. Jahn. Electric propulsion. *Encyclopedia of Physical Science and Technology, Third Edition*, 5, 2002.

[30] G. Colonna, L. D. Pietanza, and M. Capitelli. A collisional-radiative model Xe electric thruster. In 31^{st} *AIAA Plasmadynamics and Laser Conference*, Denver, CO, June 2000. also AIAA–2000–2349.

[31] M. W. Crofton. New laser applications for electric propulsion. In 27^{th} *International Electric Propulsion Conference*, Pasadena, CA, October 2001. IEPC-2001-305.

[32] F. R. Chang Diaz, J. P. Squire, E. A. Bering, J. A. George, A. V. Ilin, A. J. Petro, and L. Cassady. The VASIMR engine approach to solar system exploration. In 39^{th} *AIAA Aerospace Sciences Meeting and Exhibit*, Reno, NV, January 2001. also AIAA–2001–0960.

[33] G. W. F. Drake. *Aromic, Molecular, and Optical Physics Handbook*. AIP Press, New York, 1996.

[34] H. W. Drawin. Atomic cross-sections for inelastic electronic collisions. *Report EUR-CEA-FC*, 1963.

[35] H. W. Drawin and K. Katsonis. Fontenay-aux-roses report. EUR-CEA-FC-837, 1976.

[36] E. N. Dyshlyuk and O. A. Gorshkov. Spectroscopic investigation of a hall thruster ceramic acceleration channel erosion rate. In 42^{nd} *Joint Propulsion Conference and Exhibit*, Sacramento, CA, July 2006. also AIAA–2006–4660.

[37] David Eberly. Special functions. Available from http://www.geometrictools.com/Documentation/SpecialFunctions.pdf, 1999.

[38] J. T. Fons and C. C. Lin. Measurement of the cross sections for electron-impact excitation into the $5p^5 6p$ levels of xenon. *Physical Review A*, 58(6), 1998.

[39] M. Gamero-Satano and I. Katz. Estimation of hall thruster erosion using HPHall. In 29^{th} *International Electric Propulsion Conference*, Princeton, NJ, November 2005. IEPC-2005-303.

[40] Tanya Cruz Garza. Optimizing wettability of externally wetted microfabricated silicon electrospay thrusters. M.S. Thesis, Massachusetts Institute of Technology, Cambridge, MA, 2007.

[41] D. Gawron, S. Mazouffre, L. Albarede, and N. Sadeghi. Examination of hall effect thruster acceleration layer characteristics by laser spectroscopy and repulsing potential analyzer. In 42^{nd} *Joint Propulsion Conference and Exhibit*, Sacramento, CA, July 2006. also AIAA–2006–4473.

[42] D. M. Goebel, K. K. Jameson, R. M. Watkins, I. Katz, and I. G. Mikellides. Hollow cathode theory and experiment. I. plasma characterization using fast miniature scanning probes. *Journal of Applied Physics*, 98(113302), 2005.

[43] A. M. Gomes. Criteria for partial LTE in an argon thermal discharge at atmospheric pressure; validity of the spectroscopically measured electronic temperature. *Journal of Physics, D: Applied Physics*, 16, 1983.

[44] H. R. Griem. *Plasma Spectroscopy*. McGraw-Hill, Inc., New York, NY, 1964.

[45] D. J. Griffiths. *Introduction to Quantum Mechanics*. Prentice Hall, Upper Saddle River, NJ, 1995.

[46] M. Gryzinski. Classical theory of atomic collisions I. theory of inelastic collisions. *Physical Review*, 138(2), 1965.

[47] F. S. Gulczinski and A. D. Gallimore. Near-field ion energy and species measurements of a 5-kW hall thruster. *Journal of Propulsion and Power*, 17(2):418–427, 2001.

[48] W. A. Hargus and J. Strafaccia. Optical boron nitride insulator erosion characterization of a 200 W xenon hall thruster. In 41^{st} *Joint Propulsion Conference and Exhibit*, Tucson, AZ, July 2005. also AIAA–2005–3529.

[49] R. H. Huddlestone and S. L. Leonard. *Plasma Diagnostics Techniques*. Academic Press, New York, 1965.

[50] I. H. Hutchinson. *Principles of Plasma Diagnostics*. Cambridge University Press, Cambridge, UK, 2002.

[51] G. F. Karabadzhak, Y. Chiu, and R. A. Dressler. Passive optical diagnostics of Xe propelled Hall thrusters. II. collisional-radiative model. *Journal of Applied Physics*, 99(113305), 2006.

[52] G. F. Karabadzhak, Y.-H. Chiu, S. Williams, and R. A. Dressler. Hall thruster optical emission analysis based on single collision luminescence spectra. In 37^{th} *Joint Propulsion Conference*, Salt Lake City, UT, July 2001. also AIAA–2001–3893.

[53] G. F. Karabadzhak, A. V. Semenkin, A. E. Solodukhin, and O. S. Teverdokhlebov. Evaluation of impurity composition and content in the TAL at various operating regimes. In 29^{th} *International Electric Propulsion Conference*, Princeton, NJ, November 2005. IEPC-2005-147.

[54] G. F. Karabadzhak, A. V. Semenkin, O. S. Teverdokhlebov, and D. Manzella. Investigation of TAL optical emissions. In 25^{th} *International Electric Propulsion Conference*, Cleveland, OH, August 1997. IEPC-97-131.

[55] K. Katsonis, C. Boisse-Laporte, J. Bonnet, S. Letout, and A. Siskos. C-R modeling and spectroscopic diagnostics of SPT plasmas. In 4^{th} *International Spacecraft Propulsion Conference*, Cagliari, Sardinia, Italy, June 2004.

[56] L. B. King and A. D. Gallimore. Mass spectral measurements in the plume of an SPT-100 hall thruster. *Journal of Propulsion and Power*, 16(6):1086–1092, 2000.

[57] K. Krane. *Modern Physics, 2nd Edition*. John Wiley and Sons, Inc., New York, 1996.

[58] P. Leray, J. Bonnet, D. Pigache, T. Minea, J. Bretagne, and M. Touzeau. Spatially resolved emission spectroscopy along a SPT channel: Interpretation of data by a collisional-radiative model. In 25^{th} *International Electric Propulsion Conference*, Cleaveland, OH, August 1997. also IEPC–97–054.

[59] G. N. Malovic, A. I. Strinic, Z. Lj. Petrovic, J. V. Boin, and S. S. Manola. Electron excitation coefficients for 2p and 3p levels of Xe. *European Physical Journal D*, 10(1):147–151, 2000.

[60] D. H. Manzella. Stationary plasma thruster plume emissions. In 23^{th} *International Electric Propulsion Conference*, 1993. also IEPC–93–097.

[61] M. Martinez-Sanchez and J. E. Pollard. Spacecraft electric propulsion - an overview. *Journal of Propulsion and Power*, 14(5):688–699, 1998.

[62] S. Mazouffre, D. Pagnon, and J. Bonnet. Two ways to evaluate the xe^+ ion flow velocity in a hall effect thruster: LIF spectroscopy and fabry-perot interferometry. In 40^{th} *Joint Propulsion Conference and Exhibit*, Forth Lauderdale, FL, July 2004. also AIAA–2004–3949.

[63] I. G. Mikellides, I. Katz, D. M. Goebel, and J. E. Polk. Hollow cathode theory and experiment. II. a two-dimensinal theoretical model of the emitter region. *Journal of Applied Physics*, 98(113303), 2005.

[64] M. Mitchner and C. H. Kruger. *Partially Ionized Gases*. John Wiley and Sons, Inc., 1973.

[65] Anne Pacros. Instrument design and testing for a hall thruster plume experiment on the space shuttle. M.S. Thesis, Massachusetts Institute of Technology, Cambridge, MA, 2002.

[66] D. Pagnon, P. Lasgorceix, and M. Touzeau. Control of the ceramic erosion by optical emission spectroscopy: Results of PPS1350-G measurements. In 4^{th} *International Spacecraft Propulsion Conference*, Cagliary, Sardinia, Italy, June 2004.

[67] C. Palmer. *Diffraction Grating Handbook, 5th Edition*. Newport Corporation, 2005.

[68] Thomas Pfrommer. Charakterisierung eines Xenon-mirowellenplasmas mittels optischer diagnostikverfahren und elektrostatischer sonden. Ph.D. Thesis, Univeristy of Stuttgart, Stuttgart, Germany, 2005.

[69] J. M. Pucci, N. Sinenian, J. Palaia, M. Celik, Z. LaBry, A. Shabshelowitz, O. Batishchev, and M. Martinez-Sanchez. Preliminary characterization of a helicon plasma source for space propulsion. In 42^{nd} *Joint Propulsion Conference and Exhibit*, Sacramento, CA, July 2006. also AIAA–2006–5255.

[70] M. M. Santi, S. Y. Cheng, M. Celik, M. Martinez-Sanchez, and J. Peraire. Further development and preliminary results of the AQUILA hall thruster plume model. In 39^{th} *Joint Propulsion Conference*, Huntsville, AL, July 2003. also AIAA–2003–4873.

[71] Mark Michael Santi. Hall thruster plume simulation using a hybrid-pic algorithm. M.S. Thesis, Massachusetts Institute of Technology, Cambridge, MA, 2003.

[72] Eric James Sheppard. Ionizational nonequilibrium and ignition in self-field magnetoplasmadynamic thrusters. D.Sc. Thesis, Massachusetts Institute of Technology, Cambridge, MA, 1994.

[73] E. Sommier, M. K. Allis, and M. A. Cappelli. Wall erosion in 2D hall thruster simulations. In 29^{th} *International Electric Propulsion Conference*, Princeton, NJ, November 2005. IEPC-2005-189.

[74] J. Vlcek. A collisional-radiative model applicable to argon discharges over a wide range of conditions I: Formulation and basic data. *Journal of Physics, D: Applied Physics*, 22, 1989.

[75] J. Vlcek and V. Pelikan. Electron energy distribution function in the collisional radiative model of an argon plasma. *Journal of Physics, D: Applied Physics*, 18, 1985.

[76] N. Z. Warner and M. Martinez-Sanchez. Design and preliminary testing of a miniaturized TAL hall thruster. In 42^{nd} *Joint Propulsion Conference and Exhibit*, Sacramento, CA, July 2006. also AIAA–2006–4994.

[77] Noah Zachary Warner. Theoretical and experimental investigation of hall thruster miniaturization. Ph.D. Thesis, Massachusetts Institute of Technology, Cambridge, MA, *in preperation.*

[78] Noah Zachary Warner. Performance testing and internal probe measurements of a high specific impulse hall thruster. M.S. Thesis, Massachusetts Institute of Technology, Cambridge, MA, 2003.

[79] M. W. Winter, M. Auweter-Kurtz, T. Pfrommer, and N. Semenova. Plasma diagnostics on Xenon for application to ion thrusters. In 29^{th} *International Electric Propulsion Conference*, Princeton, NJ, November 2005. IEPC-2005-079.

[80] A. Yanguas-Gil, J. Cotrino, and A.R. Gonzales-Elipe. Collisional-radiative model of an argon atmospheric capillary surface-wave discharge. *Physics of Plasmas*, 11(12), 2004.

[81] J. T. Yim, M. Keidar, and I. D. Boyd. An investigation of factors involved in hall thruster wall erosion modeling. In 42^{nd} *Joint Propulsion Conference and Exhibit*, Sacramento, CA, July 2006. also AIAA–2006–4657.

[82] D. Yu, Y. Li, and S. Song. Ion sputtering erosion of channel wall corners in hall thrusters. *Journal of Physics D: Applied Physics*, 39, 2006.

[83] T. Ziemba, J. Carscadden, J. Slough, J. Prager, and R. Winglee. High power helicon thruster. In 41^{st} *Joint Propulsion Conference and Exhibit*, Tucson, AZ, July 2005. also AIAA–2005–4119.